Developing Multiscale Methodologies for Computational Fluid Mechanics

Hammad Alotaibi
Supervisors: Prof. Anthony Roberts & Dr. Barry Cox

June 29, 2017

Thesis submitted for the degree of
Doctor of Philosophy
in
Applied Mathematics
at The University of Adelaide
Faculty of Engineering, Computer and Mathematical Sciences
School of Mathematical Sciences

SUB CRUCE LUMEN
THE UNIVERSITY
of ADELAIDE

Contents

Signed Statement

I certify that this work contains no material which has been accepted for the award of any other degree or diploma in my name, in any university or other tertiary institution and, to the best of my knowledge and belief, contains no material previously published or written by another person, except where due reference has been made in the text. In addition, I certify that no part of this work will, in the future, be used in a submission in my name, for any other degree or diploma in any university or other tertiary institution without the prior approval of the University of Adelaide and where applicable, any partner institution responsible for the joint-award of this degree. I give consent to this copy of my thesis, when deposited in the University Library, being made available for loan and photocopying, subject to the provisions of the Copyright Act 1968. I also give permission for the digital version of my thesis to be made available on the web, via the Universitys digital research repository, the Library Search and also through web search engines, unless permission has been granted by the University to restrict access for a period of time.

Signed: Hammad Alotaibi Date: June 27, 2017

Acknowledgements

I gratefully acknowledge the people who have made this thesis possible. First of all I express my deepest appreciation to my supervisors Prof. Tony Roberts and Dr. Barry Cox for their expert guidance, insightful comments and incredible attention to detail for this dissertation. Without their informal approach, unwavering support, never ending advice and countless appointments, this thesis would never have been possible.

Special thanks to Tony Roberts who has been my guide and philosopher since I did my master degree and who gave me the chance to undertake research for my Ph.D in the field of applied mathematics. I thank people in the Mathematical School, for their help and for attending my presentations. I acknowledge the Mathematical School of the Adelaide University providing a good environment for this research. I would also like to thank Taif University for the awarding of a Ph.D Scholarship.

Abstract

The development of multiscale computational methods is a key research area in mathematics, physics, engineering and computer science. Engineers and scientists often perform detailed microscale computational simulations of a large scale complicated spatio-temporal system. For most problems of practical interest, there are two major complications in simulating the dynamical behaviour on large macroscopic space-time scales. The first is the often prohibitive computational cost when only a microscopic model is available. The second complication is the memory constraints which often make the simulation over the whole domain of interest infeasible. To overcome these obstacles, the equation-free approach was proposed by Keverkidis and colleagues in 2000. This approach is a multiscale method for capturing the behaviour on large scales of some complicated systems using only relatively small bursts of the microscale models. The patch dynamics scheme was proposed as an essential component of the equation-free framework. The patch scheme promises a great saving in computation time by predicting the macroscopic dynamics using detailed microscopic computation only on relatively small widely distributed patches of the spatial domain. This thesis provides mathematical analysis and computational simulation of some basic atom dynamics on small patches. The most significant novel result of this research is that patches with microscale periodic boundary conditions can be used to efficiently predict macroscale properties of interest. This result is important because microscale computations are often easiest with microscale periodic boundary conditions. As a major test of the approach, we analyse, implement and evaluate such a scheme for a computationally intensive atomistic simulation.

Chapter 1 of this dissertation introduces the challenge of multiscale problems and highlights some recent developments of multiscale methods for complex systems. Chapter 2 explores atomistic simulations in three-dimensional space. The microscale atomistic simulator is used to predict a macroscale temperature field. This is achieved by performing atomistic simulation on a small triply-periodic patch. The method uses locally averaged properties

over small space-time scales to advance and predict relatively large space scale dynamics. Our ultimate aim for this chapter is to explore the macroscopic properties of a system through atomistic simulation in small periodic patches, but as a pilot study this thesis only considers one small patch coupled over the macroscale to boundaries. The computation is implemented only on the periodic patch, while over most of the domain we interpolate in order to predict the macroscale temperature. The thesis develops appropriate control terms to the microscale action regions of the patch. The control is applied to the left and right action regions surrounding a core region. A proportional controller dependent upon the relatively distant boundaries enables reasonably accurate macroscale predictions. The analysis and computational simulations indicate that this innovative patch scheme empowers computation of large scale simulations of microscale systems.

Chapter 3 analyses the case of a one-dimensional microscale diffusion system in a single microscale patch to predict the macroscale dynamics over a comparatively large spatial region. The nature of the solutions of the patch scheme is explored when operating with time-varying boundary conditions that mimic coupling with neighbouring, dynamically varying patches. The patch eigenfunctions and their adjoints form a biorthogonal basis to determine the spectral coefficients in formal series solutions. We also explore this patch scheme with time delays in the communication of boundary values. This models a patch when information from the neighbouring patches is subject to communication delays. The delayed patch scheme prediction is compared with a scheme without delays to delineate when such delays are significant.

Chapter 4 analyses diffusion dynamics on multiple coupled patches. Centre manifold theory supports the patch scheme. The patch coupling conditions are standard Lagrange interpolation from the macroscale values at the centre of surrounding patches to the boundaries of each patch. The results of this chapter demonstrate the feasibility of the microscale patch scheme to model diffusion over large spatial scales.

Chapter 5 extends the analysis to one-dimensional microscale advection-diffusion dynamics in a single patch and for multiple patches. Eigenvalue analysis suggests that a slow manifold exists on the macroscale. Computer algebra constructs the slow manifold model for the advection-diffusion dynamics. The long-time dynamics behaviour of numerical solutions on one patch is compared with the prediction of the slow manifold. Comparisons among the patch dynamics scheme, the microscale model over the complete domain, and published experimental data determines regimes where the patch dynamics accurately predicts the large scale advection-diffusion dynamics.

Chapter 1

Introduction

1.1 Multiscale methods

In recent years there has been a growing interest in the development of multiscale modelling and computation, with applications in many areas including materials science, fluid mechanics, chemistry, and biology (E & Engquist 2003, Lucia 2010, Fish 2010, e.g.). Problems in these areas generally involve multiple length scales in time and space. In addition, multiscale problems are often multiphysics in nature which makes the transfer of information between different scales challenging, particularly when the processes at different scales are governed by physical laws with different characters. An example is molecular dynamics at the microscale, and continuum mechanics at the macroscale (E & Engquist 2003, Bunder et al. 2013, e.g.). Molecular dynamics simulations at the fine scale are constrained to limited space-time domains due to the high computational cost. One aim of Chapter 2 is to circumvent such limitations (by restricting microscale simulations to small computational domains) and enable molecular dynamics simulations to make accurate and efficient predictions of the macroscale dynamics at large space-time scales.

Over the past few centuries, engineers and scientists have successfully described many physical phenomena in a quantitative manner using macroscopic models that coarsely parameterise microscopic mechanisms (Nielsen et al. 2003, e.g.). One of the popular examples of such models is partial differential equations (PDEs), which typically only use some specific average properties of particles such as density, momentum and energy. In spite of this parameterisation, PDE models still capture most macroscopic effects exhibited in these systems (Luna-Ortiz & Theodoropoulos 2005, e.g.).

Examples of macroscopic models are the commonly used continuum models (the Navier–Stokes equations) of fluid flow, heat transfer, and mass transfer (Nielsen et al. 2003, Fish 2010, E 2011, e.g.). Such macroscopic models describe the evolution of density (momentum and thermodynamic potentials) in space and time, while the basic laws of motion of each particle have disappeared.

Despite their tremendous successes, macroscopic models are limited in accuracy for some important classes of problems (Galvanetto & Aliabadi 2010, E et al. 2007, E 2011, Murashima et al. 2012, e.g.). This limited accuracy is especially problematic for complex systems such as polymeric fluids, liquid crystals and surfactant systems. When the modelling error is larger than the solution error, the effectiveness of the macroscopic model becomes an issue. Another limitation of macroscopic models is that discretisation at a coarse level ignores the fine scale features and processes, such as those occurring at the nanometer and femtosecond scales (E 2011, e.g.). That is, macroscopic models do not always explain the underlying physical, chemical or biological mechanisms in enough detail. For instance, in polymeric fluids, we are often interested in the microstructural information such as the conformation of the polymers, not only the macroscopic flow field (Murashima et al. 2012, e.g.).

These limitations have often guided researchers and physicists toward microscopic models that provide more physical descriptions and insight than a simple descriptive macroscopic model. Examples of such microscopic models include molecular dynamics (Schlick 2010, e.g.), kinetic Monte Carlo (Gillespie 1976), and lattice Boltzmann models (Succi 2001, e.g.). However, in most problems across all fields ranging from ecology to materials science, and from chemistry to engineering, these microscopic models operate on vastly different scales in time and space compared to the time-scales at which the overall system evolves (Dolbow et al. 2004, e.g.).

These systems that depend inherently on physical processes at multiple spatial and temporal scales pose notorious difficulties. These multiscale challenges constitute a major stumbling block to future progress in fields of science and engineering as diverse as environmental and geosciences, climate, materials, combustion, high energy density physics, fusion, bioscience, chemistry, and networks (Dolbow et al. 2004). Since a direct fully detailed numerical simulation is typically prohibitively expensive, the traditional technique is to analytically derive an effective model that is valid at the scale of interest, and neglect other scales by assuming there is nothing relevant happening in such scales in the problem.

Depending on the form of the microscopic model, many mathematical techniques have been developed to study multiscale problems, including homogenisation (Pavliotis & Stuart 2008, e.g.), boundary layer analysis (Kevorkian & Cole 2012, e.g.), averaging methods in classical mechanics (Arnol'd 2013, e.g.), inertial manifold theory (Constantin et al. 2012, Gorban & Karlin 2005, e.g.), and semiclassical methods (Maslov & Fedoriuk 2001, e.g.).

Distributed microstructure models, also called double porosity or dual porosity models, (Carr & Turner 2014, Lewandowska et al. 2004, Showalter 1997, Szymkiewicz & Lewandowska 2008, e.g.) are also among the multiscale models with concurrent coupling (Broughton et al. 1999, e.g.). This approach is applicable to the specific case where the domain is composed of two sub-domains occupied by homogeneous material where one is connected and the other forms isolated inclusions. Based on the homogenisation approach, Lewandowska et al. (2004) presents a macroscopic model (mathematical and numerical) of water flow in unsaturated double-porosity soils. This method is able to derive the macroscopic model and its effective parameters from a description of physical phenomena at the local scale, without any a priori hypothesis for the functional form of the model.

From a modern perspective, major concerns of the computational techniques are the efficient representation or solution of the fine-scale problem. For many practical problems, full representation of the fine-scale solution is unlikely to be achieved in the foreseeable future due to unacceptably long computation times and large memory requirements (Miyoshi et al. 2014, Nguyen et al. 2014, Ortega et al. 2013, Kiuchi et al. 2014, e.g.). Without aiming to be complete, the following Section 1.2 overviews recent multiscale approaches that propose efficient solutions to some of these issues.

1.2 A new class of multiscale methods

This section discusses the key attributes of developing multiscale methods for studying the long-time evolution of complex systems. Section 1.2.1 begins with a brief history and description of the equation-free approach and its main components. By explicitly taking advantage of the separation of scales, the gap-tooth (Section 1.2.2) and patch (Section 1.2.3) schemes make the equation-free approach more efficient in computational multiscale methods.

1.2.1 The equation-free approach

Recently, we have seen an explosive growth of activities in developing a systematic framework for multiscale methods, based on the idea that, for some appropriate set of macroscopic variables, although closed form model descriptions conceptually exist, we cannot obtain this description explicitly in closed form (Cisternas et al. 2004, e.g.). Such problems occur in molecular dynamics when the atomistic potential is not explicitly given, or in continuum simulations of complex fluids such as polymeric liquids in which the constitutive relations are unknown (Murashima et al. 2012, e.g.). In this scenario, Kevrekidis et al. (2003) forego closed form model descriptions and use microscopic models as if they were almost black boxes or experiments that result from wrapping software around whatever simulator has been provided. The aim of the equation-free approach is to efficiently capture the macroscale behaviour of a system by using only the underlying microscopic models. The approach makes use of scale separation between macroscale and microscale time to ensure a quick relaxation to functionals of the coarse macrostates. Scale separation is done by restricting the size of the spatio-temporal domain over which the microscale models are simulated—as in the Knap–Ortiz version of the quasicontinuum method (Knap & Ortiz 2001, e.g.) and the Prendergast–Xu version of the kinetic scheme (Xu & Prendergast 1994, e.g.). Such scale separation is an effective strategy for potentially reducing the expensive numerical simulations of complicated systems over large physical domains.

The equation-free approach requires techniques including projective integrators (which are based on the idea of extrapolation) (Gear & Kevrekidis 2003, Kevrekidis et al. 2003, Hummer & Kevrekidis 2003, e.g.), the gap-tooth scheme and the patch scheme, which is the combination of the projective integrators and the gap-tooth scheme. The key to equation-free, multi-scale modelling is the two-way transformation between small-scale and large-scale lengths. Lifting is the process used to transfer from the large to the small scale length. Restricting, on the other hand, is the reverse transformation, from the small to the large scale. In space, the equation-free approach implements the gap tooth scheme where the microscopic simulation would be realised in small boxes (teeth). By using interpolation, the gaps in between these boxes are filled.

Inspired by the work of Kevrekidis et al. (2003), Frederix et al. (2007) introduced equation-free methods in molecular dynamics. Also, in other branches of science and engineering, Abdulle et al. (2012) recast the equation-free approach into an algorithm called the heterogeneous multiscale method as a general strategy for numerical problems with a multiphysics nature and multiscales. The heterogeneous multiscale method is also similar to the equation-free approach in terms of making use of scale separation.

Here I briefly review the basic setup of the heterogeneous multiscale method. Suppose we are interested in studying the macroscale behaviour of a system for which the macroscale model is either only partly known (lack the detailed constitutive relation) or it is invalid in some parts of the computational domain due to the presence of defects or localised singularities (E et al. 2007). However, we do have an accurate microscale model at our disposal, but it is too expensive to abandon the macroscale model completely and only perform microscopic simulations directly to attack problems with large spatial and temporal scales. When this is the case, the heterogeneous multiscale method starts by selecting a suitable numerical method for the macroscale model, as if the macroscale model is roughly known and valid in the whole physical domain, but some details of the model are missing. This method then focuses on how to obtain the necessary information to implement the selected macroscale numerical method. In some parts of the computational domain where the macroscale model is invalid, or where constitutive relations are missing, the microscopic model is solved locally to estimate the missing macroscopic data needed for the implementation of the macroscopic scheme (E et al. 2007). Scale separation can be shown by observing that in the data estimation step, the microscale computational domain is uncoupled from the macroscale physical domain. The heterogeneous multiscale method could be applied to the simulation of complex fluid where the advection of memory is neglected (Ren et al. 2005, e.g.). On the other hand, there are some difficulties in applying the heterogeneous multiscale method. The main shortcoming of this method is that it relies on some assumptions such as the appearance of macroscale model. The use of these assumptions is not only for selecting the macroscale solver, but also for formulating the constraints on the microscopic solver.

1.2.2 The gap-tooth scheme

The gap-tooth scheme was introduced by Kevrekidis et al. (2003) to address an important class of time dependent multiscale problems. Such problems are known to exhibit macroscopically smooth behaviour in time and space, while only a microscopic evolution law is known. This scheme is used instead of performing (stochastic) time integration in the entire physical domain. It is intended to provide smooth spatial descriptions on the large length scale from information inferred from the underlying microscopic simulation at the small scale.

The main idea of the gap-tooth scheme is to apply microscopic simulations restricted to small regions of space (teeth), separated by large gaps, followed by interpolation to estimate macroscopic fields in the gaps. Figure 1.1 shows an example by Roberts & Kevrekidis (2007) of gap-tooth simulation applied to Burgers' equation on the macroscale domain $[0, 2\pi]$ through the microscopic simulation within eight teeth; each of width $\pi/20$. The scheme couples the teeth effectively by bridging the gaps to describe the dynamics over the macroscale domain. Thus, the challenges are to explore the dy-

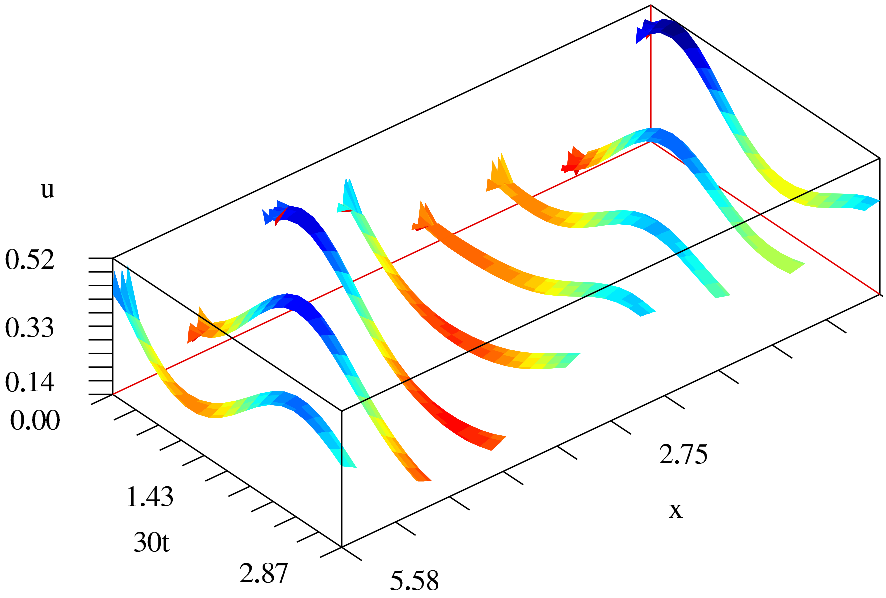

Figure 1.1: Gap-tooth solution of Burgers' equation on $[0, 2\pi]$ via microsimulation on eight teeth, each of small width $\pi/20$ (Roberts & Kevrekidis 2007).

namics inside a tooth and the coupling conditions that able to couple widely separated teeth of the microscopic simulation.

The fundamental issue in multiscale modelling and simulation relates to coupling between elements (Frauenheim et al. 2000, Deymier et al. 2016, e.g.). The dynamics of each tooth must be connected as seamlessly as possible. For this scenario, Roberts & Kevrekidis (2007) construct boundary conditions for coupling patches in the gap-tooth scheme to obtain higher order accurate schemes. One aim of Chapter 4 is to show that analogous coupling works straightforwardly for the diffusion PDE with time-varying boundary forcing. The boundary conditions for the microscopic patch are obtained by interpolating the macroscale average quantities at the grid points, providing communication across the unsimulated space between patches.

Chapter 3 analyses only one patch for the class of diffusion equations in order to mimic a microscopic simulation performed over the entire physical domain. We show how the dynamics of a small patch coupled to the distant macroscale boundaries is able to predict the slow emergent macroscale dynamics. Section 3.4 shows that for the patch dynamics scheme, eigenfunctions and their adjoints form a biorthogonal basis to determine the spectral coefficients in formal series solutions. Section 3.6 proposes a modified patch dynamics scheme with time delays in the communication of boundary values. This models a patch when information transmissions from the neighbouring patches are subject to communication delays.

Chapter 5 extends the analysis in Chapters 3 and 4 for diffusion problems to the case of the one-dimensional advection-diffusion problems. Algebraic analysis and numerical determination of eigenvalues for non-overlapping, coupled patches demonstrate the existence of a slow manifold. By computing only on a small fraction of the computational domain, we show that the scheme is reasonably able to describe the dynamics at the large scale.

1.2.3 Patch scheme

In many problems of practical interest, ranging from chemistry to materials science, we are often interested in a system of interacting atoms and how macroscopic behaviour emerges from these microscopic interactions. Many mathematical models describing, for example, geophysical fluid dynamics are typically written directly at the scale at which we are interested in particularly modelling the behaviour of the system. However, the scale at which the underlying turbulent flow and physics are understood is much finer than the macroscopic scale in which we are interested (Dada & Mendes 2011, Givon et al. 2004). Unfortunately, sufficiently explicit and accurate macroscopic closures do not exist in many multiscale and multiphysics problems; instead scientists and engineers use the microscopic model to simulate the macroscale quantities of interest on a large spatial domain, resulting in a huge amount of computation (Kiuchi et al. 2014, Nguyen et al. 2014). In this scenario, we aim to develop efficient computational schemes to wrap around fine scale microscopic level computer models of dynamical systems.

The methodology is to evaluate automatically 'on demand', directly through short computational bursts of the microscopic description, for which the macroscopic modelling closures are not explicitly available for the emergent dynamics (Cisternas et al. 2004, e.g.). Here I develop a novel patch scheme which makes no attempt to derive a macroscale closed form from the original microscale computation model, in contrast to, for example, homogenisation (Pavliotis & Stuart 2008, e.g.).

Patch schemes, like those proposed by Kevrekidis et al. (2003), are intended to simulate the macroscale quantities of interest through interpolation in space and extrapolation in time. The procedures of a patch scheme are described in two main steps. The first step is to define the gap-tooth scheme which enables a "small space, short time" timestepper to perform "large space, short time" computational framework. The second step is to combine the gap-tooth scheme with projective integration. This combination provides an equation-free framework bridging "small space, short time" simulations and "large space, long time" evolution. In this dissertation, we do not consider projective integration, only the gap-tooth precursor to the full patch scheme.

The main aim of this dissertation is to develop and provide support for the patch scheme (Hyman 2005, Li et al. 2007, Frederix et al. 2007, Bunder & Roberts 2012, e.g.).

1.3 Atomistic simulations

In the late 1950s, molecular dynamics was introduced by Alder & Wainwright (1957, 1959) to study the interaction of hard spheres. Rahman (1964) then used a realistic potential to carry out the first simulation for liquid argon. Such computational simulations have significant impacts on science and engineering due to revolutionary advances in computer technology and algorithmic improvements. Nowadays, molecular dynamics methods describe the world from the nanoscopic perspective and model the physical properties accurately at the atomic scale. However, these methods are not suitable for engineering due to the extreme computational costs that limit their application to systems of just a few million atoms (Kalweit & Drikakis 2011, Gates et al. 2005, e.g.). Because of these limitations, there is an effort to develop mesoscale and multiscale methods with the aim to provide efficient predictions for large scale macroscale dynamics. The equation-free approach aims to use such microscale molecular simulations to efficiently compute and predict large macroscale space-time dynamics. Chapter 2 focuses on establishing the basis for a novel design of the equation-free approach in predicting emergent macroscale properties over large space scales by computing atomistic dynamics only on relatively small widely distributed periodic patches.

The equation-free approach has been used by Frederix et al. (2007) and Roose et al. (2009) to empower molecular simulations. However, these approaches concentrate on issues associated with long-time integration, whereas Chapter 2 focuses on designing effective algorithms for large space domains. Future work will focus on the development of a full multiscale equation-free scheme that combines both aspects.

Other multiscale methods have been proposed that are based upon analogous simulations at the fine scale: for example, in the flow through a porous medium, Hassard et al. (2016) used smoothed particle hydrodynamics on the microscale to estimate macroscale volume averaged fluxes, with a view to forming a two-scale model that appears like a finite volume scheme on the macroscale. For general gradient driven transport processes, Carr et al. (2016) correspondingly proposed an Extended Distributed Microstructure Model where the macroscale flux is determined as the average of microscale

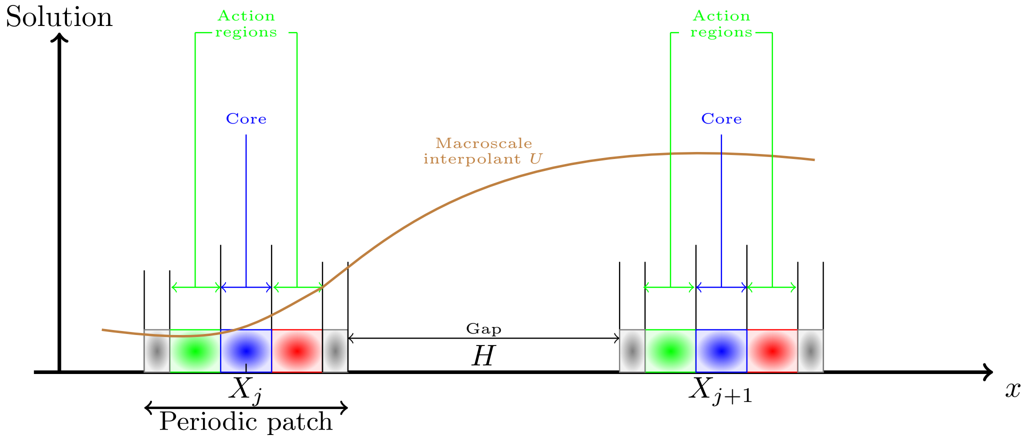

Figure 1.2: Schematic diagram of a microscale periodic-patch divided into four equal-sized regions.

fluxes within micro-cells. Such approaches suggest that microscale simulations can be coupled usefully across macroscales.

Our innovation, detailed in Chapter 2, is to develop one way to construct computationally efficient 'wrappers' around whatever microscopic level computer models a scientist chooses for any given system. An example of this fine scale, microscopic, detailed model is molecular dynamics, which mimics the behaviour of a system at large scale and makes predictions more efficiently and effectively at the macroscale 'continuum' level. The simulation is only performed in one, relatively small, triply-periodic, atomistic patch coupled to the distant macroscale boundaries. Such coupling is accomplished by implementing a proportional controller near the edges of the patch, in the so-called 'action regions'. The regions shaded in green and red in Figure 1.2 represent the left and right action regions of the patch, respectively. Other macroscale modelling techniques use a different approach by applying patch dynamics coupling conditions only to the edges of the patch (Roberts et al. 2014, e.g.)

The global macroscale solution $U_j(t)$ at X_j is extracted after solving microscale fields within the patch. The average kinetic energy in the centre of the patch, termed 'core region', estimates the local temperature in a patch. The core of the patch is centred around the grid point in the middle of the patch. The blue shaded region in Figure 1.2 represents the core region of the patch. Then, interpolating such core temperatures over the unsimulated space estimates the macroscale temperature field. The applied control aims to appropriately drive the average kinetic energy in each action region to the corresponding macroscale temperature and thence couple the patch to its neighbours and the surrounding boundaries.

1.4 Centre manifold theory

Centre manifold theory is becoming more widely used since it empowers us with great flexibility in modelling complex dynamical systems (Meron & Procaccia 1986, Procaccia 1988, e.g.) such as stochastic systems (Schöner & Haken 1986, Namachchivaya & Lin 1991), dispersion (Mercer & Roberts 1994, Rosencrans 1997, e.g.), thin fluid films (Roberts 1996, Roy et al. 2002, e.g.) and turbulent floods (Roberts et al. 2003). In this dissertation, most of the analysis of Chapters 4 and 5 is based upon centre manifold theory. The application of centre manifold theory is based upon modifying linear dynamics so that the theory guarantees that an appropriate and relevant low-dimensional description of the nonlinear dynamics may be obtained. The theory is applied after dividing the macroscale domain into small patches, with each patch centred around one macroscale grid point. Centre manifold theory (Roberts 1988, Pötzsche & Rasmussen 2006, e.g.) then supports the existence of slow manifold models.

The key idea of the centre manifold approach is to find a domain where there is a separation of time scales between long lasting modes of interest (macroscale modes) and rapidly decaying modes (microscale modes) which are not of interest to the macroscale dynamics. In particular, Figure 5.12 shows one example of clear separation between the dynamics of the macroscale modes of interest, and the microscale modes within each patch. The results of Chapter 5 demonstrate the feasibility of the microscale patch scheme to model advection-diffusion on large spatial scales.

1.5 Overview and contributions

This dissertation contributes to the development of the multiscale equation-free method which has been introduced recently to empower the macroscale simulation. The most significant novel outcome of this research is that patches with microscale periodic boundary conditions can be used to efficiently predict macroscale fields of interest.

Most attention is given to the analysis of gap-tooth schemes. We concentrate on establishing the basis for a novel design of multiscale methods in predicting the macroscale quantities of interest over large spatial domains by utilising atomistic simulations only on a relatively small periodic patch.

We show how to impose a particular boundary conditions onto a molecular dynamics simulation by applying a controller. A small periodic patch is coupled over the macroscale to the boundaries so that the overall scheme predicts the correct macroscale dynamics. Numerical simulations show that applying a suitable proportional controller within action regions of a patch of atomistic simulation effectively predicts the macroscale transport of heat. Rigorous mathematical analyses and simulation results presented throughout Chapter 2 demonstrate that the proposed patch scheme has good potential for predicting the evolution of the macroscopic transport phenomena based upon simulation at the microscale level.

The second objective of the dissertation is to study the application of boundary conditions onto patches. We analyse whether a set of small patches in the spatial domain is able to make predictions of the coupled macroscale dynamics when the transport phenomena at the microscale level are governed by different PDEs, including diffusion, advection-diffusion, and reaction-diffusion equations. We show that the scheme efficiently captures the large scale features of the solutions, taking advantage of the separation of scales which make such modern multiscale methods much more efficient than solving the full fine-scale problem. Chapter 3 discusses solving a one-dimensional microscale diffusion equation with forcing boundary conditions in a single patch so that the large-scale phenomena can be predicted. Two classes of eigenfunctions are considered: symmetric and asymmetric. The spectral problem associated with a small patch is a non-self-adjoint. We show that for the patch dynamics scheme, the eigenfunctions and their adjoints form biorthogonal sets, and the spectral coefficients in the eigenfunction expansion are obtained by means of the eigenfunction of the adjoint problem. Time delays in the communication of boundary values are also explored in the patch scheme and compared to the scheme without delays to ascertain when such delays are significant.

Chapter 4 analyses diffusion dynamics on multiple coupled patches distributed over the domain. The eigenvalue analysis together with centre manifold theory support the existence of a slow manifold. The patch coupling conditions are obtained by interpolating the macroscale average quantities at the grid points, and provide communication across the unsimulated space between patches. Chapter 5 extends the analysis presented in Chapters 3 and 4 to more general advection-diffusion problems for both a single patch and for multiple patches. Numerical approximation of the eigenvalues for non-overlapping, coupled patches demonstrates the existence of a slow manifold, and computer algebra is used to construct a model to confirm the advection-diffusion dynamics.

Chapter 2

A periodic patch scheme in atomistic simulations

Computational simulations have become a valuable tool to the point where they now stand alongside theoretical and experimental methods in addressing problems in materials science (Dove 2008, e.g.). The most direct of these simulation techniques is atomistic simulation, in which a suitable inter-atomic potential is used to characterise the inter-atomic forces between atoms, and then Newton's second law is computationally integrated with appropriate boundary conditions. Despite this simple basis, very complex phenomena have been accurately simulated. Atomistic simulations are accomplished without a priori assumptions about the form of the macroscale mode, which is in contrast to, for example, many continuum mechanics approaches (Buehler 2008, e.g.), which often include such assumptions.

Limitation Atomistic simulations provide insightful details into many problems of interest. However, obtaining a good atomistic description of physical problems is a challenging task due to the time scale limitation of molecular dynamics (MD) methods (Kalweit & Drikakis 2011, Gates et al. 2005, e.g.). The excessive computational demand of simulating even just thousands of atoms interacting over a sufficiently long time, places a stringent limitation on length and time scales for the problem of interest. In particular, the small time step, generally in the range of $10^{-15}\,$s, limits long simulation times (Kalweit & Drikakis 2011). Therefore, modelling the evolution of systems, particularly those of atomistic nature, with length scales in the range of tens of nanometres and for times of up to a few tens of nanoseconds, is problematic.

Several multiscale methods have been previously proposed that combine atomistic simulation with traditional continuum scientific computation and

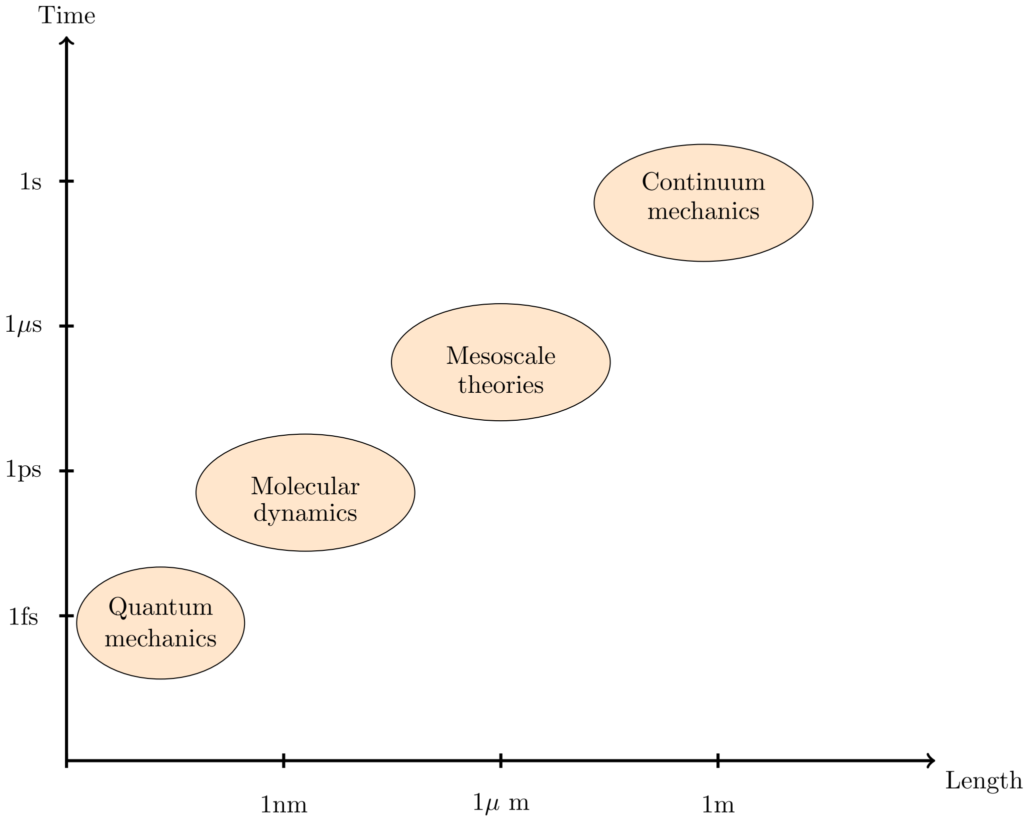

Figure 2.1: Different properties and processes of materials are described by different methods at different length and time scales.

numerical analysis to deal with problems in which a macroscopic model alone cannot accurately describe the system dynamics. Multiscale coupling is increasingly popular due to the potential to link structural property relationships from nano to macroscale levels (Smith & Todd 2001, Shilkrot et al. 2002).

Figure 2.1 overviews a hierarchy of physical models between macroscale models and the quantum many-body problems. This figure indicates the typical ranges of length and time scales for problems tackled by quantum mechanics based methods, molecular dynamics, and continuum mechanics methods. Quantum mechanics are applicable to very short time and length scales, on the order of a few nanometres and picoseconds. Once interactions are assumed in the MD method, the length and time scales of interest approach micrometers and nanoseconds (Abraham et al. 2002). Continuum mechanics integrated with other computational simulation tools can treat virtually any length scale; however, they lack a realistic description at fine scales and are therefore not appropriate to describe materials failure processes with full atomistic information (Dolbow et al. 2004, Solhjoo & Vakis 2015).

In the last two decades, the equation-free method (Kevrekidis et al. 2003, e.g.), has been developed to overcome the high computational cost of atomistic simulations. The equation-free method aims to use such microscale molecular simulations, and averaged properties over short space-time scales, to advance and predict macroscale space-time dynamics. This method is intended to be used when the macroscopic description is not available in closed form (Cisternas et al. 2004). Bypassing the need to use macroscale models, accurate microscale models capture the macroscale behaviour for the system of interest.

The principle aim of this chapter is to develop and provide theoretical support for and to further develop the equation-free patch dynamics scheme (Hyman 2005, Li et al. 2007, Frederix et al. 2007, Bunder & Roberts 2012, e.g.) to multiscale modelling. In particular, this chapter empowers novel atomistic patch simulations over large spatial dimensions from a *given* microscopic atomistic simulator. The key to support the patch dynamics scheme (Kevrekidis et al. 2003, Frederix et al. 2007, Bunder & Roberts 2012, Cao & Roberts 2016) is to perform atomistic simulations only on relatively small widely distributed patches. In the scenario where a user has coded a microscale simulator with microscale periodicity, our innovation is to show how to couple a small microscale periodic patch over unsimulated space so that the overall scheme predicts the correct macroscale spatial dynamics.

For patch dynamics in space-time, a full implementation involves projective integration forward in time (Samaey et al. 2004, Givon et al. 2004, Möller et al. 2005, Runborg et al. 2002). However, in this pilot study, we focus attention on an isolated triply-periodic patch of the spatial domain, as described in Section 2.1, and leave projective integration of periodic patches to future research. In space, patch dynamics, also referred to as the gap-tooth scheme (Roberts & Kevrekidis 2007), has been applied successfully to the one-dimensional Burgers' equation (Roberts 2001, e.g.) and a Ginzburg–Landau model (Roberts et al. 2011, e.g.). More recently it has been extended to solving a one-dimensional wave-like system (Cao & Roberts 2013).

Section 2.1 establishes a computational scheme for the atomistic simulation of a dense gas in $3D$ space (listed in Appendix A). The microscale simulation is performed in a triply-periodic domain. Section 2.2 describes the potential used to describe the interactions between atoms, together with the simulation strategies used. Newton's laws of motion determine the motion of the atoms as they interact with others in a microscale patch of space-time.

Such a scheme is also at the core of more complicated schemes for more complicated molecular simulations (Koumoutsakos 2005, Horstemeyer 2009, e.g.). Section 2.2.4 describes periodic boundary conditions for the atomistic patch simulation where an atom crossing any face is re-injected into the cubic patch across the opposing face. As in many scenarios, imposing microscale periodic boundary conditions for a micro-simulator eliminates surface effects from the computation, and makes the simulation computation significantly easier. One major advantage of the equation-free approach is that it uses whatever simulator has been provided, and adapts it to macroscale simulations. Hence the important new challenge we address is to use a triply-periodic atomistic simulation code as 'a given' for the computed patches in an equation-free scheme.

In order to research realistic problems in the future we expect to implement the methodology within one of the established powerful MD simulators such as LAMMPS (Plimpton et al. 2016). However, here we focus attention on establishing a proof-of-principle and the fundamental effectiveness of the scheme: for that purpose, our straightforward code is sufficient. This code is written to ensure that we have freedom to modify it easily to explore any new idea.

Section 2.3 discusses the mathematical details of a patch dynamics scheme which includes the patch construction, coupling conditions, proportional control, and the numerical simulation results. Section 2.3.1 demonstrates how we implement a proportional controller (Bechhoefer 2005, e.g.) in the so-called 'action regions' that surround the 'core' of the periodic patch. We then discuss the method for obtaining the macroscale temperature field solutions and define the coupling conditions. The average kinetic energy in the core region estimates the local temperature in a patch. Interpolating these temperatures over the unsimulated space provides an estimate of the macroscale temperature field. The applied control aims to appropriately drive the average kinetic energy in each action region to the corresponding interpolated macroscale temperature.

Numerical simulations, Section 2.3.2, demonstrate that the proportional controlled coupling of the periodic patch is effective for atomistic simulations.

Section 2.4 analyses the control and confirms the proposed controlled coupling of a microscale periodic patch is effective. Section 2.4.1 discusses an eigenproblem of the controlled patch scheme. Two classic families of eigenfunctions are derived in Sections 2.4.2 and 2.4.3. All possible wavenumbers and eigenvalues on an arbitrary single patch then determine the single macroscale mode across the domain.

Section 2.5 establishes the spectral gap of the patch system, and shows the slow emergent macroscale dynamics. Section 2.5.2 then approximates the

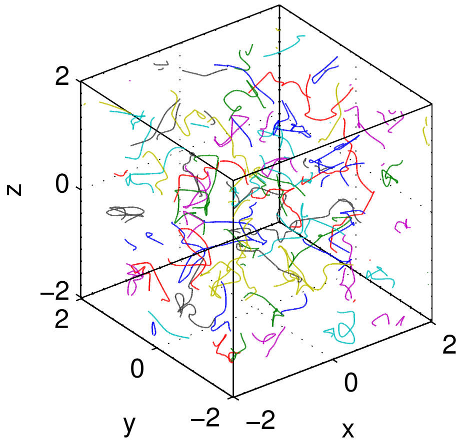

Figure 2.2: Atomic trajectories of interacting 64 atoms in a monatomic gas, over a time $0 \leq t \leq 3$, in a triply-periodic, cubic, spatial domain, showing the beginnings of the complicated inter-atomic interactions.

eigenvalue that characterises such emergent macroscale dynamics. Based on approximating the eigenvalue of macroscale interest, Section 2.5.3 determines a good value for the control strength. Section 2.6 estimates the diffusivity to determine the best control for the simulation by calculating the temperature difference between heated/cooled action regions.

2.1 An isolated triply-periodic patch

This section describes an atomistic simulator for the isolated dynamics of atoms in a cubic patch. We are interested in the macroscale behaviour of large complex systems. We assume that only atomistic simulations describing the microscopic behaviour of the system are available. The atomistic models can either be classical MD or kinetic Monte Carlo methods. In this chapter, as a first test of our novel methodology, our atomistic, detailed, simulator is the MD of a monatomic gas in $3D$ space. The simulator computes the motions of N atoms in a microscale patch of space-time as they react to forces originating from interactions with the other atoms in the patch. For our purposes typically there are up to a few thousand atoms in a patch. Figure 2.2 shows the apparently chaotic path in space of $N = 64$ atoms in a patch for one example short-time simulation. We implemented atomistic simulations in a triply-periodic cubic domain, where an atom leaving the cubic patch by crossing any of the six faces of the cube is re-injected into the cube across the opposing face.

Our challenge is to develop methods that use such triply-periodic atomistic simulations to predict macroscopic properties of experimental interest.

Consider a system of N atoms where each individual atom is denoted by subscript i. Let $\vec{r}_i(t)$ denote the position vector in space of the ith atom as a function of time t, and $\vec{q}_i$ denote their velocity, then the velocity of the ith atom is

$$\frac{d\vec{r}_i}{dt} = \vec{q}_i, \quad i = 1, \dots, N. \tag{2.1}$$

For atoms of non-dimensional mass one, as illustrated in Figure 2.2, these atoms evolve in time according to Newton's second law

$$m_i \frac{d\vec{q}_i}{dt} = \vec{F}_i, \quad i = 1, \dots, N, \tag{2.2}$$

where m_i, $\vec{F}_i$ are respectively the atomic mass and the force vector acting upon the ith atom at time t due to interactions with the other atoms in the cubic patch. We assume that the force on atom i at time t is the negative gradient of the potential energy function

$$\vec{F}_i = -\frac{\partial}{\partial \vec{r}_i} V(\vec{r}_1, \vec{r}_2, \dots, \vec{r}_N),$$

where V is the potential energy which is a function of the atomic coordinates ($3N$) of all the atoms. The inter-atomic potential in any realistic system represents a highly nonlinear function of the $3N$ coordinates so that the equations of motion (2.1)–(2.2) present great difficulty when trying to obtain an analytical solution. Indeed even the numerical integration of these equations of motion is not trivial. Therfore, to deal with this complixity, we consider the MD technique to solve the equations of motion numerically.

2.2 Equations of motion

This section describes the mathematical basis of the simulator in a triply-periodic cubic patch. Section 2.2.1 describes the potential model used to calculate the inter-atomic forces. Section 2.2.2 non-dimensionalises all quantities with respect to the atomic scale. Section 2.2.3 details the integration of Newton's equations of motion (2.5)–(2.6). Section 2.2.4 discusses the implementation of periodic boundary conditions.

2.2.1 The inter-atomic potential energy

The most critical quantity in MD simulation is the interaction potential. The interaction potential determines the numerical and algorithmic simplicity or complexity of an atomic simulation and the degree of physical fidelity for the simulation results. It is convenient to use the Lennard-Jones potential for computational simulation because it models short-range pairwise interactions, and can be implemented in ways that are computationally undemanding (Kairn et al. 2004). The Lennard-Jones potential is a pair interaction energy that is commonly used to describe the interactions between uncharged atoms, and it is widely considered a reasonably accurate model of interactions between closed-shell atoms (noble gases, Ne, Ar, Kr, and Xe) and covalently bonded molecules. In our simulations, we use the classic $12-6$ Lennard-Jones potential (Jones 1924, e.g.)

$$V_{LJ}(r_{ij}) = 4\epsilon\left[\left(\frac{\sigma}{r_{ij}}\right)^{12} - \left(\frac{\sigma}{r_{ij}}\right)^{6}\right], \tag{2.3}$$

where the potential parameters ϵ and σ are chosen to fit the physical properties of the atomic species being considered. The parameter ϵ governs the strength of the interaction, σ is an inter-atomic length scale, and r_{ij} is the separation distance between atom i and atom j.

Atoms do not only exert attractive forces on each other. If two atoms approach very close to each other, their electron clouds repel one another. The term proportional to $1/r_{ij}^{12}$, dominating at very short distances, models the repulsion between atoms when they get too close to one another due to the overlap of the electron clouds belonging to the interesting atoms. The attractive term proportional to $1/r_{ij}^{6}$ dominates at longer distances and models the van der Waals forces caused by transitive dipole-dipole interactions.

In MD simulations, the inter-atomic force on each atom is calculated at each time step. The simulator then integrates these forces to calculate the new positions and velocities of every atom. The force calculation constitutes the majority of computational effort.

Inter-atomic Forces

Given the potential, the force acting on an atom from another is determined by the negative gradient of the potential energy function with respect to spatial coordinates. The inter-particle force exerted by all atoms on atom i arising from the Lennard-Jones potential (2.3) is

$$\vec{F}_i = \sum_{j\neq i}^{N} \vec{f}_{ij}, \quad \text{where} \quad \vec{f}_{ij} = -24\epsilon\left[2\left(\frac{\sigma}{r_{ij}}\right)^{12} - \left(\frac{\sigma}{r_{ij}}\right)^{6}\right]\frac{\vec{r}_{ij}}{r_{ij}^2}, \tag{2.4}$$

where $\vec{r}_{ij} = \vec{r}_i - \vec{r}_j$ is the relative position vector of atom i to atom j, and the distance $r_{ij} = |\vec{r}_{ij}|$.

2.2.2 Non-dimensionalisation of the variables

In our simulations, we prefer to deal with a non-dimensional system, in which the governing equations and all macroscopic quantities such as temperature, pressure, and density are non-dimensionalised by chosen representative values (Satoh 2010, p.72). Therefore, it is convenient to non-dimensionalise all quantities with respect to atomic scales so that, for example, the inter-atomic equilibrium distance is scaled to one, as shown in Figure 2.2.

In our simulations of a monatomic gas, all the parameters are non-dimensionalised using the parameters of the Lennard-Jones potential (2.3). Thus, we choose the reference length σ, reference energy ϵ, and reference mass m. From these basic units, the reference time is $\sigma\sqrt{m/\epsilon}$, and reference temperature ϵ/k .

Here we describe some of the computer codes in Appendix A.1.3 developed for our atomistic simulations. For non-dimensional quantities, the velocity of each atom is in the set of ordinary differential equations (ODEs) for the system of (§A.1.3, lines 13–16):

$$\frac{d\vec{r}_i}{dt} = \vec{q}_i, \quad i = 1, \ldots, N. \tag{2.5}$$

The other set of ODEs for the system come from the inter-atomic interactions. For atoms of non-dimensional mass one, the acceleration of each atom is described by Newton's second law as (§A.1.3, lines 33–35)

$$\frac{d\vec{q}_i}{dt} = \sum_{j\neq i}^{N} \vec{f}_{ij}, \quad i = 1, \ldots, N, \tag{2.6}$$

in which the force on the ith atom resulting from the interaction with the jth atom is non-dimensionalized from (2.4) as (§A.1.3, lines 27–31)

$$\vec{f}_{ij} = \left(\frac{1}{r_{ij}^6} - \frac{1}{r_{ij}^{12}}\right)\frac{\vec{r}_{ij}}{r_{ij}^2}.$$

We emphasise that the factors σ and ϵ no longer appear due to non-dimensionalisation.

Due to the triple periodicity in the patch, the inter-atomic sum in (2.6) should be over all periodic images of the atoms. However, in the sum atoms and their images further away than a patch half-width are neglected (§A.1.3, lines 19–24). Section 2.2.4 describes atoms and their periodic images in the triple-periodic simulation domain. Due to the $1/r^7$ decay of long range attraction, and with a typical patch of size $10 \times 10 \times 10$ atoms, the error

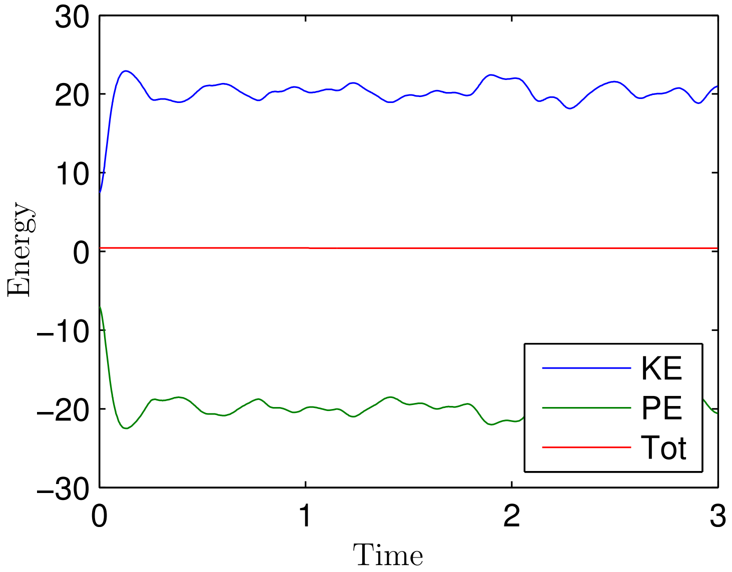

Figure 2.3: For the case of Figure 2.2, this plot of nondimensional Kinetic Energy (KE), Potential Energy (PE), and their sum (Tot) illustrates the conservation of energy by the coded simulation.

in accounting for only these atoms/images is roughly $5^{-7} \approx 10^{-5}$ which is reasonably negligible. For the purpose of checking, we verify that the mean momentum is conserved to machine precision which reflects the symmetry in the simulator. Figure 2.3 shows one example of the kinetic and potential energy, and their sum: we found the total energy is typically conserved to a relative error of about 10^{-5}.

2.2.3 Numerical integration of the equations of motion

The integration of Newton's equations (2.5)–(2.6) is performed by MATLAB's generic integrator `ode23`. The outputs are the velocities and positions as functions of time. The equations of motion (2.5)–(2.6) are deterministic; meaning that once the positions and velocities of each atom are known at time zero, the state of the system is uniquely determined at all later times.

Verlet algorithms are among the most popular families of algorithms for the solution of the classical ODEs of motion in MD simulations (Armstrong et al. 1970). These algorithms use the positions and accelerations of each atom at time t, and the positions from the previous step, $r(t - \Delta t)$ to calculate the new positions at the next time step, $r(t + \Delta t)$. At time $t = 0$ there is no previous time step available. Hence, initial velocities could be generated as a Boltzmann distribution of velocities for a given temperature (Armstrong et al. 1970, e.g.). As an improvement to the Verlet algorithm, the leap-frog algorithm has been developed (Frenkel & Smit 1996). In this algorithm, the positions and velocities are not obtained simultaneously. The positions are evaluated at integer time steps and velocities at half-integer time steps (Frenkel & Smit 1996, Armstrong et al. 1970, e.g.). For simplicity in this proof-of-principle study, the time integration was performed over the short time range by MATLAB's `ode23` routine (§A.1.1, line 31) rather than any of the more accurate symplectic integrators that apply to these Hamiltonian equations (Yoshida 1993, Hairer et al. 2003, e.g.). The generic integration routine `ode23` produces satisfactory results such as a conserved quantity like energy (Figure 2.3).

Multipole expansion algorithms have been developed to speed up the calculation of long-ranged forces in the N-body problems (Carrier et al. 1988, Cheng et al. 1999, e.g.). However, preliminary exploration of such an algorithm indicated that for a few thousand atoms per patch the fast techniques are not effective here.

Most of the remaining code in the time derivative routine (§A.1.3) couples the patch simulation to the macroscale surroundings described by Section 2.3.

2.2.4 Periodic boundary conditions

This section aims to describe the boundary conditions of our atomistic simulations. We implement simulation in a cubic domain of equal dimensions $2h \times 2h \times 2h$ in each direction. Then, due to the size limitation of atomistic simulations, usually at the nanoscale level, a large number of atoms is near the cube faces relative to the total number of atoms, which can lead to the surface effects (Fan 2011, e.g.).

Periodic boundary conditions are the most convenient way to overcome the problems of surface effects (Allen & Tildesley 1989). With periodic boundary conditions, the cubic patch simulation is replicated throughout space to form an infinite lattice with no surface. Figure 2.4 schematically illustrates the concept of the periodic boundary condition for a two-dimensional system comprised of three atoms. The cubic patch is surrounded by its images. When an atom leaves the central patch on one side, one of its images enters the central patch on the other side, such that the number of atoms in the simulation region is always conserved. In addition, periodic boundary conditions conserve quantities such as mass and energy in the patch simulation, since no atoms carrying mass or energy can escape.

The generic integration routine `ode23` as discussed in Section 2.2.3, would not handle the discontinuous reinjection of atoms that leave the cubic atom-

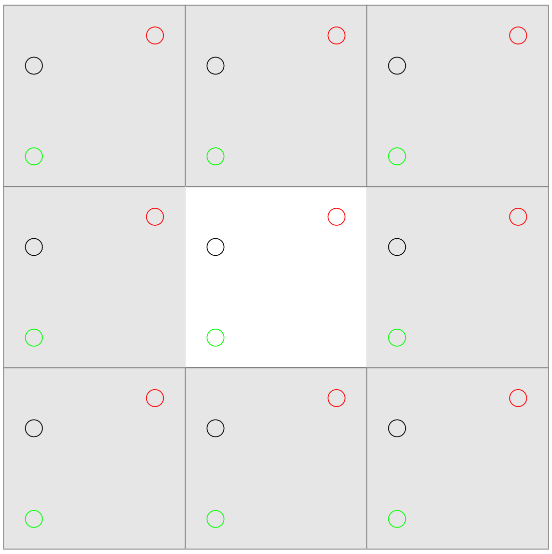

Figure 2.4: Two-dimensional schematic of periodic boundary conditions. The orignal patch is surrounded by its periodic images. Atoms can leave the box by crossing any of the four edges. In a three-dimensional example, atoms are free to leave the box by crossing any of the six faces.

istic simulation region: consequently, we allow the integrated atom positions to exit the cube smoothly, but map such atoms inside the cubic patch (§A.1.2) for computing inter-atomic forces.

2.3 Couple patches with a proportional controller

The previous Sections 2.1 and 2.2 describe a microscale simulation code for the isolated dynamics of atoms in a cubic domain. Our innovative challenge is to use such code, as if it were almost a 'black-box' fine scale dynamics simulator, to simulate over large spatial domains. In the equation-free methodology, a large scale-time simulation is efficiently accomplished by executing bursts of microscopic simulation on relatively small, spatially separated patches and coupling them by bridging the gaps in the spatial domain in which no computation is done (Samaey et al. 2005, Kevrekidis & Samaey 2009, e.g.).

In this pilot study of the case of periodic-patches, we only address the scenario of one large spatial dimension. For simplicity in this first implementation, the other space dimensions are assumed small. Further, as a proof-of-principle, this section addresses the very restricted case of one such

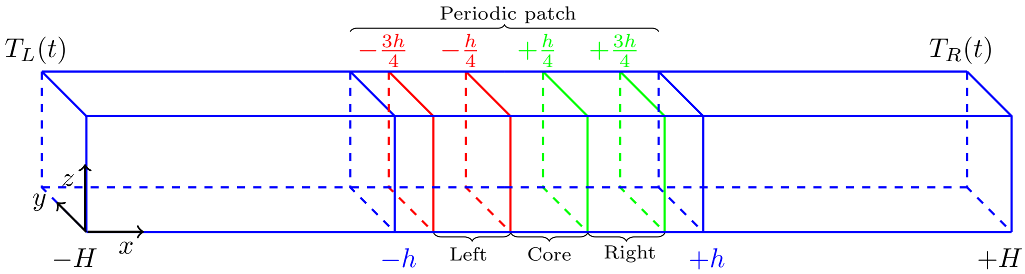

Figure 2.5: The simplest case is one triply-periodic patch of atomistic simulation, $-h < x < h$, coupled to distant sidewalls, at $x = \pm H$, of specified temperature. The patch's core region defines its local temperature, and a proportional controller is applied in the left and right action regions to generate a good macroscale prediction.

periodic-patch coupled to 'distant' imposed boundary conditions. Figure 2.5 illustrates the scenario with one 'small' periodic-patch centred on $x = 0$, $-h < x < h$, in a long thin macroscale domain $-H < x < H$.

This basic scenario focuses on the key methodological innovation: namely how to effectively couple a microscale periodic-patch to the surrounding macroscale environment. Here the macroscopic quantity of interest is the temperature field $T(x, t)$ of the monatomic gas as a function of position x and time t. We restricted ourselves to a macroscopically one-dimensional system. However, the atomistic simulations are done in three spatial dimensions.

For the purpose of validating our novel patch scheme, in this pilot study we suppose that we want to predict macroscale heat transport by the atomistic simulation. Thus, we compare the scheme's predictions for the temperature field $T(x, t)$ with that of the continuum heat diffusion PDE

$$\frac{\partial T}{\partial t} = K\frac{\partial^2 T}{\partial x^2}, \tag{2.7}$$

with physical boundary conditions

$$T(-H, t) = T_L(t) \quad \text{and} \quad T(+H, t) = T_R(t). \tag{2.8}$$

We centre at the origin a $2h \times 2h \times 2h$-periodic-patch of the atom simulation, as in Figure 2.5. This patch extends over $-h < x < h$ in the macroscale domain $-H < x < H$ with specified temperatures, $T_L(t)$ and $T_R(t)$, on the ends of the domain, $x = -H$ and $x = H$ respectively. The unsimulated spaces are the comparatively large gaps $h < |x| < H$. To distinguish between microscopic and macroscopic quantities we generally use lowercase letters for microscale quantities, such as $\vec{x}$, $\vec{q}$, and h, and uppercase letters for macroscale quantities, such as H and T. Here the problem is assumed to be doubly-$2h$-periodic in the other two spatial dimensions; that is, the macroscale physical domain is long and thin (Figure 2.5).

We divide the patch simulation into four equal-sized regions (§A.1.3, lines 38–43), denoted as the core region, left action, right action, and buffer region as illustrated schematically in Figures 2.5 and 2.6. The core region is of width $h/2$, and extends over $-h/4 \leq x \leq h/4$ in the microscale domain. This core region is surrounded by left and right action regions.

The atoms inside the core region, $j \in$ core, estimate the macroscopic temperature at the centre of the patch. This macroscopic temperature T_c is used for interpolation between the patch and the environmental boundary values over the macroscale (2.10). In multiple patches as discussed in Chapter 4, for example, the interpolation is done through the neighbouring macroscale grid values of neighbouring patches, thus providing a solution which approximates that of the whole domain.

The left and right action regions are centred at the quarter points of the patch $x = \mp\frac{h}{2}$, and extend over $|x \pm h/2| < h/4$. These action regions couple the patch to surrounding macroscale information such as the environmental boundary values. Such coupling conditions are accomplished via a forcing control acting on the action regions. The applied control is proportional to the difference between the interpolated macroscale fields (2.12) and the averages over the action regions (2.9). Section 2.3.1 details the macroscale variables, averaging action regions and a proportional controller.

The idea of using averaging techniques over action regions and core in MD simulation of fluid was initiated by Li et al. (1998), where artificial actions were applied in the so-called "extended boundary conditions" on an outer MD region. This is used to minimize disturbance to the atomistic dynamics in the physical region of interest (core). Similar methods of current interest resulted from extensive research in coupling continuum modelling with atomistic simulations, resulting in hybrid continuum-atomistic simulations (OConnell & Thompson 1995, Hadjiconstantinou & Patera 1997, Hadjiconstantinou 1999).

The buffer region is located near both 'edges' of a patch simulation and is separated from the core region. As shown in Figure 2.5 the buffer regions extend from the patch edges to the action edges, $|x| > 3h/4$. The buffer caters for a smooth transition between the action regions. Figure 2.6 shows an alternative schematic view of the patch: this view emphasises the microscale $2h$-periodicity in x and the role of the 'buffer' region between the two action regions, on the opposite 'side' to the important core region. Our approach

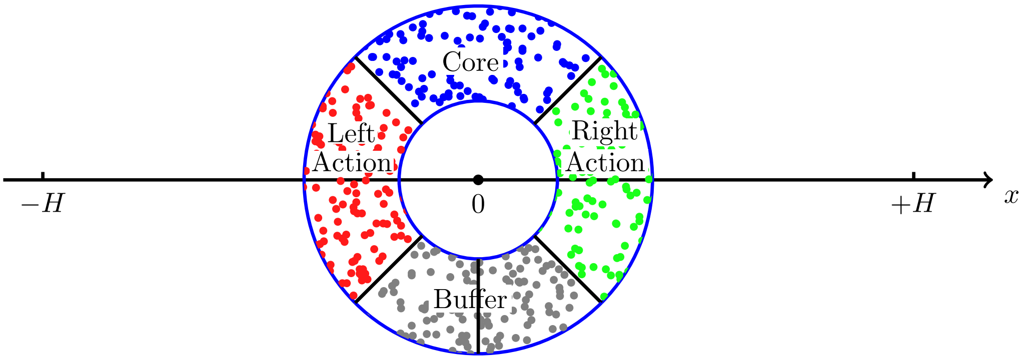

Figure 2.6: A schematic view of a microscale patch that emphasises the $2h$-periodicity in x and indicating the need for the lower 'buffer' region allowing for a smooth transition between the action regions.

does not implement buffer regions between the action regions and the core region (Bunder & Roberts 2012, Bunder et al. 2013), as shown in Figures 2.5 and 2.6.

Some approaches of multiscale methods have proposed patch schemes with buffer regions that are used for a different purpose than the buffers used in our model. For example, Kevrekidis et al. (2003) and Samaey et al. (2006) imposed appropriate boundary conditions for micro-simulator using buffer regions. The buffers temporarily shield the internal region of the patches from the artificial disturbance caused by the repeatedly updated boundary conditions. The relation between buffer size, time step and accuracy are discussed in detail by Kevrekidis et al. (2003), Samaey et al. (2006) and Bunder & Roberts (2012). For homogenisation problems, Samaey et al. (2006) also suggested that buffers are not required when the microscale structures are smooth.

In the multiscale finite element method, the idea of a buffer region was also introduced to reduce or eliminate the effect of the boundary layer (Holian & Ravelo 1995).

2.3.1 Coupling atomistic simulations

This section details the new approach to couple the periodic patch simulation to the surrounding macroscale environment. The coupling is achieved by implementing a proportional controller (Bechhoefer 2005, e.g.) in the action regions. The applied control is proportional to the differences between the interpolated macroscale field and the microscale patch simulator.

According to the kinetic energy theory of gases, the average kinetic energy of a collection of gas atoms is directly proportional to the temperature (Loeb 2004). Therefore, in our simulations, the non-dimensional temperatures are computed in the core and left and right action regions from the average kinetic energy of the atoms in each region (§A.1.3, lines 45–48):

$$T_c = \operatorname*{mean}_{j\in\text{core}} \mathrm{KE}_j\,, \quad T_l = \operatorname*{mean}_{j\in\text{left}} \mathrm{KE}_j\,, \quad T_r = \operatorname*{mean}_{j\in\text{right}} \mathrm{KE}_j\,, \tag{2.9}$$

in terms of the non-dimensional kinetic energy of each atom, $\mathrm{KE}_j = |\vec{q}_j|^2/2$ (the initial conditions and conservation of momentum in the algorithm ensure the mean velocity of the atoms is zero).

For a single periodic patch centred at $x = 0$ coupled to the distant boundaries at $x = \pm H$, the scheme's predicted macroscale field for the temperature is the parabolic interpolation through the three values T_L, T_0 and T_R,

$$T_{\text{int}}(x,t) = \frac{T_L}{2}\left(\frac{x^2}{H^2} - \frac{x}{H}\right) + T_0\left(1 - \frac{x^2}{H^2}\right) + \frac{T_R}{2}\left(\frac{x^2}{H^2} + \frac{x}{H}\right), \tag{2.10}$$

where the small finite width of the core results in the central temperature T_0 being slightly different to the core mean $T_c(t)$. Elementary algebra gives

$$T_0 = \left[\frac{T_c(t)}{(1 - r^2/48)} - \frac{r^2(T_R + T_L)}{96 - 2r^2}\right], \tag{2.11}$$

where the patch ratio $r = h/H$ is the geometric parameter that will appear frequently in this thesis, which is used to characterise the relative size of the patch and hence also that of the gap. In practice, the patch ratio r needs to be as small as possible to minimise the computational cost, but it has to be big enough to contain enough atoms for sensible averages.

This macroscale interpolation (2.10) empowers us to express values on the left and right action averages, in terms of the macroscales T_c, T_l and T_r. Averaging the predicted macroscale field (2.10) over each action region determines that the action regions should have the average temperatures

$$T_{\text{int},\pm} = \left(1 - \frac{13r^2}{48}\right)T_0 + \left(\frac{T_R + T_L}{2}\right)\frac{13r^2}{48} \mp \left(\frac{T_R - T_L}{2}\right)\frac{r}{2}, \tag{2.12}$$

where ± is for the right/left action region respectively. Some molecular simulations (Sotomayor 2007, p.157 e.g.) control the system temperature by adding a small friction term, $-\mu m_j\vec{q}_j$, with Gaussian noise, $\vec{R}(t)$, so that

$$m_j\frac{d\vec{q}_j}{dt} = \vec{F}_j - \mu_j m_j \vec{q}_j + \vec{R}(t). \tag{2.13}$$

In our atomistic simulations, inspired by this approach, we modify (2.13) by changing the friction term to an appropriate control and assuming that the noise term is small and therefore negligible. The applied control is proportional to the differences between the macroscale predictions on the action regions (2.12) and the temperatures (2.9) in the patch simulation (§A.1.3, lines 50–56). The controller accelerates or decelerates the atoms in the action region accordingly. That is, for each atom, Newton's second law (2.6) is modified by the control to (§A.1.3, lines 58–60)

$$\frac{d\vec{q}_j}{dt} = \vec{F}_j + \begin{cases} \frac{K\mu}{h^2T_r}(T_{\text{int},+} - T_r)\vec{q}_j\,, & j \in \text{right action,} \\ \frac{K\mu}{h^2T_l}(T_{\text{int},-} - T_l)\vec{q}_j\,, & j \in \text{left action,} \\ 0\,, & \text{otherwise,} \end{cases} \tag{2.14}$$

where the $\vec{F}_j$ are the inter-atomic forces defined by (2.6), and μ is the non-dimensional proportional control strength. Consequently, when the atoms in an action region are too cool, below $T_{\text{int},\pm}$, then the control accelerates the atoms to heat them up, and vice versa. The proportional controller is of strength μ, to be chosen optimally in our simulations.

2.3.2 Numerical simulations verify the validity of the proportional control

Numerical simulations of the microscopic system (2.14) for the controlled patch verify that the proposed proportional control is effective. Figure 2.7 shows the patch atomistic simulation of the microscale temperature T in the core and action regions in the governing equation (2.14). The simulations were carried out inside the cubic periodic patch $|x| < 3.5$, simulating $N = 343$ atoms of monatomic gas. The periodic patch is coupled to boundaries at $x = \pm 7$ with specified temperatures $T_L = 0.5$ and $T_R = 1.5$ by implementing the proportional controller defined by equation (2.16). No computations were performed on the gaps between the periodic patch and boundaries. The non-dimensional control strength used in this simulation is $\mu = 30$. In the example shown in Figures 2.7 there are two time scales apparent.

- At the microscale level, time scale of $\Delta t < 1$, the proportional control establishes that the temperatures in the action regions differ according to the local gradient of macroscale temperature. In this realisation the temperature gradient is $1/(2H) = 1/14$, so that over the distance $2/7$ between mid-action regions a temperature difference of 0.25 is maintained as shown by Figure 2.7(b). The atomistic fluctuations about

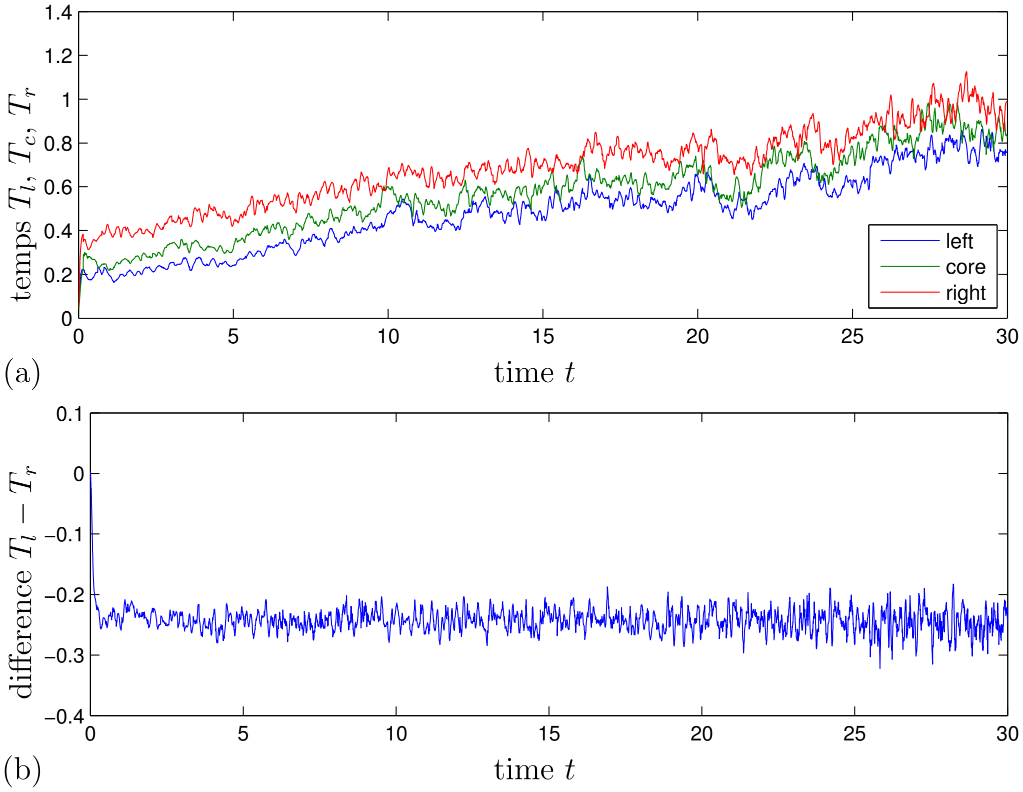

Figure 2.7: Temperatures over macroscale times in the sub-patch regions (a), and the temperature difference $T_l - T_r$ (b). The simulation is of 343 atoms in a patch of spatial periodicity $2h = 7$ and with control strength $\mu = 30$ to couple with macroscale boundary temperatures $T_R = 1.5$ and $T_L = 0.5$ at $x = \pm 7$.

this mean increase in time as the overall temperature increases (Figure 2.7(a)).

- At the macroscale level, time scale of $\Delta t \approx 30$, Figure 2.7(a) shows that the core temperature heats towards the correct mean of 1.0 — albeit exhibiting some fluctuations arising from the stochastic nature of the atomistic dynamics. This macroscopic time-scale is the diffusion time for heat across the macroscopic length scale $2H = 14$.

For completeness, proportional controllers should be applied for the other macroscale quantities of density, pressure and average velocity. However, here there is little to control in these variables as, through conservation in the code of atoms and overall momentum, in the patch the density is constant, and the average velocity zero from the initial conditions. Thus, in this pilot study, we just control the non-trivial dynamics of the temperature.

2.4 Analyse optimal control for a single patch

This section analyses the heat diffusion PDE (2.15)–(2.16) that models the controlled patch atomistic simulation (2.14) of the previous Section 2.3. We compare this patch model with the heat diffusion PDE (2.7) on the entire macroscale domain.

The equilibrium solution to the diffusion PDE (2.15) with constant boundary temperatures is the linear field $T = \frac{1}{2}(T_R + T_L) + \frac{x}{2H}(T_R - T_L)$. The dynamics superimposed on this equilibrium are an arbitrary linear combination of the modes

$$T_n = e^{\lambda_n t} \sin\left[k_n \left(x + H\right)\right],$$

with associated eigenvalues $\lambda_n = -K k_n^2$ for wavenumbers $k_n = n\pi/(2H)$, for $n = 1, 2, 3, \ldots$. With only one patch in the whole physical domain as shown in Figure 2.5, the patch atomistic simulation can only approximate the gravest $n = 1$ mode

$$T_1 = e^{\lambda_1 t} \cos(k_1 x),$$

with wavenumber $k_1 = \pi/(2H)$ and rate $\lambda_1 = -K k_1^2 = -K\pi^2/(4H^2)$. We find a control so the predictions of the single patch scheme (§2.3) match this gravest mode as well as the linear field.

The atomistic simulation within a patch will also be reasonably well modelled by the continuum heat diffusion PDE albeit with significant microscale fluctuations. In our restricted microscale patch scheme, Figure 2.5, the macroscale quantities are assumed to be homogeneous in the cross-sectional variables y and z so we only explore the xt-structure of the temperature field, $T(x,t)$. The corresponding continuum PDE for the controlled patch is then

$$\frac{\partial T}{\partial t} = K\frac{\partial^2 T}{\partial x^2} + \frac{K\mu}{h^2}g(x,T), \quad 2h\text{-periodic in } x, \tag{2.15}$$

where the control shape, piecewise constant, is

$$g(x,T) = \begin{cases} T_{\text{int},+} - T_r\,, & \frac{h}{4} < x < \frac{3h}{4}\,, \\ T_{\text{int},-} - T_l\,, & -\frac{3h}{4} < x < -\frac{h}{4}\,, \\ 0, & \text{otherwise.} \end{cases} \tag{2.16}$$

The temperatures $T_{\text{int},\pm}$, given by (2.12), come from the predicted field (2.19) via the core average

$$T_c = \frac{2}{h}\int_{-h/4}^{+h/4} T\,dx, \tag{2.17}$$

and values T_R and T_L at the macroscale boundaries $x = \pm H$. Let T_l and T_r , in equation (2.16), be the averages over the left and right action regions on the microscale patch

$$T_l = \frac{2}{h}\int_{-3h/4}^{-h/4} T\,dx, \qquad T_r = \frac{2}{h}\int_{h/4}^{3h/4} T\,dx. \tag{2.18}$$

The core average $T_c(t)$ is not quite the centre field value $T_0 = T(0,t)$. Substituting the centre patch value field T_0 (2.11) into (2.10) gives the macroscale interpolation

$$\begin{aligned} T_{\text{int}}(x,t) &= \left(1-\frac{x^2}{H^2}\right)\left[\frac{T_c(t)}{(1-r^2/48)} - \frac{r^2(T_R+T_L)}{96-2r^2}\right] \\ &\quad + \left(\frac{T_R+T_L}{2}\right)\frac{x^2}{H^2} + \left(\frac{T_R-T_L}{2}\right)\frac{x}{H}. \end{aligned} \tag{2.19}$$

Thus, the interpolation determines that the action regions should have the average temperatures

$$\begin{aligned} T_{\text{int},\pm} &= \pm\frac{2}{h}\int_{\pm h/4}^{\pm 3h/4} T_{\text{int}}(x,t)\,dx \\ &= \left(1-\frac{13r^2}{48}\right)T_0 + \left(\frac{T_R+T_L}{2}\right)\frac{13r^2}{48} \mp \left(\frac{T_R-T_L}{2}\right)\frac{r}{2}, \end{aligned} \tag{2.20}$$

where T_0 is given by (2.11).

In the case of constant boundary temperatures, the controlled patch problem (2.15)–(2.16) has equilibrium, with $T_c = T_0 = \frac{1}{2}(T_R + T_L)$, of

$$T = \begin{cases} T_0 + \frac{\mu\Delta T}{4} x/h, & |x| < \frac{h}{4}\,, \\ T_0 + \frac{\mu\Delta T}{16}\left[\frac{3}{2} - 2(2x/h - 1)^2\right]\operatorname{sign} x, & \frac{h}{4} < |x| < \frac{3h}{4}\,, \\ T_0 + \frac{\mu\Delta T}{4}(\operatorname{sign} x - x/h), & |x| > \frac{3h}{4}\,, \end{cases} \tag{2.21}$$

where $\Delta T = (T_R - T_L)h/(4H)/[1 + \mu/12]$. A first important check is that this equilibrium has the correct mean core temperature of $T_0 = (T_R + T_L)/2$.

To understand the dynamics of the patch scheme (2.15)–(2.16), Section 2.4.1 characterises the general solution, relative to the equilibrium, in terms of spatial eigenfunctions.

2.4.1 An eigenproblem of the controlled patch scheme

This section forms an eigenproblem for the patch model (2.15)–(2.16) via separation of variables. The ultimate aim of this section is to derive the good control (2.42) which is obtained in Section 2.5.3.

Relative to the equilibrium (2.21), consider the case in which the boundary temperatures are zero $T(\pm H, t) = 0$. On the controlled patch assume that the temperature field

$$T(x,t) = e^{\lambda t}\hat{T}(x), \tag{2.22}$$

for eigenvalue $\lambda = -Kk^2$ corresponding to some wavenumber k to be determined. Substituting the solution form (2.22) into PDE (2.15) yields

$$0 = \hat{T}_{xx} + k^2\hat{T} + \frac{\mu}{h^2} g(x, \hat{T}), \tag{2.23}$$

for eigenfunctions $\hat{T}$ which are $2h$-periodic. We solve algebraically this eigenproblem (2.23) in four pieces: in the core region $|x| < h/4$, in the left and right action regions $\frac{h}{4} < |x| < \frac{3h}{4}$, and finally in the buffer region $|x| > \frac{3h}{4}$. The four pieces are connected by continuity conditions. There are two classes of eigenfunctions, symmetric and antisymmetric within the patch, found respectively by the following Sections 2.4.2 and 2.4.3.

2.4.2 Symmetric eigenfunctions

This section finds the symmetric eigenfunctions of the patch scheme. We find that all but one of the associated wavenumbers k scale with $\propto 1/h$, and the corresponding decay rate scales with K/h^2 that characterise microscale modes of the PDE within the patch. The exception is the smallest wavenumber which is largely independent of h and corresponds to the emergent macroscale mode.

We seek solutions of the eigenproblem (2.23) for the temperature field $\hat{T}$ that are piecewise smooth and symmetric about the mid-patch $x = 0$ (and then necessarily about the 'edges' of the periodic patch $x = \pm h$). Symmetric eigenfunctions corresponding to temporal decay e^{-Kk^2t}, $k > 0$, are of the form

$$\hat{T} = \begin{cases} A\cos kx, & |x| < h/4\,, \\ C + D\cos[k(x \mp \frac{h}{2})] \pm E\sin[k(x \mp \frac{h}{2})], & \pm h/4 \lessgtr x \lessgtr \pm 3h/4\,, \\ B\cos[k(x \mp h)], & x \gtrless \pm 3h/4\,, \end{cases} \tag{2.24}$$

for some constants A, B, C, D and E. The upper version of the middle case in (2.24) is for the right action, whereas the lower version is for the left action region. The corresponding derivative fields are

$$\hat{T}_x = \begin{cases} -kA\sin kx, & |x| < h/4\,, \\ -kD\sin[k(x \mp \frac{h}{2})] \pm kE\cos[k(x \mp \frac{h}{2})], & \pm h/4 \lessgtr x \lessgtr \pm 3h/4\,, \\ -kB\sin[k(x \mp h)], & x \gtrless \pm 3h/4\,. \end{cases} \tag{2.25}$$

The forcing control g of (2.16), encoded in the simulation, is a constant in x for each region of the patch. The symmetric eigenfunctions (2.24) satisfy the governing ODE (2.23) in the core and buffer regions. To satisfy the governing ODE (2.23) in the action regions requires

$$-Dk^2\cos\left[k\left(x \mp \frac{h}{2}\right)\right] + k^2\left\{C + D\cos\left[k\left(x \mp \frac{h}{2}\right)\right]\right\} + \frac{\mu}{h^2}g_{\pm} = 0,$$

that is,

$$k^2C + \frac{\mu}{h^2}g_{\pm} = 0. \tag{2.26}$$

Substituting the symmetric eigenfunctions (2.24) into the macroscale interpolation (2.19) gives

$$\begin{aligned} \hat{T}_{\text{int}} &= \left(1 - \frac{x^2}{H^2}\right)\left(\frac{1}{1 - r^2/48}\right)\frac{2}{h}\int_{-h/4}^{h/4}\hat{T}(x,t)\,dx \\ &= \left(1 - \frac{x^2}{H^2}\right)\left(\frac{1}{1 - r^2/48}\right)\frac{2A}{h}\int_{-h/4}^{h/4}\cos kx\,dx \\ &= \left(1 - \frac{x^2}{H^2}\right)\left(\frac{1}{1 - r^2/48}\right)\frac{4A}{hk}\sin\frac{kh}{4}. \end{aligned}$$

Averaging this interpolation over the right and left action regions is the same by symmetry:

$$\begin{aligned}\hat{T}_{\text{int},\pm} &= \pm\frac{2}{h}\int_{\pm h/4}^{\pm 3h/4}\hat{T}_{\text{int}}(x,t)\,dx\\ &= \frac{4A}{kh}\left(\frac{1-13r^2/48}{1-r^2/48}\right)\sin\frac{kh}{4}.\end{aligned}$$

Substituting the symmetric eigenfunction (2.24), in the action regions, into the definition of the right action region (2.18) yields

$$\begin{aligned}\hat{T}_r &= \frac{2}{h}\int_{h/4}^{3h/4}\hat{T}(x,t)\,dx\\ &= \frac{2}{h}\int_{h/4}^{3h/4} C+D\cos\left[k\left(x-\frac{h}{2}\right)\right]+E\sin\left[k\left(x-\frac{h}{2}\right)\right]\,dx\\ &= C+D\frac{4}{kh}\sin\frac{kh}{4}.\end{aligned}$$

The control depends on the difference in the action regions between the macroscale field and the microscale patch simulator. Therefore, taking the difference of these last two averages, the forcing control (2.16) in both action regions is

$$g_\pm = \frac{4A}{kh}\left(\frac{1-13r^2/48}{1-r^2/48}\right)\sin\frac{kh}{4} - C - D\frac{4}{kh}\sin\frac{kh}{4}.$$

Substituting this forcing control $g_\pm$ into equation (2.26) and multiplying by h^2 gives

$$k^2h^2C+\mu\left[\frac{4A}{kh}\left(\frac{1-13r^2/48}{1-r^2/48}\right)\sin\frac{kh}{4}-C-D\frac{4}{kh}\sin\frac{kh}{4}\right]=0. \qquad (2.27)$$

This equation, combined with the continuity equations, determines the wavenumbers and the structures of internal modes in this microscale patch.

Continuity of the symmetric eigenfunctions

Solving the ODE (2.23) on the patch domain requires continuity for the symmetric eigenfunctions $\hat{T}$ and their derivatives $\hat{T}_x$ at $x=\pm h/4$ and $x=\pm 3h/4$.

- Continuity of the symmetric eigenfunctions $\hat{T}$, (2.24), requires

$$\begin{aligned} A\cos\frac{kh}{4} &= C+D\cos\frac{kh}{4}-E\sin\frac{kh}{4}, &\quad \text{at } x=\pm h/4,\\ B\cos\frac{kh}{4} &= C+D\cos\frac{kh}{4}+E\sin\frac{kh}{4}, &\quad \text{at } x=\pm 3h/4.\end{aligned} \qquad (2.28)$$

- Continuity of the derivatives $\hat{T}_x$ of the eigenfunctions (2.25), requires

$$\begin{aligned} khA\sin\frac{kh}{4} &= -khD\sin\frac{kh}{4} - khE\cos\frac{kh}{4}, &\quad \text{at } x = \pm h/4,\\ khB\sin\frac{kh}{4} &= -khD\sin\frac{kh}{4} + khE\cos\frac{kh}{4}, &\quad \text{at } x = \pm 3h/4. \end{aligned} \tag{2.29}$$

Now we form equations (2.27) and (2.28)–(2.29) as the matrix-vector system

$$\begin{bmatrix} \cos\frac{kh}{4} & 0 & -1 & -\cos\frac{kh}{4} & \sin\frac{kh}{4} \\ 0 & \cos\frac{kh}{4} & -1 & -\cos\frac{kh}{4} & -\sin\frac{kh}{4} \\ \sin\frac{kh}{4} & 0 & 0 & \sin\frac{kh}{4} & \cos\frac{kh}{4} \\ 0 & \sin\frac{kh}{4} & 0 & \sin\frac{kh}{4} & -\cos\frac{kh}{4} \\ \frac{4\mu}{kh}\left(\frac{1-13r^2/48}{1-r^2/48}\right)\sin\frac{kh}{4} & 0 & k^2h^2-\mu & -\frac{4\mu}{kh}\sin\frac{kh}{4} & 0 \end{bmatrix} \begin{bmatrix} A \\ B \\ C \\ D \\ E \end{bmatrix} = \vec{0}.$$

The determinant of the matrix has to be zero for non-trivial solutions, namely,

$$\begin{aligned} \det &= \frac{2}{kh}\left[\left(1 - \frac{1-7r^2/48}{1-r^2/48}\right) 4\mu\sin^2\frac{kh}{4}\left(\sin^2\frac{kh}{4} - \cos^2\frac{kh}{4}\right)\right. \\ &\qquad \left. + 2kh(k^2h^2-\mu)\sin\frac{kh}{4}\cos\frac{kh}{4}\left(\sin^2\frac{kh}{4} - \cos^2\frac{kh}{4}\right)\right] = 0. \end{aligned}$$

Using the double–angle identity

$$\sin^2\frac{kh}{4} - \cos^2\frac{kh}{4} = -\cos\frac{kh}{2},$$

the characteristic equation becomes

$$-4\cos\frac{kh}{2}\sin\frac{kh}{4}\left[\mu\left(\frac{1-7r^2/48}{1-r^2/48}\right)\frac{4}{kh}\sin\frac{kh}{4} + (k^2h^2-\mu)\cos\frac{kh}{4}\right] = 0. \tag{2.30}$$

Algorithm 1 numerically computes these wavenumbers kh for equation (2.30) as shown in Table 2.1. For two different patch ratios, $r = 0.1$ and $r = \pi/2$, Table 2.1 displays one small eigenvalue which is the leading symmetric microscale eigenvalue, and all the remaining eigenvalues are large and negative, $\lambda < -9.87$. These eigenvalues with large negative real-parts are microscale sub-patch modes as they correspond to the dissipative modes within a patch.

Now let us establish how the pattern shown by Table 2.1 occurs. Algebraically, setting each factor on the left-hand side of the characteristic equation (2.30) to zero, gives us three cases.

Algorithm 1 Numerically solve equation (2.30) to determine the wavenumbers kh for symmetric modes.

```
% numerically solve det=0 for symmetric modes
% ratio of patch to domain size (r<=1)
r=0.1
hh=pi/2 % for simplicity the macroscale domain is length pi
h=r*hh; % patch half-size
mu=34.673
Fq=1-7*r^2/48
F0=1-r^2/48
%fn=@(kh) 4./kh.*tan(kh/4)-47/41;
fn=@(kh)-4*cos(kh/2).*sin(kh/4).*(mu*Fq/F0*sin(kh/4)*4./kh...
+(kh.^2-mu).*cos(kh/4));
format bank
kh=fsolve(fn,1:50);
kh=sort(kh);
kh=kh(diff([kh 1e99])>1e-5)
%khh=(kh/h)' wavenumber(k)
khh=kh'
lambda=-(kh).^2/h^2;
```

Table 2.1: Set of numerical wavenumbers kh and the corresponding decay rate $\lambda h^2/K$ of each mode of the characteristic equation (2.30) for symmetric modes with parameters $\mu = 34.673$, and $H = \pi/2$.

Patch ratio $r = 0.1$		Patch ratio $r = 2/\pi$	
kh	$\lambda h^2/K$	kh	$\lambda h^2/K$
0.16	-1.02	1.02	-1.04
3.14	-400.00	3.14	-9.87
8.20	-2724.20	8.16	-66.55
9.42	-3600.00	9.42	-88.83
12.57	-6400.00	12.57	-157.91
15.71	-10000.00	15.71	-246.74

- First, $\cos\frac{kh}{2} = 0$ requires $\frac{kh}{2} = \frac{n\pi}{2}$ for odd n; that is, wavenumber $k = n\pi/h$ for odd n corresponding to rapidly decaying microscale structures of internal modes of the patch with eigenvalue $\lambda = -Kk^2 = -Kn^2\pi^2/h^2$ as shown in the second and fourth lines of Table 2.1.

- Second, $\sin\frac{kh}{4} = 0$ requires $\frac{kh}{4} = n\pi$ for an integer n; that is, wavenumber $k = 4n\pi/h$ for an integer n, corresponding to another representation of rapidly decaying microscale structures of internal modes of the patch with eigenvalues $\lambda = -Kk^2 = -16Kn^2\pi^2/h^2$ as shown in the fifth line of Table 2.1.

- The last factor being zero is
$$\mu\left(\frac{1-7r^2/48}{1-r^2/48}\right)\frac{4}{kh}\sin\frac{kh}{4} + (k^2h^2-\mu)\cos\frac{kh}{4} = 0,$$
which rearranges to
$$\frac{4}{kh}\tan\frac{kh}{4} = \left(1-\frac{k^2h^2}{\mu}\right)\left(\frac{1-r^2/48}{1-7r^2/48}\right). \tag{2.31}$$
Figure 2.8 plots the two sides of equation (2.31) as a function of wavenumbers kh. For the case $r = 2/\pi$, as shown in Figure 2.8 there is one small wavenumber, $kh \approx 1.02$, and all the rest satisfy $kh > 2\pi > \pi$, corresponding to rapid decaying microscale modes with eigenvalues $\lambda < -K\pi^2/h^2$. The eigenvalue of macroscale interest corresponds to this small wavenumber $kh \approx 1.02$, as it is the long lasting macroscale mode. Section 2.5 proves that this pattern of the eigenvalues seen in Table 2.1 and Figure 2.8 holds in general.

2.4.3 Antisymmetric eigenfunctions

Section 2.4.2 explores symmetric eigenfunctions and determines the eigenvalues corresponding to each of these symmetric modes. This section determines the antisymmetric eigenfunctions within our periodic patch simulation and finds algebraically all the possible wavenumbers and eigenvalues.

We start by seeking solutions of the eigenproblem (2.23) for the temperature field $\hat{T}$ that are piecewise smooth and antisymmetric about the mid-patch $x = 0$ (and then necessarily about the 'edges' of the periodic patch $x = \pm h$). Such solutions have the form

$$\hat{T} = \begin{cases} A\sin kx, & |x| < h/4\,, \\ \pm C + D\sin[k(x\mp\frac{h}{2})] \pm E\cos[k(x\mp\frac{h}{2})], & \pm h/4 \lessgtr x \lessgtr \pm 3h/4\,, \\ B\sin[k(x\mp h)], & x \gtrless \pm 3h/4\,, \end{cases} \tag{2.32}$$

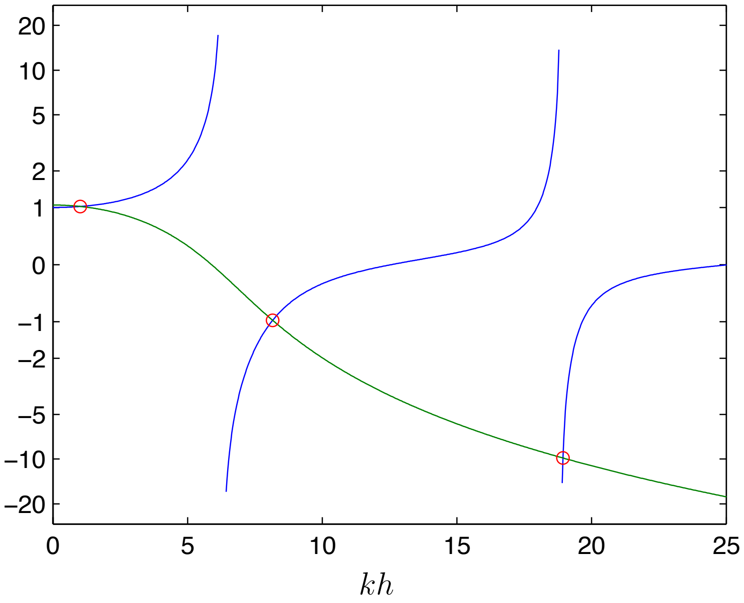

Figure 2.8: The LHS of equation (2.31) (blue) has an infinite number of vertical asymptotes at $kh = 2n\pi$ for odd n; the RHS of equation (2.31) (green) intersects it infinitely often (red circles) (here the control $\mu = 34.673$, and the patch ratio $r = 2/\pi$). The vertical axis is nonlinearly scaled.

for some constants A, B, C, D and E. The corresponding derivative fields are

$$\hat{T}_x = \begin{cases} kA\cos kx, & |x| < h/4\,, \\ kD\cos[k(x \mp \frac{h}{2})] \mp kE\sin(x \mp \frac{h}{2})], & \pm h/4 \lessgtr x \lessgtr \pm 3h/4\,, \\ kB\cos[k(x \mp h)], & x \gtrless \pm 3h/4\,. \end{cases} \quad (2.33)$$

The forcing control $g_\pm$, defined by (2.16), is piecewise constant in x, so solving the ODE (2.23) in the left and right action regions leads to requiring

$$k^2\left\{\pm C + D\sin\left[k\left(x \mp \frac{h}{2}\right)\right] \pm E\cos\left[k\left(x \mp \frac{h}{2}\right)\right]\right\} - Dk^2\sin\left[k\left(x \mp \frac{h}{2}\right)\right]$$
$$\mp Ek^2\cos\left[k\left(x \mp \frac{h}{2}\right)\right] + \frac{\mu}{h^2}g_\pm = 0,$$

that is,

$$\pm k^2 C + \frac{\mu}{h^2}g_\pm = 0. \quad (2.34)$$

We need to express the forcing control $g_\pm$ in terms of the macroscale interpolated field in both action region averages. Substituting the antisymmetric eigenfunctions $\hat{T}$ (2.32) into the macroscale interpolation (2.19) gives

$$\begin{aligned}\hat{T}_{\text{int}}(x) &= \left(1-\frac{x^2}{H^2}\right)\left(\frac{1}{1-r^2/48}\right)\frac{2}{h}\int_{-h/4}^{h/4}\hat{T}(x,t)\,dx \\ &= \left(1-\frac{x^2}{H^2}\right)\left(\frac{1}{1-r^2/48}\right)\frac{2A}{h}\int_{-h/4}^{h/4}\sin kx\,dx \\ &= 0.\end{aligned}$$

Interpolating this average to the left and right action regions yields $T_{\text{int},\pm} = 0$. Substituting the antisymmetric eigenfunctions (2.32), defined in the action regions, into the definition of the right action region (2.18) yields

$$\begin{aligned}\hat{T}_r &= \frac{2}{h}\int_{h/4}^{3h/4}\hat{T}(x,t)\,dx \\ &= \frac{2}{h}\int_{h/4}^{3h/4} C + D\sin\left[k\left(x-\frac{h}{2}\right)\right] + E\cos\left[k\left(x-\frac{h}{2}\right)\right]\,dx \\ &= C + E\frac{4}{kh}\sin\frac{kh}{4}.\end{aligned}$$

For antisymmetric eigenfunctions, the average over the left action region is

$$\hat{T}_l = -C - E\frac{4}{kh}\sin\frac{kh}{4}.$$

Therefore, the forcing control (2.16) in both action regions is

$$g_\pm = \mp C \mp E\frac{4}{kh}\sin\frac{kh}{4}. \tag{2.35}$$

Substituting this forcing control $g_\pm$ (2.35) into equation (2.34) and multiplying by h^2 gives

$$k^2h^2C + \mu\left[-C - E\frac{4}{kh}\sin\frac{kh}{4}\right] = 0. \tag{2.36}$$

This equation is combined with the continuity equations in order to determine all possible wavenumbers and eigenvalues.

Continuity of antisymmetric eigenfunctions

Solving the ODE (2.23) on the patch domain requires continuity for the antisymmetric eigenfunctions $\hat{T}$ and their first derivatives $\hat{T}_x$.

- Continuity for the antisymmetric eigenfunctions $\hat{T}$ (2.32) at $x=\pm\frac{h}{4}$, requires
$$A\sin\frac{kh}{4}=C-D\sin\frac{kh}{4}+E\cos\frac{kh}{4},$$
and at $x=\pm\frac{3h}{4}$, requires
$$C+D\sin\frac{kh}{4}+E\cos\frac{kh}{4}=-B\sin\frac{kh}{4}.$$

- Continuity for the derivative $\hat{T}_x$ (2.33) of the antisymmetric eigenfunctions at $x=\pm\frac{h}{4}$, requires
$$kA\cos\frac{kh}{4}=kD\cos\frac{kh}{4}+kE\sin\frac{kh}{4},$$
and at $x=\pm\frac{3h}{4}$, requires
$$kD\cos\frac{kh}{4}-kE\sin\frac{kh}{4}=kB\cos\frac{kh}{4}.$$

Adjoining equation (2.36) with the above four continuity equations for the antisymmetric eigenfunctions forms the matrix-vector system

$$\begin{bmatrix}\sin\frac{kh}{4} & 0 & -1 & \sin\frac{kh}{4} & -\cos\frac{kh}{4}\\ 0 & -\sin\frac{kh}{4} & -1 & -\sin\frac{kh}{4} & -\cos\frac{kh}{4}\\ \cos\frac{kh}{4} & 0 & 0 & -\cos\frac{kh}{4} & -\sin\frac{kh}{4}\\ 0 & \cos\frac{kh}{4} & 0 & -\cos\frac{kh}{4} & +\sin\frac{kh}{4}\\ 0 & 0 & k^2h^2-\mu & 0 & -\frac{4\mu}{kh}\sin\frac{kh}{4}\end{bmatrix}\begin{bmatrix}A\\B\\C\\D\\E\end{bmatrix}=\vec{0}.$$

The determinant of this matrix has to be zero for non-trivial solutions, namely,

$$\begin{aligned}\det &= \frac{-4}{kh}\Big[4\mu\cos^2\frac{kh}{4}\sin^2\frac{kh}{4}+kh(k^2h^2-\mu)\cos^3\frac{kh}{4}\sin\frac{kh}{4}\\ &\qquad -kh(k^2h^2-\mu)\cos\frac{kh}{4}\sin^3\frac{kh}{4}\Big]=0.\end{aligned}\tag{2.37}$$

Simplify the above characteristic equation (2.37) by using double angle formula and factoring gives

$$-4\cos\frac{kh}{4}\sin\frac{kh}{4}\left\{\frac{2\mu}{kh}\sin\frac{kh}{2}+(k^2h^2-\mu)\left[\cos^2\frac{kh}{4}-\sin^2\frac{kh}{4}\right]\right\}=0.$$

Algorithm 2 Numerically solve equation (2.38) for antisymmetric modes.

```
% numerically solve det=0 for Antisymmetric modes
r=0.1 % ratio of patch to domain size (r<=1)
hh=pi/2 % for simplicity the macroscale domain is length pi
h=r*hh; % patch half-size
mu=34.673
fn=@(kh)-2*sin(kh/2).*( mu*sin(kh/2)*2./kh+(kh.^2-mu).*cos(kh/2));
format bank
kh=fsolve(fn,1:50);
kh=sort(kh);
kh=kh(diff([kh 1e99])>1e-5);
lambda=-(kh).^2/h^2;
```

Table 2.2: Set of numerical wavenumbers kh, and eigenvalues λ for equation (2.38) for antisymmetric modes with parameters $\mu = 34.673$, and $H = \pi/2$.

Patch ratio $r = 0.1$		Patch ratio $r = 2/\pi$	
kh	$\lambda h^2/K$	kh	$\lambda h^2/K$
6.02	−1467.62	6.02	−36.21
6.28	−1600.00	6.28	−39.48
9.67	−3787.89	9.67	−93.46
12.57	−6400.00	12.57	−157.91
15.75	−10052.61	15.75	−248.04
18.85	−14400.00	18.85	−355.31

For further simplification, we use double angle identities in the first and second factor to derive

$$-2\sin\frac{kh}{2}\left[\frac{2\mu}{kh}\sin\frac{kh}{2} + (k^2h^2 - \mu)\cos\frac{kh}{2}\right] = 0. \tag{2.38}$$

Equation (2.38) determines all possible wavenumbers and eigenvalues which describe antisymmetric modes within the patch. Algorithm 2 numerically computes these wavenumbers kh for equation (2.38) as shown in Table 2.2. For two different patch ratios, $r = 0.1$ and $r = \pi/2$, Table 2.2 displays all antisymmetric microscale eigenvalues with large negative real-parts $\lambda < -36.21$. These eigenvalues represent microscale modes within the patch.

Analogous to the case of symmetric eigenfunctions in Section 2.4.2, we establish how the pattern shown by Table 2.2 occurs. Algebraically, setting each factor on the left-hand side of equation (2.38) to zero, gives two cases.

- The first factor being zero $\sin\frac{kh}{2} = 0$ requires $\frac{kh}{2} = n\pi$ for integer n; that is, wavenumber $kh = 2n\pi$ for integer n, corresponding to rapidly

Algorithm 3 Matlab code plotting the two sides of equation (2.39) showing there are an infinite number of wavenumbers k.

```matlab
%This is plot for the antisymmetric second case where
%(2/kh)* tan(kh/2)=-(k^2h^2/mu-1)
hh=pi/2;% for simplicity the macroscale domain is length pi
r=2/pi;% ratio of patch to domain size (r<=1)
h=hh*r;
ll=25;
mu=34.673
kh = linspace(1e-4,ll,999);
v1=(2./kh).*tan(kh./2);
v1(abs(v1)>20)=nan;
v2= -(kh.^2./mu-1);
v2(abs(v2)>20)=nan;
[xout,yout] = intersections(kh,asinh(v1),kh,asinh(v2),1);
plot(kh,asinh(v1),kh,asinh(v2),xout,yout,'ro','markersize',5)
tickx=[-20 -10 -5 -2 -1 0 1 2 5 10 20]
set(gca,'Ytick',asinh(tickx),'YtickLabel',num2cell(tickx))
xlabel('kh')
```

decaying microscale structures of internal modes of the patch with eigenvalue $\lambda = -Kk^2 = -Kn^2\pi^2/h^2$, as shown in the second and fourth lines of Table 2.2.

- The second factor in (2.38) being zero rearranges to

$$\frac{2}{kh}\tan\frac{kh}{2} = 1 - \frac{k^2h^2}{\mu}. \tag{2.39}$$

Figure 2.9 plots the two sides of this equation. It shows the general pattern of an infinite number of possible wavenumbers $k > 0$ of intercepts, all for $\frac{kh}{2} > \frac{\pi}{2}$, corresponding to rapidly decaying microscale modes (the algebraic formula (2.32) for eigenfunctions degenerates at $k = 0$ so that this apparent intersection is not a possible wavenumber). The wavenumbers kh are roots of the transcendental equation (2.39). Figure 2.9 illustrates that equation (2.39) has only non-zero wavenumbers $kh > \pi$.

2.5 A spectral gap generally exists

For different parameters of control strength μ, and for small enough patch ratio r, we prove the spectral gap of the patch system, namely all eigenvalues $\lambda \le -K\pi^2/h^2$, except one eigenvalue relatively near zero. Let us start with antisymmetric modes first as discussed in Section 2.4.3.

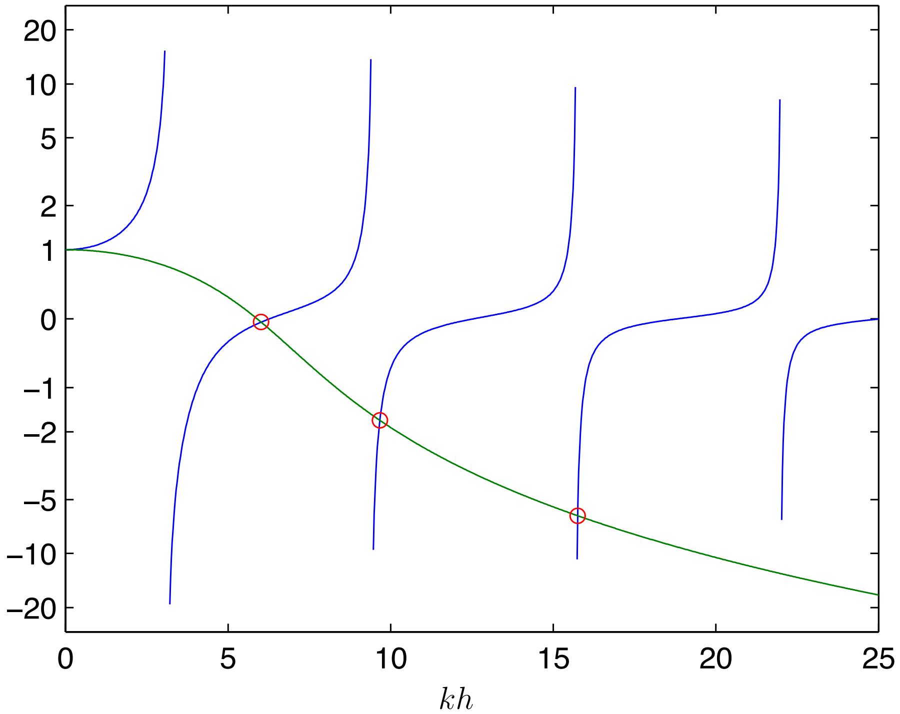

Figure 2.9: The LHS of equation (2.39) (blue) has an infinite number of vertical asymptotes at $kh = n\pi$ for odd n; the RHS of equation (2.39) (green) intersects it infinitely often (red circles). Algorithm 3 generates this figure where the strength control $\mu = 34.673$, and the patch ratio $r = 2/\pi$. The vertical axis is nonlinearly scaled.

- For the first factor $\sin\frac{kh}{2}$ of the characteristic equation (2.38) to be zero requires $\frac{kh}{2} = n\pi$ for $n = 1, 2, 3, \ldots$. Therefore, the corresponding eigenvalues are large and negative

  $$\lambda = -Kk^2 \leq -K\frac{4\pi^2}{h^2} < -K\pi^2/h^2,$$

  as seen in the second, fourth and sixth lines of Table 2.2 for example.

- The second factor of the characteristic equation (2.38) rearranges to equation (2.39).

  Consider the first branch of the tan function such as seen in Figure 2.9, that is for $kh/2 < \pi/2$. In equation (2.39)

  $$\text{LHS} = \frac{2}{kh}\tan\frac{kh}{2} > 1, \quad \text{whereas} \quad \text{RHS} = 1 - \frac{k^2h^2}{\mu} < 1.$$

  Thus, there is no intersection between the two curves for $0 < kh < \pi$. The smallest solution to equation (2.39) must lie in the second branch of the tan function, which for $kh/2 > \pi/2$. Therefore, all solutions satisfy $kh > \pi$. This holds for all control strength μ.

Consequently, all the corresponding eigenvalues for the antisymmetric modes are large and negative $\lambda = -Kk^2 < -K\pi^2/h^2$.

Now we discuss the symmetric modes which include the one relatively small eigenvalue λ.

- For the first factor $\cos\frac{kh}{2}$ of the characteristic equation (2.30) to be zero requires $kh/2 \geq \pi/2$, that is, eigenvalue $\lambda \leq -K\pi^2/h^2$, as shown in the second, fourth and sixth lines of Table 2.1.

- For the second factor $\sin\frac{kh}{4}$ of the characteristic equation (2.30) to be zero requires $kh \geq 4\pi$, that is, eigenvalue $\lambda \leq -K16\pi^2/h^2 < -K\pi^2/h^2$ as seen in the fifth line of Table 2.1.

- The third factor of the characteristic equation (2.30) rearranges to equation (2.31). There are two subcases, as seen in Figure 2.8 for example: the smallest wavenumber kh; and all the rest.
  - Except for the smallest wavenumber kh, all wavenumbers $kh > 2\pi$, with corresponding eigenvalues $\lambda < -K4\pi^2/h^2$ for all branches of the tangent.
  - The smallest wavenumber occurs on the first branch, $kh < 2\pi$, of the tangent.

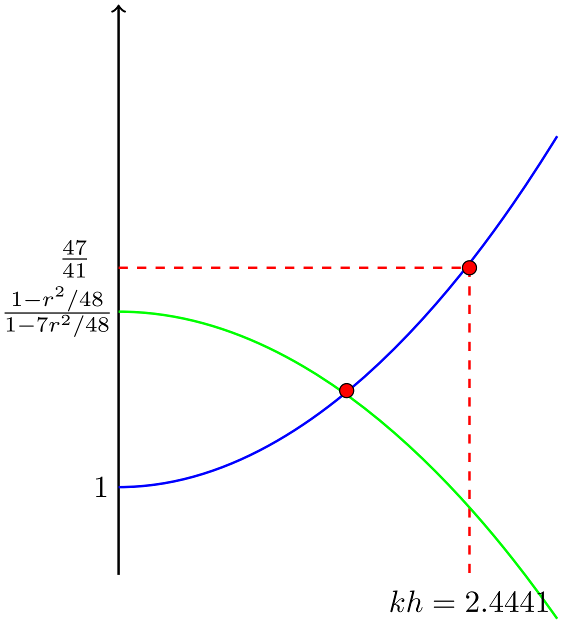

Figure 2.10: Schematic digram of the LHS (blue) and RHS (green) of equation (2.31); bounding the smallest wavenumber $kh \leq 2.4441$ by considering patch ratios $r \leq 1$.

Now we establish the conditions of parameters r and μ, so that a useful spectral gap exists in the patch system. To show there is a clear spectral gap we explore the first branch of $\frac{4}{kh}\tan\frac{kh}{4}$ on $0 < kh < 2\pi$ in the two cases of patch ratios $r \leq 1$ and the more practical case $r \leq 0.5$.

- For patch ratios $r \leq 1$, the left-hand side of equation (2.31), $\frac{4}{kh}\tan\frac{kh}{4}$, is an increasing function of kh, and the right-hand side, $(1-k^2h^2/\mu)\left(\frac{1-r^2/48}{1-7r^2/48}\right)$ is a decreasing function of kh. For $r \leq 1$ the maximum values in the right-hand side of equation (2.31) are
$$0 < \left(\frac{1-r^2/48}{1-7r^2/48}\right) \leq \frac{47}{41} \quad \text{and} \quad \left(1-\frac{k^2h^2}{\mu}\right) \leq 1,$$
as shown in Figure 2.10. Therefore, for all parameters μ, kh, and $r \leq 1$ the the right-hand side of equation (2.31) is
$$\left(1-\frac{k^2h^2}{\mu}\right)\left(\frac{1-r^2/48}{1-7r^2/48}\right) \leq \frac{47}{41}.$$
Numerically solving $\frac{4}{kh}\tan\frac{kh}{4} = \frac{47}{41}$ we obtain the bounding wavenumber $kh = 2.4441$. This is an upper bound for the smallest

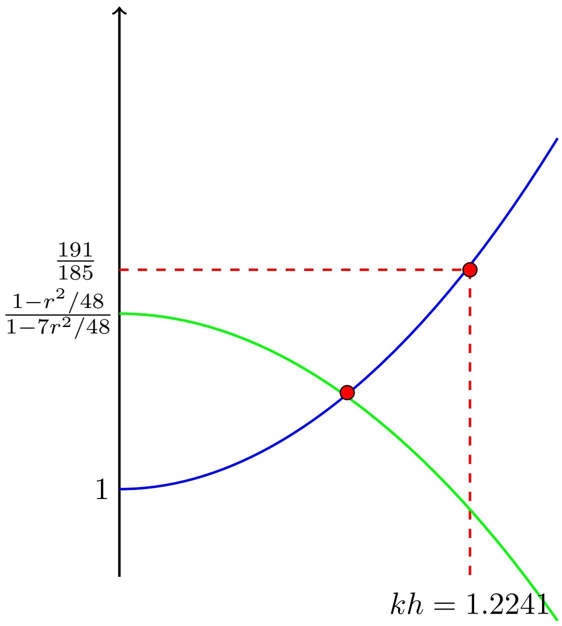

Figure 2.11: Schematic digram of the LHS (blue) and RHS (green) of equation (2.31); bounding the smallest wavenumber $kh \le 1.2241$ by considering patch ratios $r \le 0.5$.

solution kh of equation (2.31) as shown in Figure 2.10. Since the smallest macroscale eigenvalue bound $\lambda_1 \ge -5.9736K/h^2$ and all the other eigenvalues $\lambda \le -\pi^2 K/h^2$, there is a spectral gap, but it is not guaranteed to be clear for all $r \le 1$.

- For patch ratios $r \le 0.5$, we bound on the smallest wavenumber kh, in the same manner as the previous case. For $r \le 0.5$ the maximum values in the right-hand side of equation (2.31) are

$$0 < \left(\frac{1-r^2/48}{1-7r^2/48}\right) \le \frac{191}{185} \quad \text{and} \quad \left(1-\frac{k^2h^2}{\mu}\right) \le 1,$$

as seen in Figure 2.11. Therefore, for all parameters μ, kh, and $r \le 0.5$ the right-hand side of equation (2.31) is

$$\left(1-\frac{k^2h^2}{\mu}\right)\left(\frac{1-r^2/48}{1-7r^2/48}\right) \le \frac{191}{185}.$$

Numerically solving $\frac{4}{kh}\tan\frac{kh}{4} = \frac{191}{185}$ we find the bounding wavenumber $kh \le 1.2241$. This is an upper bound for the solution kh of equation (2.31), with corresponding eigenvalue

Table 2.3: Numerical wavenumbers kh and eigenvalues λ using finite differences method agree with the exact wavenumbers kh and eigenvalues λ from equation (2.30) and (2.38). The parameters, $\mu = 34.693$, $r = 2/\pi$ and $H = \pi/2$. The magenta numbers are for symmetric modes, whereas the blue numbers are for antisymmetric modes.

kh	λ	kh, (2.30) &(2.38)	λ, (2.30)& (2.38)
1.02	-1.03	1.02	-1.04
3.14	-9.87	3.14	-9.87
6.00	-36.01	6.02	-36.21
6.28	-39.48	6.28	-39.48
8.14	-66.32	8.16	-66.55
9.42	-88.82	9.42	-88.83
9.66	-93.40	9.67	-93.46
12.57	-157.89	12.57	-157.91
12.57	-157.89	12.57	-157.91
15.71	-246.69	15.71	-246.74

bound $\lambda_1 \geq -1.4984K/h^2$. Thus, there is a clear spectral gap between the smallest eigenvalue $\lambda_1 \geq -1.4984K/h^2$ and all the other eigenvalues $\lambda \leq -\pi^2 K/h^2$, guaranteed for all $r \leq 0.5$ and all μ.

This spectral gap indicates the existence of an emergent $1D$ slow manifold in this dynamics of the patch scheme (2.15) (Roberts 1988, Pötzsche & Rasmussen 2006). Because of the persistence of slow manifolds under perturbations, such a slow manifold here indicates that the controlled periodic patch scheme will possess such an emergent slow manifold for a wide variety of cognate systems.

2.5.1 Numerical eigenvalue analysis of a controlled patch verifies derived exact eigenvalues

Numerical examples verify the analytical results. Algorithm 4 calculates the wavenumbers and the eigenvalues of the continuum PDE for the controlled patch (2.15). For the purpose of comparison, Table 2.3 lists the macroscale numerical wavenumbers kh and eigenvalues λ and the exact wavenumbers kh and eigenvalues λ from equations (2.30) and (2.38) respectively, where the patch ratio $r = 2/\pi$. The numerical eigenvalues are in reasonable agreement with the exact eigenvalues.

Algorithm 4 Numerical wavenumbers and eigenvalues of the controlled patch scheme (2.15)–(2.16) (in matrix form) are determined in MATLAB.

```
% Explore coupling periodic one patch to the distance boundary
%Here just the diffusion PDE with a control  at quarter
%centred action regions.
r=2/(pi) % ratio of patch to domain size (r<=1)
nc=5;% averaging regions over the 2nc+1 grid points centred
n=(2*nc+1)*4 % this choice means core and averaging regions abutt
hh=pi/2 % for simplicity the macroscale domain is length pi
dx=2*r*hh/n; % microscale lattice spacing
% key microscale lattice indices
i0=n/2+(-nc:nc);
il=n/4+(-nc:nc);
ir=3*n/4+(-nc:nc);
wts=ones(1,2*nc+1)/(2*nc+1);
xpp=dx*((0:n)-n/2); % patch coordinates
c=(nc+0.5)*dx;  % halfwidth of averaging/action regions
% put physical location of the wrapped quarter points is
% halfway to the physical boundary
xq=r*hh/2; % xq=h/2 therfor xq=1/2
% field averages should be this factor
Fq=1-13*r^2/48;
F0= 1-r^2/48;
% periodic diffusion lattice op
format bank
ll=toeplitz([-2 1 zeros(1,n-3) 1]/dx^2);
i=(1:n)'; % microscale index vector
% compute spectrum for various control strengths
d1=Inf;
mu=34.673
% apply control strength mu, distributed over averaging regions
a=ll;
a([il ir],[il i0 ir])=a([il ir],[il i0 ir]) ...
+mu/(r*hh)^2*[ones(2*nc+1,1)*[-F0*wts Fq*wts 0*wts]
ones(2*nc+1,1)*[0*wts Fq*wts -F0*wts]];
[v,d]=eig(a);
complexity=norm(imag(diag(d)))
[d,j]=sort(real(diag(d))','descend')
% \mu and first 16 eigenvalus
muevals=[mu d(1:16) d(end)];
mmuevalues=muevals'
kh=r*hh*sqrt(-d(1:16));
if abs(d(1)+1)<abs(d1(1)+1), d1=d; v1=v(:,j); mu1=mu; end
% for the best of the above control strengths, plot some eigenvectors
v=v1; d=d1; mu=mu1
v=v.*meshgrid(sign([1 1e-20 1e-40]*v(1:3,:)));
v=v./meshgrid(max(abs(v)));
clf()
plot(xpp,v([n 1:n],1:5)*diag(1./max(1,sqrt(abs(d(1:5))))),'o-')
legend(num2str(d(1:5)',4))
```

Table 2.4: Numerical eigenvalues λ using finite differences method agree with the exact eigenvalues λ from equation (2.30) and (2.38). The parameters, $\mu = 34.693$, $r = 0.1$ and $H = \pi/2$. The magenta numbers are for symmetric modes, whereas the blue numbers are for antisymmetric modes.

λ	λ, (2.30) & (2.38)
-1.02	-1.02
-400.00	-400.00
-1467.40	-1467.62
-1599.95	-1600.00
-2723.94	-2724.20
-3599.74	-3600.00
-3787.60	-3787.89
-6399.19	-6400.00
-6399.19	-6400.00
-9998.02	-10000.00
-10050.63	-10052.61

With one exception, all of these possible wavenumbers $k \propto 1/h$, and the corresponding decay rate $\propto K/h^2$ characterises microscale modes within the patch. All these microscale modes cause the spatial structure internal in the patch to rapidly approach a quasi-equilibrium: in a time proportional to a cross-patch diffusion time.

Let us consider the small patch ratio $r = 0.1$ as an example closer to a practically useful configuration. The numerical computation represented in Table 2.4 shows a large gap between the smallest eigenvalue $\lambda = -1.02$ and all the other eigenvalues $\lambda \leq -400$.

2.5.2 Approximation to the eigenvalue of macroscale interest

In the controlled patch dynamics (2.15) the interesting macroscale, long-term, emergent dynamics are characterised by the smallest magnitude eigenvalue. This section approximates this interesting eigenvalue. The eigenvalue of macroscale interest is the one eigenvalue corresponding to the smallest kh. The corresponding small eigenvalue to the smallest kh occurs in the third case, equation (2.31), as illustrated in Figure 2.8. Two asymptotics are of interest in solving equation (2.31).

- Approximate equation (2.31) for strong control μ 'large', and for small kh and small patch size ratio r :

$$\begin{aligned}
\left(\frac{1-7r^2/48}{1-r^2/48}\right)\frac{4}{kh}\sin\frac{kh}{4} &\approx \cos\frac{kh}{4}\\
\left(\frac{1-7r^2/48}{1-r^2/48}\right)\left[1-\frac{1}{6}\left(\frac{kh}{4}\right)^2\right] &\approx 1-\frac{1}{2}\left(\frac{kh}{4}\right)^2\\
(1-7r^2/48)\left[1-\frac{1}{6}\left(\frac{kh}{4}\right)^2\right] &\approx (1-r^2/48)\left[1-\frac{1}{2}\left(\frac{kh}{4}\right)^2\right]\\
1-7r^2/48-\frac{1}{6}\left(\frac{kh}{4}\right)^2 &\approx 1-r^2/48-\frac{1}{2}\left(\frac{kh}{4}\right)^2\\
\frac{1}{3}\left(\frac{kh}{4}\right)^2 &\approx \frac{r^2}{8}\\
kh &\approx \pm\sqrt{6}r=\pm\sqrt{6}\frac{h}{H}
\end{aligned}$$

That is, wavenumber $k\approx\pm\sqrt{6}/H$ giving eigenvalue $\lambda\approx -6K/H^2$.

- Approximate equation (2.31) for arbitrary control μ and for the macroscale mode of small wavenumber kh :

$$\mu\left(\frac{1-7r^2/48}{1-r^2/48}\right)\left(1-\frac{k^2h^2}{96}\right)+(k^2h^2-\mu)(1-\frac{k^2h^2}{32})=\mathcal{O}(k^4h^4).$$

Omit products of small quantities to derive

$$\begin{aligned}
\mu\left(\frac{1-7r^2/48}{1-r^2/48}\right)\left(1-\frac{k^2h^2}{96}\right)+k^2h^2-\mu+\mu\frac{k^2h^2}{32} &= \mathcal{O}(k^4h^4)\\
k^2h^2\left[\frac{1}{\mu}+\frac{1}{32}-\frac{1}{96}\left(\frac{1-7r^2/48}{1-r^2/48}\right)\right]-\left[1-\left(\frac{1-7r^2/48}{1-r^2/48}\right)\right] &= \mathcal{O}(k^4h^4).
\end{aligned}$$

That is, straightforward algebra leads to

$$k^2h^2=\frac{r^2/8}{\frac{(1+2r^2/48)}{48}+\frac{(1-r^2/48)}{\mu}}+\mathcal{O}(k^4h^4).$$

From the numerator $kh\propto r$ so the r^2 terms in the denominator are negligable, giving

$$k^2h^2=\frac{6r^2}{1+48/\mu}+\mathcal{O}(r^4). \qquad (2.40)$$

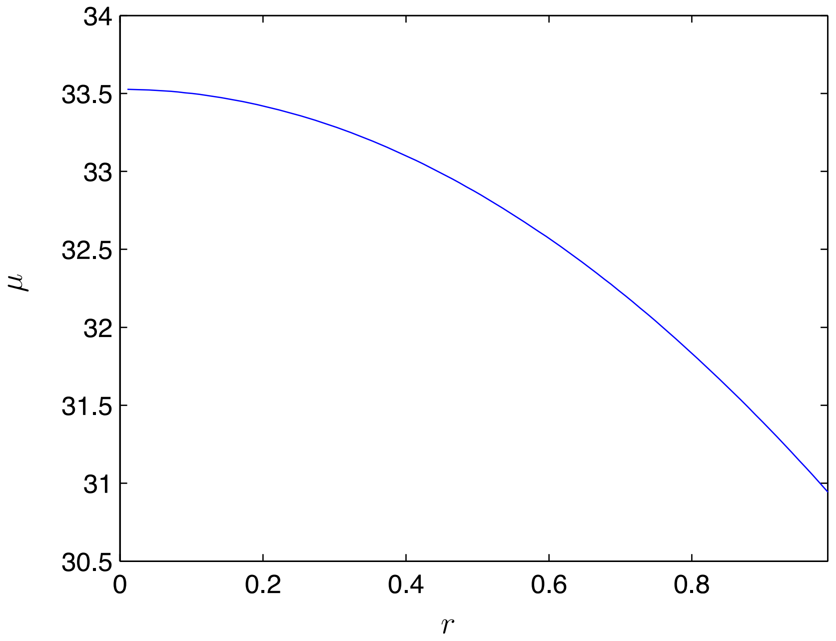

Figure 2.12: Best forcing control μ (2.42) on the interval $0 < r < 1$.

This gives eigenvalue

$$\lambda \approx -\frac{6K}{H^2(1+48/\mu)}. \tag{2.41}$$

For the purpose of checking this result, for a small patch ratio r and large control strength μ, the approximate (2.41) reduces to the previous case of eigenvalue $\lambda \approx -6K/H^2$. This small eigenvalue corresponds to the slow decay of the macroscale mode. This dominates the long-term dynamics of the controlled periodic patch of the diffusion equation PDE.

2.5.3 Determining optimal forcing control for a single patch

This section aims to determine a good forcing control μ within the periodic patch scheme. For the controlled patch simulation to best predict the correct macroscale dynamics of this mode, we need the wavenumber (2.40) to match the gravest wavenumber of the heat PDE (2.7)–(2.8) on the macroscale domain. Section 2.4 found the wavenumber to be $k_1H = \pi/2$, that is $k_1h = \frac{\pi}{2}r$. Thus obtain a best control by substituting this desired wavenumber into the

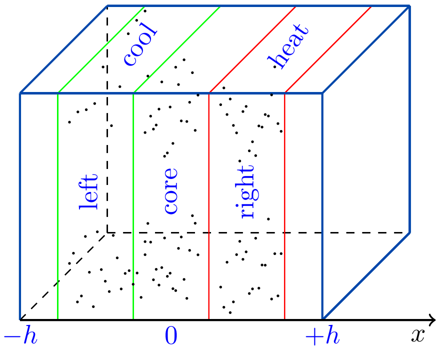

Figure 2.13: Cooling/heating atoms in the left/right action regions of a patch, and molecules decreases/increases their motion, resulting in a decrease/an increase in temperature.

characteristic equation (2.31) to yield

$$\frac{8}{\pi r}\tan\frac{\pi r}{8}=\left(1-\frac{\pi^2r^2}{4\mu}\right)\left(\frac{1-r^2/48}{1-7r^2/48}\right).$$

Rearrange this equation gives

$$\begin{aligned}\left(1-\frac{\pi^2r^2}{4\mu}\right)&=\frac{8}{\pi r}\tan\frac{\pi r}{8}\left(\frac{1-7r^2/48}{1-r^2/48}\right)\\ \frac{\pi^2r^2}{4\mu}&=1-\frac{8}{\pi r}\tan\frac{\pi r}{8}\left(\frac{1-7r^2/48}{1-r^2/48}\right)\\ \mu&=\frac{\pi^2r^2}{4\left[1-\frac{8}{\pi r}\tan\frac{\pi r}{8}\left(\frac{1-7r^2/48}{1-r^2/48}\right)\right]}.\end{aligned}\tag{2.42}$$

Figure 2.12 plots this good control (2.42) as a function of patch ratio r and shows weak dependence: μ varies by just 10% over $0<r<1$.

In an application, the optimal control (2.42) cannot immediately be used because the result (2.42) requires an estimate of the diffusivity K for any microscale system that is diffusive-like on the microscale. Nonetheless, simulations give a rough estimate for any microscale system that is largely diffusive on the microscale. The following Section 2.6 describes one way to estimate the diffusivity.

2.6 Estimate the diffusivity

Diffusivity, also called the diffusion coefficient, is the proportionality constant between the heat flux due to heat diffusion and the gradient in the temperature. Diffusivity is not only encountered in heat transport, but also in numerous other equations of physics and chemistry. This section estimates the effective diffusivity K of the temperature field in the atomistic simulations of this chapter. Figure 2.13 shows a single periodic patch with cooling and heating of the left and right action regions of the patch, respectively. Then the resultant temperature difference between the right and left action regions characterises the effective heat diffusion through the core.

Here we match the atomistic simulation with the mesoscale heat diffusion PDE in a patch. On the mesoscale, the continuum diffusion PDE modified by cooling/heating in the left and right regions is

$$\frac{\partial T}{\partial t} = K\frac{\partial^2 T}{\partial x^2} + \frac{\nu}{h^2}G(x), \tag{2.43}$$

where

$$G(x) = \begin{cases} 1, & \text{for } h/4 \le x \le 3h/4, \\ -1, & \text{for } -3h/4 \le x \le -h/4, \\ 0, & \text{otherwise.} \end{cases} \tag{2.44}$$

The parameter ν is the strength of the forcing cooling/heating, not the feedback control of Section 2.3.2.

In order to match the temperature field $T(x,t)$ of this continuum heat diffusion PDE (2.43)–(2.44) we compare it with atomistic simulations. For example, Figure 2.14 illustrates temperatures over macroscale times in the sub-patch regions and the temperature difference $T_r - T_l$. The simulation is of 512 atoms in a patch of spatial periodicity $2h = 8$ and with cooling/heating parameter $\nu = 0.9$. The temperature difference $T_r - T_l$ (Figure 2.14 (b)) suggests that the initial microscale transient increases on a time scale of roughly two (and then evolves slowly on a macroscale time to maintain a temperature difference of approximately about 0.15).

In the atomistic simulator we cool and heat atoms in the left and right action regions of the patch as shown in Figure 2.13. That is, the atomic equation of motion (2.6) is modified by the heating/cooling to (§A.2.3, lines 53–56)

$$\frac{d\vec{q}_j}{dt} = \vec{F}_j + \vec{q}_j g_j, \quad \text{where} \quad g_j = \begin{cases} \frac{\nu}{2h^2T_r}, & j \in \text{right}, \\ -\frac{\nu}{2h^2T_l}, & j \in \text{left}, \\ 0, & \text{otherwise.} \end{cases} \tag{2.45}$$

Recall that Section 2.3.1 computes the non-dimensional temperature in the left region in (2.9) as $T_l = 1/(2n_l)\sum_{j\in\text{left}}|\vec{q}_j|^2$. Hence, the rate of change of

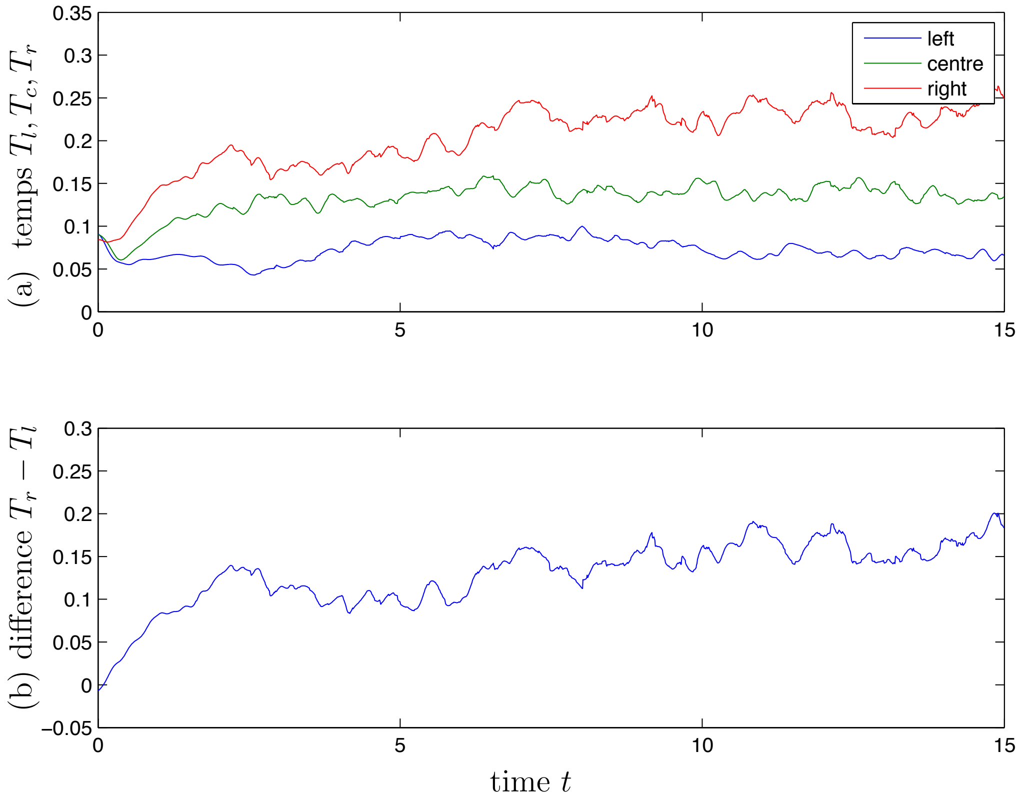

Figure 2.14: Temperatures over macroscale times in the sub-patch regions (a), and the temperature difference $T_r - T_l$ (b). The simulation is of 512 atoms in a patch of spatial periodicity $2h = 8$ and with cooling/heating strength $\nu = 0.9$.

temperature, neglecting the movement of atoms in and out of the region, is

$$\frac{dT_l}{dt} = \frac{d}{dt}\left[\frac{1}{2n_l}\sum_{j\in\text{left}}|\vec{q}_j|^2,\right] = \frac{1}{n_l}\sum_{j\in\text{left}}\vec{q}_j\cdot\frac{d\vec{q}_j}{dt}.$$

Substituting the modified equation (2.45) into this equation gives

$$\begin{aligned}\frac{dT_l}{dt} &= \frac{1}{n_l}\sum_{j\in\text{left}}\vec{q}_j\cdot\left(\vec{F}_j+\vec{q}_j g_j\right) = \frac{1}{n_l}\sum_{j\in\text{left}}\vec{q}_j\cdot\vec{F}_j + \frac{1}{n_l}\sum_{j\in\text{left}} g_j\cdot|\vec{q}_j|^2\\ &= \frac{1}{n_l}\sum_{j\in\text{left}}\vec{q}_j\cdot\vec{F}_j - \frac{\nu}{2h^2T_l}\left(\frac{1}{n_l}\sum_{j\in\text{left}}|\vec{q}_j|^2\right)\\ &= \frac{1}{n_l}\sum_{j\in\text{left}}\vec{q}_j\cdot\vec{F}_j - \frac{\nu}{h^2}.\end{aligned} \tag{2.46}$$

This equation represents the rate of temperature change in the left action region. Analogously, the rate of temperature change in the right action region of the patch is

$$\frac{dT_r}{dt} = \frac{1}{n_r}\sum_{j\in\text{right}}\vec{q}_j\cdot\vec{F}_j + \frac{\nu}{h^2}. \tag{2.47}$$

In the continuum approximation, it is well established that the first term on the RHS of equations (2.46) and (2.47) corresponds to the diffusion term KT_{xx}. Hence the cooling and heating terms in equations (2.46) and (2.47) are modelled in the mesoscale diffusion PDE by the term $\nu/h^2G(x)$ in the continuum heat diffusion PDE (2.43)–(2.44).

We use Fourier series expansion to approximately solve PDE (2.43)–(2.44). By the antisymmety of G, Figure 2.15, we express the piecewise constant source/sink G as a Fourier sine series

$$G(x) = \sum_{n=1}^{\infty} b_n \sin\left(\frac{n\pi x}{h}\right),$$

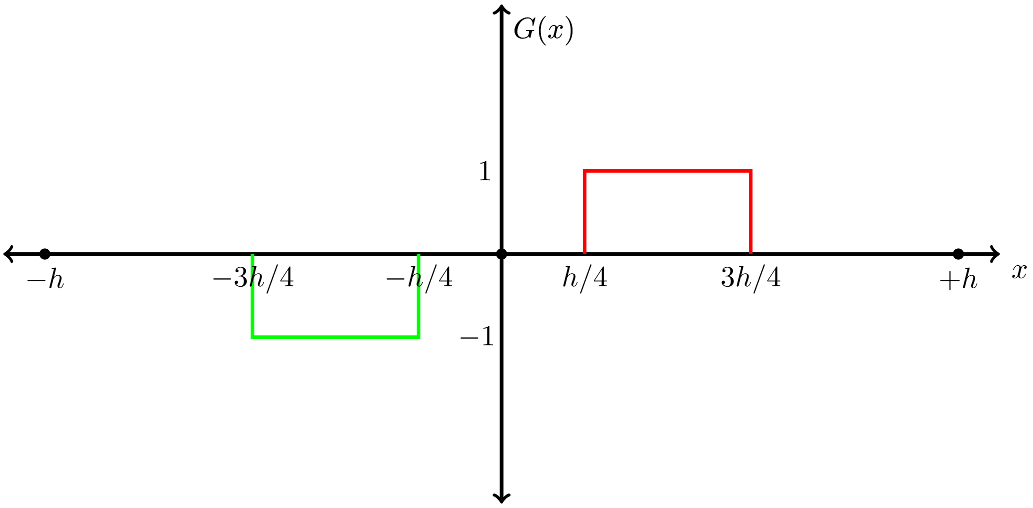

Figure 2.15: Constant cooling and heating the left and right action regions.

where coefficients

$$\begin{aligned}
b_n &= \frac{1}{h}\int_{-h}^{h} G(x)\sin\frac{n\pi x}{h}\,dx \\
&= \frac{2}{h}\int_{0}^{h} G(x)\sin\frac{n\pi x}{h}\,dx \quad \text{by symmetry} \\
&= \frac{2}{h}\int_{h/4}^{3h/4} \sin\frac{n\pi x}{h}\,dx \quad \text{by (2.44)} \\
&= \frac{2}{n\pi}\left[-\cos\frac{3n\pi}{4} + \cos\frac{n\pi}{4}\right] \\
&= \frac{2}{n\pi}[(2)\cos\frac{n\pi}{4}] \\
&= \frac{4}{n\pi}\cos\frac{n\pi}{4}.
\end{aligned}$$

Thus, on $x \in (-h, h)$

$$G(x) = \frac{4}{\pi}\sum_{n=1,\text{odd}}^{\infty} \frac{1}{n}\cos\left[\frac{n\pi}{4}\right]\sin\left[\frac{n\pi x}{h}\right].$$

For simplicity in this estimation and because we only need a rough approximation to estimate ν, we neglect all terms except the first term in the

Fourier series for $G(x)$. Therefore, the forced diffusion PDE (2.43) becomes

$$\frac{\partial T}{\partial t} \approx K\frac{\partial^2 T}{\partial x^2} + \frac{2\sqrt{2}\nu}{\pi h^2}\sin\frac{\pi x}{h}. \tag{2.48}$$

The equilibrium in the macroscale modelling is obtained by setting $\frac{\partial T}{\partial t} = 0$ in the forced diffusion PDE (2.48)

$$K\frac{\partial^2 T}{\partial x^2} \approx -\frac{2\sqrt{2}\nu}{\pi h^2}\sin\frac{\pi x}{h}.$$

Integrating this ODE twice with respect to x gives

$$T(x) \approx \frac{2\sqrt{2}\nu}{K\pi^3}\sin\frac{\pi x}{h} + c_1 x + T_*.$$

The constant c_1 has to be zero, since the patch is periodic, whereas the arbitrary constant T_* represents the mean patch temperature. Now we compute averages of the patch field on the left and right action regions. The average temperature on the left action region is

$$\begin{aligned} T_l &= \frac{2}{h}\int_{-3h/4}^{-h/4} T(x)\,dx \\ &= -\frac{4\sqrt{2}\nu}{K\pi^3 h}\left(\frac{h}{\pi}\right)\left[\cos\frac{\pi}{4} - \cos\frac{3\pi}{4}\right] + \frac{2}{h}\left[\frac{h}{2}T_*\right] \\ &= -\frac{8\nu}{K\pi^4} + T_*. \end{aligned}$$

By symmetry, the average of the microscale patch field on the right action region is

$$T_r = \frac{2}{h}\int_{h/4}^{3h/4} T(x)\,dx = \frac{8\nu}{K\pi^4} + T_*.$$

Hence, the temperature difference between the left and right action regions is

$$T_r - T_l \approx \left(\frac{16\nu}{\pi^4}\right)\frac{1}{K}, \quad \text{that is} \quad K \approx \frac{16\nu}{\pi^4(T_r - T_l)}. \tag{2.49}$$

Now the task is to use atomistic simulations to see how $T_r - T_l$ varies with ν and hence determine the diffusivity K from (2.49). After fifteen simulations, with different parameters ν and different initial conditions, Table 2.5 lists the average temperature differences $T_r - T_l$ and the core temperatures T_c,

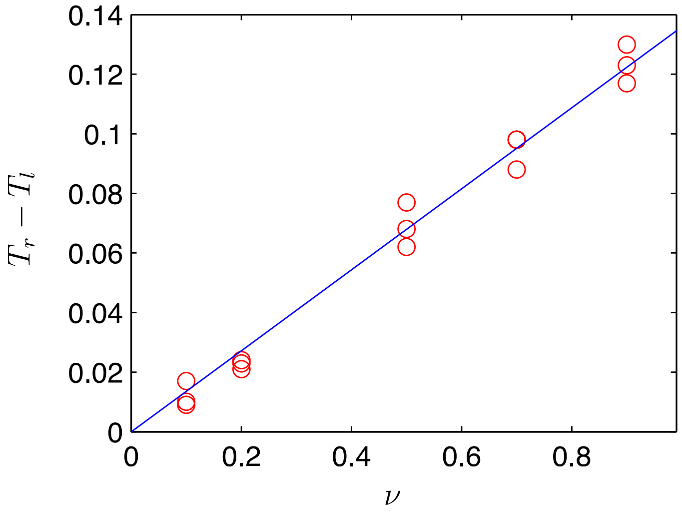

Figure 2.16: Plot the temperature differences $T_r - T_l$ for three run simulations shown by Table 2.5.

Algorithm 5 Plot the average of the temperature differences $T_r - T_l$ for different forcing cooling/heating parameters ν shown in Table 2.5.

```
%Plot the  average of the temperature difference Tl-Tr for different
% with different paramter mu
% Atomistic simulations are perform with 512 atoms and with time=15
% Relax the intial transient ts<2 is negeleted
% a particle has an initial velocity of 6 m/s
% add random position and random velocity
%xq=xq+0.1*diag([1,1,1,6,6,6])*(rand(6,nAtom)-0.5);
nu = [0.1 0.2 0.5 0.7 0.9]';
td= [0.009  0.021 0.077 0.088 0.123
0.010  0.024 0.068 0.098 0.130
0.017 0.023 0.063 0.098 0.117]';
cs=polyfit(repmat(nu,3,1),td(:),1)
cc=repmat(nu,3,1)\td(:)
% Plot
figure(1)
nus=[0;1];
%plot(nu,y,'ro',mus,[cs(2)+cs(1)*nus cc*nus])
plot(nu,td,'ro',nus,[cc*nus])
```

Table 2.5: Compute the average temperature differences $T_r - T_l$, and core temperatures T_c for $t > 2$, and their standard deviations σ_d and σ_c, respectively, for different forcing cool/heat parameters ν. The simulation is of 512 atoms in a patch of spatial periodicity $2h = 8$.

ν	$T_r - T_l$	σ_d	T_c	σ_c
01	0.009	0.012	0.126	0.010
0.1	0.010	0.012	0.123	0.008
0.1	0.017	0.013	0.123	0.008
0.2	0.021	0.014	0.135	0.012
0.2	0.024	0.013	0.125	0.007
0.2	0.023	0.013	0.131	0.008
0.5	0.077	0.025	0.129	0.009
0.5	0.068	0.009	0.131	0.009
0.5	0.062	0.014	0.136	0.013
0.7	0.088	0.013	0.135	0.015
0.7	0.098	0.023	0.132	0.007
0.7	0.098	0.021	0.141	0.012
0.9	0.123	0.024	0.132	0.014
0.9	0.130	0.020	0.132	0.007
0.9	0.140	0.027	0.138	0.009

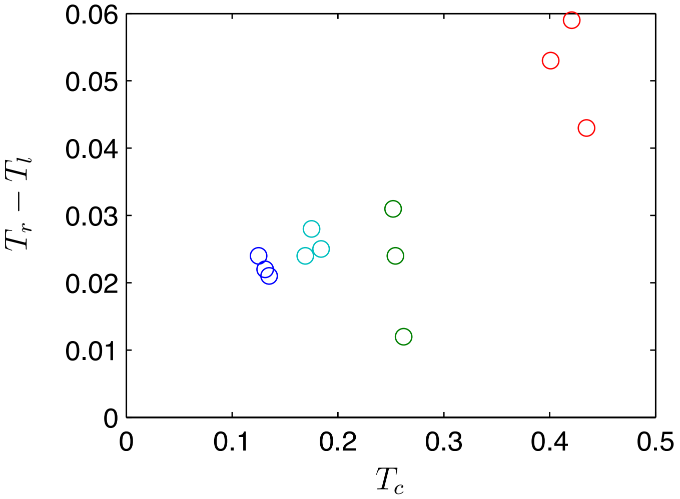

Figure 2.17: Plot the temperature differences $T_r - T_l$ against the core temperatures T_c for fixed $\nu = 0.2$.

averaged over $t > 2$. These averages were determined from simulation data such as that plotted by Figure 2.14.

Figure 2.16 plots the temperature differences $T_r - T_l$ as a function of ν. The data points are well fitted by a straight line through the origin which confirms (2.49). The slope of the line in Figure 2.16 determines the diffusivity K (non-dimensionalised) when the average of the temperature differences T_c is approximately 0.12. Since the slope is approximately 0.135, the nondimentional diffusion constant in (2.49) is $K \approx 1.12$. This approximation holds for temperatures near $0.12 - 0.14$ in Table 2.5. However, Figure 2.17 illustrates that $T_r - T_l$ may depend on T_c.

Appendix A.3 lists some results of numerical simulations in space of $N = 512$ atoms in a patch of size $8 \times 8 \times 8$. To avoid a significant amount of simulation time when exploring different parameters, the code is executed in parallel, presented in Appendix A.2.1. So far we have run simulations where the temperature after initial transients evolves approaching a quasi-equilibrium with different heating/cooling parameters ν range of $0.1 \leq \nu \leq 0.9$, and a core temperature T_c, range of $0.1 \leq T_c \leq 0.2$. Appendix A.3 lists results of the computational experiment repeated, about 60 times, with different heating/cooling parameters ν range of $0.1 \leq \nu \leq 0.9$, and a wider variety of random initial conditions. We want to fit a curve in the form, $T_r - T_l \approx (a + bT_c)\nu$, where $T_r - T_l, T_c, \nu$ are the data presented in Appendix A.3. MATLAB's fitting routine `fit` gives values for the coefficients $a \approx 0.14$ ranges from 0.13 to 0.15, and $b \approx -0.02$ ranges from -0.09 to 0.05. Since the coefficient $-0.09 \leq b \leq 0.05$, we take the approximate value as $b = 0$. The goal of this section is to find an estimate of the diffusivity K, and determine the best control for the simulation. From the computational experiment we take $a \approx 0.14$ and $b \approx 0$, then the temperature difference becomes $T_r - T_l \approx 0.14\nu$. Substituting this into (2.49) gives diffusivity $K \approx 16/(0.14\pi^4) = 1.17$ for a core temperature T_c in range of $0.1 - 0.2$.

Consequently, the good control strength (2.42) would be $\mu \approx 32.86$. This estimate is roughly the control strength we found convenient for generating Figure 2.7. The importance of this section is to illustrate that more simulations can determine a reasonably good control of the microscale periodic patch.

2.7 Conclusion

The atomistic simulation described by Section 2.1 presents one important example of microscale simulators used widely in engineering and science. In particular, we address the class of simulators that are given with periodic conditions on the microscale. The challenge is to create a computational wrapper around such microscale periodic simulators in order to to effectively predict macroscale behaviour over large spatial domains.

Section 2.3 implemented a suitable proportional controller applied to action regions in the patch of atomistic simulation to couple the periodic patch to its neighbours over unsimulated space. Local averaged properties over small spatial scales are used to predict the large-scale phenomena. Numerical simulations presented in Section 2.3.2 indicate that the applied control works effectively for atomistic simulations. The theoretical analysis establishes the effectiveness and efficiency of such an approach, and also determines good values for the strength of the proportional controller.

For small patch ratios $r \leq 0.5$, Section 2.5 shows a clear spectral gap in the patch dynamics which in turn indicates the existence of an emergent $1D$ slow manifold in the dynamics of the patch scheme. The emergent behaviour of this controlled, periodic patch, potentially predicts the appropriate macroscale, system level, dynamics for a wide range of microscale simulators. Section 2.6 presents an interesting outcome of the research by estimating the diffusivity, using a technique similar to homogenisation, to determine the best control for the simulation.

We emphasise that the main contribution for the method presented here lies in its potential to empower systematic analysis and understanding at a macroscopic system level when only a given microscale simulator is available. Further research based on this chapter could extend the analysis herein to establish the potential for high order accuracy, in multiple dimensions, analogous to what has been proven for patches with Dirichlet/Neumann/Robin boundaries (Roberts & Kevrekidis 2007, Roberts et al. 2014).

Chapter 3

One patch scheme for diffusion with time-varying boundary forcing

Many multiscale modelling methods for dissipative systems have been under investigation in the last two decades. Roberts & Kevrekidis (2005), and Kevrekidis & Samaey (2009) developed new techniques for multiscale modelling aiming to empower scientists and engineers to bridge space and time scales to simulate over the macroscale of interest. In particular, the patch method helps us predict macroscale behaviour over large spatial regions. Hyman (2005) discusses briefly the patch dynamics algorithm for time-dependent problems, while Kevrekidis et al. (2003) discuss the scheme in more detail and provide several physical applications.

For either dissipative or non-dissipative systems, the physical domain is divided into small, well-separated patches. A micro-simulator is only computed inside these small patches. Each patch requires suitable coupling conditions to bridge the gaps in the physical domain in which no solution is simulated. Initially, we limit our attention to the consideration of only one patch on a one-dimensional domain and postpone considering multiple patches to Chapter 4. We explore the general solution of microscale dynamics on a single small patch with the aim of predicting the system level behaviour and also to understand how the patch behaves.

This chapter considers a one-dimensional diffusion PDE with varying boundary forcing. Let x be the spatial variable and t be the time variable. Consider a field $u(x,t)$ satisfying the non-dimensionalised diffusion PDE

$$\frac{\partial u}{\partial t} = \frac{\partial^2 u}{\partial x^2}, \tag{3.1}$$

with time-dependent macroscale boundary conditions

$$u(-H,t) = a(t) \quad \text{and} \quad u(+H,t) = b(t). \tag{3.2}$$

The aim is to predict the evolution of the temperature field $u(x,t)$, on the macroscale domain, $-H \le x \le H$. The predictions are to be made by solving the PDE (3.1) only on a small patch. Solving the PDE only on a patch is the analytic analogue of computing an expensive simulation only on a small patch.

For simplicity, let us define one small patch in the macroscale domain, namely, $-h \le x \le h$. In implementation, we only run the simulation on this small fraction of the physical domain, and for the rest of the domain, we simply use interpolation. Since the simulation is only performed on this small patch, $-h \le x \le h$, the edge values $u(\pm h,t)$ have to be somehow specified.

The patch boundary conditions are determined in Section 3.1 by using the classic Lagrange interpolation. Section 3.2 then presents an algebraic analysis for determining the microscale eigenvalues of the patch dynamics. The eigenfunctions of the patch dynamics are partitioned into two categories: orthogonal and non-orthogonal. For orthogonal eigenfunctions, Section 3.3.2 computes the spectral coefficients in a straightforward manner. For non-orthogonal eigenfunctions, Section 3.3.3 finds the adjoint operator of the linear constant diffusion PDE (3.19) on the patch with nonlocal coupling conditions in (3.10). Section 3.4 then finds the eigenfunctions of the adjoint operator to form a biorthogonal complete basis which determines the spectral coefficients in formal series solutions. Section 3.5 constructs the patch solutions, and analyses the long time behaviour of the patch dynamics. Finally, Section 3.6 explores a modified patch scheme with time-delayed communications. The aim is to quantify the effect of such a delay on the patch scheme.

3.1 Patch boundary conditions

The simulator, PDE (3.1), for the microscale patch requires boundary conditions. Define the macroscale grid point $x = 0$ at the midpoint of the patch, and define the macroscale patch value

$$U(t) = u(0,t). \tag{3.3}$$

By exploiting the gap-tooth scheme, we couple this small microscale patch of simulation to the distant boundaries at $x = \pm H$ with classic Lagrange interpolation (Roberts & Kevrekidis 2007). The gap-tooth scheme interpolates between the three points $u(-H,t)=a$, $u(H,t)=b$, and $u(0,t)=U$ to estimate the macroscale field as the parabola

$$u(x,t)=u(0,t)\left(1-\frac{x^2}{H^2}\right)+\frac{x^2}{H^2}\left(\frac{a+b}{2}\right)+\frac{x}{H}\left(\frac{b-a}{2}\right). \qquad (3.4)$$

Hence, the gap-tooth scheme estimates the field on the edges of the patch as

$$u(\pm h,t)=u(0,t)(1-r^2)+\frac{r^2}{2}(a+b)\pm\frac{r}{2}(b-a), \qquad (3.5)$$

where $r=h/H$. Thus, the one patch scheme is to solve the PDE (3.1) with BCS (3.5) in order to predict the macroscale grid-value $U(t)$ and the macroscale field (3.4).

In the first step, we reduce the non-homogeneous boundary conditions (3.5) to the homogeneous case. Let us define the smooth function

$$w(x,t)=u(x,t)-\frac{C(t)}{H}x-D(t), \qquad (3.6)$$

so that

$$u(0,t)=w(0,t)+D(t),$$
$$u(\pm h,t)=w(\pm h,t)\pm C(t)r+D(t).$$

Substituting these equations into (3.5) gives

$$w(\pm h,t)\pm C(t)r=w(0,t)(1-r^2)+\frac{r^2}{2}(a+b)\pm\frac{r}{2}(b-a)-r^2D(t).$$

By choosing

$$D=\frac{a+b}{2}\quad\text{and}\quad C=\frac{b-a}{2},$$

we obtain the homogeneous boundary conditions for $w(x,t)$ as

$$w(\pm h,t)=w(0,t)(1-r^2). \qquad (3.7)$$

Substituting equation (3.6) into the diffusion PDE (3.1) yields

$$w_t=w_{xx}-\frac{\dot C(t)}{H}x-\dot D(t), \qquad (3.8)$$

where a dot over a variable denotes the first derivative with respect to time. This forced diffusion PDE (3.8) is subject to the patch homogeneous boundary conditions (3.7).

3.2 Solving the homogeneous equation

Consider the corresponding homogeneous problem of the linear diffusion PDE (3.8), namely,

$$\frac{\partial w}{\partial t} = \frac{\partial^2 w}{\partial x^2}, \tag{3.9}$$

with the patch homogeneous boundary conditions (3.7). To apply the method of separation of variables, we seek solutions in the form $w(x,t) \propto e^{\lambda t} v(x)$, where $v(x)$ is an eigenfunction corresponding to microscale eigenvalue of λ. The corresponding boundary value problem is

$$\frac{d^2 v}{dx^2} - \lambda v = 0, \quad v(\pm h) = v(0)(1 - r^2). \tag{3.10}$$

For microscale eigenvalue $\lambda = -k^2 (< 0)$, we expect spatially trigonometric solutions of the constant coefficient eigenproblem (3.10). Thus, a general solution to eigenproblem (3.10) is

$$v(x) = c_1 \cos kx + c_2 \sin kx,$$

where c_1 and c_2 are two constants, and k denotes a microscale wavenumber. The patch homogeneous boundary conditions in (3.10) imply that $c_1 \cos(kh) \pm c_2 \sin(kh) = (1 - r^2)c_1$. That is,

$$\begin{bmatrix} \cos(kh) - (1 - r^2) & \sin(kh) \\ \cos(kh) - (1 - r^2) & -\sin(kh) \end{bmatrix} \begin{bmatrix} c_1 \\ c_2 \end{bmatrix} = \begin{bmatrix} 0 \\ 0 \end{bmatrix}.$$

The determinant of this system's matrix must be zero for non-trivial solutions to exist and therefore we require

$$-2 \sin(kh)[\cos(kh) - (1 - r^2)] = 0. \tag{3.11}$$

Figure 3.1 illustrates the solutions of the characteristic equation (3.11) by asterisks and circles.

3.2.1 The spectrum

This subsection determines the microscale eigenvalues λ_n and the corresponding microscale eigenfunctions $v_n(x)$ of the patch dynamics. The characteristic equation (3.11) is zero in two cases.

- First, the microscale eigenvalues λ satisfy $\sin(kh) = 0$, where kh is a zero of the sine function, that is, $kh = n\pi/2$ for n even. The microscale wavenumbers $k = n\pi/2h$. Then the microscale eigenvalues
$$\lambda = -\left(\frac{n\pi}{2h}\right)^2, \quad n \text{ even},$$
are all negative, and the corresponding eigenfunctions
$$v(x) = \sin\left(\frac{n\pi x}{2h}\right), \quad n \text{ even}. \tag{3.12}$$
- Second, the microscale eigenvalues λ satisfy $\cos(kh) = (1 - r^2)$. In this particular case, the microscale wavenumbers k_n are non-trivial functions of the patch ratio r. Set $k_1 h = \cos^{-1}(1 - r^2)$ where $0 < k_1 < \pi/2$. Then from the periodicity and symmetry of $\cos k_n x$, as shown in Figure 3.1, the microscale wavenumbers take the form
$$k_{n\pm1} = k_n \pm k_1, \quad \text{for } n \in 4\mathbb{N},$$
which gives the microscale wavenumbers of $k_3 = k_4 - k_1$, $k_5 = k_4 + k_1$, $k_7 = k_8 - k_1$, $k_9 = k_8 + k_1$, and so on. Hence, the microscale eigenvalues take the form
$$\lambda_{n\pm1} = -\left(\frac{n\pi}{2h} \pm k_1\right)^2, \quad \text{for } n \in 4\mathbb{N},$$
with the corresponding eigenfunctions
$$v(x) = \cos(k_n x), \quad n \text{ odd}. \tag{3.13}$$

By applying the principle of superposition, we obtain a general solution to the homogeneous PDE (3.9)–(3.10) as
$$w(x,t) = \sum_{n \text{ even}}^{\infty} a_n e^{\lambda_n t} \sin(k_n x) + \sum_{n \text{ odd}}^{\infty} a_n e^{\lambda_n t} \cos(k_n x). \tag{3.14}$$

3.3 Non-homogeneous problem

The method of eigenfunction expansion is employed to solve the non-homogeneous problem (3.7)–(3.8) with the patch homogeneous boundary conditions (3.7). We assume eigenfunctions (3.12) and (3.13) of the eigenproblem (3.9)–(3.10) form a complete set with respect to piecewise smooth

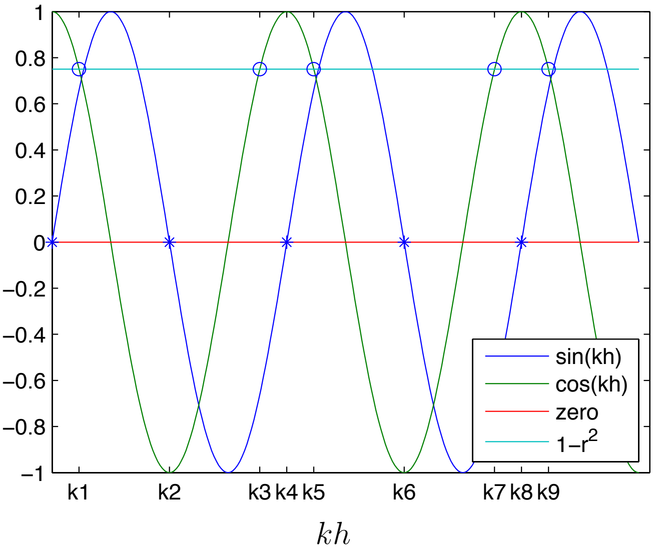

Figure 3.1: Illustration of the solutions of the characteristic equation (3.11) for the case $r = 1/2$. The intersection points are of two types: circles represent the roots of $\cos(kh) = (1 - r^2)$ the wavenumbers of eigenfunctions $\cos(k_n x)$ where n is odd; asterisks represent the wavenumbers of eigenfunctions $\sin(k_n x)$ where n is even.

function over the microscale patch $x \in [-h, h]$, and find the generalised Fourier series expansion of the forcing terms in terms of the eigenfunctions. The forcing terms in PDE (3.8) are represented using the eigenfunction expansions

$$x = \sum_{n \text{ even}}^{\infty} c_n \sin(k_n x) \quad \text{and} \quad 1 = \sum_{n \text{ odd}}^{\infty} d_n \cos(k_n x). \tag{3.15}$$

The factors c_n and d_n are the corresponding spectral expansion coefficients. In order to determine these spectral coefficients c_n and d_n, the orthogonality and biorthogonality conditions need to be considered.

Orthogonality (Haberman 2004, p.51). We say functions $f(x)$ and $g(x)$ are *orthogonal* over the interval $-h \le x \le h$, if $\int_{-h}^{h} f(x)g(x)\,dx = 0$.

3.3.1 The biorthogonal eigenfunction expansion

An eigenfunction expansion is a standard method for solving partial differential equations. Illustrations of the expansion for self-adjoint systems are typically found in numerous textbooks (Weinberger 2012, e.g.). The properties of self-adjoint operators lead to the orthogonality between two different eigenfunctions and to a straightforward algorithm for eigenfunction expansion. However, for non-self-adjoint differential operators, in fluid dynamics for example, the eigenfunctions are not necessarily orthogonal (Li et al. 2009, e.g.).

Here the eigenfunctions separate into two sets:

- The asymmetric sine functions are orthogonal and so are straightforwardly dealt with first; and
- The symmetric cosine functions are not orthogonal and so need further analysis.

3.3.2 Determining the spectral sine coefficients

Determining the spectral coefficients c_n in (3.15) is easily achieved by exploiting the orthogonality of the sine function. Multiplying both sides of equation (3.15) by $\sin(k_m x)$ and integrating from $-h$ to h.

$$\int_{-h}^{h} x\,\sin(k_m x)\,dx = \sum_{n\text{ even}}^{\infty} c_n \int_{-h}^{h} \sin(k_n x)\,\sin(k_m x)\,dx,$$

orthogonality yields

$$\begin{aligned}\int_{-h}^{h} x\sin(k_m x)\,dx &= c_m \int_{-h}^{h} \sin^2(k_m x)\,dx \\ &= \frac{c_m[2k_m h - \sin(2k_m h)]}{2k_m}.\end{aligned}$$

Rearranging gives

$$c_m = \frac{2k_m}{2k_m h - \sin(2k_m h)} \int_{-h}^{h} x\sin(k_m x)\,dx. \tag{3.16}$$

Integrating equation (3.16) by parts we obtain

$$c_m = \frac{4[\sin(k_m h) - hk_m\cos(k_m h)]}{k_m[2hk_m - \sin(2k_m h)]}, \tag{3.17}$$

where $k_m = m\pi/2h$, for even m, are the wavenumbers of eigenfunctions $\sin(k_m x)$ in the characteristic equation (3.11). Hence the eigenfunction expansion of the antisymmetric forcing in PDE (3.8) is

$$x = \sum_{m\text{ even}}^{\infty} \frac{4[\sin(k_m h) - hk_m\cos(k_m h)]}{k_m[2hk_m - \sin(2k_m h)]} \sin(k_m x). \tag{3.18}$$

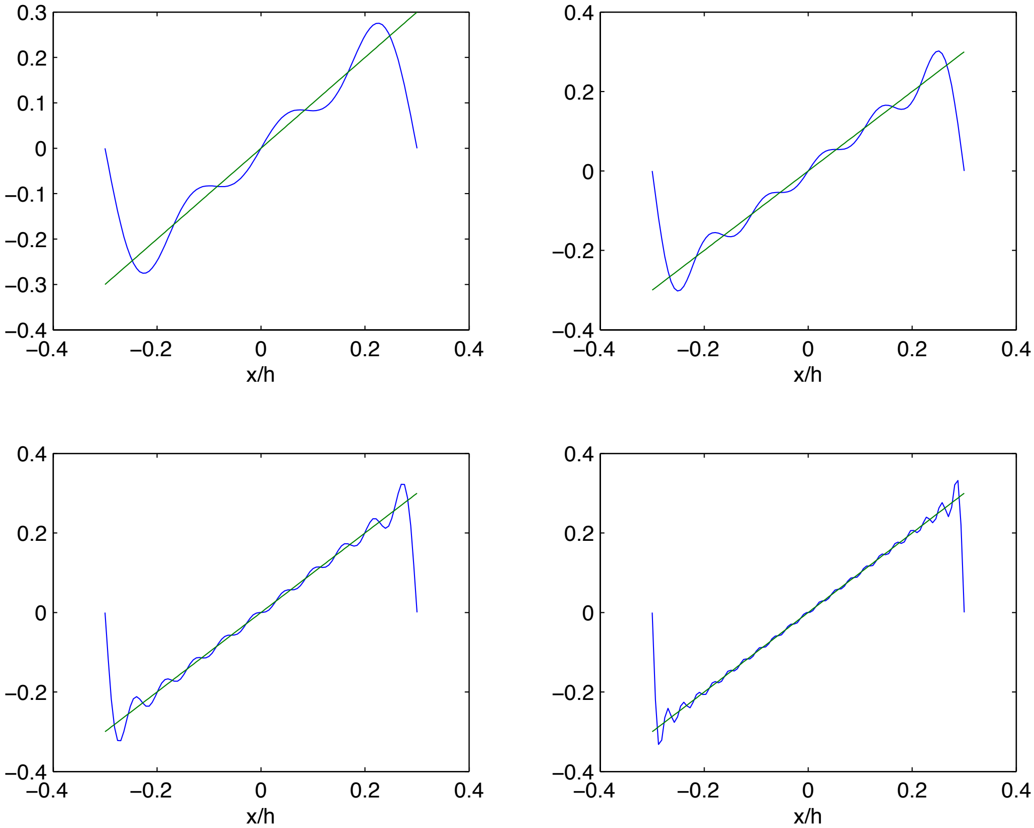

Figure 3.2: Spectral approximations (3.18) to the function x for the various partial sums of $3, 5, 10$, and 20 eigenmodes and in the case of patch ratio $r = 0.3$.

Figure 3.2 shows this spectral approximations (3.18) for the various partial sums of $3, 5, 10$, and 20 eigenmodes and in the case of patch ratio $r = 0.3$.

3.3.3 Determining the spectral cosine coefficients

Determining the spectrum coefficients d_n in (3.15) is more involved due to the non-orthogonality of the eigenfunctions $\cos(k_n x)$ for the particular wavenumbers k_n for odd n. The eigenfunctions over the microscale domain $[-h, h]$, for the case in which n is odd, are not mutually orthogonal. This is due to the non-self-adjointness of the system (Eckhaus 2012, p.16). However, we exploit the property of biorthogonality by finding the adjoint eigenfunctions, and then we compute the spectral coefficients in the eigenfunction expansion using eigenfunctions of the adjoint problem.

The first goal of this subsection is to find the corresponding adjoint operator. On the patch $|x| < h$ define the spatial diffusion operator

$$\mathcal{L}v := \frac{d^2}{dx^2}v, \tag{3.19}$$

such that $v(x)$ and its first derivative v_x are continuous at $x = 0$ and with boundary conditions in (3.10).

Let $v(x)$ and $z(x)$ be functions of x. Define the inner product over the patch to be

$$\langle v, z\rangle := \int_{-h}^{h} vz\,dx. \tag{3.20}$$

We aim to find the adjoint operator $\mathcal{L}^\dagger$ satisfying the fundamental property of the adjoint operator

$$\langle \mathcal{L}v, z\rangle = \langle v, \mathcal{L}^\dagger z\rangle, \tag{3.21}$$

for all v in the domain of $\mathcal{L}$ and z in the domain of $\mathcal{L}^\dagger$. To find the adjoint operator observe that the microscale patch is effectively subdivided into two subregions by the patch boundary conditions in (3.10). Additionally, there exists implicit conditions that the subgrid field v and its first derivative v_x are continuous at $x = 0$. Apply the definition of the inner product (3.20), the definition of the operator $\mathcal{L}$ (3.19) and integrating by parts twice to expand the LHS of (3.21) as

$$\begin{aligned}\langle \mathcal{L}v, z\rangle \;&=\; \langle v, z_{xx}\rangle + (v_x z - v z_x)|_{-h} + (v_x z - v z_x)|_{+h}\\ &\quad + (v_x z - v z_x)|_{-0} + (v_x z - v z_x)|_{+0}\,,\end{aligned}$$

where subscripts denote differentiations with respect to x. Also, with superscripts denoting evaluation, continuity requires $v^{\pm 0} = v^0$ and $v_x^{\pm 0} = v_x^0$. Further, using the patch boundary conditions in (3.10), the inner product

$$\begin{aligned}\langle \mathcal{L}v, z\rangle \;&=\; \langle v, z_{xx}\rangle + v_x^0\left[z^{-0} - z^{+0}\right]\\ &\quad + v^0\left[-z_x^{-0} + z_x^{+0} + (1-r^2)(z_x^{-h} - z_x^{h})\right] - v_x^{-h}z^{-h} + v_x^h z^h.\end{aligned}$$

Thus, for the fundamental property of the adjoint operator (3.21) to hold, the adjoint operator must be defined as

$$\mathcal{L}^\dagger := \frac{d^2}{dx^2}, \tag{3.22}$$

with the following conditions:

- firstly, that the subgrid field z satisfies Dirichlet boundary conditions at the edges of the patch

$$z^{-h} = z^{+h} = 0; \tag{3.23}$$

- secondly, that z is continuous at the centre of the patch, $x = 0$,

$$z^{-0} = z^{+0}; \tag{3.24}$$

- thirdly, there is a jump in the first derivative at $x = 0$,

$$z_x^{+0} - z_x^{-0} = (1 - r^2)(z_x^{+h} - z_x^{-h}). \tag{3.25}$$

These conditions make the boundary terms in the integration by parts vanish.

3.4 Eigenfunctions of the adjoint operator

Section 3.3.3 finds the adjoint operator (3.22) with its BCs (3.23)–(3.25). We now determine the spectrum and the eigenfunctions of the adjoint. Consider the eigenvalue problem for the adjoint operator

$$\mathcal{L}^\dagger z = \lambda z, \quad \text{equivalently} \quad \frac{d^2 z}{dx^2} - \lambda z = 0, \tag{3.26}$$

with BCs (3.23)–(3.25). This PDE (3.26) is a constant coefficient in x. For eigenvalue $\lambda = -k^2 < 0$, we expect spatially trigonometric solutions of the constant coefficient eigenproblem (3.26). Since the eigenfunction $z(x)$ is continuous at the origin, then a general solution to the differential equation (3.26) is

$$z(x) = \begin{cases} \alpha \cos kx + \beta_1 \sin kx, & x < 0, \\ \alpha \cos kx + \beta_2 \sin kx, & x > 0, \end{cases} \tag{3.27}$$

where α, β_1, and β_2 are constants. The first derivative of $z(x)$ (3.27) is to be used to satisfy the jump condition (3.25):

$$z_x(x) = \begin{cases} -\alpha k \sin kx + \beta_1 k \cos kx, & x < 0, \\ -\alpha k \sin kx + \beta_2 k \cos kx, & x > 0. \end{cases}$$

Satisfying the adjoint boundary conditions Evaluating the boundary conditions (3.23)–(3.25) we obtain the following homogeneous system of algebraic equations

$$\alpha\cos(kh)-\beta_1\sin(kh)=0, \tag{3.28}$$

$$\alpha\cos(kh)+\beta_2\sin(kh)=0, \tag{3.29}$$

$$\alpha[2\kappa k\sin(kh)]+\beta_1[-k+\kappa k\cos(kh)]+\beta_2[k-\kappa k\cos(kh)]=0,$$

where $\kappa=(1-r^2)$. Divide the last equation by k leads to

$$\alpha[2\kappa\sin(kh)]+\beta_1[-1+\kappa\cos(kh)]+\beta_2[1-\kappa\cos(kh)]=0 \tag{3.30}$$

Now rewrite this homogeneous system of algebraic equations (3.28)–(3.29) and (3.30) as the matrix equation

$$\begin{bmatrix}\cos(kh) & -\sin(kh) & 0\\ \cos(kh) & 0 & \sin(kh)\\ 2\kappa\sin kh & -1+\kappa\cos kh & 1-\kappa\cos kh\end{bmatrix}\begin{bmatrix}\alpha\\ \beta_1\\ \beta_2\end{bmatrix}=\vec{0}. \tag{3.31}$$

For non-trivial solutions to this system's matrix (3.31), the determinant of the matrix must be zero, providing the same characteristic equation (3.11).

To proceed further, as before the characteristic equation (3.11) is zero in two cases characterised by n even and n odd.

3.4.1 Case in which n is even

First, the characteristic equation (3.11) is zero when microscale wavenumbers $k_nh=n\pi/2$, for even n. Then the matrix equation (3.31) becomes

$$\begin{bmatrix}\pm1 & 0 & 0\\ \pm1 & 0 & 0\\ 0 & -1\pm\kappa & 1\mp\kappa\end{bmatrix}\begin{bmatrix}\alpha\\ \beta_1\\ \beta_2\end{bmatrix}=\vec{0},$$

where the upper and the lower case of each entry in this matrix are obtained from

$$\cos(n\pi/2)=\begin{cases}+1, & \text{for } n\in 4\mathbb{N},\\ -1, & \text{for } n\in 4\mathbb{N}-2.\end{cases}$$

Solving the above matrix equation we obtain $\alpha=0$ and $\beta_1=\beta_2$. Hence, when we substitute $\alpha=0$ and $\beta_1=\beta_2$ into the general solution (3.27) we obtain eigenfunctions of the adjoint operator for n even as

$$z_n=\sin k_nx,\quad \text{for } n \text{ even}, \tag{3.32}$$

which are identical to the corresponding eigenfunctions of the original system (because the operator $\mathcal{L}$ is self-adjoint when restricted to the space of antisymmetric functions).

3.4.2 Case in which n is odd

The second factor of the determinant (3.11) requires that $\cos k_nh = (1 - r^2)$. Replacing each function κ in the matrix equation (3.31) with $\cos k_nh$ yields

$$\begin{bmatrix} \cos(k_nh) & -\sin(k_nh) & 0 \\ \cos(k_nh) & 0 & \sin(k_nh) \\ 2\cos(k_nh)\,\sin(k_nh) & -\sin^2(k_nh) & \sin^2(k_nh) \end{bmatrix} \begin{bmatrix} \alpha \\ \beta_1 \\ \beta_2 \end{bmatrix} = \vec{0}.$$

Solving this matrix equation we obtain

$$\beta_1 = \frac{\alpha\,\cos(k_nh)}{\sin(k_nh)} = \cot(k_nh), \qquad \beta_2 = -\frac{\alpha\,\cos(k_nh)}{\sin(k_nh)} = -\cot(k_nh),$$

when $\alpha = 1$. By substituting α, β_1 and β_2 into the general solution (3.27) we obtain eigenfunctions of the adjoint operator for n odd as

$$z_n(x) = \begin{cases} \cos(k_nx) + \cot(k_nh)\,\sin(k_nx), & x < 0, \\ \cos(k_nx) - \cot(k_nh)\,\sin(k_nx), & x > 0. \end{cases} \tag{3.33}$$

The eigenfunctions z_n (3.32)–(3.33) (for both n even and odd) of the adjoint operator form a biorthogonal set of functions to the original sets v_n (3.12) and (3.13), that is

$$\langle v_n, z_m \rangle = 0, \quad \text{for} \quad n \neq m. \tag{3.34}$$

3.4.3 The spectral coefficients d_n

In this subsection, the biorthogonality condition (3.34) determines the spectral coefficients d_n in (3.15). By taking the inner product of the adjoint eigenfunctions z_m for m odd and the expansions (3.15) we obtain

$$\langle 1, z_m \rangle = \left\langle \sum_{n\ \mathrm{odd}}^{\infty} d_n \cos(k_nx), z_m \right\rangle = \sum_{n\ \mathrm{odd}}^{\infty} d_n \langle \cos(k_nx), z_m \rangle.$$

By using biorthogonality condition (3.34) we obtain $\langle \cos k_nx, z_m \rangle = 0$ whenever $n \neq m$. In summing over n, only the $n = m$ term remains and we obtain

$$\langle 1, z_m \rangle = d_m \langle \cos(k_mx), z_m \rangle.$$

Rearranging gives the spectral expansion coefficients

$$d_m = \frac{\langle 1, z_m \rangle}{\langle \cos(k_mx), z_m \rangle}. \tag{3.35}$$

By applying the definition of the inner product (3.20), the numerator on the right-hand side of equation (3.35) becomes

$$\begin{aligned} \langle 1, z_m\rangle &= \int_{-h}^{h} \cos(k_m x)\,dx + \cot(k_m h)\left[\int_{-h}^{0} \sin(k_m x)\,dx - \int_{0}^{h} \sin(k_m x)\,dx\right] \\ &= \frac{-2[\cos(k_m h) - 1]}{k_m \sin(k_m h)}. \end{aligned}$$

Similarly, evaluating the denominator on the right-hand side of equation (3.35) yields

$$\begin{aligned} \langle \cos(k_m x), z_m\rangle &= \int_{-h}^{h} \cos^2(k_m x)\,dx + \cot(k_m h)\int_{-h}^{0} \cos(k_m x)\sin(k_m x)\,dx \\ &\quad - \cot(k_m h)\int_{0}^{h} \cos(k_m x)\sin(k_m x)\,dx \\ &= h + \frac{\sin(2k_m h)}{2k_m} - \frac{\cot(k_m h)\sin^2(k_m h)}{k_m} \\ &= h. \end{aligned}$$

Thus, the spectral coefficients

$$\begin{aligned} d_m &= \frac{2[1 - \cos(k_m h)]}{k_m h\ \sin(k_m h)} \\ &= \frac{2\left\{1 - [1 - 2\sin^2(k_m h/2)]\right\}}{2k_m h\ \sin(k_m h/2)\ \cos(k_m h/2)} \\ &= \frac{2\sin(k_m h/2)}{k_m h\ \cos(k_m h/2)} \\ &= \frac{2}{k_m h}\tan(k_m h/2). \end{aligned} \tag{3.36}$$

Hence the eigenfunction expansion of the forcing 1 in PDE (3.8) is

$$1 = \sum_{m\text{ odd}}^{\infty} \frac{2}{k_m h}\tan\left(\frac{k_m h}{2}\right)\cos(k_m x). \tag{3.37}$$

Figure 3.3 shows this spectral approximations (3.37) to the function 1 for the various partial sums, and in the case of patch ratio $r = 0.3$. Evidently, the partial sums converge to the function 1 except at the endpoints where the Gibbs phenomenon appears.

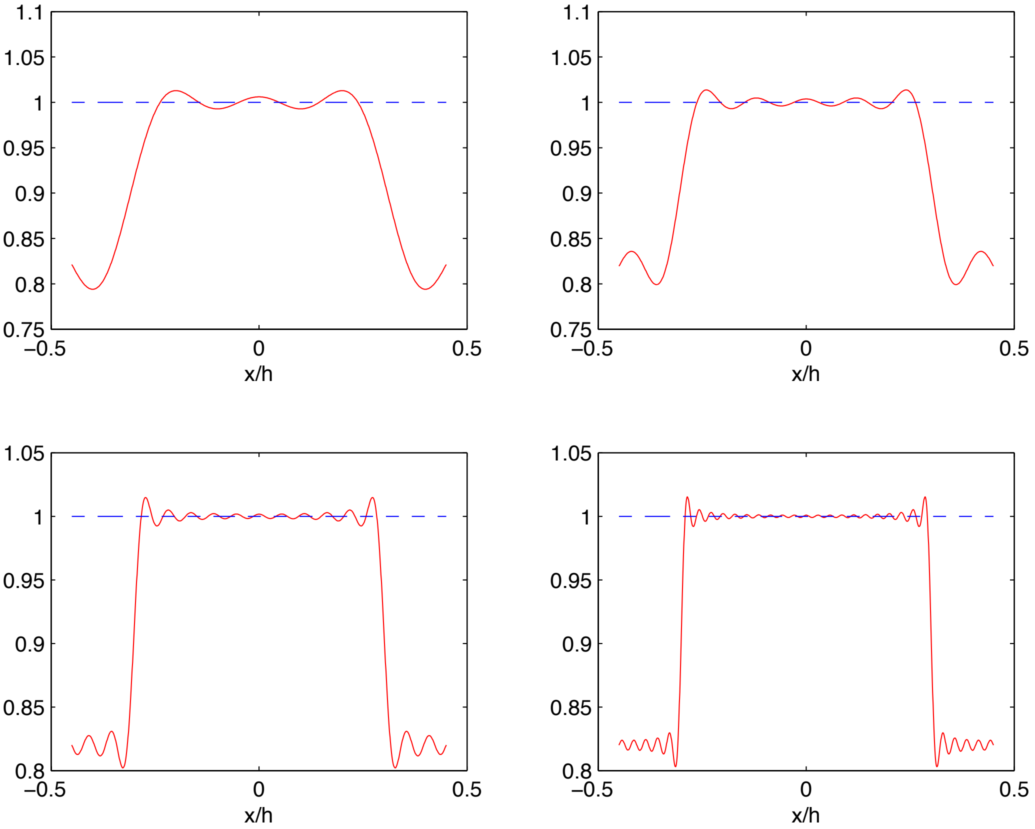

Figure 3.3: Spectral approximations (3.37) to the function 1 : plot the Nth partial sums for $N = 3, 5, 11$, and 21 eigenmodes and in the case of patch ratio $r = 0.3$.

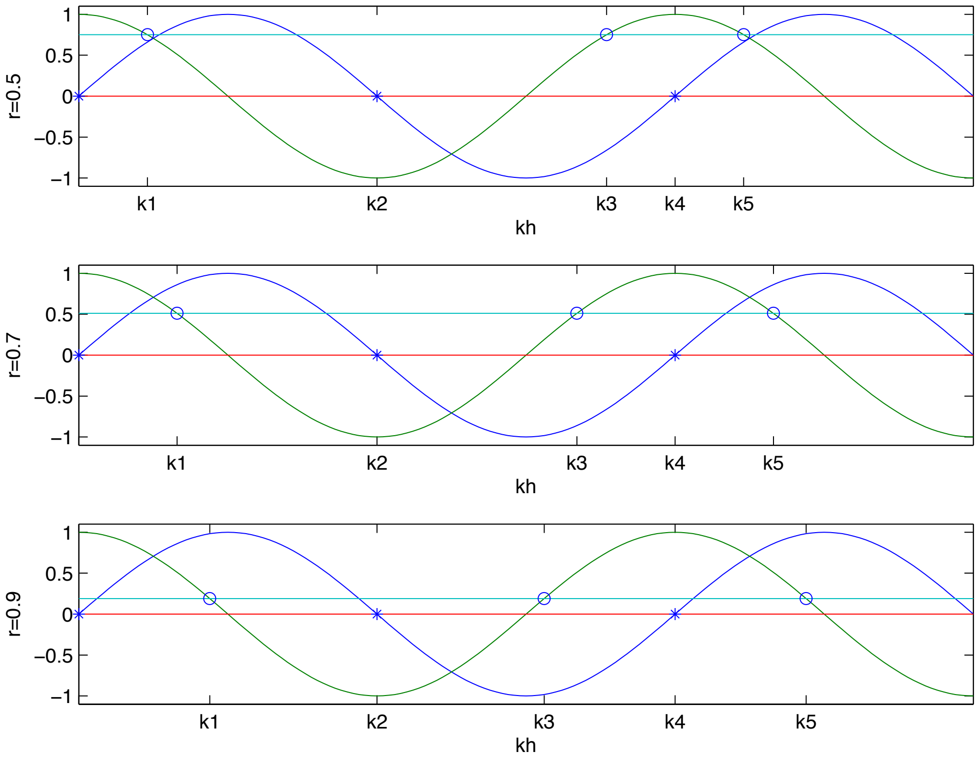

Figure 3.4: Illustration of the solutions of the characteristic equation (3.11), where k_n for n odd are functions of r which tends to one.

3.4.4 Finding the coefficients for $r = 1$

Here we explore one limit of theoretical interest. Consider the case when the microscale patch covers the whole physical domain; that is when patch ratio $r = h/H \to 1$. When patch ratio $r = 1$, the patch homogeneous boundary conditions (3.7) reduce to the exact macroscale boundary conditions (3.2). Setting the patch ratio $r = 1$ reduces the spectrum coefficients to the traditional Fourier series coefficients. For $r = 1$, Figure 3.4 shows that the wavenumbers $k_1 = \pi/2h$, $k_2 = \pi/h$, $k_3 = 3\pi/2h$ and $k_4 = 2\pi/h$.

- The Fourier coefficients c_m, m even, as r goes to one

$$\begin{aligned}\lim_{r\to 1} c_m &= \lim_{r\to 1} \frac{2}{hk_m^2(r)} \sin(k_m(r)h) - \lim_{r\to 1} \frac{2}{k_m(r)} \cos(k_m(r)h), \\ &= \frac{2}{hk_m^2} \sin(k_m h) - \frac{2}{k_m} \cos(k_m h), \\ &= -\frac{4h}{m\pi}(-1)^{(m+2)/2}.\end{aligned}$$

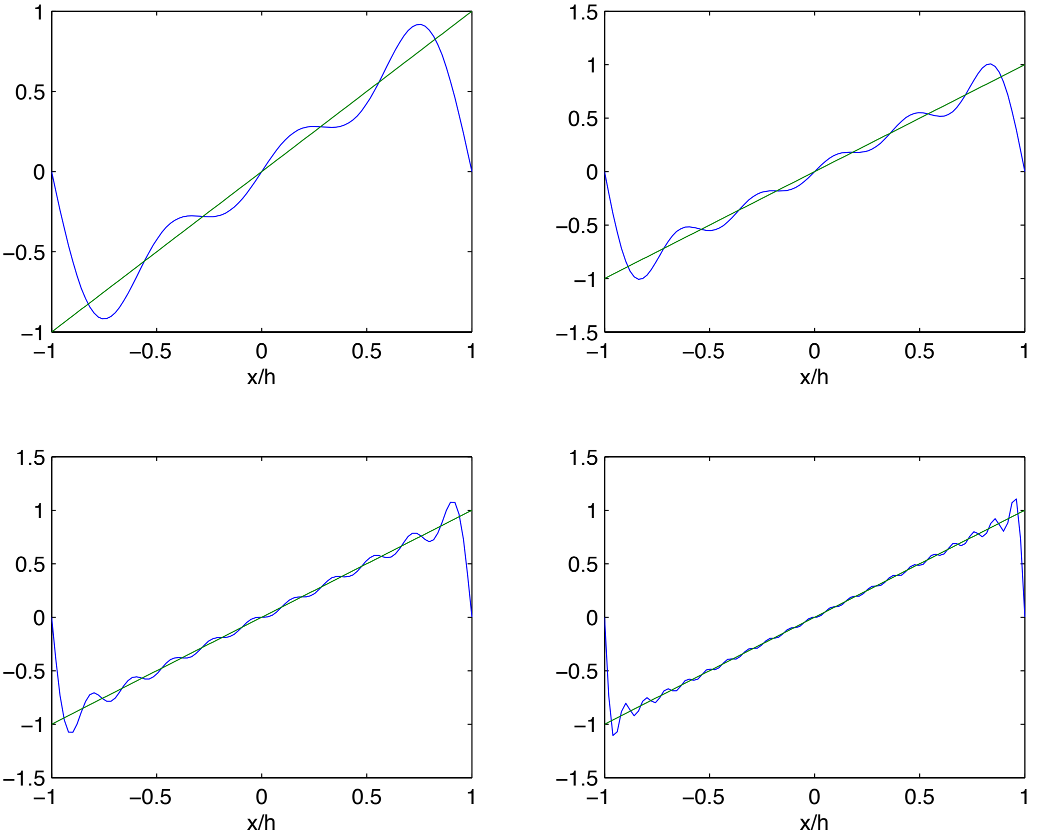

Figure 3.5: Spectral approximations (3.38) to the function x for the various partial sums for $N = 3, 5, 10$, and 20 eigenmodes and in the case of patch ratio $r = 1$.

Hence the eigenfunction expansion of the forcing x in PDE (3.8) becomes

$$x = -\sum_{m \text{ even}}^{\infty} \frac{4h}{m\pi}(-1)^{(m+2)/2}\sin(k_m x). \tag{3.38}$$

Figure 3.5 shows this approximation (3.38) to the function x for the various partial sums, and in the case $h = 1$, $H = 1$ and $r = 1$. In this case, these coefficients are well known as the Fourier expansion of a sawtooth wave.

- For coefficients d_m, where m is odd,

$$\lim_{r\to 1} d_m = \lim_{r\to 1} \frac{2}{k_m h}\tan(k_m h/2) = \frac{4}{m\pi}(-1)^{(m-1)/2}.$$

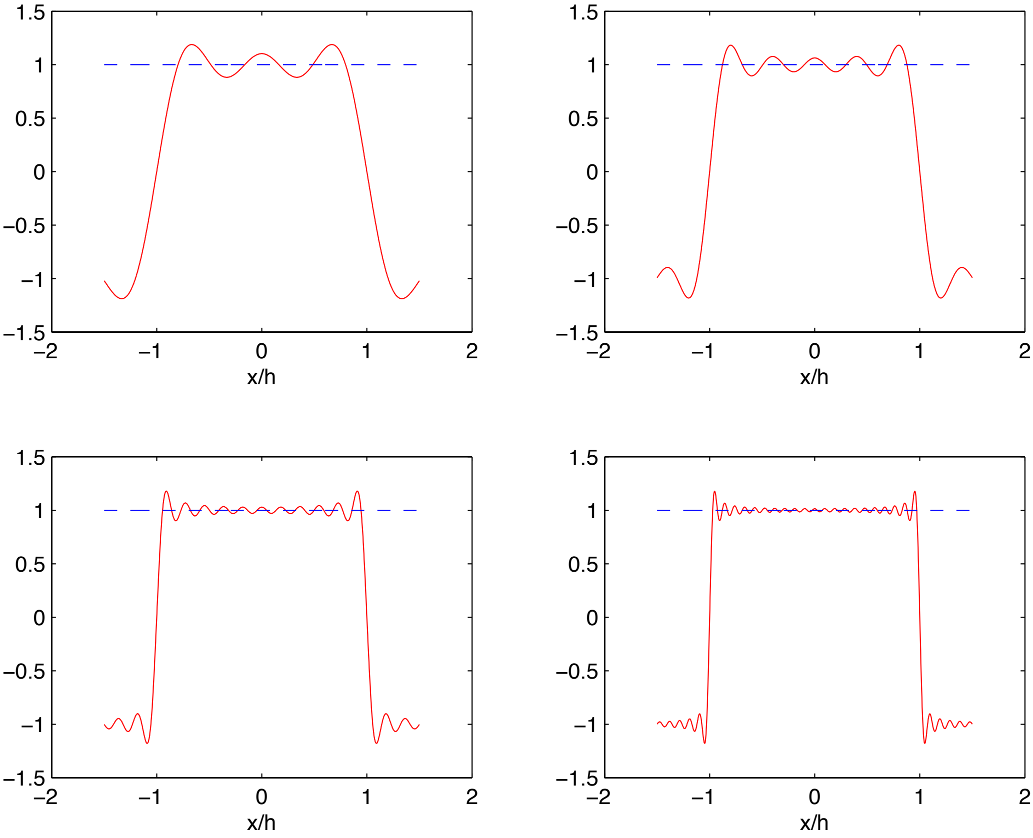

Figure 3.6: Spectral approximations (3.39) to function 1 for the various partial sums for $N = 3, 5, 11,$ and 21 eigenmodes, and in the case of patch ratio $r = 1$.

Hence the eigenfunction expansion of the forcing 1 in PDE (3.8) is

$$1 = \sum_{m \text{ odd}}^{\infty} \frac{4}{m\pi} (-1)^{(m-1)/2} \cos(k_m x). \tag{3.39}$$

Figure 3.6 shows this approximations (3.39) to the function 1 for the various partial sums in the case $h = 1$, $H = 1$ and $r = 1$. In this case, these coefficients are well known as the Fourier approximation to a square wave.

3.5 Constructing the formal solution

All that remains to solve the non-homogeneous PDE (3.8) is to find the generalised Fourier coefficients in the particular forced solution. We seek a spectral expansion

$$w(x,t) = \sum_{n \text{ even}}^{\infty} w_n(x,t)\sin(k_n x) + \sum_{n \text{ odd}}^{\infty} w_n(x,t)\cos(k_n x).$$

Term-by-term differentiation of $w(x,t)$, first with respect to t, and separately twice with respect to x yields

$$\begin{aligned} w_t(x,t) &= \sum_{n \text{ even}}^{\infty} \frac{dw_n(t)}{dt}\sin k_n x + \sum_{n \text{ odd}}^{\infty} \frac{dw_n(t)}{dt}\cos k_n x, \\ w_{xx}(x,t) &= \sum_{n \text{ even}}^{\infty} \lambda_n w_n(t)\sin k_n x + \sum_{n \text{ odd}}^{\infty} \lambda_n w_n(t)\cos k_n x. \end{aligned}$$

Substituting these results into the forced diffusion PDE (3.8) yields

$$\sum_{n \text{ even}}^{\infty}\left[\frac{dw_n(t)}{dt} - \lambda_n w_n(t)\right]\sin k_n x + \sum_{n \text{ odd}}^{\infty}\left[\frac{dw_n(t)}{dt} - \lambda_n w_n(t)\right]\cos k_n x = -\frac{\dot{C}(t)}{H}x - \dot{D}(t).$$

Replace the RHS (the forcing terms x and 1) by their decompositions (3.15)

$$\begin{aligned} &\sum_{n \text{ even}}^{\infty}\left[\frac{dw_n(t)}{dt} - \lambda_n w_n(t)\right]\sin k_n x + \sum_{n \text{ odd}}^{\infty}\left[\frac{dw_n(t)}{dt} - \lambda_n w_n(t)\right]\cos k_n x \\ &= \sum_{n \text{ even}}^{\infty} \dot{C}(t)c_n \sin k_n x + \sum_{n \text{ odd}}^{\infty} \dot{D}(t)d_n \cos k_n x, \end{aligned} \tag{3.40}$$

where c_n and d_n are the spectral coefficients obtained in (3.17) and (3.36), respectively. The eigenfunctions $\sin k_n x$ and $\cos k_n x$ are linearly independent on the microscale interval $[-h, h]$, so equate the Fourier coefficients in equation (3.40) to give (Kreyszig 2011)

$$\frac{dw_n(t)}{dt} - \lambda_n w_n(t) = \dot{C}(t)c_n + \dot{D}(t)d_n, \tag{3.41}$$

where $c_n = 0$ when n odd and $d_n = 0$ when n even. For simplicity, we denote $\dot{F}_n(t) = \dot{C}(t)c_n + \dot{D}(t)d_n$. Therefore, the ODE (3.41) becomes

$$\frac{dw_n(t)}{dt} - \lambda_n w_n(t) = \dot{F}_n(t),$$

and this equation is a non-homogeneous, linear, first order, differential equation which has a general solution (Zill & Wright 2012, p.157)

$$w_n(t) = w_n(0)e^{\lambda_n t} + \int_0^t e^{\lambda_n(t-s)}\dot{F}_n(s)\,ds,$$

for some constants $w_n(0)$ depending upon the initial conditions. Therefore, a general solution for the non-homogeneous PDE (3.8) with the patch homogeneous boundary conditions (3.7) is

$$\begin{aligned} w(x,t) &= \sum_{n \text{ even}}^{\infty} \sin(k_n x)\left[w_n(0)e^{\lambda_n t} + \int_0^t e^{\lambda_n(t-s)}\dot{F}_n(s)\,ds\right] \\ &\quad + \sum_{n \text{ odd}}^{\infty} \cos(k_n x)\left[w_n(0)e^{\lambda_n t} + \int_0^t e^{\lambda_n(t-s)}\dot{F}_n(s)\,ds\right]. \qquad (3.42) \end{aligned}$$

One can straightforwardly check that (3.42) satisfies the governing patch equations for all $w_n(0)$, $C(t)$ and $D(t)$.

3.5.1 The eigenvalue of macroscale interest

Section 3.5 determines the general patch dynamics solutions (3.42) based on solving the microscopic dynamics on a small patch in one spatial dimension. Here the aim is to use the general solutions (3.42) to develop a better understanding of the way the patch scheme behaves and, in particular, the way it predicts for the macroscale dynamics.

Section 3.2.1 computes the spectrum of the patch scheme to be

$$\begin{aligned} \lambda_n &= -k_n^2 = -\left(\frac{n\pi}{2h}\right)^2, \quad \text{for } n \text{ even}, \\ \lambda_{n\pm1} &= -\left(k_n \pm k_1\right)^2, \quad \text{for } n \in 4\mathbb{N}, \end{aligned}$$

where k_1 is the smallest solution of (3.11), namely $k_1 h = \cos^{-1}(1-r^2)$. This Section 3.5.1 discusses the microscale eigenvalues and determines the slowest mode and its dynamics. This slowest mode approximates the macroscale dynamics.

Consider wavenumbers k_n and eigenvalues λ_n on a 'small' patch; that is small h. Being divided by h, where $h = rH$ all these microscale wavenumbers k_n (Figure 3.1), except for the smallest wavenumber k_1, are large and the corresponding eigenvalues represent the rapidly decaying microscale structure of internal modes of the patch with rate $-\lambda_n = k_n^2$. These rapidly decaying microscale modes are not of interest to the macroscale dynamics.

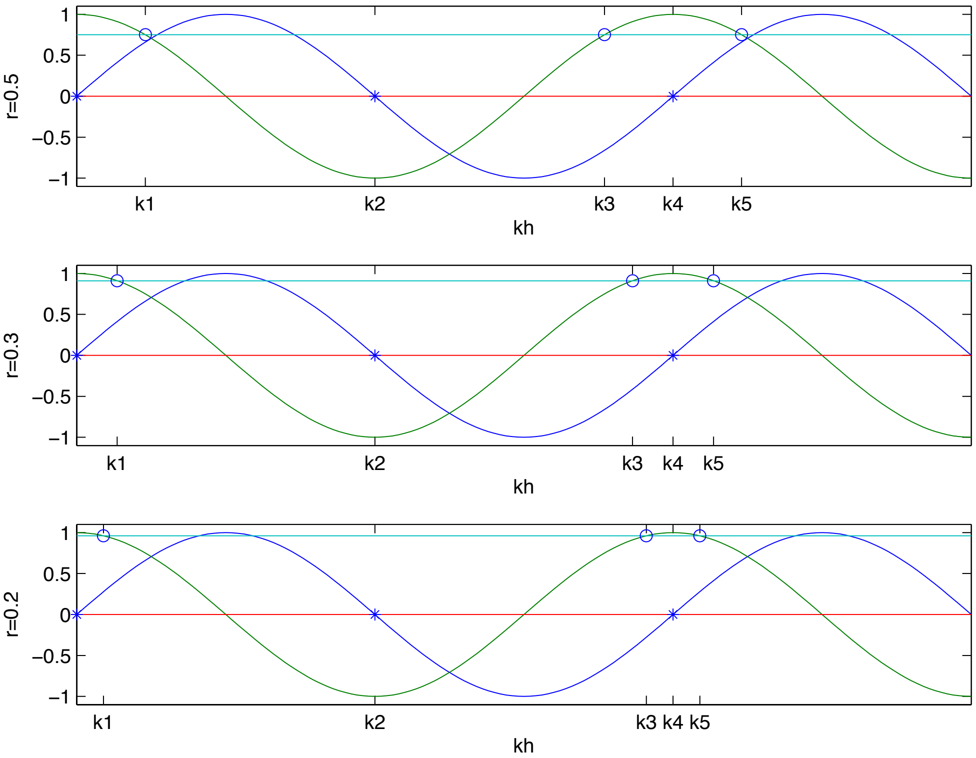

Figure 3.7: Illustration of the solutions of the characteristic equation (3.11), where wavenumbers k_n for n even are a function of r which tends to zero.

The eigenvalue of macroscale interest is the one eigenvalue corresponding to the small wavenumber k_1 : the closest eigenvalue to the zero. This small eigenvalue λ_1 has the smallest decay and the longest lasting structure which captures all significant information of the macroscale behaviour. Figure 3.7 illustrates that as the patch ratio r tends to zero, smaller patches, this small wavenumber k_1 approaches zero.

To approximate this small eigenvalue λ_1, we use a Taylor series for the cosine in the characteristic equation (3.11). That is, $\cos k_1 h = 1-r^2$ is approximately $1-\frac{1}{2}(k_1 h)^2 \approx 1-r^2$. Therefore, $k_1 \approx \sqrt{2}r/h = \sqrt{2}/H$ since $r = h/H$. This gives spatial structure in the patch of the smooth $\cos(\sqrt{2}\,x/H)$. The corresponding macroscale eigenvalue is

$$\lambda_1 = -k_1^2 \approx -2/H^2.$$

So, physically the long lasting eigenvalue corresponds to a reasonable macroscale mode independent of the patch half-width h. Contrastingly, the rest of the eigenvalues λ_n strongly depend upon the patch half-width h.

3.5.2 Analyse the long-time behaviour of the patch dynamics solutions

This section aims to predict the long-time behaviour of the patch scheme solution (3.42) to the diffusion PDE (3.1), now with time-varying boundary values (3.2). First, let $\mathbb{T} = 1/H^2$ be the macroscale diffusion time. The time scale of the nth patch mode is $\frac{1}{|\lambda_n|}$. For $t \gtrsim \mathbb{T}$ all the 'bare' exponential terms in the sum (3.42) tend to zero except $e^{\lambda_1 t}$. However, the forcing functions $\dot{F}_n$ inside the integral in the sum (3.42) are functions of t and these may force modes significantly in the long-term. Therefore, the patch scheme solution (3.42) becomes

$$\begin{aligned} w(x,t) \quad &\approx \quad w_1(0)\cos(k_1 x)e^{\lambda_1 t} + \sum_{n \text{ odd}}^{\infty} \cos(k_n x) \int_0^t e^{\lambda_n (t-s)} \dot{F}_n(s)\, ds \\ &\qquad + \sum_{n \text{ even}}^{\infty} \sin(k_n x) \int_0^t e^{\lambda_n (t-s)} \dot{F}_n(s)\, ds. \end{aligned}$$

Here we derive an asymptotic expansion to approximate the integral terms. The first term of the expansion is determined by integrating by parts: define

$$\mathcal{I}[f] := \int_0^t e^{\lambda_n (t-s)} \dot{F}_n(s)\, ds,$$

then

$$\begin{aligned} \mathcal{I}[f] \quad &= \quad -\frac{1}{\lambda_n} \int_0^t \dot{F}_n(s) \frac{d}{ds} e^{\lambda_n (t-s)}\, ds \\ &= \quad -\left[\frac{\dot{F}_n(t)}{\lambda_n} - \frac{\dot{F}_n(0)}{\lambda_n} e^{\lambda_n t} \right] + \frac{1}{\lambda_n} \int_0^t \frac{d}{ds}[\dot{F}_n(s)] e^{\lambda_n (t-s)}\, ds. \end{aligned}$$

The term $-\left[\frac{\dot{F}_n(t)}{\lambda_n} - \frac{\dot{F}_n(0)}{\lambda_n} e^{\lambda_n t} \right]$ approximates the integral $\mathcal{I}[f]$ with error

$$\frac{1}{\lambda_n} \mathcal{I}\left[\frac{d}{ds} \dot{F}_n(s) \right] = \mathcal{O}(\lambda_n^{-2}),$$

where the integral decays like $\mathcal{O}(\lambda_n^{-1})$ (Stein & Murphy 1993). Integrating by parts again yields

$$\begin{aligned} \mathcal{I}[f] \quad &= \quad -\left[\frac{\dot{F}_n(t)}{\lambda_n} - \frac{\dot{F}_n(0)}{\lambda_n} e^{\lambda_n t} \right] - \left[\frac{1}{\lambda_n^2} \frac{d^2}{ds^2} \dot{F}_n(t) - \frac{1}{\lambda_n^2} \frac{d^2}{ds^2} (\dot{F}_n(0)) e^{\lambda_n t} \right] \\ &\qquad + \frac{1}{\lambda_n^2} \int_0^t \frac{d^2}{ds^2} [\dot{F}_n(s)] e^{\lambda_n (t-s)}\, ds, \end{aligned}$$

where the term

$$-\left[\frac{\dot{F}_n(t)}{\lambda_n}-\frac{\dot{F}_n(0)}{\lambda_n}e^{\lambda_n t}\right]-\left[\frac{1}{\lambda_n^2}\frac{d^2}{d^2 s}\dot{F}_n(t)-\frac{1}{\lambda_n^2}\frac{d^2}{d^2 s}(\dot{F}_n(0))e^{\lambda_n t}\right],$$

approximates the value of the integral $\mathcal{I}[f]$ with an error

$$\frac{1}{\lambda_n^2}\mathcal{I}\left[\frac{d^2}{ds^2}\dot{F}_n(s)\right]=\mathcal{O}(\lambda_n^{-3}).$$

Iterating this procedure results in an asymptotic expansion

$$\mathcal{I}[f]\approx\sum_{m=1}^{p}\frac{-1}{\lambda_n^m}\left[\dot{F}_n^{(m)}(t)-\dot{F}_n^{(m)}(0)e^{\lambda_n t}\right]+\frac{1}{\lambda_n^p}\mathcal{I}\left[\frac{d^p}{ds^p}\dot{F}_n(s)\right],\tag{3.43}$$

where

$$\dot{F}_n^{(1)}=\dot{F}_n,\quad \dot{F}_n^{(m)}=\frac{d^{m-1}}{ds^{m-1}}\dot{F}_n,\quad k\geq 1.$$

For definiteness, assume that the forcing function $\dot{F}$ is sufficiently smoothly varying, say bounded by

$$\left|\frac{d^p}{ds^p}\dot{F}_n\right|\leq C\,\omega^p,$$

for some positive constants C and ω for all p. Then the error integral

$$\begin{aligned}\left|\frac{1}{\lambda_n^p}\int_0^t e^{\lambda_n(t-s)}\frac{d^p}{ds^p}\dot{F}_n(s)\,ds\right| &\leq \frac{1}{|\lambda_n^p|}\int_0^t e^{\lambda_n(t-s)}\left|\frac{d^p}{ds^p}\dot{F}_n(s)\right|\,ds\\ &\leq \frac{C\omega^p}{|\lambda_n^p|}\left|\int_0^t e^{\lambda_n(t-s)}\,ds\right|\\ &\leq \frac{C\omega^p}{|\lambda_n^p|}\left|\frac{1}{\lambda_n}\left(1-e^{\lambda_n t}\right)\right|\\ &\leq \frac{C}{|\lambda_n|}\left(\frac{\omega}{|\lambda_n|}\right)^p,\end{aligned}$$

since λ_n is negative. Then, as $n\to\infty$, $\frac{C}{|\lambda_n|}(\omega/|\lambda_n|)^p\to 0$, provided $|\omega|<|\lambda_n|$. Assume $|\omega|<|\lambda_2|$ and approximate only the modes $n\geq 2$ in the following. The integral term on the right-hand side of the integral (3.43) is negligible, for all n and p. Hence, the remaining terms of the integral (3.43) are

$$\mathcal{I}[f]\approx\sum_{m=1}^{p}\frac{-1}{\lambda_n^m}\left[\dot{F}_n^{(m)}(t)-\dot{F}_n^{(m)}(0)e^{\lambda_n t}\right].\tag{3.44}$$

Table 3.1: The values of the microscale wavenumbers k_n and the microscale eigenvalues λ_n of general solution (3.42) for $n = 1, 2, 3, \ldots, 10$, where parameters $H = \pi$ and $r = 0.1$.

n	k_n	λ_n
1	0.4505	-0.2030
2	10.0	-100
3	19.5	-382
4	20.0	-400
5	20.4	-418
6	30.0	-900
7	39.5	-1564
8	40.0	-1600
9	40.4	-1636
10	50.0	-2500

For even n, $\lambda_n = (\pi^2 n^2/4H^2 r^2)$; whereas for odd n, $\lambda_3, \lambda_5, \lambda_7, \ldots$ have the form $\lambda_{n\pm1} = -k_{n\pm1}^2 = -(k_n \pm k_1)^2$ where $n \in 4\mathbb{N}$ and k_1 is the smallest root of (3.11).

The next step is to neglect rapidly decaying transients. As $n \to \infty$, each term involves the exponential function $e^{\lambda_n t} F_n^p(0)$ and is divided by λ_n^p on the right-hand side of the approximate integral term (3.44) is neglected where $k \geq 1$. Therefore, the approximate integral term (3.44) becomes

$$\mathcal{I}[f] \approx \sum_{m=1}^{p} \frac{-1}{\lambda_n^m} \left[\dot{F}_n^k(t) \right]. \tag{3.45}$$

Now we decide which terms should be neglected and which terms should be kept in the approximation (3.45) for $n \geq 2$. We address the issue of neglecting and keeping these terms by considering three different cases for different values of r with, for example, an estimation error of $1\,\%$.

- First case ($r = 0.1$), neglecting integral terms in (3.45) is determined based on how large the eigenvalue λ is. For $n \geq 2$ all the integral terms (3.45) are small compared to the estimate error of $1\,\%$ as all $|\lambda_n| \geq 100$, as shown in Table 3.1. Therefore, these integral terms are neglected. Thus, the patch dynamics predicts the solution to the

Table 3.2: The values of the microscale wavenumbers k_n and the microscale eigenvalues λ_n of diffusion equation for $n = 1, 2, 3, \ldots, 10$, where parameters $H = \pi$ and $r = 0.3$.

n	k_n	λ_n
1	0.45	−0.20
2	3.33	−11.11
3	6.21	−38.60
4	6.66	−44.44
5	7.12	−50.69
6	10.00	−100.00
7	12.87	−165.88
8	13.33	−177.77
9	13.78	−190.07
10	16.66	−277.77

diffusion PDE (3.1) to an error roughly $0.01\,|F_2(s)|$, as

$$u(x,t) \approx w_1(0)\cos(k_1x)e^{\lambda_1 t} + d_1\cos(k_1x)\int_0^t e^{\lambda_1(t-s)}\dot D(s)\,ds + \frac{C(t)}{H}x + D(t). \tag{3.46}$$

Recall that the spectral coefficients $d_n = 2\,\tan(k_nh/2)/k_nh$ from (3.36), so that $d_1 = 1.0017$. Hence, the approximate solution of the single patch scheme to the diffusion PDE (3.1) is

$$\begin{aligned} u(x,t) \approx{}& w_1(0)\cos(0.4505x)e^{-0.2030t} \\ &+ 1.0017\cos(0.4505x)\int_0^t e^{-0.2030(t-s)}\dot D(s)\,ds + \frac{C(t)}{\pi}x + D(t). \end{aligned} \tag{3.47}$$

- Second case ($r = 0.3$). Table 3.2 shows that the values of the microscale wavenumbers k_n and the microscale eigenvalues λ_n for $n = 1, 2, 3, \ldots, 10$, when parameters $H = \pi$ and $r = 0.3$. For $n = 1, 2, 3, 4, 5$, the integral terms (3.45) are too large to be neglected compared to the estimate error of 1 %. Contrastingly, for $n \geq 6$ the integral terms (3.45) are small compared to the estimate error. Hence, the integral terms for $n \geq 6$ are neglected. Therefore, the patch scheme predicts the

Table 3.3: The values of the approximate wavenumbers k_n and the microscale eigenvalues λ_n of diffusion equation for $n = 1, 2, 3, \ldots, 20$, where parameters $H = \pi$ and $r = 1$.

n	k_n	λ_n
1	1/2	−1/4
2	1	−1
3	3/2	−9/4
4	2	−4
5	5/2	−25/4
6	3	−9
7	7/2	−49/4
8	4	−16
9	9/2	−81/4
⋮	⋮	⋮
20	10	−100

solution of the diffusion PDE (3.1) to an error roughly $0.01\,|F_6(s)|$ as

$$u(x,t) \approx w_1(0)\cos(k_1x)e^{-\lambda_1 t} + \sum_{n\in\{1,3,5\}} \cos(k_nx)\int_0^t e^{\lambda_n(t-s)}\dot C(s)\,c_n\,ds + \sum_{n\in\{2,4\}} \sin(k_nx)\int_0^t e^{\lambda_n(t-s)}\dot D(s)\,d_n\,ds + \frac{C(t)}{H}x + D(t).$$

- Third case ($r = 1$), gives a full domain solution to the original diffusion equation. Table 3.3 shows the values of the approximate exact wavenumbers k_n and eigenvalues λ_n for $n = 1, 2, 3, \ldots, 20$, when parameters $H = \pi$ and $r = 1$. For $n = 1, 2, 3, 4, \ldots, 19$, the integral terms (3.45) are too large to be neglected compared to the estimate error of 1 %. Contrastingly, for $n \geq 20$ the integral terms (3.45) are small compared to the estimate error. Hence, the integral terms for $n \geq 20$ are neglected. The approximate exact solution to the diffusion PDE

(3.1) to an error roughly $0.01\,|F_{20}(s)|$ is

$$u(x,t) \approx w_1(0)\cos(k_1x)e^{-\lambda_1 t} + \sum_{n=1,\text{ odd}}^{19} \cos(k_nx)\int_0^t e^{\lambda_n(t-s)}\dot C(s)\,c_n\,ds + \sum_{n=2,\text{ even}}^{18} \sin(k_nx)\int_0^t e^{\lambda_n(t-s)}\dot D(s)\,d_n\,ds + \frac{C(t)}{H}x + D(t). \tag{3.48}$$

From these three cases, we deduce that the patch scheme solution depends on the patch ratio r. We aim for the patch ratio r to be as small as possible so that the patch is a small fraction of the physical domain and the computational cost is minimised.

To investigate the effectiveness of predicting solutions of the diffusion PDE using microscale patches, we need to compare and contrast the patch dynamics solution for small r, such as $r = 0.1$, to the full domain solution which is obtained for $r = 1$. Bear in mind that for definiteness we consider the estimate error of $1\,\%$. Observe that the microscale patch dynamics solution ($r = 0.1$) has approximately one mode, whereas the full domain solution (3.48) has more, approximately 19 modes for 1% error. For the first mode, the microscale wavenumber ($k_1 = 0.4505$) and eigenvalue ($\lambda_1 = -0.2030$) are reasonably close to the full domain wavenumber ($k_1 = 0.5$) and eigenvalue ($\lambda_1 = -0.25$). Whereas, the other patch modes do not closely correspond to the macroscale modes. Therefore, the dominant mode of the microscale patch dynamics solution (3.47) reasonably predicts the first mode of the full domain solution (3.48).

3.6 Patch dynamics with time-delayed communications

This section explores the effect of time-delay communications between microscale patches on the quality of the patch scheme (Figure 3.8 illustrates a typical scenario). Suppose we are interested in simulating the dynamics of the field $u(x,t)$ on small spatial patches where each patch is assumed to be computed on a single CPU (one patch per processor). Networked CPUs allow computers to exchange information during simulations. Here the core values of the patches communicate with each other which then determines local boundary values. The patches communicate with each other through the patch boundary conditions at each microscale time step (Kevrekidis et al. 2003, Roberts & Kevrekidis 2007, Roberts 2001), which in turn requires the

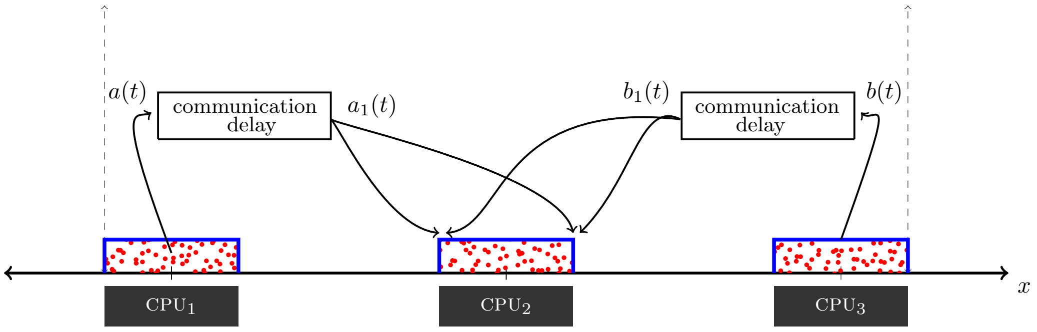

Figure 3.8: Patch dynamics simulation on a system of small patches. We investigate that one CPU for each patch. The patches communicate through patch computed core values determining neighbouring boundary values. Here we assume communication involves some time-delay.

transfer of data between CPUs. The boundary values of each patch have to be updated continuously in time to ensure the high quality of the patch dynamic scheme (Kevrekidis et al. 2003, Roberts & Kevrekidis 2007). Here we assume that a time-delay exists between transmitting the core information computed in one patch and its reception by the neighbouring patches, as shown in Figure 3.8.

We take a first step in analysing such delayed communications by considering only one patch with delayed information (signals) from two neighbouring 'patches' acting as a non-autonomous forcing of the central patch.

For the purposes of this discussion we consider that the microscopic model is the non-dimensional diffusion PDE (3.1) on the macroscopic dimension $-H \leq x \leq H$, and that there is only one field of macroscopic interest $u(x,t)$. We define one microscale patch of size $2h$ in the centre of the domain, say $-h \leq x \leq h$ where we aim $h \ll H$. At each time step during execution, the micro-simulator requires boundary values at the edges of the patch (Roberts & Kevrekidis 2007).

Figure 3.8 shows that the $a(t)$ and $b(t)$ are two macroscopic signals which are notionally generated from neighbouring patches. The signals $a(t)$ and $b(t)$ computed by CPU$_1$ and CPU$_3$ are communicated but with delay. That is, the signals required by CPU$_2$ are updated at mesoscale time steps which are larger than the microscale time step of microprocessor CPU$_2$. Such time-delays between inputs and outputs signals are very common in engineering and biological systems (Morari & Zafiriou 1989, e.g.). Our aim in this section is to quantify the effects of such delays.

Delay differential equations (DDEs) are an extensive and important class of dynamical systems. Such systems arise in which a significant time-delay exists between the applications of input to the system and their output effects in either natural or technological control problems. DDEs have several features which make their analysis more complicated. Numerical methods, asymptotic solutions, and graphical tools have been employed to address DDEs. An analytical approach to linear DDEs was addressed by Falbo (1995). Analytical solutions were obtained by solving the characteristic equation of DDEs under different conditions. For nonlinear DDEs, Wright (1946) explored the Fourier-like analysis of the existence of the solution and its properties. However, here we only address the effect of delays in the boundary forcing so the microscale system in a patch is *not* a DDE.

To simplify matters we assume that the delays are distributed according to a first order delay differential equation with a single delay

$$\tau\frac{da_1}{dt}+a_1=a(t),\quad \tau\frac{db_1}{dt}+b_1=b(t),\tag{3.49}$$

where $a(t)$, $b(t)$ are the input signals to the communication system, a_1, b_1 are the output to the patch, and τ denotes the average delay time. The output signal of the delay model (3.49) is usefully expressed as the following convolution over the past history of the signal:

$$\begin{aligned}a_1(t)&=a_1(0)\,e^{-t/\tau}+\frac{1}{\tau}\int_0^t e^{(s-t)/\tau}a(s)\,ds,\\ b_1(t)&=b_1(0)\,e^{-t/\tau}+\frac{1}{\tau}\int_0^t e^{(s-t)/\tau}b(s)\,ds.\end{aligned}$$

3.6.1 Parabolic interpolation provides patch boundary values

The macroscale domain has a specified field at the physical boundaries, namely $u(-H,t)=a(t)$ and $u(H,t)=b(t)$. In addition, the predicted macroscale field has to pass through the field u in the microscale patch, namely at $x=0$, it is to be the core centre patch value $U(t)=u(0,t)$.

The micro-simulator requires boundary values at the edges of the single patch. To obtain such microscale boundary values, we interpolate the three points $(-H,a_1)$, (H,b_1), and $(0,U)$ with the parabola

$$u(x,t)=U(t)\left(1-\frac{x^2}{H^2}\right)+\frac{x^2}{H^2}\left(\frac{a_1+b_1}{2}\right)+\frac{x}{H}\left(\frac{b_1-a_1}{2}\right).$$

Crucially, this interpolation, assumed by the patch, uses the delayed values a_1 and b_1. Hence the gap-tooth scheme estimates the field on the edges of the patch as

$$u(\pm h,t)=U(t)(1-r^2)+\frac{r^2}{2}(a_1+b_1)\pm\frac{r}{2}(b_1-a_1), \tag{3.50}$$

where the patch ratio is $r=h/H$. To analyse the effect of communication delays we use these boundary conditions (3.50).

3.6.2 Homogeneous boundary conditions

Observe that the patch boundary conditions (3.50) are not homogeneous. In order to obtain a PDE with homogeneous BCs, define the field

$$w(x,t)=u(x,t)-\frac{C_1(t)}{H}x-D_1(t), \tag{3.51}$$

so then

$$\begin{aligned} u(0,t)&=w(0,t)+D_1(t),\\ u(\pm h,t)&=w(\pm h,t)\pm C_1(t)r+D_1(t). \end{aligned}$$

Substituting these identities into the patch boundary conditions (3.50) gives

$$w(\pm h,t)\pm C_1(t)r=w(0,t)(1-r^2)+\frac{r^2}{2}(a_1+b_1)\pm\frac{r}{2}(b_1-a_1)-r^2D_1(t). \tag{3.52}$$

Define

$$D_1(t):=\frac{a_1(t)+b_1(t)}{2}=D_1(0)\,e^{-t/\tau}+\frac{1}{\tau}\int_0^t e^{(s-t)/\tau}D(s)\,ds, \tag{3.53}$$

$$C_1(t):=\frac{b_1(t)-a_1(t)}{2}=C_1(0)\,e^{-t/\tau}+\frac{1}{\tau}\int_0^t e^{(s-t)/\tau}C(s)\,ds, \tag{3.54}$$

where $D(s)=[a(s)+b(s)]/2$, and $C(s)=[b(s)-a(s)]/2$, and substituting the above definitions of $D_1(t)$ and $C_1(t)$ into the expression (3.52) gives the patch homogeneous boundary conditions (3.7) for the field $w(x,t)$. Substituting the field (3.51) into the microscale diffusion PDE (3.1) requires that the field w satisfies the non-homogeneous PDE

$$w_t=w_{xx}-\frac{\dot C_1(t)}{H}x-\dot D_1(t), \tag{3.55}$$

where, as before, a dot over a variable denotes the first derivative with respect to time. This forced diffusion PDE is subject to the patch homogeneous boundary conditions (3.7).

3.6.3 Analyse the forced patch dynamics

This section analyses the forced microscale diffusion PDE (3.55), which involves some delayed signals with the patch homogeneous boundary conditions (3.7). The microscale diffusion PDE (3.55) with the patch homogeneous boundary conditions (3.7) is symbolically the same forced diffusion PDE (3.8) as in Section 3.1. Therefore, all the analysis of the microscale patch in Section 3.5.2 holds identically when the $a(t)$, $b(t)$, $D(t)$, and $C(t)$ are replaced by the delayed macroscale variables $a_1(t)$, $b_1(t)$, $D_1(t)$, and $C_1(t)$.

Recall that in Section 3.5.2 the patch scheme predicts the solution (3.46) to the microscale diffusion PDE (3.1) on a small patch $r = 0.1$ as

$$u(x,t) \approx w_1(0)\cos(k_1x)e^{\lambda_1 t} + d_1\cos(k_1x)\int_0^t e^{\lambda_1(t-s)}\dot D(s)\,ds + \frac{C(t)}{H}x + D(t).$$

Hence, replacing all macroscale variables with delayed macroscale variables, the patch scheme predictions (3.46) become

$$u(x,t) \approx w_1(0)\cos(k_1x)e^{\lambda_1 t} + d_1\cos(k_1x)\int_0^t e^{\lambda_1(t-s)}\dot D_1(s)\,ds + \frac{C_1(t)}{H}x + D_1(t). \tag{3.56}$$

To determine the time derivative of the average of the delayed signals $\dot D_1(s)$ notice that the definition (3.53) represents the solution of

$$\tau\dot D_1(t) = -D_1(t) + D(t). \tag{3.57}$$

Differentiating both sides of this equation with respect to t yields

$$\tau\ddot D_1(t) = -\dot D_1(t) + \dot D(t). \tag{3.58}$$

This equation symbolically has the same solution as equation (3.57) where $D_1(t)$ and $D(t)$ are replaced by $\dot D_1(t)$ and $\dot D(t)$. Therefore, the solution of equation (3.58) is

$$\dot D_1(t) = \dot D_1(0)\,e^{-t/\tau} + \frac{1}{\tau}\int_0^t e^{(s-t)/\tau}\dot D(s)\,ds.$$

Then the forcing term in (3.56) is

$$\dot D_1(s) = \dot D_1(0)\,e^{-s/\tau} + \frac{d_1}{\tau}\int_0^s e^{(s_1-s)/\tau}\dot D(s_1)\,ds_1. \tag{3.59}$$

Hence, substitute $D_1(t), C_1(t)$ from (3.53) and (3.54), and $\dot{D}(s)$ from (3.59), into the approximate solution (3.56) in the field u becomes

$$\begin{aligned} u(x,t) \quad \approx \quad & w_1(0)\cos(k_1 x)e^{\lambda_1 t} + \dot{D}_1(0)\, d_1\, \cos(k_1\, x) \int_0^t e^{-s(\lambda_1+1/\tau)}\, e^{\lambda_1\, t}\, ds \\ & + \frac{d_1}{\tau}\cos(k_1\, x) \int_0^t e^{\lambda_1(t-s)} \left[\int_0^s e^{(s_1-s)/\tau}\dot{D}(s_1)\, ds_1\right] ds \\ & + \frac{C_1(0)}{H}\, x\, e^{-t/\tau} + \frac{x}{\tau\, H}\int_0^t e^{(s-t)/\tau} C(s)\, ds \\ & + D_1(0)\, e^{-t/\tau} + \frac{1}{\tau}\int_0^t e^{(s-t)/\tau} D(s)\, ds. \end{aligned} \tag{3.60}$$

The double integral on the second line of the right-hand side of this approximate solution (3.60) is simplified as

$$\begin{aligned} & \int_0^t e^{\lambda_1(t-s)} \left[\int_0^s e^{(s_1-s)/\tau}\, D(s_1)\, ds_1\right] ds \\ & \quad = \int_0^t \int_{s_1}^t e^{\lambda_1 t+(s_1/\tau)}\, e^{-s(\lambda_1+1/\tau)}\, ds\, D(s_1)\, ds_1 \\ & \quad = \frac{\tau}{\lambda_1\, \tau + 1}\int_0^t \left[e^{\lambda_1\,(t-s_1)} - e^{(s_1-t)/\tau}\right] D(s_1)\, ds_1 \\ & \quad = \frac{\tau}{\lambda_1\, \tau + 1}\int_0^t \left[e^{\lambda_1\,(t-s)} - e^{(s-t)/\tau}\right] D(s)\, ds. \end{aligned} \tag{3.61}$$

Substituting this integral term (3.61), into the approximate solution (3.60) we obtain

$$\begin{aligned} u(x,t) \quad \approx \quad & w_1(0)\cos(k_1 x)e^{\lambda_1 t} + \frac{d_1\, \tau\, \dot{D}_1(0)}{\lambda_1\, \tau + 1}\cos(k_1\, x)\left(e^{-t/\tau} - e^{\lambda_1\, t}\right) \\ & + \frac{d_1\, \cos(k_1 x)}{(\lambda_1\, \tau + 1)}\int_0^t \left[e^{\lambda_1\,(t-s)} - e^{(s-t)/\tau}\right] \dot{D}(s)\, ds \\ & + \frac{C_1(0)}{H}\, x\, e^{-t/\tau} + \frac{x}{\tau\, H}\int_0^t e^{(s-t)/\tau}\, C(s)\, ds \\ & + D_1(0)\, e^{-t/\tau} + \frac{1}{\tau}\int_0^t e^{(s-t)/\tau}\, D(s)\, ds. \end{aligned} \tag{3.62}$$

Now we evaluate the integrals in the third and fourth lines of equation (3.62) by using integration by parts to obtain

$$\begin{aligned}
u(x,t) \;\approx\;& w_1(0)\cos(k_1x)e^{\lambda_1 t} + \frac{d_1\,\tau\,\dot{D}_1(0)}{\lambda_1\,\tau+1}\cos(k_1\,x)\left(e^{-t/\tau}-e^{\lambda_1\,t}\right)\\
&+\frac{d_1\,\cos(k_1x)}{(\lambda_1\,\tau+1)}\int_0^t\left[e^{\lambda_1\,(t-s)}-e^{(s-t)/\tau}\right]\dot{D}(s)\,ds\\
&+\frac{C_1(0)}{H}\,x\,e^{-t/\tau}+\frac{C(t)}{H}\,x+\frac{C(0)}{H}\,x\,e^{-t/\tau}-\frac{x}{H}\int_0^t e^{(s-t)/\tau}\,\dot{C}(s)\,ds\\
&+D_1(0)\,e^{-t/\tau}+D(t)+D(0)\,e^{-t/\tau}-\int_0^t e^{(s-t)/\tau}\,\dot{D}(s)\,ds. \quad (3.63)
\end{aligned}$$

This is delayed patch dynamics approximation to the diffusion PDE (3.1) where the microscale boundary values involve some communication delays.

The delayed patch dynamics approximations (3.63), in comparison to the scheme without delays (3.46), include all the effective terms in established patch scheme predictions without delays (3.46). The delayed patch dynamics approximations (3.63) also exhibit some time-delays in all other terms which can be significant in the case of multiple processors which require substantial and effectively prohibitive data transfer between such patches. For example, in the case of only one patch the exponential term $e^{(s-t)/\tau}$ in the second line of the delayed patch scheme approximations (3.63) is small provided that the delay time τ is smaller than the macroscale diffusion time $1/\lambda_1$. In such circumstances the delay then has little effect.

At this stage we cannot give some typical delay times. The delay time simulation depends on physical delay time of hardware in ways which depend upon hardware and the size of simulations. Here we assume that a time-delay exists between transmitting the core information computed in one patch and its reception by the neighbouring patches. In an alternative approach, Bunder et al. (2015) discussed the accuracy of patch dynamics with mesoscale temporal coupling for efficient exascale simulation. If one processor was to evaluate the dynamics of a small number of adjacent patches, then coupling data should be updated at microscale times for the patches evaluated on that one processor. However, coupling data transfered at mesoscale times should be maintained for patches evaluated on different processors.

3.7 Conclusion

This chapter describes a one patch dynamics scheme for the computational simulation of multiscale problems. A single patch scheme is invoked in one spatial dimension for diffusion problems with forcing boundary conditions.

In Chapter 4 we analyse the scenario where, in applications, the patch scheme would involve many small patches distributed throughout the macroscopic domain.

The scheme predicts the macroscopic dynamics over large spatial regions when only a microscopic model is explicitly available. The microscopic model is solved within a small fraction of the space domain, and the coupling conditions effectively bridge large intervening spatial gaps in which no solution is computed. Symmetric and asymmetric eigenfunctions within the patch are considered. We found that the patch coupling conditions in the microsystem (3.10) do not form a self-adjoint Sturm–Liouville system. This indicates how critical the choice is for the boundary conditions of these microproblems. Further exciting research would explore other patch coupling conditions that preserve self-adjointness and also predict the correct macroscale behaviour.

To perform the spectral expansions, it is required to determine eigenfunctions of the adjoint operator. These two sets of eigenfunctions are then biorthogonal to each other, and the spectral coefficients in the eigenfunction expansion are found using the eigenfunctions of the adjoint problem. After obtaining these expansion, Section 3.5.2 analyses the long-term dynamics behaviour of this scheme for a one-dimensional diffusion equation with time-varying boundary forcing. Then we predict the microscale field for a small patch ratio and compare such predictions with the field on the complete domain. In a dissipative system such as (3.1) the long-term, emergent dynamics are characterised by the smallest decay and the longest lasting eigenvalue λ_1. This interesting eigenvalue is determined in Section 3.5.1. We expect the same approach will also accurately couple the patch scheme in higher spatial dimensions.

Section 3.6 presents a delayed patch scheme where we assume that one processor only calculates the dynamics of one patch. We analyse this delayed scheme and compare the results with a scheme without delays to delineate when such delays are significant. Interesting future research would adapt the delayed patch scheme for massive parallelisation where each processor simulates the macroscale properties on a few patches.

Chapter 4

Multiple patches for diffusion with time-varying boundary forcing

Chapter 3 explores the behaviour of a single patch scheme when it is applied to the diffusion PDE with time-varying boundary forcing. This chapter extends the technique by solving the microscale dynamics within multiple patches when the boundary of the macroscale domain has time-varying forcing. For dissipative systems, Kevrekidis et al. (2003) and Samaey et al. (2010) introduced and reviewed gap-tooth schemes. Such schemes perform microscale simulations only on small separated patches, coupling the patch simulations across space, to simulate the macroscopic behaviour of interest over the macroscopic domain. Roberts & Kevrekidis (2007) developed cross–space coupling conditions to achieve higher order accuracy over the macroscale in the gap-tooth scheme for a class of dissipative systems. One aim of this chapter is to show that analogous coupling works straightfor-

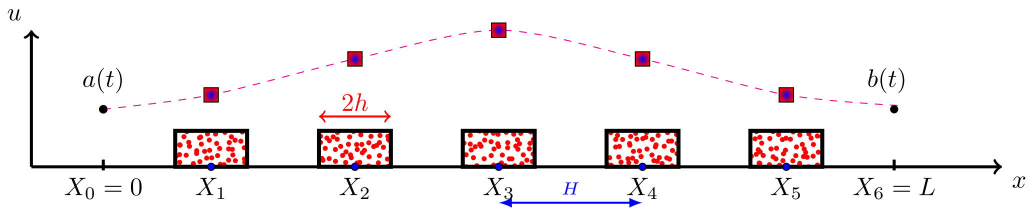

Figure 4.1: Create small patches of space, of size $2h$, on the macroscale domain $[0, L]$. This digram shows the case for $N = 5$ patches, with the jth patch centred on macroscale grid points $X_j = jH$.

wardly for the diffusion PDE with time-varying boundary forcing. The new research here explores the effects of such time-varying boundary forcing and confirms the gap-tooth scheme behaves reasonably.

As a prototypical problem, this chapter considers the non-dimensional diffusion PDE

$$\frac{\partial u}{\partial t} = \frac{\partial^2 u}{\partial x^2}, \tag{4.1}$$

for some field $u(x,t)$ on the physical domain of length L with initial condition $u(x,0) = u_0(x)$ for each $x \in [0,L]$. The diffusion PDE (4.1) is subject to Dirichlet boundary conditions

$$u(0,t) = a(t), \quad u(L,t) = b(t), \tag{4.2}$$

where a and b are functions of time. The aim is to predict the evolution of the field $u(x,t)$ on the macroscopic domain of length L.

Following analogues in one dimension (Roberts 2003*b*, MacKenzie & Roberts 2006), Section 4.1 couples adjacent patches with a strength characterised by an artificial homotopy parameter γ. Such multiple patches of microscale simulator are coupled by interpolation across the unevaluated space between patches in order to mimic a microscopic simulation performed over the entire physical domain. Section 4.1.2 explores the eigenvalues of the linear dynamics and shows how centre manifold theory (Carr & Muncaster 1983, Vanderbauwhede 1989, Chicone & Latushkin 1997, e.g.) assures us of the existence of a slow manifold. The computer algebra in Appendix B then constructs the slow manifold of the system to any specified order of error.

Section 4.1.4 constructs the slow manifold discretisation of PDEs with physical boundary conditions. Section 4.2 then compares the slow manifold approximations for the field u in one patch with analytical solutions of the diffusion PDE (4.1)–(4.2) on the complete domain.

4.1 Divide the macroscale domain into small patches

As shown schematically in Figure 4.1, we place over the macroscale domain a grid, $0 = X_0 < X_1 < \cdots < X_{N+1} = L$, where we define N interior grid points $X_j = jH$, for $j = 1, 2, \ldots, N$. The main macroscale quantities of interest comprise the field evaluated at the internal grid points $u(X_j, t)$. We divide the macroscale domain into small patches of space, of size $2h$, centred around each interior grid point so that the edge of each small patch is a distance h from its central macroscale grid point. Microscale simulations would be performed only in these small patches.

Our aim here is to obtain effective macroscale simulations over the entire macroscopic domain by coupling such small, spatially separated patches of simulation. The microscopic simulator requires boundary values on the edges of each microscopic patch which must be obtained from the near neighbouring grid values. Appropriate coupling conditions (4.23) bridge the gaps in the spatial domain in which no simulations are performed.

4.1.1 Couple multiple patches across the whole domain

This section couples the dynamics of each patch across gaps. The coupling conditions interpolate information from neighbouring grid values of each patch into boundary values of the microscale patch as shown schematically in Figure 4.2. We define $u_j(x,t)$ to be the field u in the jth patch. We also define the patch ratio $r = h/H$ to characterise the size of each patch relative to the distance between neighbouring patches. Overlapping patches occur when the patch ratio $r = 1$, which is the case of holistic discretisation as discussed by Roberts (2003*b*). Here we aim for the patch ratio r to be small so that the patches form a relatively small part of the entire physical domain which in turn would minimise the computational cost for a multiscale simulation.

We define the macroscale grid values (amplitudes)

$$U_j(t) = u_j(X_j, t), \quad \text{for } j = 1, 2, \ldots, N. \tag{4.3}$$

Roberts & Kevrekidis (2007) prove classic interpolation ensure high order accuracy in the gap-tooth scheme for the macroscale dynamics. With analogous coupling conditions, we couple multiple patches for the diffusion PDE (4.1) with time-varying boundary forcing. We define a shift operator across the macroscale field so that

$$\mathcal{E}f(x) = f(x+H) \quad \text{and} \quad \mathcal{E}_j f_j = f_{j+1}. \tag{4.4}$$

Then we use the following definitions and identities for discrete opera-

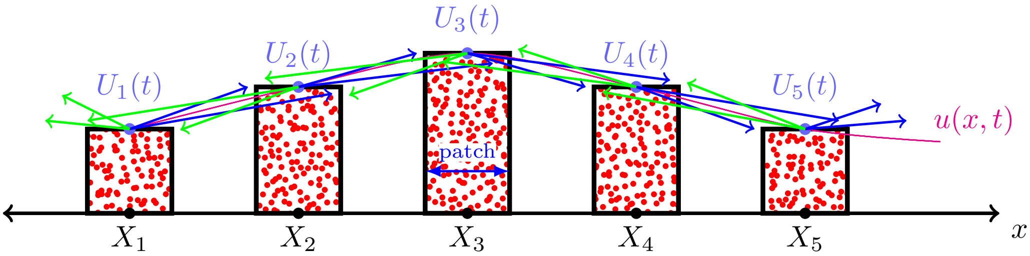

Figure 4.2: Scheme of interpolating macroscale grid patch values U_j to provide boundary values at the edges of each patch. The green and blue arrows provide edge values on the right and left of each patch.

tors (Chitode 2008, p.293).

$$\begin{aligned}
\text{centred mean} \quad \mu &= \frac{1}{2}(\mathcal{E}^{1/2}+\mathcal{E}^{-1/2}), && (4.5)\\
\text{centred difference} \quad \delta &= \mathcal{E}^{1/2}-\mathcal{E}^{-1/2}, && (4.6)\\
\text{translate/shift} \quad \mathcal{E} &= 1+\mu\delta+\frac{1}{2}\delta^2, && (4.7)\\
\text{derivative in } x \quad H\partial_x &= 2\sinh^{-1}\frac{1}{2}\delta, && (4.8)\\
\text{operator identity} \quad \mu^2 &= 1+\frac{1}{4}\delta^2. && (4.9)
\end{aligned}$$

We also use discrete operators on the microscale field size h instead of the macroscale field size H : the shift operator $\mathcal{E}_h f(x) = f(x+h)$, and similarly for μ_h and δ_h.

To derive the coupling patch conditions, we use a consistent discretisation for the first and second derivatives of the microscale diffusion PDE (4.1). For convenience, we start by using a consistent discretisation for the second derivative on the microscopic and macroscopic fields, and then proceed with the first derivative. For notational simplicity, we omit t for time.

Second derivative We expand the microscale operator

$$\begin{aligned}
\delta_h^2 u_j(X_j) &= [\mathcal{E}_h+\mathcal{E}_h^{-1}-2]u(X_j)\\
&= u_j(X_j+h)-2u_j(X_j)+u_j(X_j-h) \quad \text{by (4.4)}.
\end{aligned}$$

The classic relationship (4.8) between the spatial derivative ∂_x and the microscale central difference operator δ_h is written as $h\partial_x = 2\sinh^{-1}\frac{1}{2}\delta_h$ (Chitode 2008, p.293). On the microscale, the second derivative at the mid-patch transforms to the equivalent discrete operator as

$$u_{xx}(X_j) = \frac{1}{h^2}(h\partial_x)^2 u_j(X_j) = \frac{1}{h^2}\left[2\sinh^{-1}\left(\frac{\delta_h}{2}\right)\right]^2 u_j(X_j). \tag{4.10}$$

Similarly by (4.8), on the macroscale, the second derivative at the mid-patch transforms to the equivalent discrete operator as

$$u_{xx}(X_j) = \frac{1}{H^2}(H\partial_x)^2 u_j(X_j) = \frac{1}{H^2}\left[2\sinh^{-1}\left(\frac{\delta}{2}\right)\right]^2 u_j(X_j), \tag{4.11}$$

equating the right-hand sides of equations (4.10) and (4.11) gives

$$\frac{1}{h^2}\left[2\sinh^{-1}\left(\frac{\delta_h}{2}\right)\right]^2 u_j(X_j) = \frac{1}{H^2}\left[2\sinh^{-1}\left(\frac{\delta}{2}\right)\right]^2 u_j(X_j).$$

Multiplying both sides by $h^2/4$ and taking the square root of the operators on both sides of the equation leads to

$$\sinh^{-1}\left(\frac{\delta_h}{2}\right) u_j(X_j) = r\sinh^{-1}\left(\frac{\delta}{2}\right) u_j(X_j),$$

where the ratio $r = h/H$. Taking the sinh of the operators on both sides gives

$$\frac{\delta_h}{2} u(X_j) = \sinh\left[r\sinh^{-1}\left(\frac{\delta}{2}\right)\right] u_j(X_j).$$

Multiplying both sides by two and squaring both operators gives

$$\delta_h^2 u_j(X_j) = 4\left\{\sinh\left[r\sinh^{-1}\left(\frac{\delta}{2}\right)\right]\right\}^2 u_j(X_j).$$

Using the amplitude definition (4.3) on the right-hand side of this equation

$$\delta_h^2 u_j(X_j) = 4\left\{\sinh\left[r\sinh^{-1}\left(\frac{\delta}{2}\right)\right]\right\}^2 U_j. \tag{4.12}$$

We insert an artificial homotopy parameter γ, $0 \leq \gamma \leq 1$, to artificially control the coupling so that equation (4.12) becomes

$$\delta_h^2 u_j(X_j) = 4\left\{\sinh\left[r\sinh^{-1}\left(\frac{\sqrt{\gamma}\delta}{2}\right)\right]\right\}^2 U_j. \tag{4.13}$$

Such coupling strength γ was discussed in detail for establishing theoretical support for patch dynamics by Roberts (2003*b*). Expanding the right-hand side of (4.13) in the Taylor series in small difference δ, the fields at both edges of each patch satisfy

$$\begin{aligned} & u_j(X_j+h) - 2u_j(X_j) + u_j(X_j-h) \\ & \quad = \Big[\gamma\delta^2 r^2 + \frac{\gamma^2 r^2(r^2-1)}{12}\delta^4 + \frac{\gamma^3 r^2(r^4-5r^2+4)}{360}\delta^6 \\ & \qquad + \frac{\gamma^4 r^2(r^6-14r^4+49r^2-36)}{20160}\delta^8 + \mathcal{O}(\delta^9)\Big] U_j. \end{aligned} \tag{4.14}$$

This empowers us to express the boundary values on the edges of each patch in terms of interpolation of the mid-patch values from neighbouring patches.

First derivative We use a similar approach to transform the first derivative, but the first derivative requires more care. Recall that the first order central difference,

$$\frac{u_j(X_j+h) - u_j(X_j-h)}{2} = \mu_h\delta_h u_j(X_j), \tag{4.15}$$

from interrelations (4.5) and (4.6) between operators (Chitode 2008, p.293). From (4.8) and (4.9), the microscale mean and difference operators are $\mu_h = \cosh\left(\frac{h\partial_x}{2}\right)$ and $\delta_h = 2\sinh\left(\frac{h\partial_x}{2}\right)$ respectively. Hence, microscale mean and difference operators on the right-hand side of equation (4.15)

$$\begin{aligned} \mu_h\delta_h u_j(X_j) &= 2\cosh\left(\frac{h\partial_x}{2}\right)\sinh\left(\frac{h\partial_x}{2}\right)u_j(X_j) \\ &= \sinh(h\partial_x)u_j(X_j). \end{aligned}$$

Comparing the operator of $u_j(X_j)$ on both sides yields $\mu_h\delta_h = \sinh(h\partial_x)$. Take inverse sinh, of both sides gives

$$h\partial_x = \sinh^{-1}(\mu_h\delta_h). \tag{4.16}$$

On the microscale grid, the first derivative of the microscale field at the mid-patch transforms to the equivalent discrete operator

$$u_x(X_j) = \frac{1}{h}(h\partial_x)u_j(X_j) = \frac{1}{h}\left[\sinh^{-1}(\mu_h\delta_h)\right]u_j(X_j) \quad \text{by (4.16)}. \tag{4.17}$$

Whereas on the macroscale grid, the first derivative at the mid-patch transforms to the equivalent discrete operator

$$u_x(X_j) = \frac{1}{H}(H\partial_x)u_j(X_j) = \frac{1}{H}\left[2\sinh^{-1}\left(\frac{\delta}{2}\right)\right]u_j(X_j). \tag{4.18}$$

Equating the right-hand sides of equations (4.17) and (4.18) gives

$$\frac{1}{h}\left[\sinh^{-1}(\mu_h\delta_h)\right]u_j(X_j)=\frac{1}{H}\left[2\sinh^{-1}\left(\frac{\delta}{2}\right)\right]u_j(X_j).$$

For both sides, we multiply by h and take sinh of the operators which leads to

$$\mu_h\delta_h u_j(X_j)=\sinh\left[2r\sinh^{-1}\left(\frac{\delta}{2}\right)\right]u_j(X_j).$$

From (4.9), multiply the right-hand side by the identity $\mu/\sqrt{1+\delta^2/4}$ gives

$$\mu_h\delta_h u_j(X_j)=\frac{\mu}{\sqrt{1+\delta^2/4}}\sinh\left[2r\sinh^{-1}\left(\frac{\delta}{2}\right)\right]u_j(X_j).$$

Introducing the amplitude definition (4.3) on the right-hand side of this equation gives

$$\mu_h\delta_h u_j(X_j)=\frac{\mu}{\sqrt{1+\delta^2/4}}\sinh\left[2r\sinh^{-1}\left(\frac{\delta}{2}\right)\right]U_j. \tag{4.19}$$

In a similar way to the second derivatives, to control the coupling we now insert an artificial homotopy parameter γ, $0\leq\gamma\leq 1$, so that equation (4.19) becomes

$$\mu_h\delta_h u_j(X_j)=\frac{\mu}{\sqrt{1+\gamma\delta^2/4}}\sinh\left[2r\sinh^{-1}\left(\frac{\sqrt{\gamma}\delta}{2}\right)\right]U_j. \tag{4.20}$$

Replacing the microscale mean and difference operators on the left-hand side of (4.20) by (4.15) gives

$$\frac{u_j(X_j+h)-u_j(X_j-h)}{2}=\frac{\mu}{\sqrt{1+\gamma\delta^2/4}}\sinh\left[2r\sinh^{-1}\left(\frac{\sqrt{\gamma}\delta}{2}\right)\right]U_j. \tag{4.21}$$

Expanding the right-hand side of (4.21) as a Taylor series in small difference δ, the fields at the edges of each patch satisfy

$$\begin{aligned}&\frac{u_j(X_j+h)-u_j(X_j-h)}{2}\\&\quad=\left[\gamma r\mu\delta+\frac{\gamma^2r(r^2-1)}{6}\mu\delta^3+\frac{\gamma^3r(r^4-5r^2+4)}{120}\mu\delta^5\right.\\&\qquad\left.+\frac{\gamma^4r(r^6-14r^4+49r^2-36)}{5040}\mu\delta^7+\mathcal{O}(\delta^9)\right]U_j.\end{aligned} \tag{4.22}$$

The expansions (4.14) and (4.22) empower us to express the boundary values on the edges of each patch, at $X_j\pm h$, in terms of the macroscale grid values U_j.

Determining boundary values on the edges of each patch Adding and subtracting expansion (4.22) to half of the expansion (4.14) provides the values on the right and left edges of each patch, at $X_j \pm h$,

$$\begin{aligned} u_j(X_j \pm h) = \Big[& 1 \pm \gamma r\mu\delta + \frac{1}{2}\gamma\delta^2 r^2 \pm \frac{\gamma^2 r(r^2-1)}{6}\mu\delta^3 \\ & + \frac{\gamma^2 r^2(r^2-1)}{24}\delta^4 \pm \frac{\gamma^3 r(r^4-5r^2+4)}{120}\mu\delta^5 \\ & + \frac{\gamma^3 r^2(r^4-5r^2+4)}{720}\delta^6 \\ & \pm \frac{\gamma^4 r(r^6-14r^4+49r^2-36)}{5040}\mu\delta^7 \\ & + \frac{\gamma^4 r^2(r^6-14r^4+49r^2-36)}{40320}\delta^8 \\ & + \mathcal{O}(\delta^9) \,\Big]\, U_j. \end{aligned} \tag{4.23}$$

This interpolation (4.23) effectively bridges the gap between the patches in the spatial domain.

The artificial coupling parameter γ in the interpolation (4.23) plays a crucial role in controlling the strength of coupling between adjacent patches. For example, when the coupling parameter $\gamma = 0$, the microscale values on the edges of each patch

$$u_j(X_j \pm h, t) = U_j(t) = u_j(X_j, t),$$

are just identical to the microscale patch grid value. Therefore, each patch is effectively isolated from its neighbours, dividing the physical domain into decoupled patches. However, when the coupling parameter $\gamma = 1$, the coupling conditions (4.23) ensure each microscale patch matches its neighbourhood.

We obtain different accuracies by truncating the coupling condition (4.23) to different orders in the artificial coupling parameter γ. For example, parabolic interpolation, $u_j = (1 \pm r\mu\delta + \delta^2 r^2/2)U_j$, from the nearest neighbour patches, as illustrated in Figure 4.2, is obtained by truncating to errors $\mathcal{O}(\gamma^2)$ and then setting $\gamma = 1$. Whereas quartic interpolation from nearest and next nearest neighbouring patches is obtained by truncating to errors $\mathcal{O}(\gamma^3)$. The details recorded in coupling condition (4.23), truncating to errors $\mathcal{O}(\gamma^5)$, are equivalent to eighth order interpolation from the eight neighbouring macroscale grid values $U_{j\pm1}$, $U_{j\pm2}$, $U_{j\pm3}$, and $U_{j\pm4}$. High order interpolations are expected to achieve a higher order of accuracy, as it does for the holistic case $r = 1$ developed by Roberts & Kevrekidis (2005).

4.1.2 Existence of slow manifold and initial approximation

This section explores the slow manifold field with coupling parameter γ. On the jth patch, consider the diffusion equation

$$\frac{\partial u_j}{\partial t} = \frac{\partial^2 u_j}{\partial x^2}, \tag{4.24}$$

with coupling conditions (4.23). Using centre manifold analysis empowers us to demonstrate that coupled patches over large spatial gaps are able to predict the macroscale dynamics over a large spatial region.

Space rescaling Let ξ be a new microscale space variable restricted to the jth patch: $\xi = (x - X_j)/H$. Using the chain rule for the derivative of a function with respect to x

$$\frac{\partial}{\partial x} = \frac{\partial \xi}{\partial x}\frac{\partial}{\partial \xi} = \frac{1}{H}\frac{\partial}{\partial \xi}. \tag{4.25}$$

Substituting (4.25) into (4.24) gives diffusion on a coupled patch system

$$\frac{\partial u_j}{\partial t} = \frac{1}{H^2}\frac{\partial^2 u_j}{\partial \xi^2}, \tag{4.26}$$

with the nonlocal patch boundary conditions, truncated to errors $\mathcal{O}(\gamma^2)$,

$$u_j(\pm r) = U_j + \gamma\left[\frac{r^2 \pm r}{2}U_{j+1} - r^2 U_j + \frac{r^2 \mp r}{2}U_{j-1}\right], \quad \text{for } j = 1, 2, \ldots, N. \tag{4.27}$$

To prove the existence and emergence of a slow manifold for diffusion on coupled patches system (4.26)–(4.27) we apply centre manifold theory.

Equilibria Centre manifold theory is based on equilibria. The system PDE (4.26)–(4.27) has equilibria of $u_j =$ constant when coupling parameter $\gamma = 0$. Further, this constant is independent in each of the N patches as each patch is isolated from each other when $\gamma = 0$.

Linearisation The spectrum of the linearised dynamics about each equilibria implies the existence of a slow manifold (Roberts 2003*b*). Each patch is isolated from all other patches, as the coupling parameter $\gamma = 0$. Hence, linearly, the dynamics in each patch determines that of the whole set of patches. On the jth patch, we assume that the field u_j has solutions of the form $u_j = e^{\lambda t}[c_1 \cos(k\xi) + c_2 \sin(k\xi)]$. The coupling (4.27) then requires

$$\begin{bmatrix} \cos(kr) - 1 & \sin(kr) \\ \cos(kr) - 1 & -\sin(kr) \end{bmatrix} \begin{bmatrix} c_1 \\ c_2 \end{bmatrix} = \begin{bmatrix} 0 \\ 0 \end{bmatrix}.$$

for eigenvalues $\lambda = -k^2/H^2 < 0$ from the PDE (4.26). This system has non-trivial solutions only when the determinant vanishes

$$\det = -2\sin(kr)\,[\cos(kr) - 1] = 0. \tag{4.28}$$

From the characteristic equation (4.28), two cases arise to determine the wavenumbers and the corresponding eigenvalues.

- Either $\sin(kr) = 0$ when microscale wavenumbers $k = \pi/r$, $2\pi/r$, $3\pi/r$, …, therefore, the wavenumbers $k_n = n\pi/r$ for $n = 1, 2, 3, \ldots$. That is, microscale eigenvalues are $\lambda_n = -n^2\pi^2/h^2$.
- Or $\cos(kr) - 1 = 0$ when microscale wavenumbers $k = 0, 2\pi/r$, $4\pi/r$, $6\pi/r$, …, therefore, the wavenumbers $k_n = n\pi/r$ for $n = 0, 2, 4, \ldots$. That is, microscale eigenvalues are $\lambda_n = -n^2\pi^2/h^2$.

Based upon the structure of this spectrum we identify the existence of a model. The spectrum of eigenvalues for the linearised system is the set $\{0, -\pi^2/h^2, -4\pi^2/h^2, \ldots\}$. The pattern of the eigenvalues is of one zero eigenvalue and the remainder are negative and large $\lambda \leq -\pi^2/h^2$. The negative and large eigenvalues characterise microscale modes within the patch. All these rapid microscale modes are generally not of interest to the macroscale dynamics.

Theory (Carr & Muncaster 1983, Vanderbauwhede 1989, Chicone & Latushkin 1997, Roberts et al. 2011, e.g.) guarantees the existence of a slow manifold in the presence of perturbation to finite coupling strength γ. The first initial approximation of this slow manifold is derived in (4.33)–(4.34). For a more accurate macroscale model, further iterations are required which we undertake by computer algebra in Section 4.1.3.

The first approximation of the slow manifold

The slow manifold of (4.24) is parametrised both by the small parameters r, γ and by grid values $U_j(t) = u_j(X_j, t)$ that are used to measure the field in the jth patch. Define $\vec U$ to be the vector of such grid values, and seek microscale fields in the form

$$u_j(\xi, t) = U_j + \hat u_j(\xi, \vec U, \gamma) \quad \text{such that} \quad dU_j/dt = \hat g_j(\vec U, \gamma),$$

for small $\hat{u}_j$ and $\hat{g}_j$. Substituting the above into the diffusion PDE (4.26), and neglecting products of small quantities, leads to

$$\hat{g}_j = \frac{1}{H^2}\frac{\partial^2 \hat{u}_j}{\partial \xi^2}, \tag{4.29}$$

with coupling conditions

$$\hat{u}_j(\pm r) - \hat{u}_j(0) = \gamma\left[\frac{r^2 \pm r}{2}U_{j+1} - r^2 U_j + \frac{r^2 \mp r}{2}U_{j-1}\right], \tag{4.30}$$

The amplitude definition (4.3), $U_j = u_j|_{\xi=0}$, requires

$$\hat{u}_j = 0, \quad \text{at } \xi = 0, \tag{4.31}$$

as the subgrid coordinate $\xi = 0$ corresponds to the patch mid-point $x = X_j$. Integrating equation (4.29) twice with respect to ξ gives the general solution

$$\hat{u}_j = \frac{\xi^2 H^2}{2}\hat{g}_j + c_1\xi + c_2. \tag{4.32}$$

The constant of integration $c_2 = 0$ by the amplitude condition (4.31). Subtracting the two coupling conditions (4.30) we determine the constant of integration $c_1 = (U_{j+1} - U_{j-1})r\gamma/2$. To determine the slow manifold evolution correction, we sum the two coupling conditions (4.30)

$$\hat{u}_j(r) + \hat{u}_j(-r) = \gamma r^2(U_{j-1} - 2U_j + U_{j+1}),$$

whereas from the microscale field (4.32), $\hat{u}_j(r) + \hat{u}_j(-r) = r^2\hat{g}_j H^2$. Thus, the slow manifold evolution correction $\hat{g}_j = \frac{\gamma}{H^2}(U_{j-1} - 2U_j + U_{j+1})$. Substituting the constants c_1, c_2 and the evolution correction $\hat{g}$ into the microscale field (4.32), leads to

$$\hat{u}_j = \frac{\gamma\xi}{2}(U_{j+1} - U_{j-1}) + \frac{\gamma\xi^2}{2}(U_{j-1} - 2U_j + U_{j+1}).$$

Therefore, the first non-trivial approximation to the slow manifold for the coupled patch system (4.26)–(4.27) is

$$u_j(\xi, t) \approx U_j + \frac{\gamma\xi}{2}(U_{j+1} - U_{j-1}) + \frac{\gamma\xi^2}{2}(U_{j-1} - 2U_j + U_{j+1}), \tag{4.33}$$

on which the evolution is

$$\frac{dU_j}{dt} \approx \frac{\gamma}{H^2}(U_{j-1} - 2U_j + U_{j+1}). \tag{4.34}$$

4.1.3 Computer algebra constructs the slow manifold

Recall that except for the zero eigenvalue all eigenvalues of the microscale system on the patch fields have negative real-parts ($\leq -\pi^2/h^2$). This ensures that for non-zero coupling parameter γ, the slow manifold persists. On a cross-patch diffusion time, the patch dynamics is attracted to this slow manifold. Then the system evolves slowly to provide the macroscale dynamics of interest.

Reduce computer algebra[1] is a free general purpose interactive system for general algebraic computations of interest to mathematicians, scientists and engineers. According to Fateman (2003) Reduce is around twenty times faster than using the MATLAB (which invokes Mupad), so it is perhaps the fastest general purpose computer algebra system. Thus, we use Reduce for many computer algebra computations and MATLAB for numerical schemes and simple computer algebra.

Computer algebra can replace much tedious manual calculation. In this section we employ computer algebra to repetitively compute the residuals of the governing equations (4.26) and coupling conditions (4.27). The algebra is iterated until the governing equations are satisfied; that is, all their residuals are zero to within a pre-specified error (Roberts 1997, e.g.). Using centre manifold theory, such as by Roberts (1988), Pötzsche & Rasmussen (2006), the correctness of the residual computation assures us of the order of accuracy of the resulting approximation.

Truncating to errors $\mathcal{O}(\gamma^3)$, the computer algebra of Algorithm 10 in Appendix B, solves the coupled patch system (4.26) and (4.23) to construct the slow manifold as

$$\begin{aligned} u_j(\xi,t) \approx{}& U_j + \frac{\gamma\xi}{2}(-U_{j-1}+U_{j+1}) + \frac{\gamma\xi^2}{2}(U_{j-1}-2U_j+U_{j+1}) \\ &+ \frac{\gamma^2(\xi-\xi^3)}{12}(U_{j-2}-2U_{j-1}+2U_{j+1}-U_{j+2}) \\ &- \frac{\gamma^2(\xi^2-\xi^4)}{24}(U_{j-2}-4U_{j-1}+6U_j-4U_{j+1}+U_{j+2}), \end{aligned} \tag{4.35}$$

on which the evolution is

$$\begin{aligned} \frac{dU_j}{dt} \approx{}& \frac{\gamma}{H^2}(U_{j-1}-2U_j+U_{j+1}) \\ &+ \frac{\gamma^2}{12H^2}(-U_{j-2}+4U_{j-1}-6U_j+4U_{j+1}-U_{j+2}). \end{aligned} \tag{4.36}$$

The right-hand side of this slow manifold (4.35) starts with a constant term independent of γ, then the two terms in γ correct the field by interactions with

---

[1] http://reduce-algebra.com/

its nearest neighbours, then the two terms in γ^2 correct by the interactions with next nearest neighbours, and so on. By evaluating at full coupling $\gamma = 1$, in the slow manifold interpolation (4.35) we obtain the approximate quartic interpolation to the field.

The slow manifold evolution (4.36) forms a classic finite difference approximation to the diffusion PDE (4.1) (Roberts et al. 2011). For examples, by truncating the slow manifold evolution (4.36) to errors of order $\mathcal{O}(\gamma^2)$ and $\mathcal{O}(\gamma^3)$ and evaluated at full coupling $\gamma = 1$, we obtain respectively

$$\frac{dU_j}{dt} \approx \frac{1}{H^2}\delta^2 U_j, \tag{4.37}$$

$$\frac{dU_j}{dt} \approx \frac{1}{H^2}\delta^2 U_j - \frac{1}{12H^2}\delta^4 U_j. \tag{4.38}$$

The right-hand sides of equations (4.37) and (4.38) respectively represent the classic second and fourth order accurate finite difference approximations to the second derivative in the diffusion PDE (4.1). Algorithm 10 could achieve a higher order in coupling of the truncation, to obtain a more accurate model.

4.1.4 Model physical boundary conditions at a grid point

Roberts (2003*a*, 2014) showed how boundaries to the physical domain are incorporated successfully into the numerical modelling of Burgers' equation. Constant boundary values were easily incorporated by replacing an internal boundary condition of an end element by a variant of the actual boundary condition. This subsection analogously constructs the slow manifold discretisation of PDEs with time-varying boundary values. For simplicity, we restrict attention to one spatial dimension. Divide the spatial domain into small patches and empower centre manifold theory by using a spatial coupling condition to support the resulting discretisation of the dynamics. The aim is to use this technique to create a good spatial discretisation of the PDEs for a subsequent numerical solution. The new feature is to account for time-varying boundary values, albeit here to errors $\mathcal{O}(\gamma^2)$.

Introduce basis variables for physical boundary conditions The challenge now is to introduce some basis vector variables to label boundary conditions. Consider the left boundary condition at $x = 0$. From the coupling conditions (4.27) the Dirichlet boundary condition at $x = 0$ provides the leftmost patch couple condition on its left edge of, to errors $\mathcal{O}(\gamma^2)$

and the neglect of cubic time derivatives of a and b,

$$u_1(X_1-h) = (1-\gamma r^2)U_1 + \frac{\gamma r}{2}\,(-1+r)\,U_2 + \frac{\gamma r}{2}\,(1+r)\,a(t). \tag{4.39}$$

Let us introduce a new parameter

$$\delta_j = \begin{cases} 1, & \text{if } j=1, \\ 0, & \text{otherwise }, \end{cases}$$

as a basis vector for the boundary conditions. Instead of (4.27) we invoke the left coupling condition

$$u_j(X_j-h) = (1-\gamma r^2)U_j + \frac{\gamma r}{2}\,(-1+r)\,U_{j+1} + \frac{\gamma r}{2}(1+r)\,[\delta_j a(t) + (1-\delta_j)U_{j-1}]\,.$$

For $j=1$ we obtain the first boundary condition (4.39); and for $j\neq 1$ we obtain the coupling condition (4.27) to errors $\mathcal{O}(\gamma^2)$.

Similarly for the right boundary, we invoke the general coupling boundary condition

$$u_j(X_j+h) = (1-\gamma r^2)U_j + \frac{\gamma r}{2}\,(-1+r)\,U_{j-1} + \frac{\gamma r}{2}(1+r)\,\left[\delta'_j b(t) + (1-\delta'_j)U_{j+1}\right],$$

for boundary condition parameter $\delta'_N = 1$ and all the rest $\delta'_j = 0$. The computer algebra of Algorithm 11 in Appendix B, successfully terminates in two iterations. It constructs the slow manifold for the diffusion PDE (4.26) with physical boundary conditions to errors $\mathcal{O}(\gamma^2)$ as

$$\begin{aligned} u_j(\xi,t) \;&=\; U_j + \frac{\gamma\xi}{2}\left(-U_{j-1} + U_{j+1} + \delta'_j b - \delta'_j U_{j+1} - \delta_j a + \delta_j U_{j-1}\right) \\ &\quad + \frac{\gamma\xi^2}{2}\left(U_{j-1} - 2U_j + U_{j+1} + \delta'_j b - \delta'_j U_{j+1} + \delta_j a - \delta_j U_{j-1}\right) \\ &\quad + \mathcal{O}(\gamma^2), \end{aligned} \tag{4.40}$$

on which the evolution is

$$\begin{aligned} \frac{dU_j}{dt} \;&=\; \frac{\gamma}{H^2}\left(U_{j-1} - 2U_j + U_{j+1} + \delta'_j b - \delta'_j U_{j+1} + \delta_j a - \delta_j U_{j-1}\right) \\ &\quad + \mathcal{O}(\gamma^2). \end{aligned} \tag{4.41}$$

In Algorithm 11 variables `lbc(j)` and `rbc(j)` denote the parameters δ_j and δ'_j which parametrise the left and right boundary conditions, respectively.

Preserving symmetry in discretised diffusion Let us now focus on the left boundary, so we neglect all terms in δ'_j. Starting with the model slow manifold equation,

$$\begin{aligned} u_j(\xi,t) &= U_j + \frac{\gamma\xi}{2}\left(-U_{j-1}+U_{j+1}-\delta_j a+\delta_j U_{j-1}\right) \\ &\quad + \frac{\gamma\xi^2}{2}\left(U_{j-1}-2U_j+U_{j+1}+\delta_j a-\delta_j U_{j-1}\right)+\mathcal{O}(\gamma^2), \end{aligned} \tag{4.42}$$

on which the evolution equation is

$$\frac{dU_j}{dt} = \frac{\gamma}{H^2}\left(U_{j-1}-2U_j+U_{j+1}+\delta_j a-\delta_j U_{j-1}\right)+\mathcal{O}(\gamma^2). \tag{4.43}$$

For interior patches, far away from the boundary, all the parameters $\delta_j = 0$ and the discretisations (4.42)–(4.43) reduce to the well established parabolic interpolation

$$u_j(\xi,t) = U_j + \frac{\gamma\xi}{2}(-U_{j-1}+U_{j+1}) + \frac{\gamma\xi^2}{2}(U_{j-1}-2U_j+U_{j+1})+\mathcal{O}(\gamma^2), \tag{4.44}$$

on which the evolution is classic finite difference approximation

$$\frac{dU_j}{dt} = \frac{\gamma}{H^2}\left(U_{j-1}-2U_j+U_{j+1}\right)+\mathcal{O}(\gamma^2). \tag{4.45}$$

We are only interested in the physical model obtained at full coupling $\gamma = 1$. Therefore, the model (4.44) becomes

$$u_j(\xi,t) \approx U_j + \frac{\xi}{2}(-U_{j-1}+U_{j+1}) + \frac{\xi^2}{2}(U_{j-1}-2U_j+U_{j+1}),$$

on which the evolution is

$$\frac{dU_j}{dt} \approx \frac{1}{H^2}\left(U_{j-1}-2U_j+U_{j+1}\right).$$

Near boundary The non-zero parameter $\delta_1 = 1$ affects patches near the left boundary, while all the others $\delta_j = 0$. Set patches $j = 1, 2$ in equation (4.40), and use that only $\delta_1 = 1$, the evolution reduce to

$$\frac{dU_1}{dt} = \frac{\gamma}{H^2}\left(-2U_1+U_2+a\right)+\mathcal{O}(\gamma^2), \tag{4.46}$$

$$\frac{dU_2}{dt} = \frac{\gamma}{H^2}\left(U_1-2U_2+U_3\right)+\mathcal{O}(\gamma^2), \tag{4.47}$$

Equations (4.46)–(4.47) only contain the amplitudes defined inside the physical domain, and show how to obtain the evolution equations for all patches from the general expression in equation (4.40) generated with the boundary factors δ_j.

4.1.5 Time-varying boundary values

Suppose we want to model a flow where the forcing at the boundary varies in time. Take the case of the diffusion of drugs from a patch into the skin. In the patch, the drug concentration diminishes with time, and therefore a time-varying flux condition on the skin boundary is needed where the drug is diffusing into the body. The same may apply in the cases of the energy or the momentum equations. Here we investigate the effects of boundary conditions that are changing with time. From a physical point of view, Roberts (2014) commented that, on finite sized elements changes in boundary values diffuse into the element, and so they take the same time to affect the subgrid field, and hence take time to affect the evolution on the slow manifold. Thus the modelling depends upon the rates of change of the forced boundary values.

Adapted from (Roberts 2014, p.609), computer algebra of Algorithm 12 in Appendix B shows the Reduce instructions to incorporate the Dirichlet boundary conditions into Algorithm 11, where the forcing at the boundary varies in time. Executing the computer algebra program of Algorithm 12 in Appendix B, the slow manifold expressions of the solution field $u(x,t)$ is, in terms of $\xi = (x - X_j)/H$, and t and with errors $\mathcal{O}(\gamma^2)$,

$$\begin{aligned}
u_j(\xi,t) \approx{}& U_j + \frac{\gamma\xi}{2}\left(-U_{j-1} + U_{j+1} - \delta_j a + \delta_j U_{j-1} + \delta_j' b - \delta_j' U_{j+1}\right)\\
&+ \frac{\gamma\xi^2}{2}\left(U_{j-1} - 2U_j + U_{j+1} + \delta_j a - \delta_j U_{j-1} + \delta_j' b - \delta_j' U_{j+1}\right)\\
&+ \frac{\dot a\delta_j\gamma H^2\xi}{24}\left(-2\xi^2 + \xi + 2r^2 - r^2\xi\right) + \frac{\dot b\delta_j'\gamma H^2\xi}{24}\left(2\xi^2 + \xi - 2r^2 - r^2\xi\right)\\
&+ (\ddot a\delta_j\gamma H^2\xi)\left(\frac{-\xi^4}{240} + \frac{\xi^5}{720} + \frac{r^2\xi^2}{72} - \frac{r^2\xi^3}{288} - \frac{7r^4}{720} + \frac{r^4\xi}{480}\right)\\
&+ (\ddot b\delta_j\gamma H^2\xi)\left(\frac{\xi^4}{240} + \frac{\xi^5}{720} - \frac{r^2\xi^2}{72} - \frac{r^2\xi^3}{288} + \frac{7r^4}{720} + \frac{r^4\xi}{480}\right),
\end{aligned} \tag{4.48}$$

where we use overdots for variables a and b to denote time derivatives. The slow manifold evolution is, to errors $\mathcal{O}(\gamma^2)$,

$$\begin{aligned}
\frac{dU_j}{dt} \approx{}& \frac{\gamma}{H^2}\left(U_{j-1} - 2U_j + U_{j+1} + \delta_j a - \delta_j U_{j-1} + \delta_j' b - \delta_j' U_{j+1}\right)\\
&- \frac{\gamma r^2}{12}\left(\dot b\delta_j' + \dot a\delta_j\right) + \frac{H^2 r^4}{240}\left(\ddot b\delta_j' + \ddot a\delta_j\right).
\end{aligned} \tag{4.49}$$

The time derivatives in the approximate slow manifold (4.48) inform us how the field changes with time-varying boundary values. The first three terms are the parabolic interpolation, modified by the first and second time derivative in the remaining terms that capture some sub-patch interactions between boundary values and the diffusion.

4.2 Comparison between slow manifold predictions and analytical solutions to diffusion dynamics

The evolutions (4.45) and (4.49) in this slow manifold modelling can capture the long-term dynamics of the original linear system. Here, we compare the solution to these slow manifold models, limited to the case of one patch, with the analytical solutions to the diffusion equation. For both constant and varying boundary forcing, there is reasonable agreement between slow manifold approximations and analytical solutions (Figures 4.3 and 4.5).

4.2.1 Evolution equations with constant and varying boundary forcing

This section finds the solution to slow manifold models (4.45) and (4.49) with incorporated constant and varying boundary conditions, respectively. We restrict attention to just $N = 1$ patch in the domain.

Solving evolution (4.45) with constant boundary conditions

For $j = 1$, the evolution (4.45), on which the physical boundary conditions are constants, becomes

$$\frac{dU_1}{dt} = \frac{\gamma}{H^2}\left(-2U_1 + b + a\right), \tag{4.50}$$

with initial condition $U_1(0) = U_0$. Integrating this equation (4.50) with respect to time we obtain

$$U_1(t) = \frac{(a+b)}{2} - \frac{1}{2}e^{-2\gamma t/H^2}(-2U_0 + b + a). \tag{4.51}$$

Substituting (4.51) into the slow manifold approximation (4.44) gives

$$\begin{aligned} u_1(\xi,t) \quad &\approx \quad \frac{(a+b)}{2} - \frac{1}{2}e^{-2\gamma t/H^2}(-2U_0 + b + a) + \frac{\gamma\xi}{2}(b-a) \\ &\quad + \frac{\gamma\xi^2}{2}\left[e^{-2\gamma t/H^2}(-2U_0 + b + a)\right]. \end{aligned} \tag{4.52}$$

Observe that on a long-time scale, $t \gg H^2/\gamma$, the slow manifold reduces to

$$u_1(\xi,t) \quad = \quad \frac{(a+b)}{2} + \frac{\gamma\xi}{2}(b-a),$$

which describes a steady state of linear variation in u that is correct in the fully coupled case of $\gamma = 1$.

Solving evolution (4.49) with periodic forcing in the boundary conditions

Consider the case where the specified boundary values vary in time as $a(t) = 0$ and $b(t) = \cos(\omega t)$ for some frequency ω. The evolution equation (4.49) becomes

$$\frac{dU_1}{dt} \approx \frac{\gamma}{H^2}\left[-2U_1 + \cos(\omega t)\right] - \frac{\gamma r^2}{12}\left[-\omega\sin(\omega t)\right] + \frac{H^2 r^4}{240}\left[-\cos(\omega t)\right].$$

When the relative patch size r is negligibly small, for the long-term response we obtain the non-autonomous system

$$\frac{dU_1}{dt} \approx \frac{\gamma}{H^2}\left[-2U_1 + \cos(\omega t)\right], \tag{4.53}$$

with initial condition $U_1(0) = U_0$. Solving this ODE (4.53) we get

$$U_1 \approx e^{-2\gamma t/H^2}\left(U_0 - \frac{2\gamma^2}{4\gamma^2 + \omega^2 H^4}\right) + \frac{\gamma}{4\gamma^2 + \omega^2 H^4}\left[2\gamma\cos(\omega t) + \omega H^2\sin(\omega t)\right]. \tag{4.54}$$

On a very long-time scale, $t \gg H^2/\gamma$, all solutions approach

$$U_1 \approx \frac{\gamma}{4\gamma^2 + \omega^2 H^4}\left[2\gamma\cos(\omega t) + \omega H^2\sin(\omega t)\right].$$

Substituting this into (4.48), this predicts the phase-lagged oscillating field. Therefore, the approximation of slow manifold (4.48) for one patch is

$$\begin{aligned} u_1(\xi,t) \;\approx\;& U_1 + \frac{\gamma\xi}{2}\cos(\omega t) + \frac{\gamma\xi^2}{2}\left[-2U_1 + \cos(\omega t)\right] \\ &- \frac{\omega\sin(\omega t)\gamma H^2\xi}{24}\left(2\xi^2 + \xi - 2r^2 - r^2\xi\right) \\ &- \left(\omega^2\cos(\omega t)\gamma H^2\xi\right)\left(\frac{\xi^4}{240} + \frac{\xi^5}{720} - \frac{r^2\xi^2}{72} - \frac{r^2\xi^3}{288} + \frac{7r^4}{720} + \frac{r^4\xi}{480}\right), \end{aligned} \tag{4.55}$$

where U_1 is given in (4.54).

4.2.2 Analytical solution for diffusion equation

This section first finds the analytical solutions for the diffusion equation with constant boundary conditions, and follows this with specified boundary values varying in time.

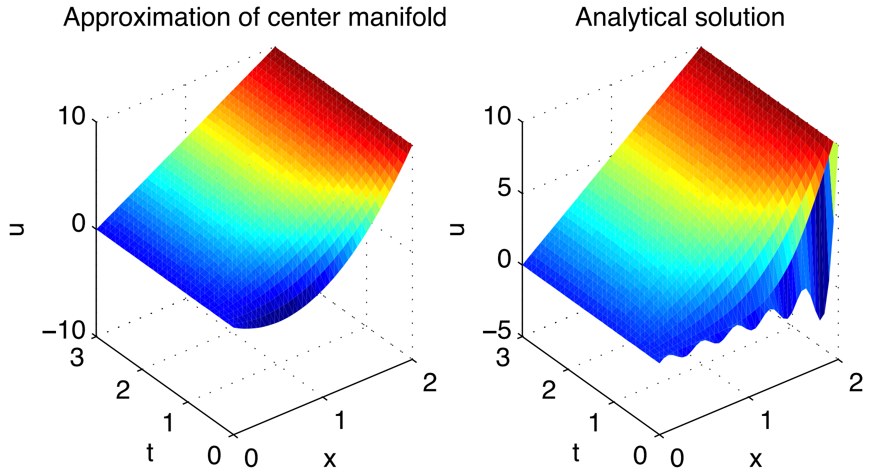

Figure 4.3: The slow manifold approximation (4.52) for the field $u(x,t)$ of the diffusion PDE with constant BCs (4.2) (left) compares with the analytical solution (4.56) of the diffusion PDE with same BCs (right). The slow manifold shows a good approximation for the field $u(x,t)$ compared with the analytical solution.

Time-independent BCs

Here we find analytical solutions for the diffusion equation with constant BCs to compare it with slow manifold expression (4.52) for the field $u(x,t)$ of the diffusion equation.

Let $u(x,t)$ be the time-varying temperature in a spatial one-dimensional domain. Consider the case of diffusion equation (4.1), with an initial temperature distribution $u(x,0)=0$; and fixed non-homogeneous boundary values (4.2) as $a=0$, and $b=10$. The system (4.1)–(4.2) has a solution in the form

$$u(x,t)=\frac{10}{L}x+\sum_{n=1}^{\infty}\frac{20(-1)^n}{n\pi}\sin\left(\frac{n\pi x}{L}\right)e^{-(n\pi/L)^2t}. \tag{4.56}$$

On the long-time scale, $t\gg L^2/\pi^2$, the temperature $u(x,t)$ approaches the equilibrium temperature $v(x)=10x/L$ as shown in Figure 4.3.

Periodic forcing in the boundary conditions

Consider the heat problem (4.1) with oscillatory boundary values $a=0$ and $b=\cos(\omega t)$. Physically, the temperature $u(L,t)=\cos(\omega t)$ keeps changing, in a periodic fashion, at the end of $x=L$. Since the temperature is changing periodically on one side, the solution depends upon time. However, after an initial transient time, we expect the solution to be periodic with angular frequency ω, such as

$$u(x,t) = v(x,t) + A(x)\cos[\omega t + \phi(x)], \tag{4.57}$$

where the transient $v(x,t)$ becomes zero after a long time.

Find the oscillatory response solution following the approach introduced by Guenther & Lee (1996) for solving the heat problem with periodic boundary conditions, we apply the fundamental relationship of Euler's formula to trigonometry, the quasi-steady state solution becomes

$$u_*(x,t) = \Re\{Q(x)e^{i\omega t}\} = \frac{1}{2}\{Q(x)e^{i\omega t} + Q^*(x)e^{-i\omega t}\}, \tag{4.58}$$

where Q^* denotes the complex conjugate of Q. We substitute the quasi-steady state (4.58) for $u(x,t)$ into PDE (4.1) to obtain

$$\frac{1}{2}\left[i\omega Q(x)e^{i\omega t} - i\omega Q^*(x)e^{-i\omega t}\right] = \frac{1}{2}\left[Q_{xx}(x)e^{i\omega t} + Q^*_{xx}(x)e^{-i\omega t}\right].$$

Multiplying both sides by two and rearranging terms yields

$$\left[i\omega Q(x) - Q_{xx}(x)\right]e^{i\omega t} + \left[-i\omega Q^*(x) - Q^*_{xx}(x)\right]e^{-i\omega t} = 0.$$

This equation is a sum of complex exponentials, and it equals zero if and only if

$$i\omega Q(x) - Q_{xx}(x) = 0 = -i\omega Q^*(x) - Q^*_{xx}(x).$$

The left and right terms are the complex conjugates of each other. The left boundary condition $u(0,t) = 0$ implies that

$$\frac{1}{2}\left\{Q(0)e^{i\omega t} + Q^*(0)e^{-i\omega t}\right\} = 0 \Rightarrow Q(0) = Q^*(0) = 0.$$

By applying the other boundary condition, $u(L,t) = \cos(\omega t)$, to the oscillatory response (4.58) yields

$$\frac{1}{2}\{Q(L)e^{i\omega t} + Q^*(L)e^{-i\omega t}\} = \frac{1}{2}\left(e^{i\omega t} + e^{-i\omega t}\right).$$

Multiplying both sides by two and rearranging terms yields

$$[Q(L) - 1]e^{i\omega t} + [Q^*(L) - 1]e^{-i\omega t} = 0,$$

this equation equals zero if and only if

$$Q(L) - 1 = 0 = Q^*(L) - 1 \Rightarrow Q(L) = Q^*(L) = 1.$$

Solving the complex amplitude $Q(x)$ of the oscillatory response u_* As derived in the previous paragraph, the problem of the complex amplitude $Q(x)$ is

$$Q_{xx}(x) - i\omega Q(x) = 0; \qquad Q(0) = 0, \qquad Q(L) = 1.$$

Thus, we obtain the desired solution of the oscillatory response to the PDE (4.1) as

$$u_*(x,t) = \Re\left\{ \frac{e^{\sqrt{\frac{\omega}{2}}(1+i)x} - e^{-\sqrt{\frac{\omega}{2}}(1+i)x}}{e^{\sqrt{\frac{\omega}{2}}(1+i)L} - e^{-\sqrt{\frac{\omega}{2}}(1+i)L}} e^{i\omega t} \right\}.$$

The real part on the right-hand side expands to

$$u_* = \frac{\cos\omega t(-\cos\beta_1\cosh\beta_2 + \cos\beta_2\cosh\beta_1) + \sin\omega t\,(\sin\beta_1\sinh\beta_2 - \sin\beta_2\sinh\beta_1)}{\cosh\left(\sqrt{2\omega}L\right) - \cos\left(\sqrt{2\omega}L\right)}, \tag{4.59}$$

where $\beta_1 = \sqrt{\frac{\omega}{2}}(x+L)$ and $\beta_2 = \sqrt{\frac{\omega}{2}}(x-L)$.

The oscillatory response solution satisfies the PDE and the periodic forcing in the boundary values of heat problem (4.1).

Determining the transient $v(x,t)$ To determine the transient $v(x,t)$ of equation (4.57) we substitute

$$u(x,t) = v(x,t) + u_*(x,t),$$

into the PDE and the periodic boundary conditions of the heat problem (4.1) to get a new problem for $v(x,t)$ with homogeneous boundary conditions

$$\begin{aligned} v_t &= v_{xx}, \quad 0 < x < L, \\ v(0,t) &= 0, \quad v(L,t) = 0, \quad t > 0, \\ v(x,0) &= -u_*(x,0), \quad 0 < x < L, \end{aligned} \tag{4.60}$$

upon assuming the initial condition $u(x,0) = 0$. Where the initial condition for $v(x,t)$ is

$$v(x,0) = -\Re\left\{ \frac{e^{\sqrt{\frac{\omega}{2}}(1+i)x} - e^{-\sqrt{\frac{\omega}{2}}(1+i)x}}{e^{\sqrt{\frac{\omega}{2}}(1+i)L} - e^{-\sqrt{\frac{\omega}{2}}(1+i)L}} \right\}.$$

System (4.60) is the basic homogeneous heat problem (4.1) which has a solution in the form

$$v(x,t) = \sum_{n=1}^{\infty} c_n \sin\left(\frac{n\pi x}{L}\right) e^{-(n\pi/L)^2 t}, \quad c_n = \frac{2}{L}\int_0^L v(x,0)\sin\left(\frac{n\pi x}{L}\right)\,dx,$$

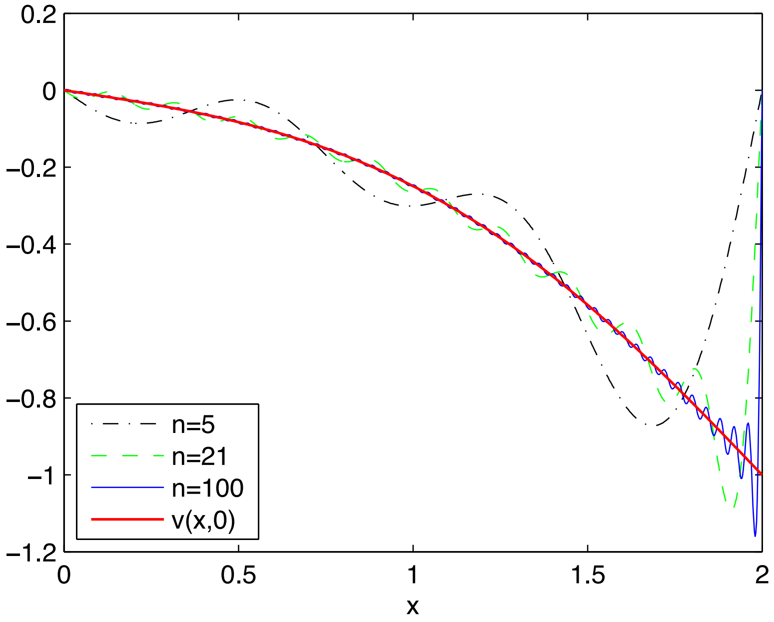

Figure 4.4: The first $5, 21,$ and 100 terms of the sine series approximation of function (4.61). The mean absolute errors are $0.10, 0.03,$ and 0.01, respectively.

where

$$v(x,0) = \frac{\cos\left[\sqrt{\frac{\omega}{2}}(x+L)\right]\cosh\left[\sqrt{\frac{\omega}{2}}(x-L)\right] - \cos\left[\sqrt{\frac{\omega}{2}}(x-L)\right]\cosh\left[\sqrt{\frac{\omega}{2}}(x+L)\right]}{\cosh\left(\sqrt{2\omega}L\right) - \cos\left(\sqrt{2\omega}L\right)}. \tag{4.61}$$

I compute coefficients c_n for this $v(x,0)$, and plot partial sums in Figure 4.4. The partial sums appear to reasonably converge to $v(x,0)$ (displaying Gibbs phenomenon near $x=2$). Therefore, the solution to the heat problem with an oscillatory boundary values (4.1) is

$$u(x,t) = \sum_{n=1}^{\infty} c_n \sin\left(\frac{n\pi x}{L}\right) e^{-(n\pi/L)^2 t} + \Re\left\{\frac{e^{\sqrt{\frac{\omega}{2}}(1+i)x} - e^{-\sqrt{\frac{\omega}{2}}(1+i)x}}{e^{\sqrt{\frac{\omega}{2}}(1+i)L} - e^{-\sqrt{\frac{\omega}{2}}(1+i)L}} e^{i\omega t}\right\}. \tag{4.62}$$

where the real part is given in (4.59). On the long-time scale, $t \gg L^2/\pi^2$, the solution approaches the oscillatory response as the transient part $v(x,t)$ decays exponentially.

As shown in Figures 4.3 and 4.5, for both constant and varying boundary forcing, there is little difference between the prediction of the slow manifold approximation for the field $u(x,t)$ and the analytical solution. This demon-

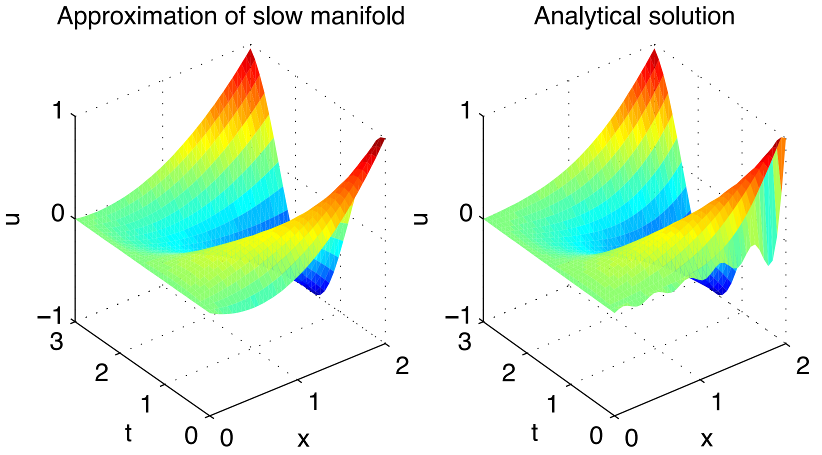

Figure 4.5: A space time simulation for a field $u(x,t)$ of the diffusion PDE with boundary values varying in time $u(0,t) = 0$ and $u(L,t) = \cos(2t)$ and initial condition $U_0 = 0$ on one patch where $r = 0.1$ and $H = 1$. (Left) the slow manifold prediction (4.55) for long-term behaviour of the dynamics system; (right) the analytical solution (4.62) of the diffusion PDE (4.1). The slow manifold shows a good approximation for the field $u(x,t)$ for the diffusion equation with varying boundary values compared with the analytical solution.

strates that the slow manifold evolution can capture the significant information of the long-term dynamics of the original linear system. Table 4.1 shows the mean absolute error (MAE), comparing the approximation of the slow manifold for the field $u(x, t)$ and the analytical solution in Figure 4.5.

4.3 Conclusion

This chapter extends the analysis of the one patch scheme applied to a one-dimensional diffusion problem in Chapter 3 to multiple patches with time-varying boundary values. The patch dynamics scheme is useful when the available mathematical model is computationally too expensive to be simulated over the entire physical domain. The patch scheme allows overall computation time to be reduced by restricting the simulations to only relatively small, strategically distributed patches located in the spatial domain.

Classic polynomial interpolation underlies the coupling of small, widely distributed patches proposed in Section 4.1. We use macroscale interpolation (4.23) to determine the boundary conditions at the edge of each patch. These boundary conditions couple adjacent patches, with a strength parametrised by γ, by interpolation across the unevaluated space between such patches in order to mimic a microscopic simulation performed over the entire physical domain. When the artificial parameter $\gamma = 0$, the patches are effectively isolated from each other, dividing the domain into decoupled patches with consequently independent dynamics; whereas when the artificial parameter $\gamma = 1$, these coupling conditions (4.23) ensure sufficient communication between patches to recover the original physical problem over all space. Centre manifold theory is applied after dividing the macroscale domain into small patches. The eigenvalue analysis in Section 4.1.2 indicates the existence of a slow manifold. Computer algebra in Section 4.1.3 then constructs the slow manifold of the system. Comparisons are made between the solution to the slow manifold models, limited to the case of one patch, with the analytical solutions to the diffusion equation. Section 4.2 shows that reasonable agreement exists between the slow manifold prediction and the analytical solution. We expect the general analysis will apply to coupled patches in higher spatial dimensions.

Table 4.1: The mean absolute error (MAE) comparing the quality of the approximation of the slow manifold for the field $u(x, t)$ and the analytical solution in Figure 4.5.

Time (t)	MAE
0.00	0.23
0.10	0.07
0.20	0.02
0.31	0.01
0.41	0.02
0.51	0.03
0.62	0.04
0.72	0.04
0.82	0.04
0.93	0.04
1.03	0.04
1.13	0.04
1.24	0.03
1.34	0.03
1.44	0.02
1.55	0.01
1.65	0.01
1.75	0.02
1.86	0.02
1.96	0.03
2.06	0.03
2.17	0.04
2.27	0.04
2.37	0.04
2.48	0.04
2.58	0.04
2.68	0.04
2.79	0.03
2.89	0.03
3.00	0.02

Chapter 5

Multiscale modeling couples patches of advection-diffusion equations

Chapters 3 and 4 analyse the patch dynamics scheme for the microscale diffusion PDE. This chapter extends the novel analysis to one-dimensional microscale advection-diffusion dynamics in a single patch first (Sections 5.1–5.5), then on multiple small, spatially separated patches (Sections 5.6–5.7).

Advection and diffusion govern the transport of heat and ground water pollutants, oil reservoir flow, in the modelling of semiconductors, and so forth (Isenberg & Gutfinger 1973, Parlange 1980, e.g.). The sources of such ground water pollutants originate from human activities. Due to the growing concern on environmental and health issues, the advection-diffusion model continues to receive attention from environmentalists, engineers and mathematical modellers. For example, obtaining analytical and numerical solutions of the advection-diffusion PDE can estimate and examine the rehabilitation process and management of a polluted water body after elimination of the pollution (Jaiswal et al. 2011). In this chapter, we aim for the patch scheme to predict the emergent large-scale behaviour of the microscale advection-diffusion PDE.

Here, in one space dimension on x and in time t we model the advection and diffusion of a field $u(x,t)$. We suppose the field satisfies the advective-diffusive PDE without any sources or sinks

$$\frac{\partial u}{\partial t} + V_0\frac{\partial u}{\partial x} = \frac{\partial^2 u}{\partial x^2}, \tag{5.1}$$

with boundary conditions to be specified later. V_0 denotes the advection velocity.

The microscale analytic solutions of microscale advection within a small patch are obtained by applying the separation of variables (Courant & Hilbert 1965, e.g.).

For non-self-adjoint problems, as occurs in Section 5.2, there is no guarantee that eigenfunctions for dissipative systems form a complete set, or that different eigenfunctions are orthogonal. For the separation of variables to be applicable to such non-self-adjoint systems, we construct some generalised eigenfunctions, Section 5.4.1, for the purpose of completion. The expansion theorems in terms of generalised eigenfunction have long been developed through extensive research. The first part of this chapter adapts the analysis, construction and interpretation of chapter 3 to the problem of advection-diffusion PDE in one spatial dimension. Section 5.3 determines all eigenvalues and eigenvectors on a small microscale patch with patch half-width h. Section 5.3.1 discusses the special case where microscale wavenumbers of the characteristic equation (5.13) occur in the complex plane for odd eigenvalue. All eigenvalues on the patch have large and negative real-parts, except for one eigenvalue which corresponds to a small macroscale wavenumber.

The spectral problem associated with a small patch appears to be a non-self-adjoint problem. To perform the spectral expansions, Section 5.4.1 finds the adjoint operator of the linear constant advection-diffusion PDE (5.19) on the patch with the nonlocal coupling conditions. Section 5.4.2 then finds the eigenfunctions of the adjoint operator. These two sets of eigenfunctions are referred to as a biorthogonal set, and the spectral coefficients in the eigenfunction expansion are obtained in Sections 5.4.5 and 5.4.6 using eigenfunctions of the corresponding adjoint problem.

In the second part of this chapter, Section 5.6 extends the model of Roberts (2003*b*) on overlapping elements to the case of patches separated by gaps. Section 5.6.3 finds the spectrum of the linear dynamics which is used to show that there exists a centre manifold of the macroscale emergent dynamics. Apart from decaying transients through microscale dissipation, the centre manifold is guaranteed to capture the most important information of the original problem. Computer algebra of Algorithm 13 in Appendix B, specified in Section 5.6.4, then constructs the slow manifold for the advection-diffusion PDE. Numerical eigenvalues of the patch dynamics, obtained in Section 5.7, confirm that our analytical representations of eigenvalues (5.60) and (5.63) are the only eigenvalues of the patch domain.

5.1 One patch boundary conditions

This section addresses the specific case of one patch coupled to distant specified boundary conditions, while Section 5.6 analyses the case of multiple coupled patches in one large dimension. Here for simplicity, we start to find the microscale solution within one small patch centred at the origin, and which extends over $-h \leq x \leq h$, for small h, in the physical domain $-H < x < H$, with time varying boundary conditions of the form

$$u(-H,t) = a(t), \quad u(H,t) = b(t). \tag{5.2}$$

In applications, a computational scheme is implemented only on the small fraction h of the domain, while over most of the domain we just interpolate. The aim here is to show that by coupling the patch to the surrounding macroscale variations, we are able to predict the large-scale behaviour of the system defined by equation (5.1), while substantially reducing the computational cost of simulating the system over the whole physical domain.

The simulator to solve (5.1) for field u in the microscale patch requires us to provide boundary conditions on the edge of the simulation domain. These boundary conditions are derived by an interpolation from $x = \pm H$. At the midpoint of the patch, $x = 0$, define the macroscale patch value to be

$$U(t) = u(0,t). \tag{5.3}$$

Then via classic Lagrange interpolation, we interpolate boundary values a, b and the patch macroscale field $U(t)$ to predict the macroscale field as

$$u(x,t) = U(t)\left(1 - \frac{x^2}{H^2}\right) + \frac{a}{2}\left(\frac{x^2}{H^2} \mp \frac{x}{H}\right) + \frac{b}{2}\left(\frac{x^2}{H^2} \pm \frac{x}{H}\right),$$

and we note that such interpolation has been proven to be effective for PDEs (Roberts & Kevrekidis 2007, e.g.). The parabolic interpolation provides non-local boundary values for the simulator within the patch as

$$u(\pm h,t) = u(0,t)\left(1 - r^2\right) + \frac{a}{2}\left(r^2 \mp r\right) + \frac{b}{2}\left(r^2 \pm r\right), \tag{5.4}$$

where $r = h/H$.

The boundary conditions (5.4) for the patch are non-homogeneous. Therefore, seek a solution in the form

$$u(x,t) = w(x,t) + \frac{C(t)}{H}x + D(t). \tag{5.5}$$

Substituting equation (5.5) into (5.4) gives

$$w(\pm h,t)\pm C(t)r = w(0,t)(1-r^2)+\frac{r^2}{2}(a+b)\pm\frac{r}{2}(b-a)-r^2D(t).$$

By choosing

$$D=\frac{a+b}{2}\quad\text{and}\quad C=\frac{b-a}{2},$$

we obtain the homogeneous boundary conditions for $w(x,t)$ of the form

$$w(\pm h,t)=w(0,t)(1-r^2). \tag{5.6}$$

Now substitute (5.5) into the advection-diffusion PDE (5.1) to obtain a new PDE whose field $w(x,t)$ evolves according to the advection-diffusion PDE

$$\frac{\partial^2 w}{\partial x^2}-V_0\frac{\partial w}{\partial x}-\frac{\partial w}{\partial t}=V_0\frac{C(t)}{H}+\frac{\dot C(t)}{H}x+\dot D(t), \tag{5.7}$$

with patch homogeneous boundary conditions (5.6) where the right-hand side of PDE (5.7) is the new source term, and a dot over a variable denotes the first derivative with respect to time.

5.2 Real homogeneous eigenfunctions

Consider the corresponding homogeneous problem of the linear advection-diffusion PDE (5.7), namely,

$$\frac{\partial^2 w}{\partial x^2}-V_0\frac{\partial w}{\partial x}-\frac{\partial w}{\partial t}=0, \tag{5.8}$$

with patch homogeneous boundary conditions (5.6). Applying separation of variables, we assume a solution of the separated form $w(x,t)\propto e^{\lambda t}v(x)$. After substitution into the homogeneous advection-diffusion PDE (5.8), we obtain the corresponding boundary value problem within the microscale patch

$$\frac{d^2v}{dx^2}-V_0\frac{dv}{dx}-\lambda v=0,\quad v(\pm h)=v(0)(1-r^2). \tag{5.9}$$

As all coefficients are constants, we seek solutions $v\propto e^{z\,x}$ to find the characteristic equation $z^2-V_0\,z-\lambda=0$. Hence, the two possible values of z are

$$z_1=\frac{1}{2}\left(V_0+\sqrt{V_0^2+4\lambda}\right),\quad z_2=\frac{1}{2}\left(V_0-\sqrt{V_0^2+4\lambda}\right), \tag{5.10}$$

and the two solutions of the homogeneous PDE (5.9) are $v_1(x) = e^{z_1 x}$ and $v_2(x) = e^{z_2 x}$. But for $V_0^2 + 4\lambda > 0$, these cannot satisfy the BCs (5.9).

For $V_0^2 + 4\lambda < 0$ and real λ, the roots of the characteristic polynomial are a complex conjugate pair

$$z_1 = \alpha + ik, \quad z_2 = \alpha - ik, \quad \text{where} \quad \alpha = \frac{1}{2}V_0 \quad \text{and} \quad k = \frac{1}{2}\sqrt{-V_0^2 - 4\lambda}.$$

The general solution to PDE (5.9) is then

$$v(x) = e^{\alpha x}\left[c_1 \cos(kx) + c_2 \sin(kx)\right], \tag{5.11}$$

where c_1 and c_2 are two constants, and k denotes a microscale wavenumber. Now, applying the patch homogeneous boundary conditions in (5.9) on the edges of the patch, at $x = \pm h$, gives

$$e^{\pm\alpha h}\left[c_1 \cos(kh) \pm c_2 \sin(kh)\right] = (1 - r^2)\, c_1.$$

Forming as a pair of linear equations,

$$\begin{bmatrix} e^{\alpha h} \cos(kh) - (1 - r^2) & e^{\alpha h} \sin(kh) \\ e^{-\alpha h} \cos(kh) - (1 - r^2) & -e^{-\alpha h} \sin(kh) \end{bmatrix} \begin{bmatrix} c_1 \\ c_2 \end{bmatrix} = \begin{bmatrix} 0 \\ 0 \end{bmatrix}, \tag{5.12}$$

this system has a non-trivial solution if its determinant is equal to zero,

$$\sin(kh)\left[\cos(kh) - (1 - r^2) \cosh(\alpha h)\right] = 0. \tag{5.13}$$

Figure 5.1 illustrates the solutions of the characteristic equation (5.13). The intersection points (asterisks) represent the roots of the functions $\sin(kh) = 0$ where the microscale wavenumbers $k_n h = n\pi$, for n even.

5.3 Complicated eigenspectrum

This section analyses the eigenvalues and their corresponding eigenfunctions which are associated with this small microscale patch.

From the characteristic equation (5.13), two cases arise to determine the eigenvalues and corresponding eigenfunctions.

- First, the microscale eigenvalue λ must satisfy $\sin(kh) = 0$, that is, $kh = n\pi/2$ for n even. Hence, the family of microscale wavenumbers is $k = n\pi/2h$. Then the microscale eigenvalues

  $$\lambda_n = -\left(\frac{n\pi}{2h}\right)^2, \quad n \text{ even}, \tag{5.14}$$

  are all negative, and the corresponding eigenfunctions

  $$v_n(x) = e^{\alpha x} \sin(k_n x), \quad n \text{ even}. \tag{5.15}$$

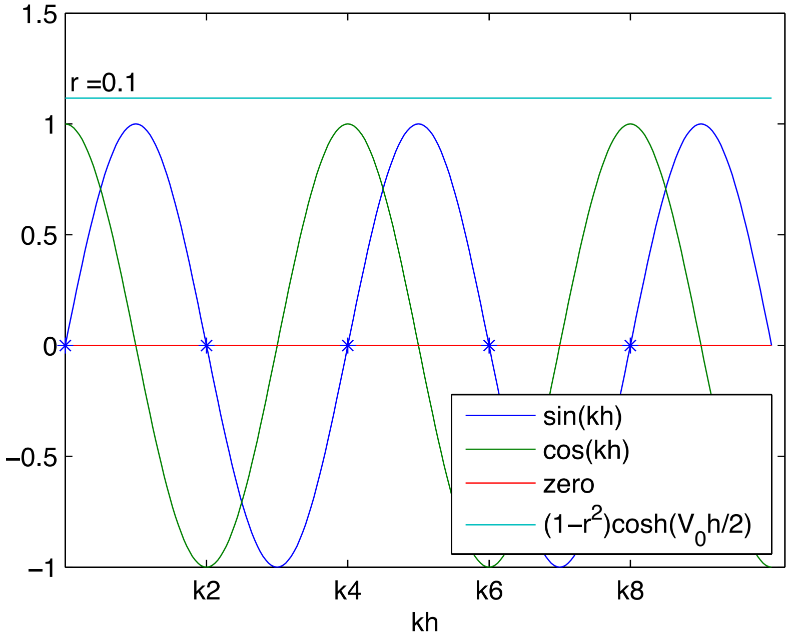

Figure 5.1: The solutions of the characteristic equation (5.13) where the patch parameters are given by $h = 1$, $H = 10$, $r = 1/10$ and the advection speed $V_0 = 1$. The intersection points (asterisks) represent the wavenumbers of eigenfunctions $\sin(k_n h)$ where n is even. The intersections between $\cos(k_n h)$ and $(1 - r^2)\cosh(V_0 h/2)$ occur only in the complex plane and require complex λ.

- Second, the microscale eigenvalue λ must satisfy $\cos(kh) - (1 - r^2)\cosh(\alpha h) = 0$. In this case when $\cosh(V_0 h/2) < 1/(1-r^2)$, approximate $|V_0| < \sqrt{2}/H$ for small patches, all solutions are real, and the microscale wavenumbers k_n are non-trivial functions of the patch ratio r, similar to those shown in Section 3.2. Setting a small microscale wavenumber $k_1 = \cos^{-1}[(1-r^2)\cosh(\alpha h)]/h$, where $0 < k_1 < \pi/2$. Then from the periodicity and symmetry of $\cos k_n x$, as shown in Figure 5.1, the family of microscale wavenumbers takes the form

  $$k_{n\pm1} = k_n \pm k_1 \quad \text{for } n = 4, 8, 12, \ldots,$$

  which gives the microscale wavenumbers of $k_3 = k_4 - k_1$, $k_5 = k_4 + k_1$, $k_7 = k_8 - k_1$, $k_9 = k_8 + k_1$, and so on. This gives the microscale eigenvalues

  $$\lambda_{n\pm1} = -\left(\frac{n\pi}{2h} \pm k_1\right)^2, \quad \text{for } n = 4, 8, 12, \ldots.$$

  The odd eigenfuntions are considerably more complex than the even eigenfunctions. To find the corresponding eigenfunctions for the second case we substitute $\cos(kh) = (1 - r^2)\cosh(\alpha h)$ into the matrix equation (5.12) to obtain

  $$\begin{bmatrix} (1-r^2)[e^{\alpha h}\cosh(\alpha h) - 1] & e^{\alpha h}\sin(kh) \\ (1-r^2)[e^{-\alpha h}\cosh(\alpha h) - 1] & -e^{-\alpha h}\sin(kh) \end{bmatrix} \begin{bmatrix} c_1 \\ c_2 \end{bmatrix} = \begin{bmatrix} 0 \\ 0 \end{bmatrix},$$

  but

  $$e^{\alpha h}\cosh(\alpha h) - 1 = e^{\alpha h}\sinh(\alpha h), \quad e^{-\alpha h}\cosh(\alpha h) - 1 = -e^{-\alpha h}\sinh(\alpha h),$$

  it follows that

  $$\begin{aligned} c_1 e^{\alpha h}\sinh(\alpha h)(1-r^2) + c_2 e^{\alpha h}\sinh(kh) &= 0, \\ -c_1 e^{-\alpha h}\sinh(\alpha h)(1-r^2) - c_2 e^{-\alpha h}\sinh(kh) &= 0. \end{aligned}$$

  Therefore, $(c_1, c_2) \propto [\sin(kh), -\sinh(\alpha h)(1-r^2)]$. By substituting the coefficients c_1 and c_2 into the general solution (5.11) we obtain the eigenfunctions as

  $$v_n(x) = e^{\alpha x}[\sin(k_n h)\cos(k_n x) - (1-r^2)\sinh(\alpha h)\sin(k_n x)], \quad \text{for } n \text{ odd.} \tag{5.16}$$

The principle of superposition constructs general solutions for the homogeneous advection-diffusion PDE (5.8) as

$$w(x,t) = \sum_{n=1}^{\infty} c_n e^{\lambda_n t} v_n(x), \tag{5.17}$$

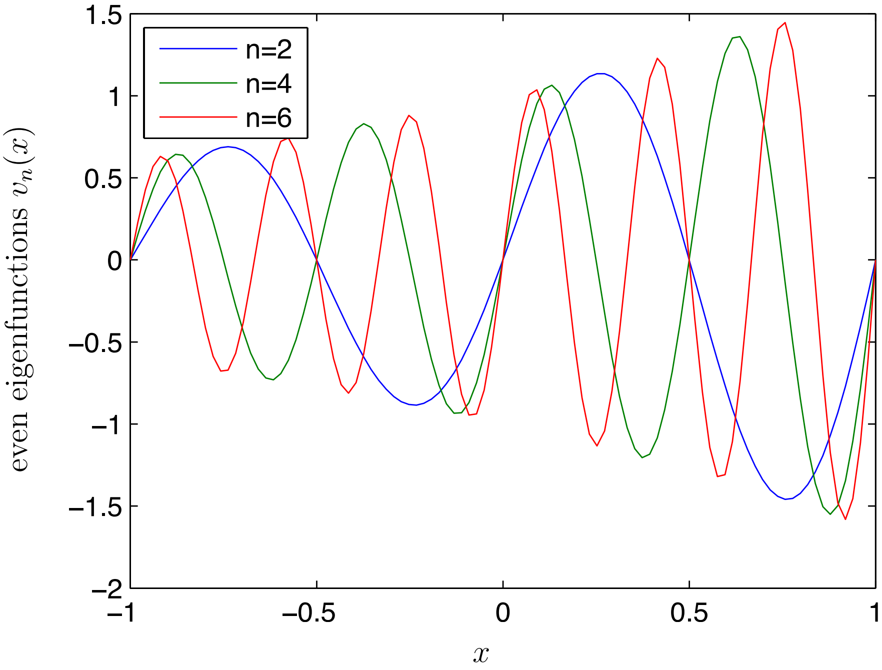

Figure 5.2: Illustration of the even microscale eigenfunctions $v_n(x)$ (5.15) for n even, with the three lowest magnitude microscale wavenumbers $k_n = n\pi/2h$, for patch parameters given by $h = 1$, $H = 10$, $r = 1/10$. Here the advection velocity $V_0 = 1$.

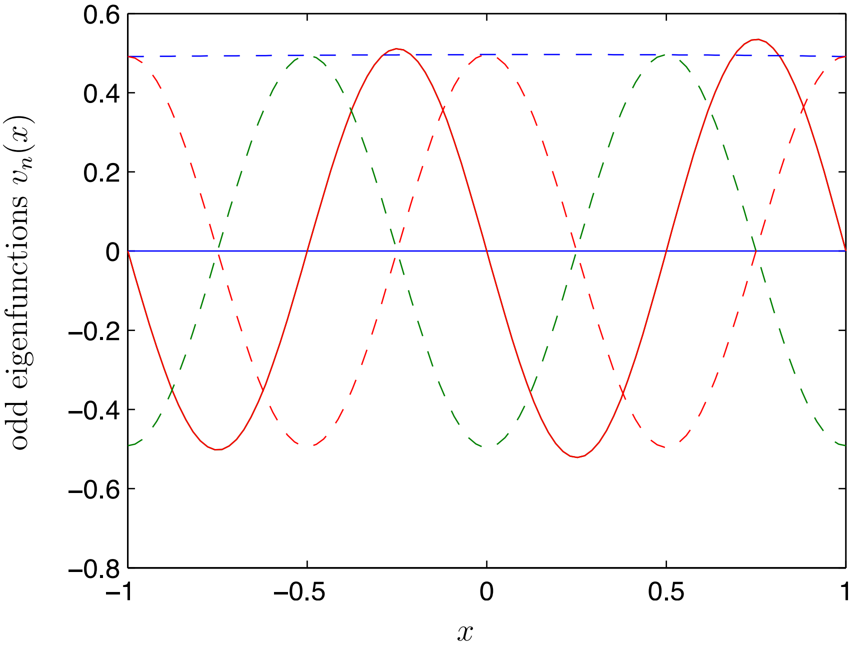

Figure 5.3: Illustration of the odd microscale eigenfunctions $v_n(x)$ (5.16) for n odd, where the parameters $h = 1$, $H = 10$, $r = 1/10$ and $V_0 = 1$. The solid line and curve represent the real part of the eigenfunctions $v_n(x)$ (5.16) for n odd, while the dashed line and curves represent the complex part of the eigenfunctions $v_n(x)$ (5.16) for n odd.

for microscale eigenfunctions given by (5.15) and (5.16). Figures 5.2 and 5.3 plot even and odd eigenfunctions associated with the three lowest magnitude eigenvalues, for patch ratio $r = 0.1$. For even n, the corresponding eigenfunctions are identical sine functions/sinusoidal multiplied by a growth exponential function. Section 5.4 uses these eigenfunctions, and adjoint eigenfunctions, in spectral expansions of the dynamics within the patch.

5.3.1 Complex eigenvalues of faster advection

This section discusses the case when $V_0 = 2\alpha$ is not small so that $(1-r^2)\cosh(\alpha h) > 1$; that is, the intersections between $\cos(kh)$ and $(1-r^2)\cosh(\alpha h)$ occur only in the complex plane. Hence, this section determines eigenvalues with imaginary parts as listed in Table 5.1: these characterise oscillating microscale modes within the patch.

From the characteristic equation (5.13), the microscale wavenumbers are given by

$$k = \frac{1}{h}\cos^{-1}[(1-r^2)\cosh(\alpha h)].$$

The smallest wavenumber is pure imaginary $k_1 = \pm i l_1$ where $l_1 \in \mathbb{R}$. As an example, consider the case when the length of the domain $H = 10$ and the length scale ratio $r = h/H = 0.1$, then the small microscale wavenumber in the characteristic equation becomes (5.13)

$$k_1 = \frac{1}{h}\cos^{-1}[(1-r^2)\cosh(\alpha h)] = \pm i0.4778,$$

so that $l_1 = 0.4778$. Then from the periodicity and symmetry of $\cos k_n h$, as shown in Figure 5.1, the microscale wavenumbers take the form

$$k_{n\pm1} = k_n \pm i l_1, \quad \text{for } n \in 4\mathbb{N},$$

which gives the microscale wavenumbers of $k_3 = k_4 - i l_1$, $k_5 = k_4 + i l_1$, $k_7 = k_8 - i l_1$, $k_9 = k_8 + i l_1$, and so on. Hence, two cases arise for the microscale eigenvalues.

- For n odd, all eigenvalues for non-zero wavenumbers occur in complex conjugate pairs. For example, as shown in Table 5.1, the eigenvalues λ_5 and λ_9 are the complex conjugate of the eigenvalues λ_3 and λ_7, respectively. The one exceptional eigenvalue is $\lambda_1 = -0.0217$ corresponding to complex conjugate pair of wavenumber with zero real part $k_1 = \pm i l_1$.
- For n even, all eigenvalues have negative and large real-parts as shown in Table 5.2.

Table 5.1: The values of the microscale wavenumbers k_n and the microscale eigenvalues λ_n for $n = 1, 3, 5, 7, 9$. The advection velocity $V_0 = 1$, and the patch parameters are $h = 1$, $H = 10$ and $r = 1/10$. With one exception, all of these eigenvalues come in complex conjugate pairs.

n	k_n	λ_n
1	$\pm il_1$	-0.0217
$3, 5$	$(2\pi \pm il_1)$	$-39.5001 \mp 6.0042i$
$7, 9$	$(4\pi \pm il_1)$	$-157.9400 \mp 12.0080i$

Complex eigenvectors For the eigenvalues which come in complex conjugate pairs, the corresponding eigenvectors also occur in conjugate pairs. For the smallest eigenvalue λ_1, the associated eigenvectors are

$$v_{1\pm}(x) = \pm ie^{x/2}[\sinh(l_1)\cosh(l_1x) - (1-r^2)\sinh(1/2)\sinh(l_1x)].$$

Both $v_{1+}(x)$ and $v_{1-}(x)$ are pure imaginary eigenvectors, and they are proportional to each other so represent the same information.

For eigenvalues λ_3 and λ_5, the associated eigenvectors are respectively

$$\begin{aligned} v_3(x) &= e^{x/2}\sin(2\pi x)[\sinh(l_1)\sinh(l_1x) - (1-r^2)\sinh(1/2)\cosh(l_1x)] \\ &\quad - ie^{x/2}\cos(2\pi x)[\sinh(l_1)\cosh(l_1x) - (1-r^2)\sinh(1/2)\sinh(l_1x)], \end{aligned}$$

and

$$\begin{aligned} v_5(x) &= e^{x/2}\sin(2\pi x)[\sinh(l_1)\sinh(l_1x) - (1-r^2)\sinh(1/2)\cosh(l_1x)] \\ &\quad + ie^{x/2}\cos(2\pi x)[\sinh(l_1)\cosh(l_1x) - (1-r^2)\sinh(1/2)\sinh(l_1x)]. \end{aligned}$$

The eigenvector v_3 is complex conjugate of the eigenvector v_5.

Let us interpret what such complex eigenfunctions mean for the patch dynamics. Consider the eigenfunctions $v_{3,5}$ corresponding to the eigenvalues $\lambda_{3,5}(-39.5001 \pm 6.0042i$ in Table 5.1). For brevity and generalisation to other values for n we denote $\lambda_n = -\mu \pm i\omega$. Set the eigenfunctions $v_{3,5} = v_R \pm iv_I$ where v_R and v_I represent the real and the imaginary part of the eigenfunctions $v_{3,5}$ respectively. Consider the general linear com-

Table 5.2: The values of the microscale wavenumbers k_n and the microscale eigenvalues $\lambda_n = -1/4 - k_n^2$ for $n = 2, 4, 6, 8, 10$, when parameters $h = 1$, $H = 10$ and $r = 1/10$.

n	k_n	λ_n
2	π	-10.1196
4	2π	-39.7284
6	3π	-89.0764
8	4π	-158.1637
10	5π	-246.9901

bination of

$$\begin{aligned} w_{3,5}(t) &= c_3e^{\lambda_3 t}v_3(x) + c_5e^{\lambda_5 t}v_5(x) \\ &= c_3e^{(-\mu+i\omega)t}(v_R + iv_I) + c_5e^{(-\mu-i\omega)t}(v_R - iv_I) \\ &= c_3e^{-\mu t}\cos(\omega t) + i\sin(\omega t)](v_R + iv_I) \\ &\quad + c_5e^{-\mu t}[\cos(\omega t) - i\sin(\omega t)](v_R - iv_I) \\ &= e^{-\mu t}(c_3 + c_5)[v_R\cos(\omega t) - v_I\sin(\omega t)] \\ &\quad + ie^{-\mu t}(c_3 - c_5)[v_I\cos(\omega t) + v_R\sin(\omega t)]. \end{aligned}$$

Since we are interested in real solutions we set $c_{3,5} = c_R \mp ic_I$ therefore,

$$w_{3,5}(t) = e^{-\mu t}\{2c_R[v_R\cos(\omega t) - v_I\sin(\omega t)] + 2c_I[v_I\cos(\omega t) + v_R\sin(\omega t)]\},$$

where c_R and c_I are arbitrary constants. Hence, $w_{3,5}(t)$ is a linear combination of two real solutions. In the long-term, for a small patch, the component $w_{3,5}(t)$ decays exponentially quickly, such as $e^{-39.5001t}$. Similarly, the other components $w_{7,9}(t), w_{11,13}(t), \ldots$ decay exponentially faster as they have eigenvalues with larger negative real-parts (Table 5.1). As $w_n(t)$ decays to zero, oscillations occur between the spatial structures of the real part $v_R(x)$ and the imaginary part $v_I(x)$. These oscillations are relatively fast, and determined by the imaginary part of the eigenvalues. These rapid microscale modes are not of interest to the macroscale dynamics. Hence, over macroscale times the dynamics of this system are dominated by the smallest eigenvalue $\lambda_1 : w(t,x) = e^{\lambda_1 t}v_1(x) +$ ignored transients.

Approximation of the macroscale eigenvalue The closest macroscale eigenvalue to zero is the most interesting one as it has the smallest decay and the longest lasting structure. In order to approximate the small eigenvalue we use a Taylor series for the cosine and the hyperbolic cosine in $\cos k_1 h = (1-r^2)\cosh(hV_0/2)$ since $V_0 h = V_0 H r$ is a small quantity: then since $r = h/H$,

$$\begin{aligned} 1-\frac{1}{2}(k_1 h)^2 &= (1-\frac{h^2}{H^2})(1+\frac{V_0^2 h^2}{8})+\mathcal{O}(h^4) \\ \Rightarrow k_1 &= \sqrt{\frac{2}{H^2}+\frac{(h^2-H^2)V_0^2}{8H^2}}+\mathcal{O}(h^2) \\ \Rightarrow k_1 &= \frac{\sqrt{2}}{H}\sqrt{1-\frac{H^2V_0^2}{16}}+\mathcal{O}(h^2). \end{aligned}$$

Therefore, $k_1 \approx \frac{\sqrt{2}}{H}\sqrt{1-\frac{H^2V_0^2}{16}}$. The corresponding spatial structure v_1 in the patch is the smooth

$$\begin{aligned} v_1 \approx{}& e^{V_0x/2}\sin\left(\sqrt{2}\,r\sqrt{1-\frac{H^2V_0^2}{16}}\right)\cos\left(\frac{\sqrt{2}}{H}\sqrt{1-\frac{H^2V_0^2}{16}}\,x\right) \\ &-e^{V_0x/2}(1-r^2)\sinh(V_0h/2)\sin\left(\frac{\sqrt{2}}{H}\sqrt{1-\frac{H^2V_0^2}{16}}\,x\right). \end{aligned}$$

The approximate small $k_1 \approx \frac{\sqrt{2}}{H}\sqrt{1-\frac{H^2V_0^2}{16}}$ and its corresponding eigenvalue $\lambda_1 \approx -1/4-2[1-\frac{H^2V_0^2}{16}]/H^2$ are only weakly dependent on the patch half-width h.

5.4 A spectral representation of the solution within a patch

Given the homogeneous microscale solutions of the previous subsection, we now explore a spectral representation of the solution within a patch. Analogous to deriving the solution to the non-homogeneous problem in Section 3.3, an eigenfunction expansion solves the non-homogeneous problem (5.7) with patch homogeneous boundary conditions (5.17). We assume the eigenfunctions (5.15) and (5.16) of the eigenproblem (5.9) form a complete set with respect to a piecewise smooth function over the microscale patch $[-h,h]$, and find the generalised Fourier series expansion of the forcing terms in terms of the eigenfunctions:

$$x=\sum_{n=1}^{\infty}a_n v_n(x) \quad\text{and}\quad 1=\sum_{n=1}^{\infty}b_n v_n(x), \tag{5.18}$$

where a_n and b_n are the spectral expansion coefficients. In order to determine these spectral coefficients a_n and b_n, the biorthogonality conditions need to be considered.

5.4.1 Determining the spectral coefficients

Determining the spectral coefficients a_n and b_n in the eigenfunction expansion (5.18) is challenging due to the non-orthogonality of the expansion basis functions $v_n(x)$ (5.15) and (5.16). The eigenfunctions over the microscale patch $[-h, h]$, for the cases in which n is odd or even, are not mutually orthogonal. This happens because of the non-self-adjointness of the system. Analogous to Section 3.4, we compute the spectral coefficients in the eigenfunction expansion using eigenfunctions of the adjoint problem.

The first goal of this subsection is to find the corresponding adjoint operator of the linear constant advection-diffusion PDE (5.9) with its associated boundary conditions. On the patch $|x| < h$, define the spatial advection-diffusion operator

$$\mathcal{L}v := \frac{\partial^2 v}{\partial x^2} - V_0\frac{\partial v}{\partial x}, \tag{5.19}$$

such that $v(x)$ and its first derivative v_x are continuous at $x = 0$ and with boundary conditions (5.9). Using the inner product (3.20) over the patch, the adjoint operator $\mathcal{L}^\dagger$ must satisfy the fundamental property (3.21). As in Chapter 3 the microscale patch is effectively subdivided into two subregions by the patch boundary conditions in (5.9). Apply the definition of the inner product (3.20), the definition (5.19) of the operator $\mathcal{L}$ and integrating by parts twice to expand the LHS of (3.21) as

$$\begin{aligned}
\langle \mathcal{L}v, z\rangle &= \left\langle \frac{\partial^2 v}{\partial x^2} - V_0\frac{\partial v}{\partial x}, z\right\rangle \\
&= \int_{-h}^{h}\left[\frac{\partial^2 v}{\partial x^2} - V_0\frac{\partial v}{\partial x}\right] z\,dx \\
&= \left[\frac{\partial v}{\partial x}z - v\frac{\partial z}{\partial x} - V_0 zv\right]_{-h}^{h} + \int_{-h}^{h} v\frac{\partial^2 z}{\partial x^2}\,dx + V_0\int_{-h}^{h} v\frac{\partial z}{\partial x}\,dx \\
&= \left[\frac{\partial v}{\partial x}z - v\frac{\partial z}{\partial x} - V_0 zv\right]_{-h}^{h} + \int_{-h}^{h} v\left(\frac{\partial^2 z}{\partial x^2} + V_0\frac{\partial z}{\partial x}\right)dx \\
&= \left[\frac{\partial v}{\partial x}z - v\frac{\partial z}{\partial x} - V_0 zv\right]_{-h}^{-0} + \left[\frac{\partial v}{\partial x}z - v\frac{\partial z}{\partial x} - V_0 zv\right]_{0}^{h} \\
&\quad + \int_{-h}^{h} v\left(\frac{\partial^2 z}{\partial x^2} + V_0\frac{\partial z}{\partial x}\right)dx.
\end{aligned}$$

Denote the partial derivatives with respect to x by subscripts, and use superscripts to denote evaluation. Using the boundary conditions in (5.9), the inner product

$$\begin{aligned}\langle \mathcal{L}v, z\rangle = {}& v_x^{-0}z^{-0} - v^{-0}z_x^{-0} - V_0v^{-0}z^{-0} - v_x^{-h}z^{-h} + v^{-h}z_x^{-h} + V_0v^{-h}z^{-h} \\ & - v_x^0z^0 + v^0z_x^0 + V_0v^0z^0 + v_x^hz^h - v^hz_x^h - V_0v^hz^h + \langle v, z_{xx} + V_0z_x\rangle.\end{aligned}$$

Since v is continuous at $x = 0$ together with its first derivative v_x, then

$$\begin{aligned}\langle \mathcal{L}v, z\rangle = {}& v_x^0\left[z^{-0} - z^0\right] + v^0\left[z_x^0 - z_x^{-0} + V_0(z^0 - z^{-0})\right. \\ & \left. + (1 - r^2)(z_x^{-h} - z_x^h - V_0(z^h - z^{-h}))\,\right] - v_x^{-h}z^{-h} + v_x^hz^h \\ & + \langle v, z_{xx} + V_0z_x\rangle.\end{aligned}$$

Thus, for the fundamental property (3.21) of the adjoint operator to hold, the adjoint operator must be defined as

$$\mathcal{L}^\dagger := \frac{\partial^2}{\partial x^2} + V_0\frac{\partial}{\partial x}, \tag{5.20}$$

with the following conditions:

- firstly, that the subgrid field z satisfies Dirichlet boundary conditions at the edges of the patch
$$z^{-h} = z^h = 0; \tag{5.21}$$
- secondly, that z is continuous at the centre of the patch, $x = 0$,
$$z^{-0} = z^0; \tag{5.22}$$
- thirdly, there is a jump in the first derivative at $x = 0$,
$$z_x^0 - z_x^{-0} = (1 - r^2)(z_x^h - z_x^{-h}). \tag{5.23}$$

These conditions make the boundary terms in the integration by parts vanish.

5.4.2 Eigenfunctions of the adjoint operator

Section 5.4.1 determines the adjoint operator (5.20)–(5.23). This section determines the spectrum and the eigenfunctions of the adjoint by solving

$$\mathcal{L}^\dagger z = \lambda z, \quad \text{equivalently} \quad \frac{\partial^2 z}{\partial x^2} + V_0\frac{\partial z}{\partial x} - \lambda z = 0, \tag{5.24}$$

with BCs (5.21)–(5.23). This PDE (5.24) is a constant coefficient in x, hence (for $\alpha = V_0/2$) we seek solutions in the form

$$z(x) = \begin{cases} e^{-\alpha x}\,[\,\zeta_0 \cos(kx) + \zeta_1 \sin(kx)],\ x < 0, \\ e^{-\alpha x}[\,\zeta_0 \cos(kx) + \zeta_2 \sin(kx)],\ x > 0, \end{cases} \tag{5.25}$$

where ζ_0, ζ_1, and ζ_2 are arbitrary constants, and k may be complex ($k = 1/2\sqrt{-V_0^2 + 4\lambda}$). The first derivative of $z(x)$ (5.25) is to be used to satisfy the jump condition (5.23):

$$z_x(x) = \begin{cases} e^{-\alpha x}\,[\cos(kx)(-\alpha\zeta_0 + k\zeta_1) + \sin(kx)\,(-\alpha\zeta_1 - k\zeta_0)],\ x < 0, \\ e^{-\alpha x}\,[\cos(kx)(-\alpha\zeta_0 + k\zeta_2) + \sin(kx)\,(-\alpha\zeta_2 - k\zeta_0)],\ x > 0. \end{cases}$$

Satisfying the adjoint boundary conditions Evaluating the boundary conditions (5.21)–(5.23) we obtain the following homogeneous system of algebraic equations

$$e^{\alpha h}[\zeta_0 \cos(kh) - \zeta_1 \sin(kh)] = 0, \tag{5.26}$$

$$e^{-\alpha h}[\zeta_0 \cos(kh) + \zeta_2 \sin(kh)] = 0, \tag{5.27}$$

$$\begin{aligned} &\zeta_0\,[2k\kappa \sin(kh)\cosh(\alpha h) - 2\alpha\kappa \cos(kh)\sinh(\alpha h)] \\ &\qquad + \zeta_1[-k + \alpha\kappa e^{\alpha h}\sin(kh) + k\kappa e^{\alpha h}\cos(kh)] \\ &\qquad + \zeta_2[k + \alpha\kappa e^{-\alpha h}\sin(kh) - k\kappa e^{-\alpha h}\cos(kh)] = 0, \end{aligned} \tag{5.28}$$

where $\kappa = (1 - r^2)$. Thus, the homogeneous system of algebraic equations (5.26)–(5.28), rewritten in matrix form, is

$$\begin{bmatrix} e^{\alpha h}\cos(kh) & -e^{\alpha h}\sin(kh) & 0 \\ e^{-\alpha h}\cos(kh) & 0 & e^{-\alpha h}\sin(kh) \\ M_0 & M_1 & M_2 \end{bmatrix} \begin{bmatrix} \zeta_0 \\ \zeta_1 \\ \zeta_2 \end{bmatrix} = \vec{0}, \tag{5.29}$$

where

$$\begin{aligned} M_0 &= 2k\kappa \sin(kh)\cosh(\alpha h) - 2\alpha\kappa\cos(kh)\sinh(\alpha h), \\ M_1 &= -k + \alpha\kappa e^{\alpha h}\sin(kh) + k\kappa e^{\alpha h}\cos(kh), \\ M_2 &= k + \alpha\kappa e^{-\alpha h}\sin(kh) - k\kappa e^{-\alpha h}\cos(kh). \end{aligned}$$

For non-trivial solutions to this system's matrix (5.29), the determinant of the matrix must be zero:

$$\begin{aligned} \det = {} & k\sin(kh)\cos(kh) - \alpha\kappa e^{\alpha h}\sin^2(kh)\cos(kh) - k\kappa e^{\alpha h}\sin(kh)\cos^2(kh) \\ & + k\sin(kh)\cos(kh) + \alpha\kappa e^{-\alpha h}\sin^2(kh)\cos(kh) - k\kappa e^{-\alpha h}\sin(kh)\cos^2(kh) \\ & - 2k\kappa\sin^3(kh)\cosh(kh) + 2\alpha\kappa\sin^2(kh)\cos(kh)\sinh(\alpha h). \end{aligned}$$

Simplifying the above expression by collecting the common factors yields

$$\begin{aligned}\det = {} & 2k\sin(kh)\cos(kh) - \alpha\kappa\sin^2(kh)\cos(kh)(e^{\alpha h} - e^{-\alpha h}) \\ & - k\kappa\sin(kh)\cos^2(kh)(e^{\alpha h} + e^{-\alpha h}) - 2k\kappa\sin^3(kh)\cosh(kh) \\ & + 2\alpha\kappa\sin^2(kh)\cos(kh)\sinh(\alpha h).\end{aligned}$$

We simplify further, first by using the definition of the hyperbolic sine and cosine $e^{\alpha h} - e^{-\alpha h} = 2\sinh(\alpha h), \quad e^{\alpha h} + e^{-\alpha h} = 2\cosh(\alpha h)$, and the trigonometric identity $\sin^3(kh) = \sin(kh) - \sin(kh)\cos^2(kh)$. Substituting these identities into the determinant we obtain the same characteristic equation (5.13) as required. As before, the characteristic equation (5.13) is zero in two cases characterised by n even and n odd.

5.4.3 Case n is even

First, this characteristic equation (5.13) is zero when microscale wavenumbers $k_n h = n\pi/2$, for n even. Then the system's matrix (5.29) becomes

$$\begin{bmatrix} \pm e^{\alpha h} & 0 & 0 \\ \pm e^{-\alpha h} & 0 & 0 \\ \mp 2\alpha\kappa\sinh(\alpha h) & -k \pm k\kappa e^{\alpha h} & k \mp k\kappa e^{-\alpha h} \end{bmatrix} \begin{bmatrix} \zeta_0 \\ \zeta_1 \\ \zeta_2 \end{bmatrix} = \vec{0},$$

where the upper and the lower case of each entry in this matrix are obtained from

$$\cos(n\pi/2) = \begin{cases} +1, & \text{for } n \in 4\mathbb{N}, \\ -1, & \text{for } n \in 4\mathbb{N} - 2. \end{cases}$$

Solving the above homogeneous system we obtain $(\zeta_0, \zeta_1, \zeta_2) \propto (0, 1 \mp \kappa e^{-\alpha h}, 1 \mp \kappa e^{\alpha h})$. By substituting ζ_0, ζ_1 and ζ_2 into (5.25) we obtain two different adjoint eigenfunctions based upon two different cases of even n.

- For $n \in 4\mathbb{N}$, the adjoint eigenfunctions

$$z_n(x) = \begin{cases} e^{-\alpha x}\sin(k_n x)\,(1 - \kappa e^{-\alpha h}), & x < 0, \\ e^{-\alpha x}\sin(k_n x)\,(1 - \kappa e^{\alpha h}), & x > 0. \end{cases} \tag{5.30}$$

- For $n \in 4\mathbb{N} - 2$, the adjoint eigenfunctions

$$z_n(x) = \begin{cases} e^{-\alpha x}\sin(k_n x)\,(1 + \kappa e^{-\alpha h}), & x < 0, \\ e^{-\alpha x}\sin(k_n x)\,(1 + \kappa e^{\alpha h}), & x > 0. \end{cases} \tag{5.31}$$

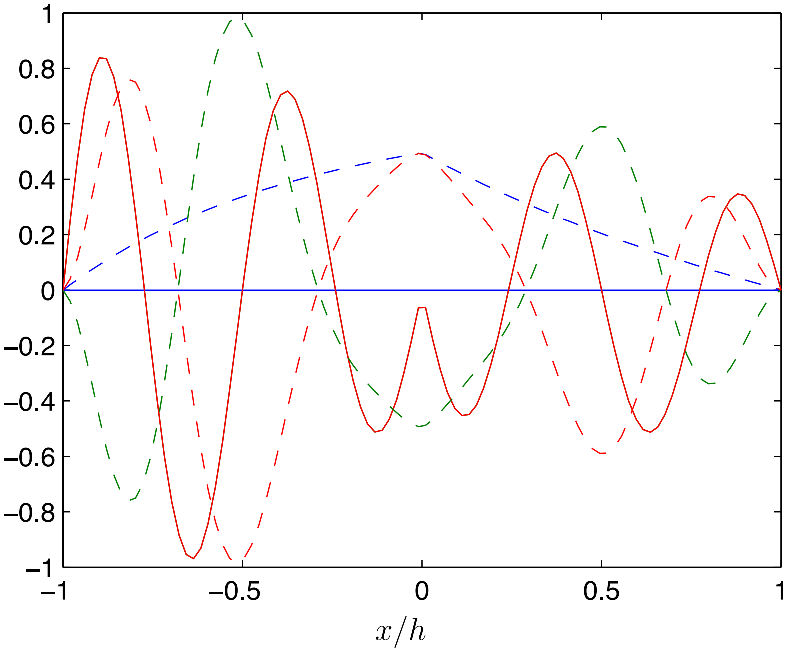

Figure 5.4: Illustration of the microscale adjoint eigenfunctions $z_n(x)$ (5.32) for n odd, where the patch parameters are $h = 1$, $H = 10$, $r = 1/10$ and $\alpha = 1/2$. The solid curves represent the real part of adjoint eigenfunctions, while the dashed curves represent the imaginary part.

5.4.4 Case n is odd

The second factor of the characteristic equation (5.13) requires that $\cos k_nh = (1-r^2)\cosh(\alpha h)$. The possible solutions k_n are detailed in Section 5.3. To solve the homogeneous system (5.29) we chose $\zeta_0 = \sin(k_nh)$ to obtain

$$\zeta_1 = \frac{\zeta_0\,\cos(k_nh)}{\sin(k_nh)} = \cos(k_nh), \quad \zeta_2 = -\frac{\zeta_0\,\cos(k_nh)}{\sin(k_nh)} = -\cos(k_nh).$$

Substituting ζ_0, ζ_1 and ζ_2 into (5.25) gives the adjoint eigenfunctions for n odd as

$$z_n(x) = \begin{cases} e^{-\alpha x}\,[\sin(k_nh)\cos(k_nx) + \cos(k_nh)\,\sin(k_nx)], & x<0, \\ e^{-\alpha x}\,[\sin(k_nh)\cos(k_nx) - \cos(k_nh)\,\sin(k_nx)], & x>0. \end{cases} \tag{5.32}$$

These eigenfunctions (5.30)–(5.32) (for both n even and odd) form a biorthogonal set of function to the original set v_n, that is

$$\langle v_n, z_m\rangle = 0 \quad \text{for} \quad n \neq m. \tag{5.33}$$

5.4.5 The spectral coefficients a_n

To compute the coefficients a_n of the spectral expansion of the function x in (5.18), we take the inner product (3.20) of x with each adjoint eigenfunction z_m (5.32) and use the properties of the inner product and biorthogonality (5.33) to find $\langle x, z_m\rangle = a_m\langle v_m, z_m\rangle$. Rearranging gives the spectral coefficients

$$a_m = \frac{\langle x, z_m\rangle}{\langle v_m, z_m\rangle}, \quad \text{for all } m. \tag{5.34}$$

The generalised spectral coefficients a_m have three different formulas from the three different cases.

- The case of m odd. The numerator on the right-hand side of expansion coefficients (5.34) is, for z_m from (5.32),

$$\begin{aligned}\langle x, z_m\rangle = &\int_{-h}^{0} xe^{-\alpha x}[\sin(k_mh)\cos(k_mx) + \cos(k_mh)\sin(k_mx)]\,dx \\ &+ \int_0^h xe^{-\alpha x}[\sin(k_mh)\cos(k_mx) - \cos(k_mh)\sin(k_mx)]\,dx.\end{aligned}$$

  An integration by parts gives

$$\langle x, z_m\rangle = \frac{k_m^3(h-he^{2\alpha h}) + k_m[\alpha^2(h-he^{2\alpha h}) + \alpha(2e^{2\alpha h} - 4e^{\alpha h}\cos(k_mh) + 2)]}{e^{\alpha h}(\alpha^2+k_m^2)^2}.$$

The denominator on the right-hand side of expansion coefficients (5.34) is, for v_m from (5.16),

$$\begin{aligned}\langle v_m, z_m\rangle = \sin^2(k_m h)&\int_{-h}^{h}\cos^2(k_m x)\,dx\\
&-\kappa\sinh(\alpha h)\sin(k_m h)\int_{-h}^{h}\cos(k_m x)\sin(k_m x)\,dx\\
&+\cos(k_m x)\sin(k_m x)\int_{-h}^{0}\sin(k_m x)\cos(k_m x)\,dx\\
&-\cos(k_m x)\sin(k_m x)\int_{0}^{h}\sin(k_m x)\cos(k_m x)\,dx\\
&-\kappa\sinh(\alpha h)\cos(k_m h)\int_{-h}^{0}\sin^2(k_m x)\,dx\\
&+\kappa\sinh(\alpha h)\cos(k_m h)\int_{0}^{h}\sin^2(k_m x)\,dx.\end{aligned}$$

Hence

$$\begin{aligned}\langle v_m, z_m\rangle &= \sin^2(k_m h)\left[h+\frac{\sin(2k_m h)}{2k}\right]-\frac{1}{k}\sin(k_m h)\cos(k_m h)\sin^2(k_m h)\\
&= \sin^2(k_m h)\left[h+\frac{\sin(2k_m h)}{2k}\right]-\frac{1}{2k}\sin(2k_m h)\sin^2(k_m h)\\
&= h\sin^2(k_m h). \qquad (5.35)\end{aligned}$$

Therefore, the expansion coefficients (5.34) of the spectral expansion of the function x for m odd are

$$a_m = \frac{k_m^3(h-he^{2\alpha h})+k_m[\alpha^2(h-he^{2\alpha h})+\alpha(2e^{2\alpha h}-4e^{\alpha h}\cos(k_m h)+2)]}{he^{\alpha h}(\alpha^2+k_m^2)^2\sin^2(k_m h)}. \qquad (5.36)$$

- The case of $m\in 4\mathbb{N}$. The numerator on the right-hand side of expansion coefficients (5.34) is, for z_m from (5.30),

$$\begin{aligned}\langle x, z_m\rangle = (1-\kappa e^{-\alpha h})&\int_{-h}^{0}xe^{-\alpha x}\sin(k_m x)dx\\
&+(1-\kappa e^{\alpha h})\int_{0}^{h}xe^{-\alpha x}\sin(k_m x)dx.\end{aligned}$$

An integration by parts gives

$$\begin{aligned}\langle x, z_m\rangle &= (\kappa e^{-\alpha h}-1)\left(\frac{2\alpha k_m + e^{\alpha h}\cos(k_m h)[hk_m^3 - 2\alpha k_m + \alpha^2 k_m h]}{(\alpha^2+k_m^2)^2}\right)\\ &\quad + (\kappa e^{\alpha h}-1)\left(\frac{-2\alpha k_m + e^{-\alpha h}\cos(k_m h)[hk_m^3 + 2\alpha k_m + \alpha^2 k_m h]}{(\alpha^2+k_m^2)^2}\right).\end{aligned}$$

The denominator on the right-hand side of expansion coefficients (5.34) is, for $m \in 4\mathbb{N}$,

$$\begin{aligned}\langle v_m, z_m\rangle &= \int_{-h}^{+h} v_m z_m\,dx\\ &= (1-\kappa e^{-\alpha h})\int_{-h}^{0}\sin^2(k_m x)\,dx + (1-\kappa e^{\alpha h})\int_0^h \sin^2(k_m x)\,dx\\ &= (1-\kappa e^{-\alpha h})\left(\frac{h}{2}-\frac{\sin(2k_m h)}{4k}\right) + (1-\kappa e^{\alpha h})\left(\frac{h}{2}-\frac{\sin(2k_m h)}{4k}\right)\\ &= \left[2-\kappa e^{-\alpha h}-\kappa e^{\alpha h}\right]\left(\frac{h}{2}-\frac{\sin(2kh)}{4k}\right)\\ &= \left[2-\kappa e^{-\alpha h}-\kappa e^{\alpha h}\right]\left(\frac{h}{2}\right) \quad \left(\text{for } k=\frac{m\pi}{2h},\quad \sin(2k_m h)=0\right)\\ &= h[1-\kappa\cosh(\alpha h)]. \qquad (5.37)\end{aligned}$$

Therefore, the expansion coefficients (5.34) for $m \in 4\mathbb{N}$ are

$$\begin{aligned}a_m &= (\kappa e^{-\alpha h}-1)\left(\frac{2\alpha k_m + e^{\alpha h}\cos(k_m h)[hk_m^3 - 2\alpha k_m + \alpha^2 k_m h]}{h[1-\kappa\cosh(\alpha h)](\alpha^2+k_m^2)^2}\right)\\ &\quad + (\kappa e^{\alpha h}-1)\left(\frac{-2\alpha k_m + e^{-\alpha h}\cos(k_m h)[hk_m^3 + 2\alpha k_m + \alpha^2 k_m h]}{h[1-\kappa\cosh(\alpha h)](\alpha^2+k_m^2)^2}\right).\end{aligned} \qquad (5.38)$$

- The case of $m \in 4\mathbb{N}-2$. The numerator on the right-hand side of expansion coefficients (5.34) is, for z_m from (5.31),

$$\begin{aligned}\langle x, z_m\rangle &= (1+\kappa e^{-\alpha h})\int_{-h}^{0} xe^{-\alpha x}\sin(k_m x)dx\\ &\quad + (1+\kappa e^{\alpha h})\int_0^h xe^{-\alpha x}\sin(k_m x)dx.\end{aligned}$$

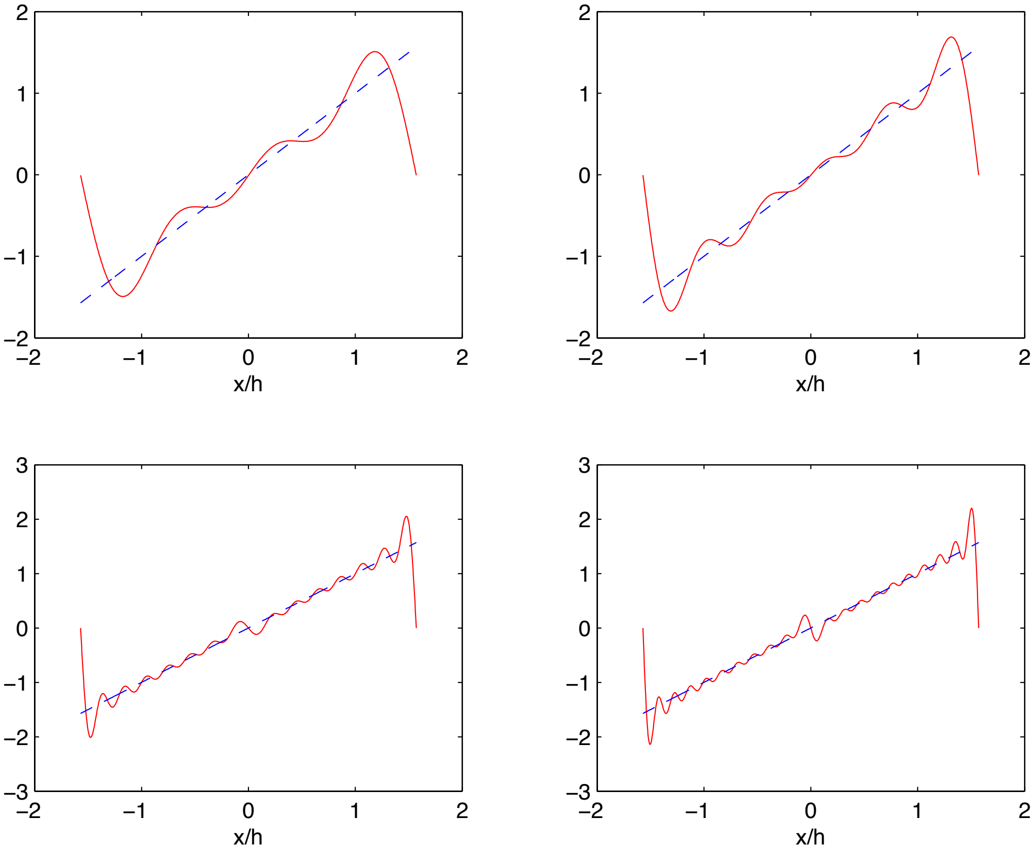

Figure 5.5: Spectral approximations (5.18) to the function x: plot the Nth partial sums for $N = 3, 5, 11$, and 21 eigenmodes, where the parameters $r = 0.5$, $V_0 = 0.1$ and $H = \pi$. The mean absolute errors are $0.23, 0.17, 0.12$ and 0.09, respectively.

An integration by parts gives

$$\begin{aligned}\langle x, z_m\rangle &= (\kappa e^{-\alpha h}+1)\left(\frac{-2\alpha k_m - e^{\alpha h}\cos(k_m h)[hk_m^3 - 2\alpha k_m + \alpha^2 k_m h]}{(\alpha^2+k_m^2)^2}\right)\\ &\quad+(\kappa e^{\alpha h}+1)\left(\frac{2\alpha k_m - e^{-\alpha h}\cos(k_m h)[hk_m^3 + 2\alpha k_m + \alpha^2 k_m h]}{(\alpha^2+k_m^2)^2}\right).\end{aligned}$$

The denominator on the right-hand side of expansion coefficients (5.34) is

$$\begin{aligned}\langle v_m, z_m\rangle &= \int_{-h}^{+h} v_m z_m\,dx\\ &= (1+\kappa e^{-\alpha h})\int_{-h}^{0}\sin^2(k_m h)\,dx + (1+\kappa e^{\alpha h})\int_{0}^{h}\sin^2(k_m h)\,dx\\ &= (1+\kappa e^{-\alpha h})\left(\frac{h}{2}\right) + (1+\kappa e^{\alpha h})\left(\frac{h}{2}\right)\\ &= \left(\frac{h}{2}\right)\left[\kappa\left(e^{\alpha h}+e^{-\alpha h}\right)+2\right]\\ &= h\left[\kappa\cosh(\alpha h)+1\right]. \qquad (5.39)\end{aligned}$$

Hence, the coefficients

$$\begin{aligned}a_m &= (\kappa e^{-\alpha h}+1)\left(\frac{-2\alpha k_m - e^{\alpha h}\cos(k_m h)[hk_m^3 - 2\alpha k_m + \alpha^2 k_m h]}{h[\kappa\cosh(\alpha h)+1](\alpha^2+k_m^2)^2}\right)\\ &\quad+(\kappa e^{\alpha h}+1)\left(\frac{2\alpha k_m - e^{-\alpha h}\cos(k_m h)[hk_m^3 + 2\alpha k_m + \alpha^2 k_m h]}{h[\kappa\cosh(\alpha h)+1](\alpha^2+k_m^2)^2}\right).\end{aligned} \qquad (5.40)$$

Figure 5.5 shows spectral approximations to the function x given by (5.18) for the various partial sums, and in the case of patch ratio $r = 0.5$. Evidently, the partial sums converge to the function x.

5.4.6 The spectral coefficients b_n

The spectral coefficients b_n in the expansions (5.18) are computed in exactly the same manner as that used to determine the spectral coefficients a_n. We take the inner product (3.20) of both sides of the expansion (5.18) with an element z_m (5.30) for some $1 \le m \le n$, and use the properties of the inner product and biorthogonality (5.33) to find $\langle 1, z_m\rangle = b_m\langle v_m, z_m\rangle$. Rearranging gives the expansion coefficients

$$b_m = \frac{\langle 1, z_m\rangle}{\langle v_m, z_m\rangle}, \quad \text{for all } m. \qquad (5.41)$$

The generalised spectral coefficients b_m have three different formulas from the three different cases.

- The case of m odd. The numerator on the right-hand side of expansion coefficients (5.41) is, for z_m from (5.32),
$$\begin{aligned}\langle 1, z_m\rangle &= \int_{-h}^{0} e^{-\alpha x}[\sin(k_m h)\cos(k_m x) + \cos(k_m h)\sin(k_m x)]\,dx \\ &\quad + \int_{0}^{h} e^{-\alpha x}[\sin(k_m h)\cos(k_m x) - \cos(k_m h)\sin(k_m x)]\,dx.\end{aligned}$$
An integration by parts gives
$$\langle 1, z_m\rangle = \frac{2k_m[\cosh(\alpha h) - \cos(k_m h)]}{\alpha^2 + k_m^2}.$$
The denominator on the right-hand side of expansion coefficients (5.41) is derived in equation (5.35) for m odd. Therefore, the coefficients
$$b_m = \frac{2k_m[\cosh(\alpha h) - \cos(k_m h)]}{(\alpha^2 + k_m^2)h\sin^2(k_m h)}. \tag{5.42}$$

- The case of $m \in 4\mathbb{N}$. The numerator on the right-hand side of expansion coefficients (5.41) is, for z_m from (5.30),
$$\begin{aligned}\langle 1, z_m\rangle &= (1 - \kappa e^{-\alpha h})\int_{-h}^{0} e^{-\alpha x}\sin(k_m x)dx + (1 - \kappa e^{\alpha h})\int_{0}^{h} e^{-\alpha x}\sin(k_m x)dx \\ &= \frac{-k_m(\kappa e^{-\alpha h} - 1)[e^{\alpha h}\cos(k_m h) - 1] + k_m(\kappa e^{\alpha h} - 1)[e^{-\alpha h}\cos(k_m h) - 1]}{(\alpha^2 + k_m^2)} \\ &= 2k_m\sinh(\alpha h)\left[\frac{\cos(k_m h) - \kappa}{\alpha^2 + k_m^2}\right].\end{aligned}$$
The denominator on the right-hand side of expansion coefficients (5.41) is derived in (5.37) for $m \in 4\mathbb{N}$. Therefore, the spectral coefficient
$$b_m = \frac{2k_m\sinh(\alpha h)\,[\cos(k_m h) - \kappa]}{h[1 - \kappa\cosh(\alpha h)](\alpha^2 + k_m^2)}. \tag{5.43}$$

- The case of $m \in 4\mathbb{N} - 2$. The numerator on the right-hand side of equation (5.41) is, for z_m from (5.31),
$$\begin{aligned}\langle 1, z_m\rangle &= (1 + \kappa e^{-\alpha h})\int_{-h}^{0} e^{-\alpha x}\sin(k_m x)dx + (1 + \kappa e^{\alpha h})\int_{0}^{h} e^{-\alpha x}\sin(k_m x)dx \\ &= \frac{k_m(\kappa e^{-\alpha h} + 1)[e^{\alpha h}\cos(k_m h) - 1] - k_m(\kappa e^{\alpha h} + 1)[e^{-\alpha h}\cos(k_m h) - 1]}{\alpha^2 + k_m^2} \\ &= 2k_m\sinh(\alpha h)\left[\frac{\cos(k_m h) + \kappa}{\alpha^2 + k_m^2}\right].\end{aligned}$$

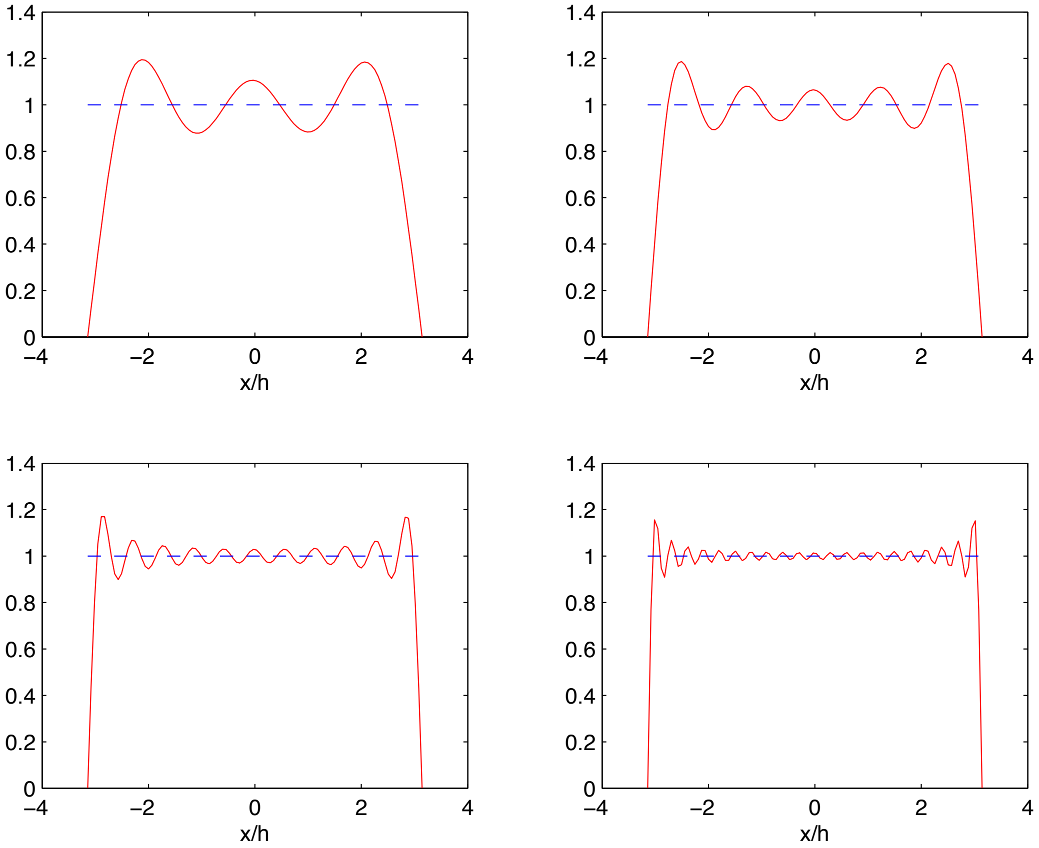

Figure 5.6: Spectral approximations (5.18) to the function 1 : plot the Nth partial sums for $N = 3, 5, 11$ and 21 eigenmodes where the parameters $H = \pi$, $r = 0.5$ and $V_0 = 0.1$. The mean absolute errors are $0.03, 0.02, 0.01$ and 0.01, respectively.

The denominator on the right-hand side of equation (5.41) is derived in (5.39) for $m \in 4\mathbb{N} - 2$. Therefore, the spectral coefficients

$$b_m = \frac{2k_m \sinh(\alpha h)\,[\cos(k_m h) + \kappa]}{h[1 - \kappa\cosh(\alpha h)](\alpha^2 + k_m^2)}. \tag{5.44}$$

Figure 5.6 shows spectral approximations to the function 1 given by (5.18). Evidently, the partial sums converge to the function 1 except at the endpoints where the Gibbs phenomenon appears.

5.5 Constructing the formal solution

This section aims to find the general solution for the advection-diffusion PDE

$$w_t = \mathcal{L}w + F(x,t), \tag{5.45}$$

where $F(x,t)$ denotes the new forcing terms in the PDE (5.7). Expanding the force $F(x,t)$ in terms of the eigenfunctions of the problem with homogeneous boundary conditions

$$F(x,t) = V_0\frac{C(t)}{H} + \frac{\dot{C}(t)}{H}x + \dot{D}(t) = \sum_{n=1}^{\infty} f_n(t)\, v_n(x), \tag{5.46}$$

where

$$f_n(t) = \frac{2}{h}\int_0^h F(x,t)\, v_n(x)\, dx.$$

We seek a particular solution of the form

$$w(t,x) = \sum_{n=1}^{\infty} w_n(t)v_n(x). \tag{5.47}$$

By substituting equations (5.46) and (5.47) into the advection-diffusion PDE (5.45) we obtain

$$\begin{aligned}\sum_{n=1}^{\infty} \dot{w}_n(t)v_n(x) &= \sum_{n=1}^{\infty} w_n(t)\mathcal{L}v + \sum_{n=1}^{\infty} f_n(t)v_n(x)\\ &= \sum_{n=1}^{\infty} w_n(t)\lambda_n v_n(x) + \sum_{n=1}^{\infty} f_n(t)v_n(x).\end{aligned} \tag{5.48}$$

The last relation in (5.48) is obtained by using the eigenfunction property $\mathcal{L}v_n = \lambda_n v_n(x)$. Since eigenfunctions $v_n(x)$ are linearly independent on the microscale patch $[-h,h]$, so equate the Fourier coefficients in equation (5.48) to give (Kreyszig 2011)

$$\dot{w}_n(t) - \lambda_n w_n(t) = f_n(t).$$

This is a first order linear ODE with an integrating factor $e^{-\lambda_n t}$. Thus

$$\frac{d}{dt}\left[e^{-\lambda_n t}w_n(t)\right] = e^{-\lambda_n t}f_n(t).$$

Integrating from 0 to t yields

$$w_n(t) = Q_n e^{\lambda_n t} + \int_0^t e^{\lambda_n(t-s)} f_n(s)\, ds, \tag{5.49}$$

for some constants Q_n depending upon initial conditions. Substituting equation (5.49) into equation (5.47) we obtain the general solutions for the advection-diffusion equation on the field $w(x,t)$

$$w(x,t) = \sum_{n=1}^{\infty} v_n(x) \left[Q_n e^{\lambda_n t} + \int_0^t e^{\lambda_n (t-s)} f_n(s)\, ds \right],$$

with the patch homogeneous boundary conditions (5.6). Recall that $w(x,t)$ (5.5) is a transformation of $u(x,t)$ as

$$u(x,t) := w(x,t) + \frac{C(t)}{H} x + D(t).$$

Therefore, the solution to the advection-diffusion equation (5.1) on a single microscale patch is

$$u(x,t) = \sum_{n=1}^{\infty} \left[v_n(x) \int_0^t e^{\lambda_n (t-s)} f_n(s)\, ds \right] + \frac{C(t)}{H} x + D(t). \tag{5.50}$$

A long-term model must determine the slowest modes in this solution dominated by the modes that have the largest magnitude. Analogous to the leading behaviour analysis in Section 3.5.2, the long-term dynamics of the slow varying mode, $n = 1$, correspond to the approximation

$$u(x,t) = v_1(x) \int_0^t e^{\lambda_1 (t-s)} f_1(s)\, ds + \frac{C(t)}{H} x + D(t),$$

where v_1 is given by (5.16). This is the patch dynamics prediction to the solution of the advection-diffusion PDE (5.1)–(5.2).

Transform back to original domain

Now our interest is in showing that in the limit $h \to H$, the patch domain (covers the entire physical domain) becomes identical to a macroscale domain $-H < x < H$. Also, the microscale patch boundary conditions (5.4) are reduced to the exact physical boundary conditions that $u(-h) = a(t)$, and $u(+h) = b(t)$. Hence, for the patch ratio $r = 1$, the microscale wavenumbers in Section 5.3 become $k_m = m\pi/2H$, for $m = 1, 2, 3, 4, 5, \ldots$. Thus the eigenvalues of the diffusion dynamics over the whole domain are

$$\lambda_m = -\left(\frac{m\pi}{2H}\right)^2, \quad \text{for } m = 1, 2, 3, \ldots.$$

Thus the predicted microscale field (5.50) in the patch should reproduce the exact dynamics upon setting the patch size to one.

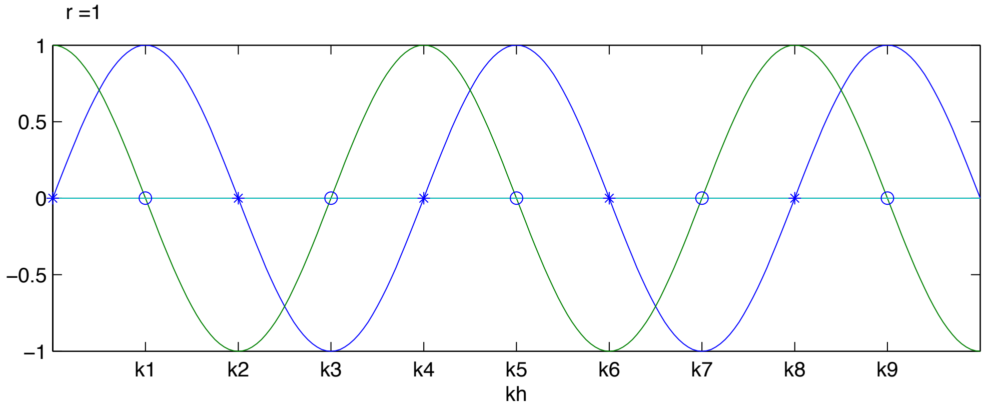

Figure 5.7: Illustration of the solutions of the characteristic equation (5.13), where the patch ratio r equals one.

Finding the spectral coefficients for $r = 1$

Setting the patch size to one, Figures 5.8 and 5.9 confirm that the spectral coefficients a_n and b_n in Sections 5.4.5 and 5.4.6 reproduce the generalised Fourier coefficients.

- For m odd, the spectral coefficients a_m (5.36) where r tends to one become

$$\begin{aligned}\lim_{r\to1} a_m &= \lim_{r\to1} \frac{k_m^3(r)(h-he^{2\alpha h})+k_m(r)[\alpha^2(h-he^{2\alpha h})}{he^{\alpha h}(\alpha^2+k_m^2(r))^2\sin^2(hk_m(r))}\\ &\quad+\lim_{r\to1}\frac{\alpha k_m(r)(2e^{2\alpha h}-4e^{\alpha h}\cos(hk_m(r))+2)]}{he^{\alpha h}(\alpha^2+k_m^2(r))^2\sin^2(hk_m(r))}.\end{aligned}$$

  Thus, for odd m

$$a_m = \frac{(m\pi/2h)^3(h-he^{2\alpha h})+(m\pi/2h)[\alpha^2h(1-e^{2\alpha h})+\alpha(2e^{2\alpha h}+2)]}{he^{\alpha h}[\alpha^2+(m\pi/2h)^2]^2}.$$

- For $m \in 4\mathbb{N}$, the spectral coefficients a_m (5.38) of the spectral expansion of the function x become

$$\begin{aligned}\lim_{r\to1} a_m &= \lim_{r\to1}(\kappa e^{-\alpha h}-1)\left(\frac{2\alpha k_m+e^{\alpha h}\cos(k_mh)[hk_m^3-2\alpha k_m+\alpha^2k_mh]}{-h[\kappa\cosh(\alpha h)-1](\alpha^2+k_m^2)^2}\right)\\ &\quad+\lim_{r\to1}(\kappa e^{\alpha h}-1)\left(\frac{-2\alpha k_m+e^{-\alpha h}\cos(k_mh)[hk_m^3+2\alpha k_m+\alpha^2k_mh]}{-h[\kappa\cosh(\alpha h)-1](\alpha^2+k_m^2)^2}\right).\end{aligned}$$

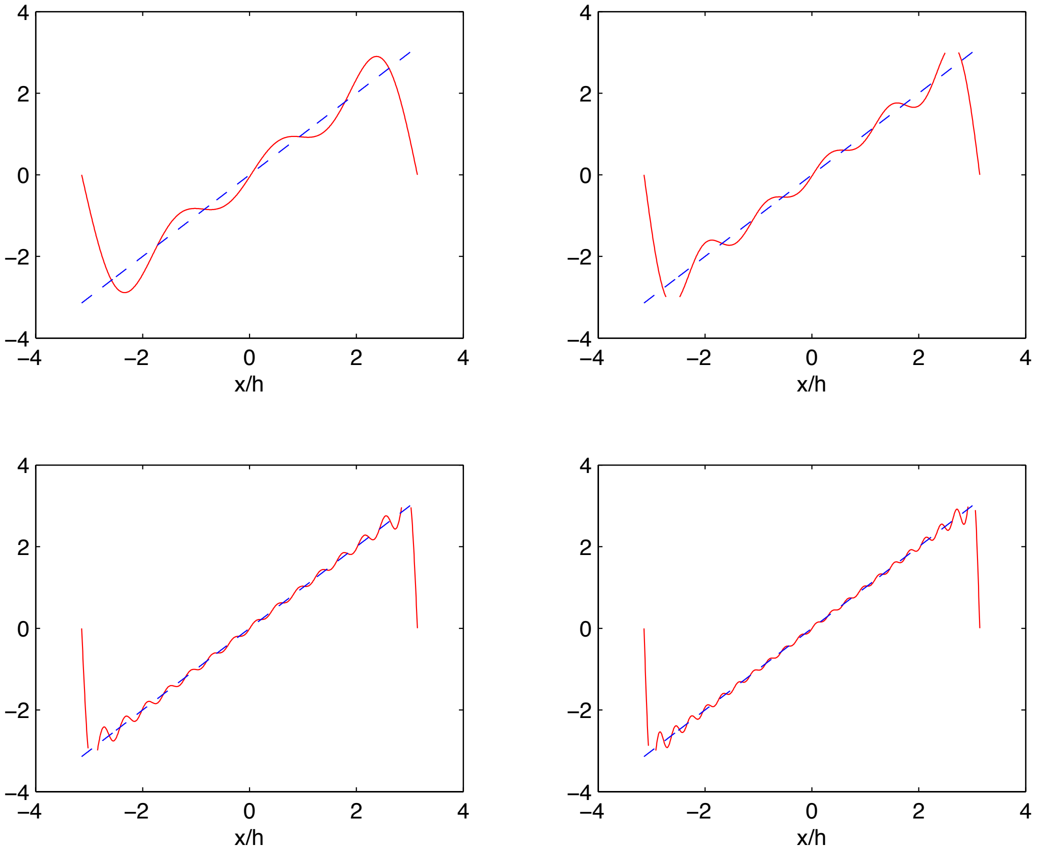

Figure 5.8: Spectral approximations (5.18) to the function x: plot the Nth partial sums for $N = 3, 5, 11$, and 21 eigenmodes, where the patch parameters are given by, $r = 1$, $V_0 = 0.1$ and $H = \pi$. The mean absolute errors are $0.46, 0.32, 0.14$ and 0.11, respectively.

Therefore, the generalised Fourier coefficients

$$\begin{aligned} a_m = & \frac{-e^{\alpha h}[h(m\pi/2h)^3 - \alpha(m\pi/h) + \alpha^2 m\pi/2]}{h(\alpha^2 + (m\pi/2h)^2)^2} \\ & + \frac{e^{-\alpha h}[h(m\pi/2h)^3 + \alpha(m\pi/h) + \alpha^2(m\pi/2)]}{h[\alpha^2 + (m\pi/2h)^2]^2}. \end{aligned}$$

- For $m \in 4\mathbb{N} - 2$, the coefficients a_m (5.40) of the spectral expansion of the function x become

$$\begin{aligned}\lim_{r\to1} a_m &= \lim_{r\to1}(\kappa e^{-\alpha h}+1)\left(\frac{-2\alpha k_m - e^{\alpha h}\cos(k_m h)[hk_m^3 - 2\alpha k_m + \alpha^2 k_m h]}{h[\kappa\cosh(\alpha h)+1](\alpha^2+k_m^2)^2}\right)\\ &\quad + \lim_{r\to1}(\kappa e^{\alpha h}+1)\left(\frac{2\alpha k_m - e^{-\alpha h}\cos(k_m h)[hk_m^3 + 2\alpha k_m + \alpha^2 k_m h]}{h[\kappa\cosh(\alpha h)+1](\alpha^2+k_m^2)^2}\right).\end{aligned}$$

Thus, the generalised Fourier coefficients

$$\begin{aligned}a_m &= \frac{e^{\alpha h}[h(m\pi/2h)^3 - \alpha(m\pi/h) + \alpha^2(m\pi/2)]}{h(\alpha^2+(m\pi/2h)^2)^2}\\ &\quad + \frac{e^{-\alpha h}[h(m\pi/2h)^3 + \alpha(m\pi/h) + \alpha^2(m\pi/2)]}{h[\alpha^2+(m\pi/2h)^2]^2}.\end{aligned}$$

Figure 5.8 shows the generalised Fourier series (5.18) of the function x for the various partial sums, and in the case of patch ratio $r = 1$. With five terms, the partial sum already looks very similar to a sawtooth wave function.

- For m odd, the spectral coefficients b_m (5.42) where r tends to one become

$$\begin{aligned}\lim_{r\to1} b_m &= \lim_{r\to1}\frac{2k_m[\cosh(\alpha h) - \cos(k_m h)]}{(\alpha^2+k_m^2)h\sin^2(k_m h)}\\ &= \frac{m\pi\cosh(\alpha h)}{[\alpha^2+(m\pi/2h)^2]h}.\end{aligned}$$

- For $m \in 4\mathbb{N}$, the coefficients b_m (5.43) of the spectral expansion of the function 1 become

$$\begin{aligned}\lim_{r\to1} b_m &= \lim_{r\to1}\frac{-k_m(\kappa e^{-\alpha h}-1)[e^{\alpha h}\cos(k_m h)-1]}{h[1-\kappa\cosh(\alpha h)](\alpha^2+k_m^2)}\\ &\quad + \lim_{r\to1}\frac{k_m(\kappa e^{\alpha h}-1)[e^{-\alpha h}\cos(k_m h)-1]}{h[1-\kappa\cosh(\alpha h)](\alpha^2+k_m^2)}.\end{aligned}$$

  Therefore, the generalised Fourier coefficients

$$b_m = \frac{(m\pi/2h)[e^{\alpha h}-1] - (m\pi/2h)[e^{-\alpha h}-1]}{h(\alpha^2+(m\pi/2h)^2)}.$$

- For $m \in 4\mathbb{N}-2$, the coefficients b_m (5.44) of the spectral expansion of the function 1 become

$$\begin{aligned}\lim_{r\to1} b_m &= \lim_{r\to1}\frac{k_m(\kappa e^{-\alpha h}+1)[e^{\alpha h}\cos(k_m h)-1]}{h[\kappa\cosh(\alpha h)+1)(\alpha^2+k_m^2)}\\ &\quad - \lim_{r\to1}\frac{k_m(\kappa e^{\alpha h}+1)[e^{-\alpha h}\cos(k_m h)-1]}{h[\kappa\cosh(\alpha h)+1)(\alpha^2+k_m^2)}.\end{aligned}$$

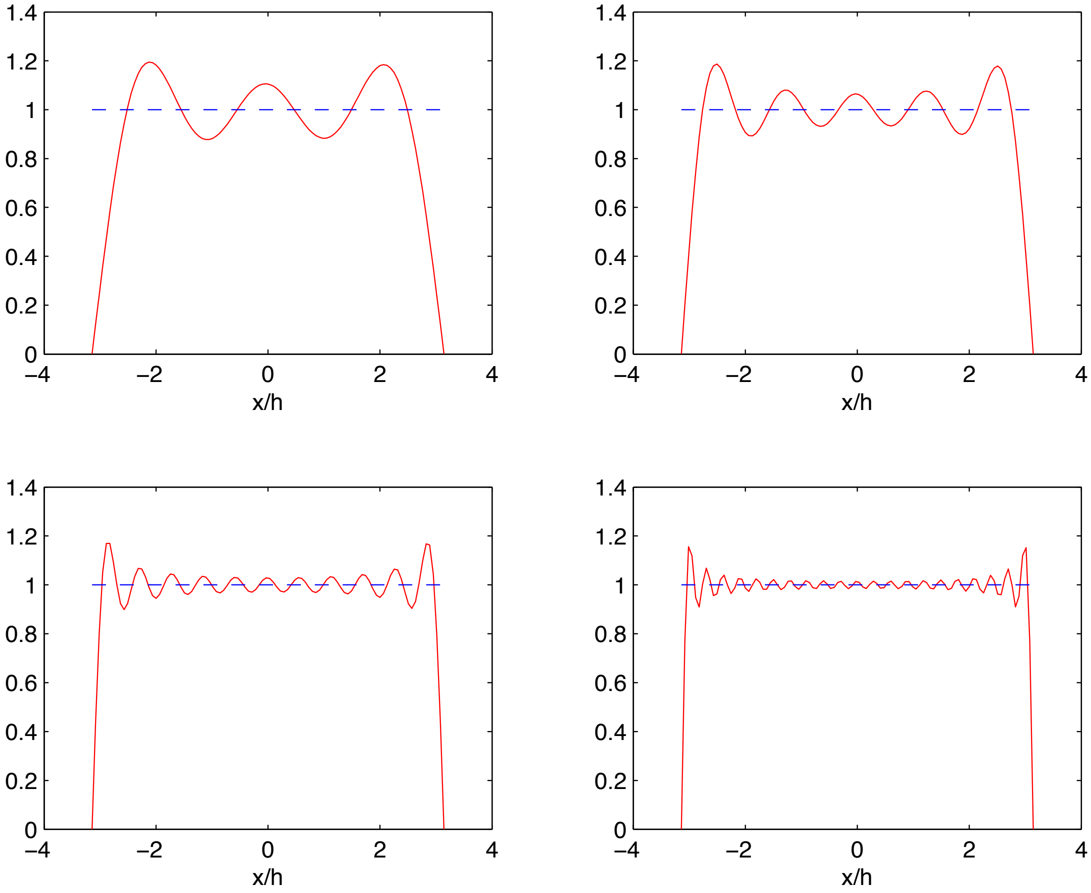

Figure 5.9: Generalised Fourier series approximations (5.18) of the function 1: plot the Nth partial sums for $N = 3, 5, 11$, and 21 eigenmodes, where the patch parameters are $H = \pi$, $r = 1$ and $V_0 = 0.1$. The mean absolute errors are $0.17, 0.12, 0.07$ and 0.04, respectively.

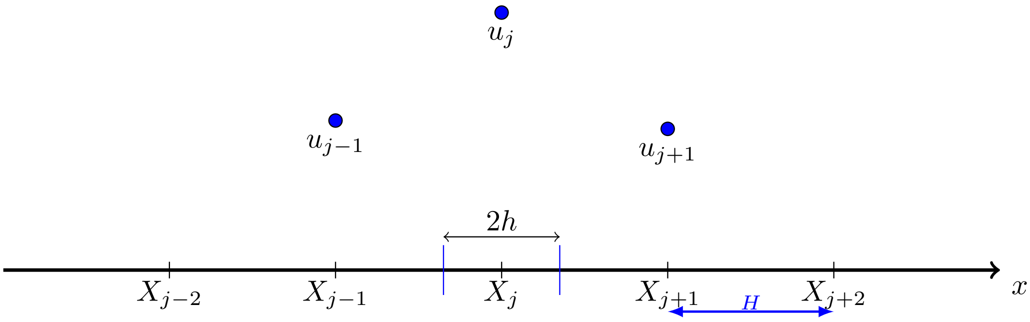

Figure 5.10: Schematic illustration of the macroscale grid of patches. Let each of N patches be centred on the macroscale grid points $Xj = jH$, inside a macroscale domain $[0, L]$.

Therefore, the generalised Fourier coefficients

$$b_m = \frac{(m\pi/2h)[-e^{\alpha h} - 1] - (m\pi/2h)[-e^{-\alpha h} - 1]}{h[\alpha^2 + (m\pi/2h)^2]}.$$

Figure 5.9 shows the generalised Fourier series (5.18) of the function 1 for the various partial sums, and in the case of patch ratio $r = 1$. With five terms, the partial sum already looks very similar to the function 1. Except for the Gibbs phenomenon, a very good approximation is obtained with 21 terms.

5.6 Multiple patches across the whole domain

An analytic microscale solution of the microscale advection-diffusion PDE is obtained in Section 5.5 by generalised eigenfunction expansion in one patch. This section extends the analysis to multiple patches. The macroscale model is based upon dividing the macroscale domain into small, spatially separated patches. The microscale model is solved within these patches, following analogues in one dimension (MacKenzie & Roberts 2006, Roberts 2003*b*, e.g.), neighbouring patches communicate with each other through coupling conditions with strength parametrised by γ.

For patch ratio $r = 1$, the patches overlap and the analysis reduces to that of holistic discretisation (Roberts 2003*b*, e.g.). Analogously, here we adapt the BCs for holistic discretisation (Roberts 2003*b*, e.g.) to the case of patch scheme $r < 1$, for the advection-diffusion PDE. In this scenario, Section 5.6.3 shows that centre manifold theory suggests there is a slow manifold in the system (Roberts 1988, Pötzsche & Rasmussen 2006, e.g.) that captures the macroscale dynamics.

5.6.1 The microscale simulator

This section describes the microscale simulator of the advection-diffusion dynamics in each patch. As shown schematically in Figure 5.10 we construct grid points X_j with spacing H, so that $X_j = jH$, where $H = L/N$ is the macroscale spacing and L is the length of the entire physical domain. The jth patch is centrered about the macroscale grid points, and with half width h. Define $u_j(x, t)$ to be the field u in the jth patch. The fields u_j evolve according to the advection-diffusion PDE (5.1); that is,

$$\frac{\partial u_j}{\partial t} + V_0 \frac{\partial u_j}{\partial x} = \frac{\partial^2 u_j}{\partial x^2}. \tag{5.51}$$

Then the fields u_j predict the original field $u(x, t)$, but only on the patches. Prediction of the evolution of the field u over the entire domain depends upon how the dynamics of each patch are coupled to its neighbours.

5.6.2 Coupling microscale patches across gaps

To solve PDEs (5.51) for microscale fields u_j within the jth patch requires boundary conditions at the edges of each patch. Such boundary conditions are obtained by interpolating macroscale information from neighbouring patches onto the edges for each of the microscale patch simulators. We need to define the macroscale grid value corresponding to the central region of each patch. As indicated in Figure 5.10 we define the macroscale grid values (amplitudes) as

$$U_j(t) = u_j(X_j, t), \quad \text{for } j = 0, 1, 2, \ldots, N, \tag{5.52}$$

which are used for interpolation between patches to provide boundary values for each microscale patch (Kevrekidis & Samaey 2009, Cao & Roberts 2013, e.g.).

Recall that Chapter 4 derived the macroscale interpolation (5.53) which couples the patches together for the diffusion equation. Here we adapt this coupling condition to couple the patches together for the advection-diffusion PDE. The values on the right and left edges of each patch, at $X_j \pm h$, are

$$\begin{aligned} u_j(\pm r,t) = \Big[& 1 \pm \gamma r\mu\delta + \frac{1}{2}\gamma\delta^2 r^2 \pm \frac{\gamma^2 r(r^2-1)}{6}\mu\delta^3 \\ & + \frac{\gamma^2 r^2(r^2-1)}{24}\delta^4 \pm \frac{\gamma^3 r(r^4-5r^2+4)}{120}\mu\delta^5 \\ & + \frac{\gamma^3 r^2(r^4-5r^2+4)}{720}\delta^6 \\ & \pm \frac{\gamma^4 r(r^6-14r^4+49r^2-36)}{5040}\mu\delta^7 \\ & + \frac{\gamma^4 r^2(r^6-14r^4+49r^2-36)}{40320}\delta^8 \\ & + \mathcal{O}(\delta^9)\,\Big]\,U_j(t). \end{aligned} \tag{5.53}$$

To apply the centre manifold theory, Roberts (2003*b*) implemented nonlocal decoupling conditions successfully through the introduction of the coupling strength γ such as

$$u_j(X_{j\pm1},t) = \gamma u_{j\pm1}(X_{j\pm1},t) + (1-\gamma)u_j(X_j,t),$$

which is used for coupling neighbouring overlapping elements. The physical problem of interest is at full coupling $\gamma = 1$. However, centre manifold theory provides full physical support for overlapping elements in a finite neighbourhood of $\gamma = 0$. The case $\gamma = 0$ is the no coupling case where each element has no influence on its neighbours. The tools and analysis in applying such coupling of overlapping elements appear to have analogues in other multiscale methods, such as the idea of border regions (introduced by Tamarkin (1928) and used in the heterogeneous multiscale method by E et al. (2007)), the concept of domain decomposition that improves the convergence of existing waveform relaxation methods (Abraham et al. 1998, Gander & Stuart 1998, e.g.), and the buffer regions of the gap-tooth scheme and patch dynamics (Samaey et al. 2005, 2006, e.g.).

The coupling strength γ is an artificial parameter which controls interactions and information flow between neighbouring patches. Such an artificial coupling is important for establishing theoretical support for multiscale dynamics. A more detailed discussion on the theoretical support for patch dynamics is given in some applications of such an artificial coupling (Roberts 2003*b*, Roberts & Kevrekidis 2007, Samaey et al. 2010, e.g.). For the unphysical case where $\gamma = 0$, each patch is completely isolated from its neighbours, dividing the entire domain into decoupled patches. For this case, all eigenvalues have negative real-parts except for one zero eigenvalue. Consequently, a slow manifold exists in the system, of dimension that equals the number of microscale patches. The relevance theorem of centre manifolds, (Vanderbauwhede 1989, p.128) or (Carr & Muncaster 1983, p.282), assures us that the evolution on the slow manifold captures the whole dynamics system on a cross-patch diffusion time. The leading eigenvalue, here $-V_0/4-\pi^2/r^2H^2$, is the estimate of the rate of attraction of the whole dynamics to the slow manifold.

5.6.3 Centre manifold theory supports multiscale models

This section determines a slow manifold (5.67) and its evolution (5.68), which are valid in the whole spatial domain for the microscale advection-diffusion PDE. This section finds that coupling conditions (5.53) lead to centre manifold theory (Carr & Muncaster 1983, Chicone & Latushkin 1997, Vanderbauwhede 1989, e.g.) supporting a slow manifold model for the advection-diffusion PDE (5.1) via its dynamics (5.51) within coupled patches. Figure 5.12, illustrates one example of the scale separation that underlies this modelling: the figure shows separation of modes into rapidly decaying modes and long lasting macroscale modes.

Space rescaling Since we consider the coupling strength γ is “small”, we rescale the patch dynamics system (5.51). Let ξ be a new microscale space variable restricted to the jth patch: $\xi=(x-X_j)/H$ in each patch as the subgrid scale variable instead of x. Thus, the advection-diffusion PDE (5.51) becomes

$$\frac{\partial u_j}{\partial t}+\frac{V_0}{H}\frac{\partial u_j}{\partial \xi}=\frac{1}{H^2}\frac{\partial^2 u_j}{\partial \xi^2}. \tag{5.54}$$

Equilibria Centre manifold theory is based on the information of the linearisation about equilibria. A family of equilibria of system (5.53)–(5.54) occurs by setting coupling parameter $\gamma=0$; then within each patch the advection-diffusion PDE (5.54) has equilibria of $u_j=$ constant. Further, this constant is independent in each of the N patches as each patch is completely decoupled from each other.

Linearisation Now we linearise the advection-diffusion PDE (5.54) about each equilibria to show the existence and emergence of a slow manifold. The spectrum of the linearised dynamics about each equilibria implies the existence of a slow manifold (Roberts 2003*b*). When the coupling parameter $\gamma=0$, then linearly, the dynamics in each patch determines that of the whole set of the patch. The dynamics of the PDE (5.54) with coupling conditions (5.53) with $\gamma = 0$ represent the dynamics within each patch isolated completely from its neighbours:

$$\frac{\partial u_j}{\partial t} + \frac{V_0}{H}\frac{\partial u_j}{\partial \xi} = \frac{1}{H^2}\frac{\partial^2 u_j}{\partial \xi^2}, \quad \text{such that} \quad u_j(\pm r, t) = U_j(t).$$

As all coefficients are constants, we seek solutions of the form $u_j \propto e^{\lambda t} v(\xi)$, for eigenvalue λ and eigenfunctions $v(\xi)$. Substituting and factoring out the exponential leads to the eigenvalue problem associated with each patch

$$\frac{1}{H^2}v'' - \frac{V_0}{H}v' - \lambda v = 0, \quad v(\pm r) = v(0), \tag{5.55}$$

where the prime denotes the derivatives with respect to ξ. We seek solutions $v \propto e^{z\xi}$ to find the characteristic equation

$$\frac{z^2}{H^2} - \frac{V_0}{H}z - \lambda = 0. \tag{5.56}$$

The roots of the above quadratic equation (5.56) are

$$z_{1,2} = \frac{H}{2}\left(V_0 \pm \sqrt{V_0^2 + 4\lambda}\right).$$

Two cases of eigenvalues λ are investigated in the following.

The case of real eigenvalue λ

Assume $\lambda \in \mathbb{R}$ so that $V_0^2 + 4\lambda < 0$. That is, the characteristic roots are $z_1 = \bar{z}_2 = \alpha + ik = \frac{H}{2}(V_0 + i\sqrt{-V_0^2 - 4\lambda})$, where, $\alpha = \frac{H}{2}V_0$ and $k = \frac{H}{2}\sqrt{-V_0^2 - 4\lambda}$. Thus, a general solution to the differential equation is

$$v(\xi) = e^{\alpha\xi}\left[c_1\cos(k\xi) + c_2\sin(k\xi)\right].$$

To satisfy the insulating[1] BCs in (5.55) we need to solve

$$\begin{bmatrix} e^{\alpha r}\cos(kr) - 1 & e^{\alpha r}\sin(kr) \\ e^{-\alpha r}\cos(kr) - 1 & -e^{-\alpha r}\sin(kr) \end{bmatrix}\begin{bmatrix} c_1 \\ c_2 \end{bmatrix} = \begin{bmatrix} 0 \\ 0 \end{bmatrix}.$$

The determinant of this system's matrix must be zero for non-trivial solutions:

$$-2\sin(kr)\left[\cos(kr) - \cosh(\alpha r)\right] = 0. \tag{5.57}$$

---

[1] When the coupling parameter $\gamma = 0$, the patches are uncoupled and the self-referential nature of the BCs result in a conserved mode.

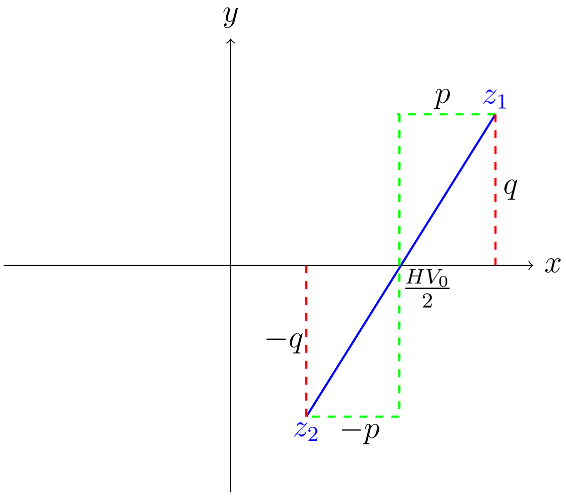

Figure 5.11: Illustration of the solutions $z_{1,2}$ for equation (5.56).

We determine the eigenvalues and the corresponding eigenfunctions from the characteristic equation (5.57). First, the factor $\sin(kr) = 0$ when microscale wavenumbers $k = \pi/r,\ 2\pi/r,\ 3\pi/r,\ \ldots$, therefore, the family of wavenumbers is $k_n = \frac{\pi n}{rH}$. That is, the microscale eigenvalues are $\lambda_n = -\frac{1}{4}V_0^2 - \left(\frac{\pi n}{rH}\right)^2$ with corresponding eigenfunctions $v_n(\xi) = e^{\alpha\xi}\sin(k_n\xi)$. There is also eigenvalue $\lambda_0 = 0$ corresponding to the equilibrium solution. The set of microscale eigenvalues of the linearised system is

$$S = \left\{0, -\frac{V_0^2}{4} - \frac{\pi^2}{(rH)^2}, -\frac{V_0^2}{4} - \frac{4\pi^2}{(rH)^2}, -\frac{V_0^2}{4} - \frac{9\pi^2}{(rH)^2}, \ldots\right\}.$$

Thus, in a spatial domain with N patches, evidently all eigenvalues of the microscale system are negative, $-V_0^2/4 - \pi^2/(rH)^2$ or less, except for one zero eigenvalue associated with each of the N patches. Centre manifold theory (Roberts 1988, Chicone 2006, Pötzsche & Rasmussen 2006, e.g.) then supports the existence of a slow manifold for (5.54) for non-zero coupling γ.

The general case of eigenvalues λ

In general, the eigenvalues $\lambda \notin \mathbb{R}$. Therefore, the roots of the quadratic equation (5.56) are

$$z_{1,2} = \frac{HV_0}{2} \pm (p + iq). \tag{5.58}$$

For the general case where the eigenvalues $\lambda \notin \mathbb{R}$, the complex roots (5.58) of the quadratic equation (5.56) is shown in Figure (5.11). A general solution to the eigenproblem associated with each patch ODE (5.55) is

$$v(\xi) = Ae^{(HV_0/2+p+iq)\xi} + Be^{(HV_0/2-p-iq)\xi}.$$

To satisfy the insulating BCs in (5.55) we need to solve

$$\begin{bmatrix} e^{(HV_0/2+p+iq)r} - 1 & e^{(HV_0/2-p-iq)r} - 1 \\ e^{(-HV_0/2-p-iq)r} - 1 & e^{(-HV_0/2+p+iq)r} - 1 \end{bmatrix} \begin{bmatrix} A \\ B \end{bmatrix} = \begin{bmatrix} 0 \\ 0 \end{bmatrix}.$$

This system has non-trivial solutions only when the determinant

$$\begin{aligned} &e^{2r(p+iq)} - e^{r(HV_0/2+p+iq)} - e^{r(-HV_0/2+p+iq)} \\ &- e^{-2r(p+iq)} + e^{r(-HV_0/2-p-iq)} + e^{r(HV_0/2-p-iq)} = 0. \end{aligned}$$

Simplifying the above expression by taking $e^{r(p+iq)}$ and $e^{-r(p+iq)}$ out as common factors

$$\begin{aligned} &[e^{2r(p+iq)} - e^{-2r(p+iq)}] - e^{r(p+iq)}[e^{rHV_0/2} + e^{-rHV_0/2}] \\ &+ e^{-r(p+iq)}[e^{rHV_0/2} + e^{-rHV_0/2}] = 0. \end{aligned}$$

A further simplification is to use the hyperbolic functions cosh and sinh :

$$\begin{aligned} &2\sinh\left[2(pr+iqr)\right] - e^{r(p+iq)}\left[2\cosh\left(\frac{rHV_0}{2}\right)\right] + e^{-r(p+iq)}\left[2\cosh\left(\frac{rHV_0}{2}\right)\right] = 0 \\ &4\sinh(pr+iqr)\cosh(pr+iqr) - 4\cosh\left(\frac{rHV_0}{2}\right)\sinh(pr+iqr) = 0 \\ &4\sinh(pr+iqr)\left[\cosh(pr+iqr) - \cosh\left(\frac{rHV_0}{2}\right)\right] = 0. \end{aligned} \tag{5.59}$$

From the characteristic equation (5.59), two cases arise to determine the decay rate of each mode associated with each patch:

- First, the factor $\sinh[r(p+iq)] = 0$ when the argument is purely imaginary so that $r(p+iq) = in\pi$, for $n = 1, 2, 3, 4, \ldots$. Therefore, implying the values of $p = 0$ and $q = \pi n/r$. That is, the microscale eigenvalues are

  $$\begin{aligned} \lambda_n &= \frac{(HV_0/2 \pm i\pi n/r)^2}{H^2} - \frac{V_0}{H}\left[\frac{HV_0}{2} \pm i\frac{\pi n}{r}\right] \\ &= -\frac{1}{4}V_0^2 - \left(\frac{\pi n}{rH}\right)^2, \quad n = 1, 2, 3, \ldots. \end{aligned}$$

  Thus, the set of microscale eigenvalues of the linearised system contains the subset

  $$S = \left\{-\frac{V_0^2}{4} - \frac{\pi^2}{(rH)^2}, -\frac{V_0^2}{4} - \frac{4\pi^2}{(rH)^2}, -\frac{V_0^2}{4} - \frac{9\pi^2}{(rH)^2}, \ldots\right\}. \tag{5.60}$$

- Second, the factor $\cosh(pr+iqr) = \cosh\left(\frac{rHV_0}{2}\right)$. In this case we expand the left-hand side using the compound angle formula and equate the real and imaginary parts, to get
$$\cosh(pr)\cos(qr) = \cosh\left(\frac{rHV_0}{2}\right), \tag{5.61}$$
and
$$\sinh(pr)\sin(qr) = 0. \tag{5.62}$$
Equation (5.62) implies either that $p = 0$ or that $q = n\pi/r$, where n is an integer.
    - First, the case when $p = 0$ in equation (5.61) leads to impossible situation
    $$\cos(qr) = \cosh\left(\frac{rHV_0}{2}\right) > 1.$$
    Therefore, the case when $p = 0$ is rejected.
    - Second, the case $q = \pi n/r$ where n is an integer in equation (5.61) leads to
    $$\cosh(pr)(-1)^n = \cosh\left(\frac{rHV_0}{2}\right).$$
    Since $\cosh\left(\frac{rHV_0}{2}\right) > 1$, then the odd values of n have to be eliminated. Hence, for n even we obtain $p = \pm\frac{HV_0}{2}$. Therefore, the microscale eigenvalues are
    $$\begin{aligned}\lambda_n &= \frac{[HV_0/2 \pm (\pm HV_0/2 + i\pi n/r)]^2}{H^2} - \frac{V_0}{H}\left[\frac{HV_0}{2} \pm \left(\pm\frac{HV_0}{2} + i\frac{\pi n}{r}\right)\right] \\ &= -\left(\frac{\pi n}{rH}\right)^2 \pm i\frac{\pi n}{rH}V_0, \quad \text{for } n = 0, 2, 4, \ldots.\end{aligned}$$
    That is, for all patches combined, but uncoupled, the spectrum contains the subset
    $$S = \left\{0, -\frac{4\pi^2}{r^2H^2} \pm i\frac{2\pi}{rH}V_0, -\frac{16\pi^2}{r^2H^2} \pm i\frac{4\pi}{rH}V_0, -\frac{36\pi^2}{r^2H^2} \pm i\frac{6\pi}{rH}V_0, \cdots\right\}. \tag{5.63}$$

In a domain with m patches, Figure 5.12 shows some complex pairs of eigenvalues with non-zero real-parts, while all other eigenvalues have negative real-parts. No eigenvalue within the patches has a large imaginary part unless it also has a relatively large negative real-part, and thus we expect that the transients decay rapidly through microscale dissipation. Also, all

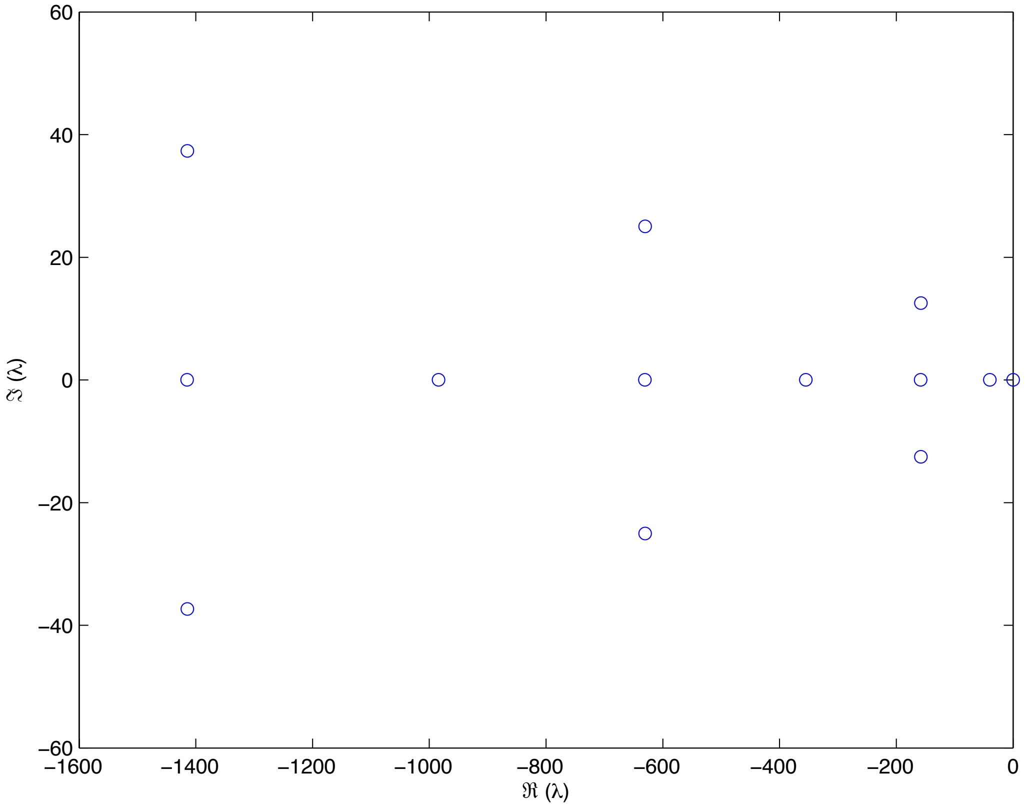

Figure 5.12: The numerical eigenvalues of the advection-diffusion PDE (5.54) in complex plane. The length scale ratio $r = 0.5$, and the macroscale spacing $H = 1$. Here advection speed in (5.54) is $V_0 = 1$. The eigenvalues show a clear separation of modes: microscale modes decay rapidly at rates faster than 39; whereas long lasting macroscale modes corespond to eigenvalue near zero.

other eigenvalues with large negative real-parts are all microscale sub-patch modes as they correspond to the dissipative modes within decoupled patches. Such rapid microscale sub-patch modes, and their decay are not of interest to the macroscale dynamics.

Evidently, from Figure 5.12 the structure of the spectrum of the linearised system (5.60) and (5.63) shows that there is one zero eigenvalue in (5.63) for $n = 0, \lambda_0 = 0$, and all the rest have negative $\Re(\lambda) \leq -\frac{\pi^2}{r^2H^2} < \beta < 0$. Based on the Existence and Emergence theorems (Carr 1981, chapter 1) and (Roberts 2014), we establish the existence and emergence of a slow manifold for the advection-diffusion PDE decay like $e^{-\beta t}$.

5.6.4 Computer algebra constructs the slow manifold

Analogous to Section 4.1.2, the slow manifold of (5.54) is parametrized both by the small parameters r, γ and by grid values $U_j(t) = u_j(X_j, t)$ that are used to measure the field in the jth patch. Define $\vec{U}$ to be the vector of such parameters, and seek a slow manifold

$$u_j = u_j(\xi; \vec{U}, \gamma, r), \tag{5.64}$$

such that evolution on the slow manifold is

$$dU_j/dt = \dot{U} = g_j(U_j, r). \tag{5.65}$$

The evolution $g \approx 0$ when we seek a slowly varying solution for system (5.54) in a neighbourhood of the piecewise constant equilibria.

Substituting the slow manifold ansatz (5.64) and (5.65) into system (5.51) we obtain

$$g_j = -\frac{V_0}{H}\frac{\partial u_j}{\partial \xi} + \frac{1}{H^2}\frac{\partial^2 u_j}{\partial \xi^2}. \tag{5.66}$$

Reduce computer algebra handles the algebraic details of the derivation of the slow manifold (5.64)–(5.65) by solving the PDE (5.66) with coupling (5.53) and amplitude conditions (5.52). The algorithm used to construct a slow manifold is an iteration based upon the residuals of the governing equations (Roberts 1997, e.g.). A successive approximation calculates a correction to reduce the residuals of the governing equation, the PDE (5.66), the BCS (5.53) and amplitude conditions (5.52). The iteration in the algebra is performed until the governing equations are satisfied; that is, all their residuals drive to zero to within a prespecified order of error. By the approximation theorems such as that by Carr & Muncaster (1983) or Roberts et al. (2011) we assuredly construct correspondingly appropriate approximations to the slow manifold of (5.52)–(5.54).

The order of errors in the construction

The order of errors in the slow manifold construction is phased in terms of the small parameters. The computer algebra of Algorithm 13 in Appendix B constructs the slow manifold for the advection-diffusion PDE to the error $\mathcal{O}(\gamma^2, V_0^3)$. We assume that the advection speed V_0 is small enough by truncating in powers of V_0 so that we treat the term $V_0\partial u/\partial x$ as a small perturbation. The construction predicts the microscale field in the patch as

$$\begin{aligned}u_j(\xi,t) \approx U_j &+ \frac{\gamma\xi}{2}(-U_{j-1}+U_{j+1}) + \frac{\gamma\xi^2}{2}(U_{j-1}-2U_j+U_{j+1})\\ &+ \frac{\gamma H V_0\xi(\xi^2-r^2)}{6}(U_{j-1}-2U_j+U_{j+1})\\ &+ \frac{\gamma H^2V_0^2\xi^2(\xi^2-r^2)}{24}(U_{j-1}-2U_j+U_{j+1}).\end{aligned} \tag{5.67}$$

The corresponding evolution of the grid values on the slow manifold is

$$\begin{aligned}\frac{dU_j}{dt} \approx &\frac{\gamma}{H^2}(U_{j-1}-2U_j+U_{j+1}) + \frac{\gamma V_0}{2H}(U_{j-1}-U_{j+1})\\ &+ \frac{\gamma r^2V_0^2}{12}(U_{j-1}-2U_j+U_{j+1}).\end{aligned} \tag{5.68}$$

By setting the coupling parameter $\gamma = 1$, the first two terms of the evolution (5.68) are standard finite difference approximations to advection-diffusion. The third term modifies the slow manifold by a diffusion which increases dissipation for finite V_0. This surprising result maintains stability for finite advection (Roberts 2014). Although the PDE is linear, the process of accurate modelling generates such a desirable term V_0^2 that is nonlinear in the coefficients of the equation.

5.7 Numerical validation of analytical computation of the eigenvalues

As an example, this section calculates the numerical eigenvalues of the eigenvalue problem associated with each patch (5.55) using finite differences. The numerically obtained eigenvalues are then compared with analytical microscale eigenvalues (5.60) and (5.63) within each patch. The good agreement between the numerical and analytical eigenvalues, as shown in Table 5.3, validates our analytical computation of the eigenvalues.

Finite differences

We are concerned with computing approximations by finite difference methods for the eigenvalues of eigenvalue problem (5.55). The intention is to represent the function by grid values $v_0, v_1, \ldots, v_m, v_{m+1}$ where v_j is our approximation to the solution $v(\xi_j)$ at the points of the domain ξ_j. We generate a finite set of microscale grids on the interval $[-r, r]$. The microscale grid spacing is $\xi_j = j\Delta\xi$. From the boundary conditions we know that $v_0^t(-r) = v(0)$

and $v^t_{m+1}(r) = v(0)$ and so we have m unknown values $v_1, v_2, \cdots, v_m$ to compute. The microscale simulator approximates equation (5.55) by central differences as

$$\frac{v^t_{j+1} - 2v^t_j + v^t_{j-1}}{\Delta\xi^2} - HV_0\frac{v^t_{j+1} - v^t_{j-1}}{2\Delta\xi} - H^2\lambda v^t_j = 0. \tag{5.69}$$

Equivalently, we write equations (5.69) as the finite dimensional eigenvalue problem

$$Mv = \lambda v,$$

where v is the m component vector $\begin{bmatrix} v_0 \\ v_1 \\ \vdots \\ v_{m-1} \\ v_m \end{bmatrix}$, and M the $m \times m$ matrix of finite differences.

Expand the system of algebraic equations (5.55), and collect common terms

$$\left(\frac{1}{\Delta x^2} - \frac{HV_0}{2\Delta x}\right) v^t_{j+1} + \left(\frac{-2}{\Delta x^2} - H^2\lambda\right) v^t_j + \left(\frac{1}{\Delta x^2} + \frac{HV_0}{2\Delta x}\right) v^t_{j-1} = 0. \tag{5.70}$$

For simplicity of notation, let $A = \frac{1}{\Delta x^2} - \frac{HV_0}{2\Delta x}$, $B = \frac{-2}{\Delta x^2}$, and $C = \frac{1}{\Delta x^2} + \frac{HV_0}{2\Delta x}$. A matrix form of the eigenvalue problem ODE (5.70) is

$$\begin{bmatrix} C & B & A & 0 & \cdots & 0 \\ 0 & C & B & A & 0 & \vdots \\ \vdots & \ddots & \ddots & \ddots & \ddots & \vdots \\ 0 & \cdots & 0 & C & B & A \end{bmatrix} \begin{bmatrix} v_0 \\ v_1 \\ \vdots \\ v_{m-1} \\ v_m \end{bmatrix} = H^2\lambda \begin{bmatrix} v_0 \\ v_1 \\ \vdots \\ v_{m-1} \\ v_m \end{bmatrix}.$$

There are various computer packages designed to solve such systems.

Form an implicit eigenproblem: Given a PDE for $u(x,t)$. Suppose we have coded a discretisation $d\vec u/dt = \vec f(\vec u)$ and found an equilibrium $\vec u^*$, which satisfies $\vec f(\vec u^*) = \vec 0$. We seek the dynamics of small perturbations away from equilibrium: seek $\vec u(t) = \vec u^* + \epsilon\vec v e^{\lambda t}$ for small ϵ. The discretisation then reduces to an eigenproblem $\lambda\vec v = M\vec v$. But instead of finding the matrix M, we invoke the procedure *eigs*() that uses just the product $A\vec v$, this product we get direct from the function $\vec f$ by evaluating $\vec f(\vec u^* + \epsilon\vec v)/\epsilon$ for some small ϵ, say 10^{-7}. Algorithm 7 implements this method for calculating the numerical

Algorithm 6 Compute the eigenvalues and eigenvectors of the coded discretisation of the ODE (5.55). Create two matrices, M and B, then solve the generalised eigenvalue problem for the eigenvalues and right eigenvectors of the pair (M, B). The patch parameters are $r = 0.5$, $H = 1$, and $V_0 = 1$.

```
%construct the matrix M and find the eigenvalues of
%advection diffusion.
N=161
r=0.5
x=linspace(-r,r,N);
dx=x(2)-x(1);
hh=1;
vv0=1;
a=1/dx^2+hh*vv0/(2*dx);
b=-2/dx^2;
c=1/dx^2-hh*vv0/(2*dx);
M=toeplitz([b,a,zeros(1,N-2)],[b,c,zeros(1,N-2)]);
c=(N+1)/2
M(1,:)=[-1 zeros(1,c-2) 1 zeros(1,c-1)];
M(N,:)=[zeros(1,c-1) 1 zeros(1,c-2) -1]
B=diag([0 ones(1,N-2) 0])
[v,e]=eig(M,B);
e=sort(diag(e));
e=e(1:10);
z1=(vv0/hh+sqrt(vv0^2/hh^2-4/hh^2*(-e)))/2*hh
z2=(vv0/hh-sqrt(vv0^2/hh^2-4/hh^2*(-e)))/2*hh
plot(real(z1), imag(z1),'*',real(z2), imag(z2),'+')
scatter(real([z1;z2]), imag([z1;z2]),N,abs([e;e]))
```

Algorithm 7 Compute the eigenvalues and eigenvectors of the coded discretisation of the ODE (5.55). The patch parameters are given by $r = 0.5$, $H = 1$, and $V_0 = 1$.

```
%Advection diffusion
% Compute spectrum of advection diffusion PDE with finite differences
global j x hh vv0
N=21
hh=1;
vv0=1;
r=0.5
x=linspace(-r,r,N)'
j=2:N-1
u0=zeros(size(x))
small=1e-7
fun=@(v) dudt(0,u0(j)+small*v)/small;
[v,d]=eigs(fun,N-2,N-2)
d=diag(d)'
v=[NaN(size(d)); v; NaN(size(d))];
subplot(2,1,1), plot(x,v(:,1:4))
legend(num2str(d(1:4)',3))
xlabel('space x'),ylabel('v(x)')
subplot(2,1,2), plot(x,v(:,end-4:end))
legend(num2str(d(end-4:end)',3))
xlabel('space x'),ylabel('v(x)')
%--------------------------------------------------
function ut=dudt(t,u)
global j x hh vv0
dx=x(2)-x(1); %  dx=diff(x(1:2))
c=(length(u)+1)/2;
u=[u(c);u;u(c)];
ut=(u(j-1)-2*u(j)+u(j+1))/dx^2-hh*vv0*(u(j+1)-u(j-1))/(2*dx);
```

Table 5.3: Numerical eigenvalues derived by Algorithm 6 for the macroscale wave modes from Figure 5.12, with patch parameters are given by $r = 0.5$, $H = 1$, and $V_0 = 1$, agree with exact eigenvalues (5.60) and (5.63). Absolute error is used to compare the quality of the approximation.

Numerical λ	Exact λ (5.60) and (5.63)	Absolute error
0	0	0
-39.72	-39.73	0.01
-158.1	-158.1	0.00
$-157.8 \pm 12.55i$	$-157.9 \pm 12.57i$	0.10
-355.1	-355.5	0.40
-630.6	-631.9	1.30
$-630.3 \pm 25.03i$	$-631.6 \pm 25.13i$	1.30
-984.0	-987.2	3.20
-1414.9	-1421.5	6.60
$-1414.7 \pm 37.35i$	$-1421.2 \pm 37.70i$	6.50
-1922.5	-1934.7	12.20
-2506.1	-2526.9	20.80
$-2505.9 \pm 49.44i$	$-2526.6 \pm 50.26i$	20.71
-3164.8	-3198.0	33.20
-3897.6	-3948.10	50.50
$-3897.4 \pm 61.22i$	$-3947.8 \pm 62.80i$	50.42

eigenvalue of the ODE (5.55) by invoking the MATLAB function *eigs*. Table 5.3 lists an example of the result of this Algorithm 7 which is consistent with the result of Algorithm 6. These results agree with the analytical results of deriving the macroscale eigenvalues as shown in Table 5.3.

5.8 Nonlinear reaction-diffusion equations

The spatial patch scheme is applied to linear partial differential equations in the previous chapters and earlier sections of this chapter. In this section, we analyse how the patch scheme behaves when applied to simulate systems that manifest themselves on the macroscale as nonlinear reaction-diffusion PDEs. This analysis of the nonlinear reaction-diffusion PDE provides insights that apply to other nonlinear systems.

Here we explore the patch dynamics scheme of the simplest non-trivial example in the class of nonlinear reaction-diffusion PDE

$$\frac{\partial u}{\partial t} = \frac{\partial^2 u}{\partial x^2} - u^3, \tag{5.71}$$

for some field $u(x,t)$ and some nonlinear reaction u^3. The reaction-diffusion PDE (5.71) is subject to the Dirichlet boundary conditions

$$u(-H,t) = a, \quad u(H,t) = b, \tag{5.72}$$

where a and b are constants. We analyse the dynamics of PDE (5.71) on one patch coupled to the domain boundary conditions (5.72) by patch coupling conditions (5.4). The linear analysis implies that the spectrum supports the existence of the slow manifold as discussed in Section 5.8.1. Section 5.8.2 then derives a non-trivial approximation of the slow manifold of the system. Following the method of holistic discretisation, introduced by Roberts (2003*a*), Section 5.8.3 analogously derives the slow manifold and the corresponding evolution of the system (5.71) with time-varying boundary forcing.

In Section 5.8.4, the nonlinear reaction-diffusion PDE with boundary conditions (5.72) is solved numerically by using method of lines. Then comparisons are made between the long-time dynamical behaviour of numerical solutions on one patch with the prediction of this slow manifold. For example, Figure 5.14 shows a slight difference between the two approaches as shown in Section 5.8.6.

Before we solve the nonlinear reaction-diffusion PDE (5.71) with the patch non-homogeneous coupling conditions (5.4), let us think about what could happen for the dynamics of the nonlinear reaction-diffusion PDE (5.71) on a small patch. Since we assume the patch is small, then the diffusion will rapidly smooth the field $u(x,t)$ across the small patch. Thus, the diffusion term is dominant in the microscale dynamics. Recall that h is the patch half-width, so the patch gets smaller as $h \to 0$. Therefore, the diffusive decay becomes increasingly more rapid. This is a singular perturbation problem. Roberts (2014), in his book, detailed how to avoid 'singular' perturbations by rescaling time. Analogously, here we address this case by rescaling the nonlinear reaction-diffusion PDE (5.71) to make it regular.

Time and space rescaling Let ξ and τ be the new microscale space-time variables. Since the patch size is proportional to the small h, we work on the scale of the patch by transforming (5.71) to the natural microscale space scaling $x = h\xi$, so that using the chain rule for the derivative of a function with respect to x

$$\frac{\partial}{\partial x} = \frac{\partial \xi}{\partial x}\frac{\partial}{\partial \xi} = \frac{1}{h}\frac{\partial}{\partial \xi}. \tag{5.73}$$

Since the time scale of cross-patch diffusion is proportional to h^2, we adopt the fast natural microscale time scale of $t = h^2\tau$ so that using the chain rule for the first derivative of a function with respect to t

$$\frac{\partial}{\partial t} = \frac{\partial \tau}{\partial x}\frac{\partial}{\partial \tau} = \frac{1}{h^2}\frac{\partial}{\partial \tau}. \tag{5.74}$$

Substituting (5.73) and (5.74) into (5.71) yields

$$\frac{1}{h^2}\frac{\partial u}{\partial \tau} = \frac{1}{h^2}\frac{\partial^2 u}{\partial \xi^2} - u^3. \tag{5.75}$$

Multiplying both sides of equation (5.75) by h^2 we obtain a new version of the nonlinear reaction-diffusion PDE

$$\frac{\partial u}{\partial \tau} = \frac{\partial^2 u}{\partial \xi^2} - r^2H^2u^3, \tag{5.76}$$

with the non-local boundary conditions

$$u(\pm 1,t) = u(0,t)\left(1 - r^2\right) + \frac{a}{2}\left(r^2 \mp r\right) + \frac{b}{2}\left(r^2 \pm r\right), \tag{5.77}$$

for the microscale field $u(\xi,\tau)$. On a small patch ratio r, we are about to establish the existence of the centre manifold for the reaction-diffusion PDE (5.71). The model predicts the emergent dynamics of the gap-tooth scheme. In order to construct a centre manifold model we identify the linearised dynamics about some equilibrium.

5.8.1 Existence of slow manifold and initial approximation

This section shows the existence of a slow manifold based upon the linear dynamics of the microscale system (5.76). The existence of a slow manifold is essential for finding the evolution on the slow manifold, which describes the large-scale dynamics of the microscale field u governed by equation (5.71).

Equilibrium and eigenspectrum

One set of equilibria in the microscale system (5.76)–(5.77) is the field $u =$ constant for $r = 0$. From the definition (5.3) the equilibria are parametrised by U as $u(\xi,\tau) = U$ and $r = 0$.

To linearise the microscale system (5.76)–(5.77) we substitute $u = U + \hat u(\xi,\tau)$ for small r and $\hat u$. Neglecting products of small quantities we obtain

$$\frac{\partial \hat u}{\partial \tau} = \frac{\partial^2 \hat u}{\partial \xi^2}, \quad \hat u(\pm 1,\tau) = \hat u(0,\tau). \tag{5.78}$$

Assuming a product solution of the form $\hat u \propto e^{\lambda\tau} v(\xi)$, equation (5.78) becomes the eigenvalue problem

$$\frac{d^2 v}{d\xi^2} - \lambda v = 0, \quad v(\pm 1) = v(0). \tag{5.79}$$

Observe that the eigenfunction has to be linear in ξ for the eigenvalue $\lambda = 0$. However, the boundary conditions in (5.79) force the eigenfunction $v(\xi)$ to be constant. Hence, an eigenvalue is $\lambda = 0$ and corresponding eigenfunction $v = 1$.

To solve the eigenvalue problem (5.79) in general we assume that $\lambda = -k^2 < 0$. Then a general solution to the differential equation (5.79) is

$$v(\xi) = c_1 \cos(k\xi) + c_2 \sin(k\xi),$$

where c_1 and c_2 are two constants, and k denotes a microscale wavenumber. Applying the patch homogeneous boundary conditions in (5.79) on the edges of the patch gives

$$c_1 \cos(k) \pm c_2 \sin(k) = c_1.$$

Forming as a pair of linear equations,

$$\begin{bmatrix} \cos(k) - 1 & \sin(k) \\ \cos(k) - 1 & -\sin(k) \end{bmatrix} \begin{bmatrix} c_1 \\ c_2 \end{bmatrix} = \begin{bmatrix} 0 \\ 0 \end{bmatrix}.$$

This system has non-trivial solutions only when the determinant

$$-2\sin(k)\,[\cos(k)-1]=0.$$

Two cases arise to satisfy this requirement.

- Either $\sin(k)=0$ whenever microscale wavenumbers $k=\pi,\ 2\pi,\ 3\pi,\ \ldots$, hence, the family of wavenumbers is $k_n=n\pi$ for $n=1,2,3,\ldots$. That is, microscale eigenvalues are $\lambda_n=-n^2\pi^2$ with corresponding eigenfunctions $v_n(\xi)=\sin(n\pi\xi)$.
- Or $\cos(k)-1=0$ when microscale wavenumbers $k=2\pi,\ 4\pi,\ 6\pi,\ \ldots$, hence, the family of wavenumbers is $k_n=n\pi$ for $n=2,4,6,\ldots$, with corresponding microscale eigenvalues $\lambda_n=-n^2\pi^2$ for even n. The corresponding eigenfunctions $v_n(\xi)=\cos(n\pi\xi)$. Observe that, for n even, there must be more than one eigenfunction since equation $\cos(k)-1=0$ has double root at $k=n\pi$. Generalised eigenfunctions occur for these eigenvalues.

Based upon the structure of this spectrum we identify the existence of a model. In a spatial domain, all eigenvalues of the linearised system on the patch is the set

$$S=\left\{0,-\pi^2,-4\pi^2,\cdots\right\}. \tag{5.80}$$

The spectrum of eigenvalues (5.80) of the linearised system is of one zero eigenvalue and all the rest have negative real-parts, $\lambda\leq-\pi^2$ or less. The theorem of the existence (Roberts 2014, e.g.), guarantees the existence of a slow manifold. The slow manifold is tangent to the field $u=$ constant and $r=0$; and it is local in the patch size r. Additionally, the slow manifold emerges on the microscale time $1/\pi^2$ which in the original time is emergence on the fast timescale r^2/π^2 as the slowest decay is $e^{-\lambda_1\tau}=e^{-\pi^2\tau}=e^{\pi^2t/r^2}$.

5.8.2 The first approximation of the slow manifold

The first non-trivial approximation of the slow manifold of the microscale reaction-diffusion PDE (5.76) is obtained by assuming that r is small, and seeking a microscale field in the form

$$u(\xi,\tau)=U+\hat{u}(\xi,U,r),$$

such that evolution on the slow manifold

$$\frac{dU}{d\tau}=\hat{g}(U,r).$$

For small $\hat{u}$ and $\hat{g}$, substitute this ansatz into system PDE (5.76)–(5.77), and omit products of small quantities to give

$$\hat{g} = \frac{\partial^2 \hat{u}}{\partial \xi^2} - r^2 H U^3, \tag{5.81}$$

with boundary conditions

$$\hat{u}(\pm 1) = \hat{u}(0) + \left(\frac{a}{2} + \frac{b}{2} - U\right) r^2 + \left(\mp\frac{a}{2} \pm \frac{b}{2}\right) r. \tag{5.82}$$

The first non-trivial approximation of the slow manifold of the microscale reaction-diffusion PDE (5.76) is determined from equation (5.81) and coupling boundary conditions (5.82). The amplitude definition

$$U = u(0,\tau), \quad \text{requires } \hat{u} = 0 \text{ at } \xi = 0. \tag{5.83}$$

Integrating equation (5.81) twice with respect to ξ gives the microscale field in the form

$$\hat{u} = \frac{\xi^2}{2}[\hat{g} + r^2 H^2 U^3] + c_1 \xi + c_2.$$

The constant of integration $c_2 = 0$ by the amplitude condition (5.83). By subtracting the two boundary conditions (5.82) we determine the constant of integration $c_1 = (-a+b)r/2$. Adding the two boundary conditions (5.82) leads to the evolution correction

$$\hat{g} = (a+b-2U)r^2 - H^2 U^3 r^2.$$

Therefore, the microscale field

$$u \approx U - \frac{\xi}{2}(a-b)r + \frac{\xi^2}{2}(a+b-2U)r^2,$$

such that

$$\frac{dU}{d\tau} \approx (a+b-2U)r^2 - H^2 U^3 r^2,$$

is the first non-trivial approximation to the slow manifold and the new evolution. For the macroscale variables, the microscale field $u \approx U - x(a-b)/(2H) + x^2(a+b-2U)/(2H^2)$, matches the interpolation from the distant BCs at $x = \pm H$ which are provided by the gap-tooth scheme. On the slow macroscale time, the evolution on slow manifold is corresponding $dU/dt \approx (a+b-2U)/H^2 - U^3$.

5.8.3 Varying boundary values with time

Analogous to the analysis of incorporating time-varying boundary forcing into the diffusion dynamics in Section 4.1.4, we investigate the effects of time-varying boundary forcing of the field $u(x,t)$ incorporated into the nonlinear reaction-diffusion PDE (5.76). The appropriate model contains time derivatives of $a(t)$ and $b(t)$.

Executing the computer algebra program of Algorithm 14 in Appendix B, adapted from (Roberts 2014, p.609), the slow manifold expressions of the solution field $u(x,t)$ is, in terms of $\xi = x/h$, and $\tau = t/h^2$,

$$\begin{aligned} u \approx U &+ r\left(\frac{b\xi}{2} - \frac{a\xi}{2}\right) + r^2\xi^2\left(-U + \frac{b}{2} + \frac{a}{2}\right) + r\left(\frac{\partial a}{\partial \tau} - \frac{\partial b}{\partial \tau}\right)\left(\frac{\xi}{12} - \frac{\xi^3}{12}\right) \\ &+ r^2\left(\frac{\partial b}{\partial \tau} + \frac{\partial a}{\partial \tau}\right)\left(-\frac{\xi^2}{24} + \frac{\xi^4}{24}\right) + r\left(\frac{\partial^2 b}{\partial \tau^2} - \frac{\partial^2 a}{\partial \tau^2}\right)\left(\frac{7\xi}{720} - \frac{\xi^3}{72} + \frac{\xi^5}{240}\right) \\ &+ r^2\left(\frac{\partial^2 b}{\partial \tau^2} + \frac{\partial^2 a}{\partial \tau^2}\right)\left(\frac{\xi^2}{480} - \frac{\xi^4}{288} + \frac{\xi^6}{720}\right). \end{aligned} \tag{5.84}$$

The time derivatives in this approximate slow manifold (5.84) are the rate of change, and it tells us how the field is changed with time-varying boundary values. The first three terms are the parabolic interpolation, modified by the first and second time derivative in other terms, which capture some sub-patch interactions between reaction and diffusion. The corresponding evolution on the slow manifold is

$$\frac{dU}{d\tau} \approx r^2\left(-2U - H^2U^3 + b + a - \frac{1}{12}\frac{\partial b}{\partial \tau} + \frac{1}{240}\frac{\partial b^2}{\partial \tau^2} - \frac{1}{12}\frac{\partial a}{\partial \tau} + \frac{1}{240}\frac{\partial a^2}{\partial \tau^2}\right). \tag{5.85}$$

The influnce of boundary value $a(\tau)$ in this evolution equation is approximately $a(\tau) - \frac{1}{12}\frac{\partial a(\tau)}{\partial \tau} \approx a(\tau - \frac{1}{12})$, and similarly for b. Thus, the time delay is $\tau - 1/12$. The time delay in term $b + a$ does affect the evolution due to the symmetry, unlike the difference between boundary values $b - a$, which does not affect the evolution on the slow manifold. This evolution on the slow manifold is able to capture the whole dynamics occurring on a time scale larger than $1/|\lambda_1| = 1/\pi^2$ (Bunder et al. 2013, Roberts 2003*b*, e.g.).

5.8.4 Method of lines

A numerical computation is one of the effective ways to investigate many hard problems, and a successful numerical study can discover the mathematical theory behind the phenomena (Presmeg 2006). This section implements the method of lines to solve numerically the nonlinear reaction-diffusion PDE (5.71) with the following boundary conditions

$$u(-H,t)=a=0,\quad u(H,t)=b=0.5\sin(2t). \tag{5.86}$$

We use the method of lines because it is effective with respect to accuracy and computational time (Sadiku & Obiozor 2000). The basic idea of implementing the method of lines for solving the nonlinear reaction-diffusion PDE (5.71) with boundary conditions (5.86) in one spatial dimension is to discretise in x and integrating in time as a set of ODE (this method is also referred to as a semi-discrete approximation (Foias et al. 1991, Foias & Titi 1991, e.g.)). It is possible to use a stiff ODE routine on the time derivatives in the resulting system.

Let us discretise the domain in space as $x_j=j\Delta x$. We replace the second derivative with respect to x with its finite difference equivalent, the scheme becomes

$$\frac{du_j^t}{dt}=\frac{u_{j+1}^t-2u_j^t+u_{j-1}^t}{\Delta x^2}-(u_j^t)^3, \tag{5.87}$$

with boundary conditions (5.86). The initial conditions $u_j^0=f(x_j)$ for each $j=1,2,\ldots,N-1$.

- At $j=1\Rightarrow$
$$\frac{du_1^t}{dt}=\frac{u_2^t-2u_1^t+u_0^t}{\Delta x^2}-(u_1^t)^3.$$
- At $j=2\Rightarrow$
$$\frac{du_2^t}{dt}=\frac{u_3^t-2u_2^t+u_1^t}{\Delta x^2}-(u_1^t)^3.$$
- At $j=N-1\Rightarrow$
$$\frac{du_{N-1}^t}{dt}=\frac{u_N^t-2u_{N-1}^t+u_{N-2}^t}{\Delta x^2}-(u_{N-1}^t)^3.$$

Therefore, the discrete reaction-diffusion PDE (5.87) is

$$\frac{d\vec u}{dt}=\frac{A}{\Delta x^2}\begin{bmatrix}a\\ \vec u\\ b\end{bmatrix}-\vec u^3,$$

where A is an $N-1\times N+1$ tridiagonal matrix representing the discretised form of the second derivative with respect to x. A matrix form of the discrete reaction-diffusion PDE (5.87) is

$$\frac{d\vec{u}}{dt} = \frac{1}{\Delta x^2}\begin{bmatrix} 1 & -2 & 1 & 0 & \cdots & 0 \\ 0 & 1 & -2 & 1 & \ddots & \vdots \\ \vdots & \ddots & \ddots & \ddots & \ddots & \vdots \\ 0 & \cdots & 0 & 1 & -2 & 1 \end{bmatrix}\begin{bmatrix} a \\ u_1 \\ \vdots \\ u_{N-1} \\ b \end{bmatrix} - \begin{bmatrix} u_1^3 \\ u_2^3 \\ u_3^3 \\ \vdots \\ u_{N-1}^3 \end{bmatrix}.$$

Algorithm 8 numerically solves for $\vec{u}(t)$ using MATLAB's `ode15s` routine.

Algorithm 8 Matlab numerically solve the reaction diffusion equation PDE (5.71) with boundary conditions (5.86) using method of lines.

```
% using the method of lines to solve the reaction diffusion
% equation u_t = u_xx-u^3
N=20 % no of grid points Xn
x=linspace(-1,1,N+1)
dx=diff(x(1:2)) % grid spacing in x direction
freq=2;
tspan = linspace(0,12/freq,21);% Defining time interval for solution
u0 = randn(size(x))/3; % initial condition
%Vary BCs
a=0;
b=@(t) 0.5*sin(freq*t);
% construct the matrix A
A=toeplitz([1 zeros(1,N-2)],[1 -2 1 zeros(1,N-2)]);
E = @(t,u) 1/dx^2*A*[a;u;b(t)]-u.^3;
[t,u] = ode15s(E, tspan, u0(2:end-1)) % calling function to solve ode
u1=[a*ones(size(t)) u b(t)];
```

5.8.5 Comparison of the long time behaviour

This section compares the numerical solutions of the nonlinear reaction-diffusion PDE in the previous Section 5.8.4 with predictions of the centre manifold theory (5.84)–(5.85).

The slow manifold evolution (5.85), upon restoring the original time $t = h^2\tau$, is

$$\frac{dU}{dt} \approx \frac{1}{H^2}\left(-2U - H^2U^3 + b + a - \frac{h^2}{12}\frac{\partial b}{\partial t} + \frac{h^4}{240}\frac{\partial^2 b}{\partial t^2} - \frac{h^2}{12}\frac{\partial a}{\partial t} + \frac{h^4}{240}\frac{\partial^2 a}{\partial t^2}\right). \tag{5.88}$$

To compare the long time behaviour, Algorithm 9 finds numerical solution to the slow manifold evolution (5.88) by using MATLAB's `ode15s` solver.

Algorithm 9 Matlab numerically solve the slow manifold evolution equation PDE (5.88) with boundary conditions (5.86).

```
% APPROXIMATION OF CENTER MINFOLD with vary BCs
N=20;
hh=1;
r=0.5;
h=r*hh;
x=linspace(-1,1,N+1)
% initial condition
y0 = randn(size(x))/3;
%u0=sum(y0)*dx/2
u0 = y0(N+1)/2;
%u0=10;% initial condition
a=0;
b=@(t) 0.5*sin(freq*t);
b1 = @(t) freq*0.5*cos(freq*t);% first derivative of (b)
b2 = @(t) -freq^2*0.5*sin(freq*t);% second derivative of (b)
f = @(t,uu) -2*uu/hh^2-uu.^3+b(t)/hh^2+a/hh^2 ...
 -r^2*b1(t)/(12)+r^2*h^2*b2(t)/(240);
g = @(t,uu) 1/hh^2*( -2*uu-hh^2*uu.^3+b(t)+a ...
-h^2*b1(t)/12+h^4*b2(t)/240 );
[t,uu] = ode15s(g, tspan, u0)
% the microscale field with Vary boundary with time
xi=x/h;
uc=uu*ones(size(x)) ...
+r/2*b(t)*xi ...
+r^2*(-uu +b(t)/2)*xi.^2 ...
+b1(t)*h^2*r*(-xi+xi.^3)/12 ...
+b1(t)*h^2*r^2*(-xi.^2+xi.^4)/24 ...
+b2(t)*h^4*r*(7/720*xi -1/72*xi.^3+1/240*xi.^5) ...
+b2(t)*h^4*r^2*(1/480*xi.^2-1/288*xi.^4+1/720*xi.^6);
```

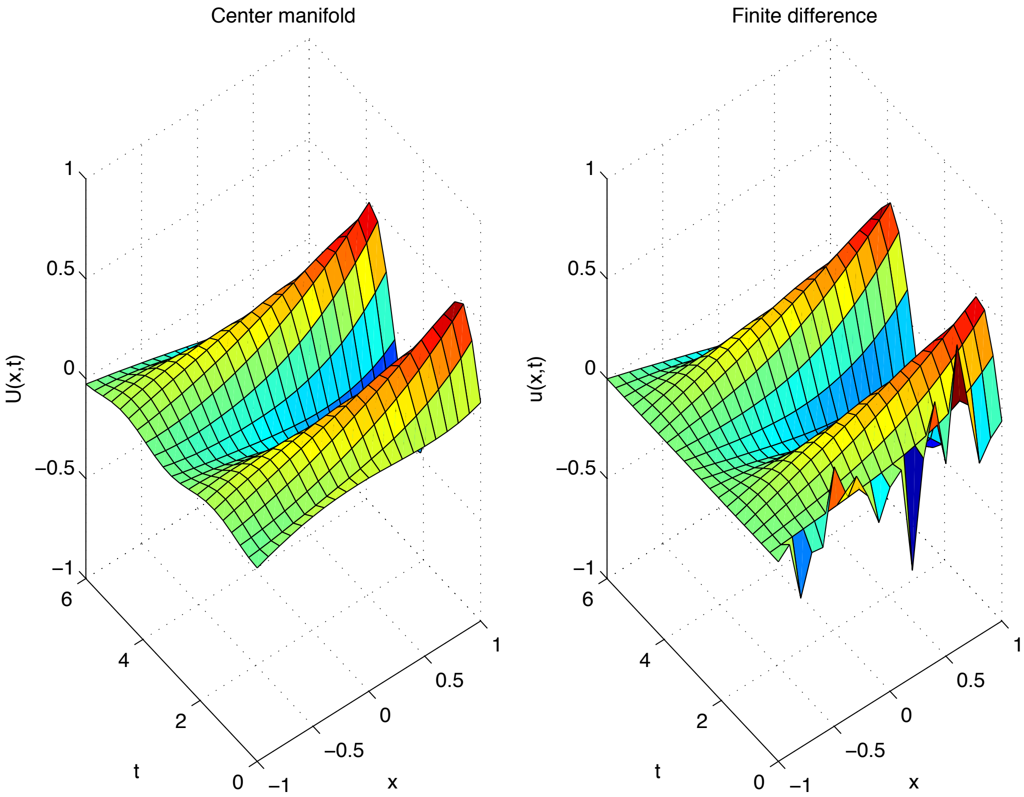

Figure 5.13: A space time simulation for a field $u(x,t)$ of the nonlinear microscale reaction-diffusion PDE on one single patch where $r = 0.5$ and $H = 1$. (Left) slow manifold predictions for long-term behaviour of the dynamics system; (right) the solution to the nonlinear reaction-diffusion PDE (5.71) using the method of lines, with random initial conditions.

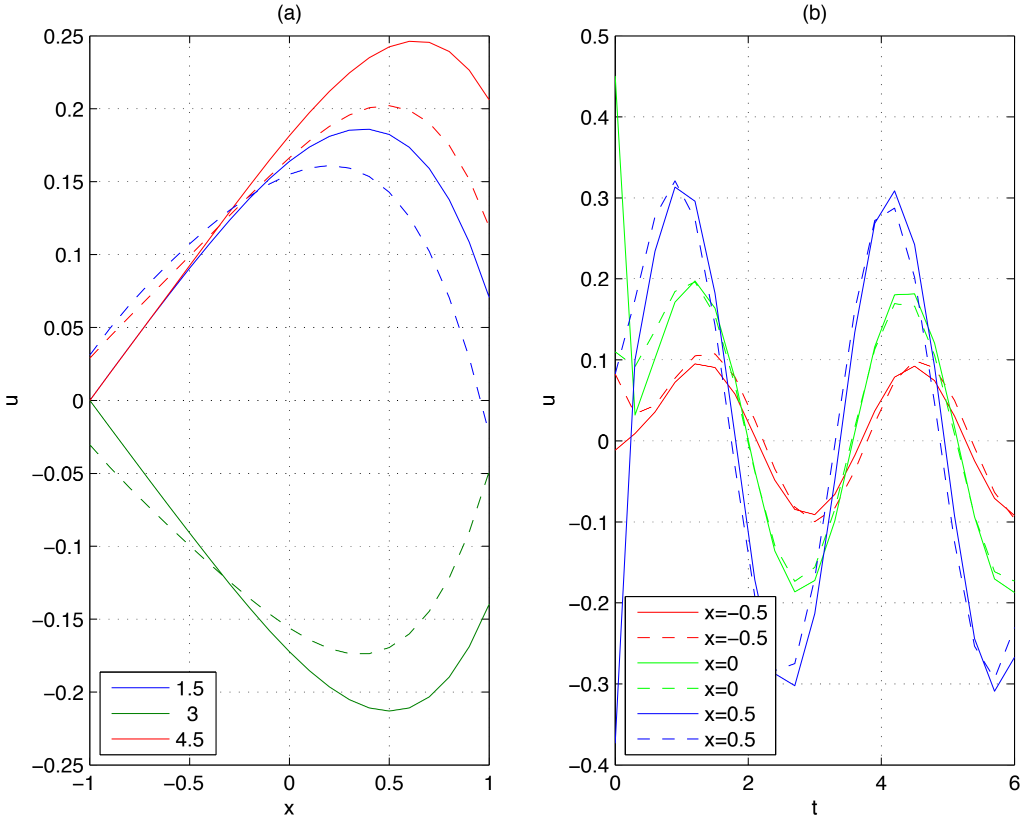

Figure 5.14: A space time simulation for a field $u(x,t)$ of the nonlinear microscale reaction-diffusion PDE on one single patch where $r = 0.5$ and $H = 1$: left, is the approximations of the slow manifold (dashed curves) and the method of lines approximations (solid curves), plotted against space, for $t = 1.3$, $t = 3$ and $t = 4.5$; right, the approximations of the slow manifold (dashed curve) and the method of lines approximations (solid curves), plotted against space, for $x = \pm 0.5$ and $x = 0$.

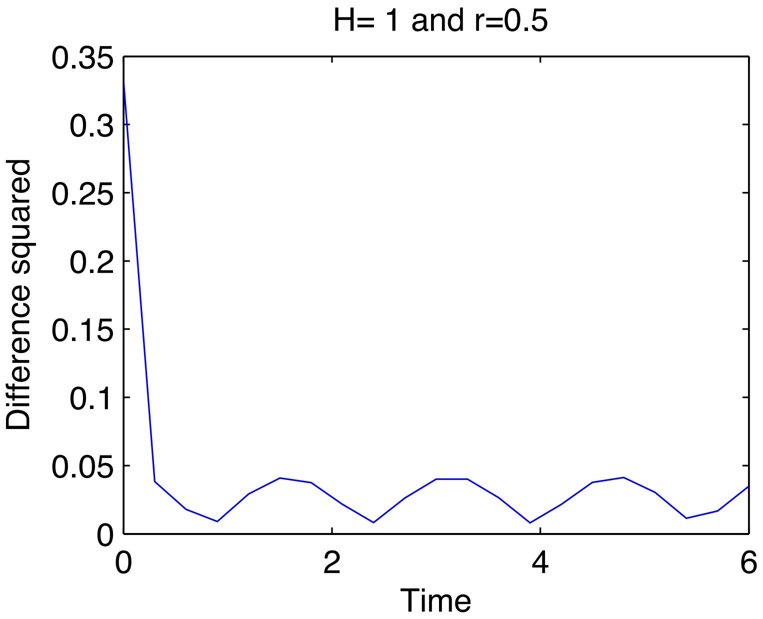

Figure 5.15: Root-mean-square difference (RMSD) of Figure 5.14. In the short-term the error decays quickly due to initial transients. Observe that RMSD fluctuates over time but remains at 0.1.

Figure 5.13 compares numerical solutions of the nonlinear reaction-diffusion PDE by the method of lines with predictions of long dynamics behaviour of the centre manifold theory. The slow manifold shows a good qualitative agreement with the solution to the nonlinear reaction-diffusion dynamics on one patch. The finite difference plot also exhibits some small amplitude noise at $x = 0$ which is due to the random initial conditions used for that method. Figure 5.14 shows that there is reasonable agreement between the quantitative properties of these predictions.

5.8.6 Evaluation of quantitative error

Measurement errors and uncertainties exist in any quantitative experiment. By improving techniques and methods, we could reduce such errors and uncertainties but they can never be completely eliminated. The assessment of the reliability of results is an important part of any quantitative experiment (Hughes & Hase 2010). This assessment involves identifying and understanding the source of errors in order to quantify the reliability and accuracy of the results.

Figure 5.14 shows a slight difference between the prediction of centre manifold and method of lines. The difference is quantified by calculating the root mean squared difference RMSD. For simplicity, let U denote the prediction of slow manifold where we define earlier $U(t) = u(0, t)$. Define

$$\text{RMSD} = \sqrt{\frac{1}{N}\sum_{j=1}^{N}(uc_j - ul_j)^2},$$

where uc_j and ul_j represent the solution of the slow manifold and method of lines, for $-1 < x < 1$, for the nonlinear reaction-diffusion PDE over $0 < t < 6$. We discretise the domain in space as $xj = j\Delta x$, for $j = 0, 1, 2, \ldots, 20$, and for some grid spacing Δx. Figure 5.15 shows an exponential decay in the short-term and small oscillatory errors in the long-term.

5.9 Conclusion

The analysis presented throughout Chapters 3 and 4 is extended in this chapter to analyse one-dimensional microscale advection-diffusion dynamics for both a single patch and for multiple patches. The microscale model is first solved within one patch, using the eigenfunction expansions which are given in terms of the biorthogonal basis. The biorthogonal basis consists of two sets of eigenfunctions which originate from the operator and its adjoint. With the aid of the biorthogonal basis, the spectral coefficients are determined.

This chapter then extends the analysis to multiple patches applied to a one-dimensional advection-diffusion equation. We extend the model of Roberts (2003*b*) on overlapping elements to the case of patches separated by gaps. The patch coupling conditions that were found in Chapter 3 are adapted in this chapter to couple the discrete patches across space. Section 5.6.3 determines all eigenvalues of the linear dynamics associated with each patch which indicates the existence of a centre manifold. In particular, Figure 5.12 shows the clear separation between the dynamics of the macroscale modes of interest, and the microscale modes within each patch. The computer algebra of Algorithm 13 then constructs the slow manifold of the system.

Section 5.8 applies the patch dynamics scheme to the nonlinear reaction-diffusion equation. The eigenvalue analysis in Section 5.8.1 supports the existence of the slow manifold. Section 5.8.2 then derives a non-trivial approximation of the slow manifold of the system. This is followed in Section 5.8.3 by deriving the slow manifold and the corresponding evolution of the system with time-varying boundary forcing. In Section 5.8.4, the nonlinear reaction-diffusion PDE with boundary conditions (5.72) is solved numerically by using method of lines. Then comparisons are made between the long-time dynamical behaviour of numerical solutions on one patch with the prediction of this slow manifold. Future work could extend the analysis of such patch scheme to spatial dimensions higher than one spatial dimension.

Chapter 6

Conclusion

This dissertation achieves two aims: first, Chapter 2 develops a patch dynamics scheme that uses only a given microscale periodic simulator, such as molecular dynamics, to predict emergent macroscale properties over large space scales; and second, Chapters 3–5 explore patch dynamics behaviour where the microscale is governed by a partial differential equation. Section 6.1 summarises the results of the first goal and Section 6.2 concludes with a summary of the main contributions of the second goal. Then, Section 6.3 gives some directions for future research.

6.1 Summary of the periodic atomistic patch simulations

The first aim of the dissertation is to develop a patch dynamics scheme that uses only a given microscale periodic simulator, such as molecular dynamics, to effectively predict macroscale behaviour over large space scales. As a pilot study of a controlled periodic patch scheme, our novel method further develops the equation-free patch dynamics scheme (Hyman 2005, Li et al. 2007, Frederix et al. 2007, Bunder & Roberts 2012, e.g.) to empower atomistic patch simulations of the system of particular interest over large spatial dimensions from a given microscopic simulator. We emphasise that the main contribution is in establishing the mathematical basis for a novel design of the equation-free scheme incorporating patches with macroscale periodic boundaries that are not reflecting of the macroscale geometry.

Chapter 2 invokes one microscale, detailed, atomistic patch in a triply-periodic cubic domain. Our innovation is to couple such a small patch over unsimulated space: the coupling mechanism has to differ from that used in patch schemes to date (Liu et al. 2015, e.g.). Analysis of atomistic simulations is based upon just one small patch divided into four equal-sized regions. Section 2.3.1 describes our implementation of a proportional controller over the action regions to couple such a triply-periodic patch to its neighbours over unsimulated space. Algebraic analysis and the determination of eigenvalues in Section 2.4 confirm that the proposed controlled coupling of the periodic patch was effective for atomistic simulations, and for a control roughly as predicted by the analysis. Numerical simulations (Section 2.3.2) of the heat diffusion PDEs were successfully implemented by such a proposed controlled patch scheme. Results (Figure 2.7) show that the developed patch dynamics scheme can quite well model the heat diffusion PDEs. Section 2.5 establishes the spectral gap of the patch system, and shows the slow emergent macroscale dynamics. Section 2.5.2 then approximates the macroscale prioritised eigenvalue that characterises such emergent macroscale dynamics. Based on the approximation of this prioritised eigenvalue, Section 2.5.3 determines good values for the strength of the proportional controller as a function of the patch ratio r. An interesting finding presented in Section 2.6 when the diffusivity was estimated, using a technique similar to homogenisation, to determine the best control for the simulation.

6.2 Summary of analysed patch dynamics scheme for different classes of pdes

The second goal of the dissertation is to analyse whether small spatial patches, such as those with patch ratios $r \ll 1$, are able to predict the coupled macroscale behaviour when the transport phenomena at the given microscopic equation is governed by a partial differential equation.

Chapter 3 invokes one patch in one spatial dimension for diffusion problems with forcing boundary conditions. The solution behaviour of the patch scheme under time-varying boundary conditions is analysed. We show that there are two classes of eigenfunctions: symmetric and asymmetric within the patch. It is found that the spectral problem associated with a small patch is a non-self-adjoint problem. To be able to find spectral expansions, Section 3.4 finds eigenfunctions of the adjoint operator. Then the eigenfunctions of an operator with those of its adjoint form biorthogonal sets, and the spectral coefficients in the eigenfunction expansion are found using the eigenfunctions of the adjoint problem. After obtaining these expansions, Section 3.5.2 predicts the microscale field in the patch, for small patch ratio $r = 0.1$, and then compares such predictions with the field on the complete domain.

Chapter 4 extends the analysis to involve many small patches distributed over the domain. The coupling conditions (4.23) with strength parametrised by γ effectively bridge the gaps between the patches in the spatial domain. Each patch notionally mimics the local evolution of the microscopic model as if it were embedded in a larger domain. The artificial small parameter γ is introduced to establish the slow manifold. However, relatively high orders of the artificial parameter are required so that evaluating at full coupling γ is accurate and presents the physical problem of interest. When the artificial parameter $\gamma = 0$, the patches are uncoupled by the effectively insulating boundary conditions between them. The eigenvalue analysis together with the centre manifold theory in Section 4.1.2 indicate the existence of a slow manifold. Computer algebra is used in Section 4.1.3 to construct a model (4.35) to confirm the diffusion dynamics.

Chapter 5 extends the analysis in Chapters 3 and 4 to the case of advection-diffusion problems. In the first part of this chapter, the microscale advection-diffusion system in a single patch is analysed so that the macroscale dynamics over a comparatively large spatial region can be predicted. The second part of this chapter analyses the microscale advection-diffusion system for multiple patches. We extend the model of Roberts (2003*b*) on overlapping elements to the case of patches separated by gaps. For patch ratio $r = 1$, the patches overlap and the analysis reduces to that of holistic discretisation (Roberts 2003*b*, e.g.). Analogously, we adapt the BCs for holistic discretisation (Roberts 2003*b*, e.g.) to the case of patch scheme $r < 1$, for the advection-diffusion PDE. Each patch captures the local evolution of the microscopic model. The algebraic analysis and numerical determination of eigenvalues in Section 5.6.3 indicate the existence of a slow manifold. In particular, Figure 5.12 shows the clear separation between the dynamics of the macroscale modes of interest, and the microscale modes within each patch.

Section 5.8 applies the patch dynamics scheme to a simple scenario involving nonlinear reaction-diffusion. The eigenvalue analysis in Section 5.8.1 supports the existence of the slow manifold. Section 5.8.2 then derives a non-trivial approximation of the slow manifold of the system. Following this, Section 5.8.3 derives the slow manifold and the corresponding evolution for the system with time-varying boundary forcing. In Section 5.8.4, the nonlinear reaction-diffusion PDE with boundary conditions (5.72) is solved numerically by using method of lines. Then comparisons are made between the long-time dynamical behaviour of numerical solutions on one patch with the prediction of this slow manifold.

6.3 Future directions

This section highlights the possible future directions based on the work in this dissertation.

In Chapter 2, we develop the patch dynamics scheme for large atomistic simulations. Further research could investigate some important issues concerning the optimal core and action region sizes, optimal weight functions for the averages in the regions, and refining the interpolation that couples the patches. Section 2.3.1 implements a proportional controller (Bechhoefer 2005, e.g.) to couple the patch to the surrounding macroscale variations. In future developments, one could explore proportional-integral and proportional-integral-derivative controllers with the aid of projective integration in time (Gear & Kevrekidis 2003, Kevrekidis & Samaey 2009, e.g.).

Although Chapter 2 focuses on the macroscale temperature diffusion emerging from an atomistic simulation, the equation-free patch scheme does usefully apply to wave systems (Cao & Roberts 2013, 2016) and so we expect that controlled periodic-patches should also be able to reasonably predict the emergent density-momentum waves of an atomistic simulation.

In computational non-Newtonian fluid dynamics, the local stresses are determined by using a model constitutive equation. However, there are some difficulties in applying computational fluid dynamics methods, which require the constitutive equation of the complicated flow problems, especially for dense polymeric liquids. These difficulties are due to the unknown constitutive relation. Nevertheless, the rheological properties of such materials could be investigated using microscopic simulations such as molecular dynamics simulations. Microscopic simulations are often used for extremely small material. For large scale and long time fluid motion, there are also difficulties in applying microscopic simulations due to the enormous computation time needed. In this scenario we could apply a patch dynamics scheme to a polymeric liquid to describe the flow behaviour of such complex fluids.

Chapter 3 derives the patch coupling conditions in (3.10) which do not form a self-adjoint Sturm–Liouville system. Further research could find efficient coupling between the patches that preserves self-adjointness and also predicts the correct macroscale behaviour. Section 3.6 proposes a modified patch dynamics scheme with time-delayed communications. One future study could adapt the delayed patch scheme for massive parallelisation where each processor simulates the macroscale properties on a few patches. One could research how to tackle slow data transfer speeds compared to processor speeds. One could also find patch coupling conditions that involve some time delay, so that some delay in data transfer is accounted for in the algorithm.

The analysis in Chapters 3–5 concentrates on issues associated with spatial coupling on a one-dimensional domain. Further work could analyse and implement efficient time simulations to empower future simulations to faithfully model microscale dynamics.

Appendix A

Ancillary material

A.1 Code for 3D atom simulation

This ancillary material provides the numerical code for simulating a microscale patch of atoms coupled over macroscale empty space to boundary values of temperature. It is included to document and potentially reproduce the results.

A.1.1 Main driver code

```
% coded 3d simulation of position and velocity of
% interacting atoms.  Uses ode23 to do time integration.
global ll mucontrol TL TR ii nfns nAux hh Khsq
nAtom=343  % number of atoms
tEnd=30 % end time of simulation
ll=nAtom.^(1/3);   % length of periodic patch (inter-atom eq is at one)
%mucontrol=34.673; % zero is no control
mucontrol=0; % zero is no control
TL=0.5, TR=1.5 % macroscale boundary values of temp
hh=ll  % macroscale BCs applied at +/-hh
rng('shuffle'); seed=100+floor(900*rand); %random realisation seed
fileroot=['ctrlpatch' num2str(seed) 'N' num2str(nAtom)]
nAux=12; % number of auxillary variables computed
Khsq=1; % coefficien of control
rng(seed);
% distribute atoms, randomly up to one per box
ns=ceil(ll);
i=linspace(-0.5,0.5,2*ns+1);
```

```
[j,i,p]=meshgrid(ll*i(2:2:end));
[~,k]=sort(rand(size(i(:)))); [tmp,k]=sort(rand(size(i(:))));
xq=[i(k(1:nAtom)) j(k(1:nAtom)) p(k(1:nAtom)) zeros(nAtom,3)]';
% add smallish, mean-zero, random position and velocity
zz=rand(6,nAtom)-0.5; zz=zz-repmat(mean(zz,2),1,nAtom);
xq=xq+0.32*diag([1,1,1,3,3,3])*zz; xq=xq(:);
%xq=xq+0.1*diag([1,1,1,2,2,2])*zz; xq=xq(:);

% for imposing triple periodicity in space
ii=1:6:6*nAtom; ii=[ii ii+1 ii+2]+nAux;
% simulation in time from given ICs
nfns=0;
[ts,Txqs]=ode23(@hctrlhddtu3dode,[0 tEnd],[zeros(nAux,1);xq]);
% impose periodicity on the computed positions
xqs=Txqs(:,nAux+1:end);  ii=ii-nAux;
xqs(:,ii)=xqs(:,ii)-round(xqs(:,ii)/ll)*ll;
% auxillary quantities at middle of time steps
Tuvws=diff(Txqs(:,1:nAux))./repmat(diff(ts),1,nAux);
tsx=(ts(1:end-1)+ts(2:end))/2;
nFunctions=nfns
hctrlgraphs % draw graphical output
```

A.1.2 Interpose periodicity on positions

This function avoids MATLAB's `ode23` objecting to discontinuities as atoms move across edges of the periodic box.

```
function dxq=hctrlhddtu3dode(t,xq)
% Computes time derivative of position and velocity of
% interacting particles for Matlab integrator.
% AJR & HA Jan 2015 -- 2016
global  ll ii nfns
nfns=nfns+1;
% impose triple periodicity on positions
xq(ii)=xq(ii)-round(xq(ii)/ll)*ll;
dxq=hctrlhddtu3d(xq,t);
end
```

A.1.3 Time derivatives of position and velocity

```
function dTxq=hctrlhddtu3d(Txq,t)
% Computes time derivative of position and velocity of
% interacting particles.  Force triply periodic in
% space, periodicity ll. For the moment ignore that this
% dynamical system is sympletic.  AJR & HA Jan 2014 -- 2016
global  ll mucontrol TL TR nAux hh Khsq
% unpack positions
xq=Txq(nAux+1:end);
x=xq(1:6:end);
y=xq(2:6:end);
z=xq(3:6:end);
% d/dt position = velocity
dxq=nan(size(xq));
dxq(1:6:end)=xq(4:6:end);
dxq(2:6:end)=xq(5:6:end);
dxq(3:6:end)=xq(6:6:end);

% Assume triple images enough to capture all significant.
[xxt,xx,lls]=meshgrid(x,x,[-ll 0 ll]);
[yyt,yy,lls]=meshgrid(y,y,[-ll 0 ll]);
[zzt,zz,lls]=meshgrid(z,z,[-ll 0 ll]);
[ddx,px]=min((xx-xxt+lls).^2,[],3);
[ddy,py]=min((yy-yyt+lls).^2,[],3);
[ddz,pz]=min((zz-zzt+lls).^2,[],3);
ds=sqrt(ddx+ddy+ddz)+1e-8;
% forces as a function of distance (with extra / dist)
fs=ds.^(-7-1)-ds.^(-13-1);
fs=-min(100,-fs); % ad hoc limit on force
fx=(xxt(:,:,1)-xx(:,:,1)-(px-2).*ll).*fs;
fy=(yyt(:,:,1)-yy(:,:,1)-(py-2).*ll).*fs;
fz=(zzt(:,:,1)-zz(:,:,1)-(pz-2).*ll).*fs;
% d/dt velocities = sum of forces
dxq(4:6:end)=sum(fx,2);
dxq(5:6:end)=sum(fy,2);
dxq(6:6:end)=sum(fz,2);

% proportional controller of the patch temperature
halfcore=ll/8; % halfwidth of core and action regions
xaction=ll/4;  % action regions centred at quareter points
```

```
% Find which atoms are in each region
jl=(abs(x+xaction)<halfcore);
jc=(abs(x        )<halfcore);
jr=(abs(x-xaction)<halfcore);
% unpack velocities and KEs, to find regional temperatures
u=xq(4:6:end); v=xq(5:6:end); w=xq(6:6:end); ke=(u.^2+v.^2+w.^2)/2;
Tl=mean(ke(jl));
Tc=mean(ke(jc));
Tr=mean(ke(jr));
% Control towards specified environmental temperature
h=ll/2;
r=h/hh;
T0=(Tc/(1-r^2/48)-r^2*(TL+TR)/(96-2*r^2));
Tintl=(1-13*r^2/(48))*T0 +(TL+TR)/2*(13*r^2/48)+(TL-TR)*r/4;
Tintr=(1-13*r^2/(48))*T0 +(TL+TR)/2*(13*r^2/48)+(TR-TL)*r/4;
Tldiff=(Tintl-Tl)*Khsq/Tl;
Trdiff=(Tintr-Tr)*Khsq/Tr;
% de/accelerate in dirn of velocity, propto control
dxq(4:6:end)=dxq(4:6:end)+mucontrol/h^2*(Tldiff*jl+Trdiff*jr).*u;
dxq(5:6:end)=dxq(5:6:end)+mucontrol/h^2*(Tldiff*jl+Trdiff*jr).*v;
dxq(6:6:end)=dxq(6:6:end)+mucontrol/h^2*(Tldiff*jl+Trdiff*jr).*w;
% energies and mean momentum, when tooclose then need more energy code
pe=(-ds.^(-6)/6+ds.^(-12)/12).*(fs>-100);
%tooclose=sum(sum(fs<=-100)-1); if tooclose>0, tooclose=tooclose, end
pe=sum(pe(:))/2; ke=sum(ke); tot=pe+ke;
% other auxillary quantities are mean velocity in regions
ul_av=mean(u(jl)); vl_av=mean(v(jl)); wl_av=mean(w(jl));
uc_av=mean(u(jc)); vc_av=mean(v(jc)); wc_av=mean(w(jc));
ur_av=mean(u(jr)); vr_av=mean(v(jr)); wr_av=mean(w(jr));
%aux=[Tl;Tc;Tr;ul_av;vl_av;wl_av;uc_av;vc_av;wc_av;ur_av;vr_av;wr_av];
aux=[Tl;Tc;Tr;ke;pe;tot;uc_av;vc_av;wc_av;ur_av;vr_av;wr_av];
% return auxillary quantities and atomic time derivatives
dTxq=[aux;dxq];
end
```

A.2 Code to compute many realisations

This ancillary material provides the numerical code for simulating a microscale patch of atoms to determine diffusivity K. It is included to document and potentially reproduce the results.

A.2.1 Main driver code

```
%coded 3d simulation of position and velocity of
% interacting atoms. Uses ode23 to do time integration.
%compute the Temp Difference between left and right action regions
global  ll ii  nfns hh nu maxfns
if 0, NnuTdsTcss=[];
else  NnuTdsTcss=load('NnuTdsTcss.txt');
end
rng('shuffle');
nAtom=512; % number of atoms
tEnd=15;% end time of simulation
maxfns=tEnd*2e3;% limit the total function evaluations
% currently, equilibrium inter-atom distance is one
ll=nAtom.^(1/3);% length of periodic patch (inter-atom eq is at one
hh=ll  % macroscale BCs applied at +/-hh should make smaller fraction

for nu=[0.1 0.2 0.4:0.4:4]
for repeatit=1:1
seed=100+floor(900*rand); %random realisation seed
fileroot=['pwoc' num2str(seed) 'N' num2str(nAtom) 'nu' num2str(round(10*nu))]
rng(seed);
% distribute atoms, randomly up to one per box
ns=ceil(ll);
i=linspace(-0.5,0.5,2*ns+1);
[j,i,p]=meshgrid(ll*i(2:2:end));
[~,k]=sort(rand(size(i(:)))); [tmp,k]=sort(rand(size(i(:))));
xq=[i(k(1:nAtom)) j(k(1:nAtom)) p(k(1:nAtom)) zeros(nAtom,3)]';
% add random position and random velocity
zz=rand(6,nAtom)-0.5; zz=zz-repmat(mean(zz,2),1,nAtom);
% 0.1,1,6 gives Tc=0.15 for N=343
% 0.2,1,6 gives Tc=0.4
% 0.25,1,6 gives Tc=0.6
%xq=xq+0.25*diag([1,1,1,6,6,6])*zz;
xq=xq+0.1*diag([6,6,6,2,2,2])*zz;

% for imposing periodicity in all three dimensions of space
%ii=1:6:6*nAtom; ii=[ii ii+1 ii+2];

% for imposing periodicity in all three dimensions of space
ii=1:6:6*nAtom; ii=[ii ii+1 ii+2]+3;
```

```
% integration in time, initially to reach quasi-equilibrium
ii=ii+3; % accounts for three Temps at front of vector
% simulation in time from given ICs
nfns=0;
[ts,Txqs]=ode23(@vaddtu3dodew,[0 tEnd],[0;0;0;xq(:)]);
xqs=Txqs(:,4:end); ii=ii-3;
xqs(:,ii)=xqs(:,ii)-round(xqs(:,ii)/ll)*ll;
% differentiate the temperature integrals in the zones
Tl=diff(Txqs(:,1))./diff(ts);
Tc=diff(Txqs(:,2))./diff(ts);
Tr=diff(Txqs(:,3))./diff(ts);
ts2=(ts(1:end-1)+ts(2:end))/2;
nFunctions=nfns
% Exclude transients from averages
j=find(ts2>2);
meanTdiff=mean(Tr(j)-Tl(j));
stdTdiff=std(Tr(j)-Tl(j));
meanTc=mean(Tc(j));
stdTc=std(Tc(j));
NnuTdsTcs=[nAtom nu meanTdiff stdTdiff meanTc stdTc]
NnuTdsTcss=[NnuTdsTcss;NnuTdsTcs];
save('NnuTdsTcss.txt','NnuTdsTcss','-ascii')
% Plot the temperature differences between left and right regions
figure(1)
subplot(2,1,1);
plot(ts2,Tr-Tl)
subplot(2,1,2);
plot(ts2,[Tl Tc Tr]),legend('left','centre','right','Location','SouthEast')
print('-depsc2', [fileroot 'Ts'])
end% repeat-loop
end% nu-loop

unix('say "I have finished the atomistic simulation"')
```

A.2.2 Interpose periodicity on positions

This function avoids MATLAB's `ode23` objecting to discontinuities as atoms move across edges of the periodic box.

```
function dxq=vaddtu3dodew(t,xq)
% Computes time derivative of position and velocity of
```

```
% interacting particles for Matlab integrator.
global  ll ii nfns maxfns
if nfns>maxfns, error('**** Too many function---abort'), end
% impose triple periodicity on position
nfns=nfns+1;
xq(ii)=xq(ii)-round(xq(ii)/ll)*ll;
dxq=vaddtu3dw(xq,t);
end
```

A.2.3 Time derivative

```
function dTxq=vaddtu3dw(Txq,t)
% Computes time derivative of position and velocity of
% interacting particles.  Force doubly periodic in
% space, periodicity ll.
global  ll  nu
xq=Txq(4:end);
% unpack positions
x=xq(1:6:end);
y=xq(2:6:end);
z=xq(3:6:end);
n=size(x,1);
% d/dt of positions are the velocities
dxq=nan(size(xq));
dxq(1:6:end)=xq(4:6:end);
dxq(2:6:end)=xq(5:6:end);
dxq(3:6:end)=xq(6:6:end);
% Assumes these are enough to capture all significant.
% Symmetry should be maintained.
% Find full distance matrix.
% those within half a period of each atom??
[xxt,xx,lls]=meshgrid(x,x,[-ll 0 ll]);
[yyt,yy,lls]=meshgrid(y,y,[-ll 0 ll]);
[zzt,zz,lls]=meshgrid(z,z,[-ll 0 ll]);
[ddx,px]=min((xx-xxt+lls).^2,[],3);
[ddy,py]=min((yy-yyt+lls).^2,[],3);
[ddz,pz]=min((zz-zzt+lls).^2,[],3);
ds=sqrt(ddx+ddy+ddz)+1e-8;
% forces as a function of distance (with extra / dist)
fs=+ds.^(-7-1)-ds.^(-13-1);
fs=-min(100,-fs);% ad hoc limit on force
```

```
fx=(xxt(:,:,1)-xx(:,:,1)-(px-2).*ll).*fs;
fy=(yyt(:,:,1)-yy(:,:,1)-(py-2).*ll).*fs;
fz=(zzt(:,:,1)-zz(:,:,1)-(pz-2).*ll).*fs;
% d/dt velocities are the sum of forces
dxq(4:6:end)=sum(fx,2);%du/dt
dxq(5:6:end)=sum(fy,2);%dv/dt
dxq(6:6:end)=sum(fz,2);%dw/dt
%%%%%%%%%%%%%%%%%%%%%%%%%%%%%%%%%%%%%%%%%%%%%%%%%%%%
% Deal with averages over x-intervals of this half size.
halfcore=ll/8;
% Set the action regions centred at the quarter points of the period
xaction=ll/4;
% find which atoms are in each region
jl=(abs(x+xaction)<halfcore);
jc=(abs(x        )<halfcore);
jr=(abs(x-xaction)<halfcore);
%unpack velocities and KEs, to find regional temper
u=xq(4:6:end); v=xq(5:6:end); w=xq(6:6:end); ke=u.^2+v.^2+w.^2;
Tl=mean(ke(jl));
Tc=mean(ke(jc));
Tr=mean(ke(jr));
% de/accelerate in dirn of velocity, forcing heating/cooling at some rate
h=ll/2;% patch half-width
dxq(4:6:end)=dxq(4:6:end)+nu/h^2*(jr/(2*Tr)-jl/(2*Tl)).*u;
dxq(5:6:end)=dxq(5:6:end)+nu/h^2*(jr/(2*Tr)-jl/(2*Tl)).*v;
dxq(6:6:end)=dxq(6:6:end)+nu/h^2*(jr/(2*Tr)-jl/(2*Tl)).*w;
%return quantities and atomic time derivatives
dTxq=[Tl;Tc;Tr;dxq];
end
```

A.3 Results of 58 computational simulations

This appendix contains the results of 58 computational simulations with different cooling/heating parameters ν and different initial conditions. The average temperature difference $T_r - T_l$, and core temperature field T_c averaged over $t > 2$, for different forcing cooling/heating parameters ν, are listed. The simulation is of 512 atoms in a patch of spatial periodicity $2h = 8$.

Table A.1: Compute the average temperature differences $T_r - T_l$, and a core temperature field T_c averaged over $t > 2$, for different forcing cooling/heating parameters ν. The simulation is of 512 atoms in a patch of spatial periodicity $2h = 8$.

ν	$T_r - T_l$	T_c
0.100	0.009	0.126
0.100	0.010	0.124
0.100	0.016	0.123
0.100	0.010	0.260
0.100	0.017	0.254
0.100	0.033	0.259
0.100	0.011	0.163
0.100	0.011	0.175
0.100	0.016	0.181
0.100	0.009	0.102
0.100	0.009	0.109
0.100	0.009	0.105
0.200	0.021	0.135
0.200	0.024	0.124
0.200	0.022	0.131
0.200	0.012	0.262
0.200	0.024	0.254
0.200	0.031	0.252
0.200	0.024	0.169
0.200	0.028	0.175
0.200	0.025	0.184
0.200	0.026	0.102
0.200	0.029	0.107
0.200	0.035	0.115
0.500	0.077	0.129
0.500	0.068	0.131
0.500	0.062	0.136
0.500	0.066	0.245
0.500	0.064	0.256
0.500	0.072	0.243
0.500	0.074	0.175
0.500	0.052	0.174
0.500	0.051	0.174
0.500	0.069	0.115
0.500	0.076	0.109
0.500	0.078	0.113
0.700	0.088	0.135
0.700	0.098	0.132
0.700	0.098	0.141
0.700	0.110	0.248
0.700	0.092	0.248
0.700	0.102	0.253
0.700	0.091	0.180
0.700	0.097	0.166
0.700	0.076	0.171
0.700	0.102	0.114
0.700	0.099	0.120
0.700	0.101	0.114
0.900	0.131	0.134
0.900	0.123	0.132
0.900	0.130	0.133
0.900	0.118	0.140
0.900	0.127	0.241
0.900	0.118	0.255
0.900	0.125	0.247
0.900	0.1132	0.170
0.900	0.126	0.177
0.900	0.119	0.173

Appendix B

Reduce programs

This appendix lists the computer algebra codes that constructed the slow manifold models. The code of Section B.1 generates the slow manifold and its evolution of the gap-tooth scheme applied to the diffusion PDE in Chapter 4. Section B.2 lists the code for constructing the slow manifold (5.67) and the corresponding evolution (5.68) on the slow manifold of the gap-tooth scheme applied to the advection-diffusion PDE by solving the PDE (5.66) with coupling conditions (5.53) and amplitude conditions in Chapter 5. Section B.2 also lists the computer algebra code to construct the slow manifold (5.84) and the corresponding evolution (5.85) (on the slow manifold) of the gap-tooth scheme applied to the reaction-diffusion PDE.

B.1 Computer algebra code constructs the slow manifold of the diffusion PDEs

This section describes how the Reduce code of Algorithm 10 solves the coupled patch system (4.26) and (4.23) to construct the slow manifold model (4.35) and its evolution (4.36).

Preliminaries

Lines 3–4 Set up the printing format to improve printing of the results

Lines 6–13 Define the operator `linv` to act as the inverse of $\mathcal{L}v = d^2v/d\xi^2$ with boundary conditions $v(0) = 0$ and $v(+1) = v(-1)$.

Lines 16–17 Firstly, define the macroscale parametric variable U to depend upon time; and secondly define time derivatives of U, that is $\frac{dU}{dt}$, as `g(j)` since $g_j = \frac{dU_j}{dt}$, by definitions in Section 4.1.2, at the time of replacement and, as `g(j)` stores the current approximation of the macroscale evolution (4.26).

Lines 18–19 Assign the linear, slow subspace, approximation of the slow manifold to be the initial value of the variables `u_j` and `g(j)`, that is, piecewise constant fields and no evolution (the initial evolution of the variables is zero)

Line 22 Execute iterations in a safe for-loop. The truncation of the asymptotic approximation is controlled by the `let` command which informs Reduce to discard any factor in γ^3 or higher. Thus all expressions are computed to an error of $\mathcal{O}(\gamma^3)$. The `let` command is one advantage of Reduce. In other computer algebra systems, one need to substitute $\gamma^3 = 0$ frequently into various expressions to achieve the same aim.

Iteratively construct slow manifold model

Line 24 Now start the iteration, repetitively find corrections until all residuals are zero (to a maximum of nine iterations).

Line 25 Within the iteration, compute the residuals, in the jth patch, of the required equations as a very direct translation of the algebraic form of the diffusion PDE (4.26), the patch boundary conditions (4.23), and the amplitude condition (4.3).

Lines 26–41 Coupling conditions are coded in terms of classic Lagrange interpolation. Thus, let the interpolation fields here to be functions of the surrounding macroscale grid values.

Line 43 Choose the correction to the evolution `g` so that at the slow manifold corrections exists.

Line 44–45 Solve for the correction to the microscale field u and update the current approximation.

Line 46–48 Terminate the iteration when all residuals are zero to the specified order.

Algorithm 10 Construct the slow manifold of the diffusion PDE (4.26) to errors $\mathcal{O}(\gamma^3)$.

```
%Use iteration to form the slow manifold model of the diffusion
% formating for printed output
on revpri; on div; off allfac;
factor gamma,hh,r,xi;
%provide linear algebra functions
operator linv; linear linv;
let { linv(xi^~p,xi)=>(xi^(p+2)-(1-(-1)^p)*xi/2)/(p+1)/(p+2)
 , linv(xi,xi)=>(xi^3-xi)/6
 ,linv(1,xi)=>(xi^2)/2 };
operator mean; linear mean;
let { mean(xi^~p,xi)=>(1+(-1)^p)/2/(p+1)
 , mean(xi,xi)=>0
 , mean(1,xi)=>1 };
% parametrise slow manifold with uu(j)
%LetU, depend on t
operator uu; depend uu,t;
let df(uu(~k),t)=>sub(j=k,gj);
% initial approximation in jth patch
uj:=uu(j); gj:=0;
% iterative refinement patch size r
%the slow manifold is local in parameter gamma so we have
% to truncate the analysis in some power of gamma
let gamma^3=>0;% We can iterate to error gamma^4 as well
% iterate until equations satisfied
for iter:=1:9 do begin
respde:=-df(uj,t)+df(uj,xi,2)/hh^2;
uuj:=sub(xi=0,uj); % mid-patch value
dduuj:=sub(j=j+1,uuj)-2*uuj+sub(j=j-1,uuj);%delta^2
mduuj:=(sub(j=j+1,uuj)-sub(j=j-1,uuj))/2;%mu*delta
dddduuj:=sub(j=j+1,dduuj)-2*dduuj+sub(j=j-1,dduuj);%delt^4
mdduuj:=(sub(j=j+1,dduuj)-sub(j=j-1,dduuj))/2;%mu *delt^3
mdddduuj:=(sub(j=j+1,dddduuj)-sub(j=j-1,dddduuj))/2;%mu *delt^5
dddddduuj:=sub(j=j+1,dddduuj)-2*dddduuj+sub(j=j-1,dddduuj);%delt^6
resrcc:=sub(xi=+r,uj)-sub(xi=0,uj)%RCC
-gamma*(+r*mduuj+r^2/2*dduuj)
-gamma^2*(+(r^3-r)/6*mdduuj+(r^4-r^2)/24*dddduuj)
-gamma^3*(+(r^5-5*r^3+4*r)/120*mdddduuj+(r^6-5*r^4+4*r^2)/720*dddddduuj);
reslcc:=sub(xi=-r,uj)-sub(xi=0,uj)%LCC
-gamma*(-r*mduuj+r^2/2*dduuj)
-gamma^2*(-(r^3-r)/6*mdduuj+(r^4-r^2)/24*dddduuj)
-gamma^3*(-(r^5-5*r^3+4*r)/120*mdddduuj+(r^6-5*r^4+4*r^2)/720*dddddduuj);
resamp:=sub(xi=0,uj)-uu(j);
write
gj:=gj+(gd:=-(resrcc+reslcc)/hh^2/r^2+mean(respde,xi));
write
uj:=uj+hh^2*linv(-respde+gd,xi)+xi*(reslcc-resrcc)/2/r;
if {respde,resrcc,reslcc,resamp}={0,0,0,0}
then write iter:=10000+iter;
end;
end;
```

B.1.1 Construct the slow manifold model with physical boundary conditions

This section lists the computer algebra code of Algorithm 11 to construct the slow manifold (4.40) and the corresponding evolution (4.41) of the diffusion PDE (4.26) with physical boundary conditions to the errors $\mathcal{O}(\gamma^2)$.

To construct the slow manifold (4.48) of the diffusion PDE (4.26) with physical boundary conditions to the errors $\mathcal{O}(\gamma^2)$, we simply execute the computer algebra code of Algorithm 11 with time-varying boundary conditions incorporated as in Algorithm 12. Algorithm 12 shows how to simply code time-varying boundary values, and that we discard any sufficiently high order derivatives in time. The iterative computer algebra considers all the information interactions between time-varying boundary values and the out-of-equilibrium dynamics of the field.

Algorithm 11 Construct the slow manifold of diffusion PDE (4.26) with physical boundary conditions to errors $\mathcal{O}(\gamma^2)$.

```
%Use iteration to form the slow manifold model of the diffusion
% connect to physical BCs
% formating for printed output
on revpri; on div; off allfac;
factor gamma,hh,r,xi;
%provide linear algebra functions
operator linv; linear linv;
let { linv(xi^~p,xi)=>(xi^(p+2)-(1-(-1)^p)*xi/2)/(p+1)/(p+2)
, linv(xi,xi)=>(xi^3-xi)/6
,linv(1,xi)=>(xi^2)/2 };
operator mean; linear mean;
let { mean(xi^~p,xi)=>(1+(-1)^p)/2/(p+1)
, mean(xi,xi)=>0
, mean(1,xi)=>1 };
% parametrise slow manifold with uu(j)
%LetU, depend on t
operator uu; depend uu,t;
let df(uu(~k),t)=>sub(j=k,gj);
% initial approximation in jth patch
uj:=uu(j); gj:=0;1
% for physical bcs
operator lbc; operator rbc;
let { lbc(~j)^2=>lbc(j), lbc(~j)*lbc(~k)=>0 when j neq k
, rbc(~j)^2=>rbc(j), rbc(~j)*rbc(~k)=>0 when j neq k };

% iterative refinement patch size r
let gamma^2=>0;
% iterate until equations satisfied
for iter:=1:9 do begin
respde:=-df(uj,t)+df(uj,xi,2)/hh^2;
resrcc:=sub(xi=+r,uj)-(1-gamma*r^2)*sub(xi=0,uj)
-gamma*r*(-1+r)/2*(lbc(j)*a+(1-lbc(j))*sub({xi=0,j=j-1},uj))
-gamma*r*(1+r)/2*(rbc(j)*b+(1-rbc(j))*sub({xi=0,j=j+1},uj));
reslcc:=sub(xi=-r,uj)-(1-gamma*r^2)*sub(xi=0,uj)
-gamma*r*(-1+r)/2*(rbc(j)*b+(1-rbc(j))*sub({xi=0,j=j+1},uj))
-gamma*r*(1+r)/2*(lbc(j)*a+(1-lbc(j))*sub({xi=0,j=j-1},uj));
resamp:=sub(xi=0,uj)-uu(j);
write
gj:=gj+(gd:=-(resrcc+reslcc)/hh^2/r^2+mean(respde,xi));
write
uj:=uj+hh^2*linv(-respde+gd,xi)+xi*(reslcc-resrcc)/2/r;
if {respde,resrcc,reslcc,resamp}={0,0,0,0}
then write iter:=10000+iter;
end;
end;
```

Algorithm 12 Construct the slow manifold of diffusion PDE (4.26) with time-varying physical boundary conditions to errors $\mathcal{O}(\gamma^2)$.

```
% connect to BCs
  depend a,t; depend b,t;
  let { df(a,t,~p)=>0 when fixp(p) and p>2
  , df(b,t,~p)=>0 when fixp(p) and p>2 };
```

B.2 Construct the slow manifold of advection-diffusion and reaction-diffusion equations

This section lists the computer algebra code of Algorithm 13 to construct the slow manifold (5.67) of the advection-diffusion PDE (5.54) to errors $\mathcal{O}(\gamma^2, V_0^3)$.

This section also lists the computer algebra code of Algorithm 14 with time-varying boundary conditions to construct the slow manifold (5.84) of the reaction-diffusion PDE (5.71) on a small patch, size r, coupled to ‘distant’ boundaries.

Algorithm 13 Construct the slow manifold of advection-diffusion PDE (5.54) to errors $\mathcal{O}(\gamma^2, V_0^3)$.

```
% Computer algebra constructs the slow manifold in the
on revpri; on div; off allfac;
% define operators
factor gamma,hh,r,xi,vv0;
operator linv; linear linv;
let { linv(xi^~p,xi)=>(xi^(p+2)-(1-(-1)^p)*xi/2)/(p+1)/(p+2)
 , linv(xi,xi)=>(xi^3-xi)/6
 ,linv(1,xi)=>(xi^2)/2 };
operator mean; linear mean;
let { mean(xi^~p,xi)=>(1+(-1)^p)/2/(p+1)
 , mean(xi,xi)=>0
 , mean(1,xi)=>1 };
% parametrise slow manifold with uu(j)
operator uu;
% this operator depends upon time
depend uu,t;
let df(uu(~k),t)=>sub(j=k,gj);
% initial approximation in jth patch
uj:=uu(j); gj:=0;
% iterative refinement patch size r
let gamma^2=>0;% We can iterate to error gamma^3 as well
let vv0^3=>0
% iterate until equations satisfied
for iter:=1:9 do begin
respde:=-df(uj,t)-vv0*df(uj,xi)/hh+df(uj,xi,2)/hh^2;
uuj:=sub(xi=0,uj); % mid-patch value
dduuj:=sub(j=j+1,uuj)-2*uuj+sub(j=j-1,uuj);%delta^2
mduuj:=(sub(j=j+1,uuj)-sub(j=j-1,uuj))/2;%mu*delta
d4uuj:=sub(j=j+1,dduuj)-2*dduuj+sub(j=j-1,dduuj);%delt^4
md3uuj:=(sub(j=j+1,dduuj)-sub(j=j-1,dduuj))/2;%mu *delt^3
md5uuj:=(sub(j=j+1,d4uuj)-sub(j=j-1,d4uuj))/2;%mu *delt^5
d6uuj:=sub(j=j+1,d4uuj)-2*d4uuj+sub(j=j-1,d4uuj);%delt^6
resrcc:=sub(xi=+r,uj)-sub(xi=0,uj)%RCC
-gamma*(+r*mduuj+r^2/2*dduuj)
-gamma^2*(+(r^3-r)/6*md3uuj+(r^4-r^2)/24*d4uuj)
-gamma^3*(+(r^5-5*r^3+4*r)/120*md5uuj+(r^6-5*r^4+4*r^2)/720*d6uuj);
reslcc:=sub(xi=-r,uj)-sub(xi=0,uj)%LCC
-gamma*(-r*mduuj+r^2/2*dduuj)
-gamma^2*(-(r^3-r)/6*md3uuj+(r^4-r^2)/24*d4uuj)
-gamma^3*(-(r^5-5*r^3+4*r)/120*md5uuj+(r^6-5*r^4+4*r^2)/720*d6uuj);
resamp:=sub(xi=0,uj)-uu(j);
write
gj:=gj+(gd:=-(resrcc+reslcc)/hh^2/r^2+mean(respde,xi));
write
uj:=uj+hh^2*linv(-respde+gd,xi)+xi*(reslcc-resrcc)/2/r;
if {respde,resrcc,reslcc,resamp}={0,0,0,0}
then write iter:=10000+iter;
end;
end;
```

Algorithm 14 Constructs the slow manifold discretisation on a finite domain with time-varying boundary conditions of the reaction-diffusion PDE (5.71) on a small patch, size r, coupled to 'distant' boundaries.

```
on div; off allfac; on revpri; factor r,df; % improve printing
depend a,tau; depend b,tau;
let { df(a,tau,~p)=>0  when numberp(p) and   p>2
 ,  df(b,tau,~p)=>0  when numberp(p) and p>2 };
% solves v''=RHS s.t. v(0)=0 and v(+1)=v(-1)
operator linv; linear linv;
let { linv(xi^~~p,xi)=>(xi^(p+2)-(1-(-1)^p)*xi/2)/(p+1)/(p+2)
 , linv(1,xi)=>(xi^2)/2 };
% solvability condition operator
operator solg; linear solg;
let { solg(xi^~~p,xi)=>(1+(-1)^p)/(p+2)/(p+1)
 , solg(1,xi)=>1 };
% parametrise slow manifold with uu
depend uu,tau; let df(uu,tau)=>g;
% linear approximation is constant field in patch
u:=uu; g:=0;
% truncate asymptotic expansion in patch size r
let c^2=>0;
respde:=-df(u,tau)+df(u,xi,2)-r^2*hh^2*u^3-c*df(u,xi);
let r^3=>0;
% iterate until equations satisfied
for iter:=1:20 do begin
respde:=-df(u,tau)+df(u,xi,2)-r^2*hh^2*u^3;
resrbc:=sub(xi=+1,u)-(1-r^2)*sub(xi=0,u)-a*(r^2-r)/2
-b*(r^2+r)/2;
reslbc:=sub(xi=-1,u)-(1-r^2)*sub(xi=0,u)-a*(r^2+r)/2
-b*(r^2-r)/2;
resamp:=sub(xi=0,u)-uu;
write
g:=g+(gd:=-(resrbc+reslbc)+solg(respde,xi));
u:=u+linv(-respde+gd,xi)+xi*(reslbc-resrbc)/2;
if {respde,resrbc,reslbc,resamp}={0,0,0,0}
then write iter:=10000+iter;
end;
u:=u; g:=g;
end;
```

Bibliography

Abdulle, A., Weinan, E., Engquist, B. & Vanden-Eijnden, E. (2012), 'The heterogeneous multiscale method', *Acta Numerica* **21**, 1–87. doi:10.1017/S0962492912000025.

Abraham, F. F., Broughton, J. Q., Bernstein, N. & Kaxiras, E. (1998), 'Spanning the continuum to quantum length scales in a dynamic simulation of brittle fracture', *EPL (Europhysics Letters)* **44**(6), 783. doi:10.1209/epl/i1998-00536-9.

Abraham, F. F., Walkup, R., Gao, H., Duchaineau, M., De La Rubia, T. D. & Seager, M. (2002), 'Simulating materials failure by using up to one billion atoms and the world's fastest computer: Brittle fracture', *Proceedings of the National Academy of Sciences* **99**(9), 5777–5782. doi:10.1073/pnas.062012699.

Alder, B. J. & Wainwright, T. (1959), 'Studies in molecular dynamics. i. general method', *The Journal of Chemical Physics* **31**(2), 459–466. doi:10.1063/1.1730376.

Alder, B. & Wainwright, T. (1957), 'Phase transition for a hard sphere system', *The Journal of chemical physics* **27**(5), 1208. doi:10.1063/1.1743957.

Allen, M. P. & Tildesley, D. J. (1989), *Computer simulation of liquids*, Vol. 42, Oxford university press. doi:10.1063/1.2810937.

Armstrong, T., Harding, R., Knorr, G., Montgomery, D., Armstrong, T., Harding, R., Knorr, G. & Montgomery, D. (1970), 'Methods in computational physics, vol. 9', *Plasma Physics (Academic, New York and London, 1970)* p. 29.

Arnol'd, V. I. (2013), *Mathematical methods of classical mechanics*, Vol. 60, Springer Science & Business Media. doi:10.1007/978-1-4757-2063-1.

Bechhoefer, J. (2005), 'Feedback for physicists: A tutorial essay on control', *Reviews of Modern Physics* **77**(3), 783–836. doi:10.1103/RevModPhys.77.783.

Broughton, J. Q., Abraham, F. F., Bernstein, N. & Kaxiras, E. (1999), 'Concurrent coupling of length scales: methodology and application', *Physical review B* **60**(4), 2391. doi:10.1103/PhysRevB.60.2391.

Buehler, M. (2008), *Atomistic modeling of materials failure*, Springer Science & Business Media. doi:10.1007/978-0-387-76426-9.

Bunder, J. E. & Roberts, A. J. (2012), 'Patch dynamics for macroscale modelling in one dimension', *ANZIAM Journal* **53**, C280–C295. doi:0.21914/anziamj.v53i0.5074 .

Bunder, J. E., Roberts, A. J. & Kevrekidis, I. G. (2013), 'Better buffers for patches in macroscale simulation of systems with microscale randomness', *preprint arXiv:1312.1415* .

Bunder, J. E., Roberts, A. J. & Kevrekidis, I. G. (2015), 'Accuracy of patch dynamics with mesoscale temporal coupling for efficient exascale simulation', *arXiv preprint arXiv:1504.01810* .

Cao, M. & Roberts, A. J. (2013), 'Multiscale modelling couples patches of wave-like simulations', *ANZIAM Journal* **54**, C153–C170. doi:10.21914/anziamj.v54i0.6137.

Cao, M. & Roberts, A. J. (2016), 'Multiscale modelling couples patches of non-linear wave-like simulations', *IMA Journal of Applied Mathematics* **81**(2), 228–254. doi:10.1093/imamat/hxv034.

Carr, E. J., Perré, P. & Turner, I. W. (2016), 'The extended distributed microstructure model for gradient-driven transport: A two-scale model for bypassing effective parameters', *Journal of Computational Physics* **327**, 810–829. doi:10.1016/j.jcp.2016.10.004.

Carr, E. J. & Turner, I. W. (2014), 'Two-scale computational modelling of water flow in unsaturated soils containing irregular-shaped inclusions', *International Journal for Numerical Methods in Engineering* **98**(3), 157–173. doi:10.1002/nme.4625.

Carr, J. (1981), 'Applications of centre manifold theory', *Applied Mathematical Sciences* **35**. doi:10.1002/zamm.19820621019.

Carr, J. & Muncaster, R. G. (1983), 'The application of centre manifolds to amplitude expansions. ii. infinite dimensional problems', *Journal of differential equations* **50**(2), 280–288. doi:10.1016/0022-0396(83)90078-5.

Carrier, J., Greengard, L. & Rokhlin, V. (1988), 'A fast adaptive multipole algorithm for particle simulations', *SIAM journal on scientific and statistical computing* **9**(4), 669–686. doi:10.1137/0909044.

Cheng, H., Greengard, L. & Rokhlin, V. (1999), 'A fast adaptive multipole algorithm in three dimensions', *J. Computational Physics* **155**, 468–498. doi:10.1006/jcph.1999.6355.

Chicone, C. (2006), *Ordinary Differential Equations with Applications*, Vol. 34, Springer New York. doi:10.1007/0-387-35794-7.

Chicone, C. & Latushkin, Y. (1997), 'Center manifolds for infinite dimensional nonautonomous differential equations', *Journal of differential equations* **141**(2), 356–399. doi:10.1006/jdeq.1997.3343.

Chitode, J. (2008), *Numerical Techniques*, Technical Publications.

Cisternas, J., Gear, C. W., Levin, S. & Kevrekidis, I. G. (2004), 'Equation-free modelling of evolving diseases: coarse-grained computations with individual-based models', *Proceedings of the Royal Society of London A: Mathematical, Physical and Engineering Sciences* **460**(2050), 2761–2779. doi:10.1098/rspa.2004.1300.

Constantin, P., Foias, C., Nicolaenko, B. & Temam, R. (2012), *Integral manifolds and inertial manifolds for dissipative partial differential equations*, Vol. 70, Springer Science & Business Media. doi:10.1007/978-1-4612-3506-4.

Courant, R. & Hilbert, D. (1965), *Methods of mathematical physics*, Vol. 1, CUP Archive.

Dada, J. O. & Mendes, P. (2011), 'Multi-scale modelling and simulation in systems biology', *Integrative Biology* **3**(2), 86–96. doi:10.1039/c0ib00075b.

Deymier, P. A., Runge, K. & Muralidharan, K. (2016), *Multiscale Paradigms in Integrated Computational Materials Science and Engineering*, Springer. doi:10.1007/978-3-319-24529-4.

Dolbow, J., Khaleel, M., Mitchell, J. et al. (2004), 'Multiscale mathematics initiative: a roadmap'.

Dove, M. T. (2008), ‘An introduction to atomistic simulation methods’, *Seminarios de la SEM* **4**, 7–37. `http://www.ehu.eus/sem/seminario_pdf/SEM_SEM_4_7-37.pdf`.

E, W. (2011), *Principles of multiscale modeling*, Cambridge University Press.

E, W. & Engquist, B. (2003), ‘Multiscale modeling and computation’, *Notices of the AMS* **50**(9), 1062–1070.

E, W., Engquist, B., Li, X., Ren, W. & Vanden-Eijnden, E. (2007), ‘Heterogeneous multiscale methods: a review’, *Commun. Comput. Phys* **2**(3), 367–450. doi:10.1.1.225.9038.

Eckhaus, W. (2012), *Studies in non-linear stability theory*, Vol. 6, Springer Science & Business Media. doi:10.1007/978-3-642-88317-0.

Falbo, C. E. (1995), Analytic and numerical solutions to the delay differential equations, *in* ‘Joint Meeting of the Northern and Southern California Sections of the MAA’.

Fan, J. (2011), *Multiscale analysis of deformation and failure of materials*, Vol. 5, John Wiley & Sons. doi:10.1002/9780470972281.

Fateman, R. (2003), ‘Comparing the speed of programs for sparse polynomial multiplication’, *ACM SIGSAM Bulletin* **37**(1), 4–15. doi:10.1145/844076.844080.

Fish, J. (2010), *Multiscale methods: bridging the scales in science and engineering*, Oxford University Press. doi:10.1093/acprof:oso/9780199233854.001.0001.

Foias, C., Jolly, M., Kevrekidis, I. & Titi, E. (1991), ‘Dissipativity of numerical schemes’, *Nonlinearity* **4**(3), 591. `http://stacks.iop.org/0951-7715/4/i=3/a=001`.

Foias, C. & Titi, E. S. (1991), ‘Determining nodes, finite difference schemes and inertial manifolds’, *Nonlinearity* **4**(1), 135. `http://stacks.iop.org/0951-7715/4/i=1/a=009`.

Frauenheim, T., Pederson, M. R. et al. (2000), *Computer simulation of materials at atomic level*, Vol. 1, John Wiley & Sons. doi:10.1002/3527603107.

Frederix, Y., Samaey, G., Vandekerckhove, C. & Roose, D. (2007), ‘Equation-free methods for molecular dynamics: a lifting procedure’, *PAMM* **7**(1), 2010003–2010004. doi:10.1002/pamm.200700025.

Frenkel, D. & Smit, B. (1996), 'Understanding molecular simulations: from algorithms to applications', *Academic, San Diego* . doi:10.1063/1.881812.

Galvanetto, U. & Aliabadi, M. (2010), *Multiscale modeling in solid mechanics: computational approaches*, Vol. 3, World Scientific. doi:10.1504/IJMMP.2010.035952.

Gander, M. J. & Stuart, A. M. (1998), 'Space-time continuous analysis of waveform relaxation for the heat equation', *SIAM Journal on Scientific Computing* **19**(6), 2014–2031. doi:10.1137/S1064827596305337.

Gates, T., Odegard, G., Frankland, S. & Clancy, T. (2005), 'Computational materials: multi-scale modeling and simulation of nanostructured materials', *Composites Science and Technology* **65**(15), 2416–2434. doi:10.1016/j.compscitech.2005.06.009.

Gear, C. W. & Kevrekidis, I. G. (2003), 'Projective methods for stiff differential equations: problems with gaps in their eigenvalue spectrum', *SIAM Journal on Scientific Computing* **24**(4), 1091–1106. doi:10.1137/S1064827501388157.

Gillespie, D. T. (1976), 'A general method for numerically simulating the stochastic time evolution of coupled chemical reactions', *Journal of computational physics* **22**(4), 403–434.

Givon, D., Kupferman, R. & Stuart, A. (2004), 'Extracting macroscopic dynamics: model problems and algorithms', *Nonlinearity* **17**(6), R55. `http://stacks.iop.org/0951-7715/17/i=6/a=R01`.

Gorban, A. N. & Karlin, I. V. (2005), 'Invariant manifolds for physical and chemical kinetics', *Lecture notes in physics* **660**, 1–489. doi:10.1007/b98103.

Guenther, R. B. & Lee, J. W. (1996), *Partial differential equations of mathematical physics and integral equations*, Courier Corporation.

Haberman, R. (2004), *Applied partial differential equations: with Fourier series and boundary value problems*, Vol. 4, Pearson Prentice Hall Upper Saddle River.

Hadjiconstantinou, N. G. (1999), 'Hybrid atomistic–continuum formulations and the moving contact-line problem', *Journal of Computational Physics* **154**(2), 245–265. doi:10.1006/jcph.1999.6302.

Hadjiconstantinou, N. G. & Patera, A. T. (1997), 'Heterogeneous atomistic-continuum representations for dense fluid systems', *International Journal of Modern Physics C* **8**(04), 967–976. doi:10.1142/S0129183197000837.

Hairer, E., Lubich, C. & Wanner, G. (2003), 'Geometric numerical integration illustrated by the Störmer–Verlet method', *Acta Numerica* **12**, 399–450. doi:10.1017/S0962492902000144.

Hassard, P., Turner, I., Farrell, T. & Lester, D. (2016), Simulation of micro-scale porous flow using smoothed particle hydrodynamics, *in* J. Sharples & J. Bunder, eds, 'Proceedings of the 17th Biennial Computational Techniques and Applications Conference, CTAC-2014', Vol. 56 of *ANZIAM J.*, pp. C463–C480. doi:10.21914/anziamj.v56i0.9408.

Holian, B. L. & Ravelo, R. (1995), 'Fracture simulations using large-scale molecular dynamics', *Physical Review B* **51**(17), 11275. doi:10.1103/PhysRevB.51.11275.

Horstemeyer, M. F. (2009), Multiscale modeling: A review, *in* J. Leszczynski & M. K. Shukla, eds, 'Practical Aspects of Computational Chemistry', Springer, chapter 4, pp. 87–135. doi:10.1007/978-90-481-2687-3_4.

Hughes, I. & Hase, T. (2010), *Measurements and their uncertainties: a practical guide to modern error analysis*, Oxford University Press.

Hummer, G. & Kevrekidis, I. G. (2003), 'Coarse molecular dynamics of a peptide fragment: Free energy, kinetics, and long-time dynamics computations', *The Journal of chemical physics* **118**(23), 10762–10773. doi:10.1063/1.1574777.

Hyman, J. M. (2005), 'Patch dynamics for multiscale problems', *Computing in science & engineering* **7**(3), 47–53. doi:10.1109/MCSE.2005.57.

Isenberg, J. & Gutfinger, C. (1973), 'Heat transfer to a draining film', *International Journal of Heat and Mass Transfer* **16**(2), 505–512. doi:10.1016/0017-9310(73)90075-6 .

Jaiswal, D. K., Kumar, A. & Yadav, R. R. (2011), 'Analytical solution to the one-dimensional advection-diffusion equation with temporally dependent coefficients', *Journal of Water Resource and Protection* **3**(01), 76. doi:10.4236/jwarp.2011.31009.

Jones, J. E. (1924), On the determination of molecular fields. ii. from the equation of state of a gas, *in* 'Proceedings of the Royal Society of London

A: Mathematical, Physical and Engineering Sciences', Vol. 106, The Royal Society, pp. 463–477. doi:10.1098/rspa.1924.0082.

Kairn, T., Daivis, P. J., Matin, M. L. & Snook, I. K. (2004), 'Effects of concentration on steady-state viscometric properties of short chain polymer solutions over the entire concentration range', *International journal of thermophysics* **25**(4), 1075–1084. doi:10.1023/B:IJOT.0000038501.03469.76.

Kalweit, M. & Drikakis, D. (2011), 'Multiscale simulation strategies and mesoscale modelling of gas and liquid flows', *IMA journal of applied mathematics* pp. 661–671. doi:10.1093/imamat/hxr048.

Kevorkian, J. & Cole, J. D. (2012), *Multiple scale and singular perturbation methods*, Vol. 114, Springer Science & Business Media. doi:10.1007/978-1-4612-3968-0.

Kevrekidis, I. G., Gear, C. W., Hyman, J. M., Kevrekidid, P. G., Runborg, O., Theodoropoulos, C. et al. (2003), 'Equation-free, coarse-grained multiscale computation: Enabling mocroscopic simulators to perform system-level analysis', *Communications in Mathematical Sciences* **1**(4), 715–762. doi:10.4310/CMS.2003.v1.n4.a5.

Kevrekidis, I. G. & Samaey, G. (2009), 'Equation-free multiscale computation: Algorithms and applications', *Annu. Rev. Phys. Chem.* **60**, 321—44. doi:10.1146/annurev.physchem.59.032607.093610.

Kiuchi, K., Kyutoku, K., Sekiguchi, Y., Shibata, M. & Wada, T. (2014), 'High resolution numerical relativity simulations for the merger of binary magnetized neutron stars', *Physical Review D* **90**(4), 041502. doi:10.1103/PhysRevD.90.041502.

Knap, J. & Ortiz, M. (2001), 'An analysis of the quasicontinuum method', *Journal of the Mechanics and Physics of Solids* **49**(9), 1899–1923. doi:10.1016/S0022-5096(01)00034-5.

Koumoutsakos, P. (2005), 'Multiscale flow simulations using particles', *Annu. Rev. Fluid Mech.* **37**, 457–487. doi:10.1146/annurev.fluid.37.061903.175753.

Kreyszig, E. (2011), *Advanced engineering mathematics*, John Wiley & Sons.

Lewandowska, J., Szymkiewicz, A., Burzyński, K. & Vauclin, M. (2004), 'Modeling of unsaturated water flow in double-porosity soils by the homogenization approach', *Advances in Water Resources* **27**(3), 283–296. doi:10.1016/j.advwatres.2003.12.004.

Li, J., Kevrekidis, P. G., Gear, C. W. & Kevrekidis, I. G. (2007), 'Deciding the nature of the coarse equation through microscopic simulations: The baby-bathwater scheme', *SIAM review* **49**(3), 469–487. doi:10.1137/070692303.

Li, J., Liao, D. & Yip, S. (1998), Imposing field boundary conditions in md simulation of fluids: optimal particle controller and buffer zone feedback, *in* 'MRS Proceedings', Vol. 538, Cambridge Univ Press, p. 473. doi:10.1557/PROC-538-473.

Li, Z., Yi-Bo, G. & Cheng, W. (2009), 'Green function and perturbation method for dissipative systems based on biorthogonal basis', *Communications in Theoretical Physics* **51**(6), 1017. doi:10.1088/0253-6102/51/6/11.

Liu, P., Samaey, G., Gear, C. W. & Kevrekidis, I. G. (2015), 'On the acceleration of spatially distributed agent-based computations: A patch dynamics scheme', *Applied Numerical Mathematics* **92**, 54–69.
URL: *http://www.sciencedirect.com/science/article/pii/S0168927414002086*

Loeb, L. B. (2004), *The kinetic theory of gases*, Courier Corporation.

Lucia, A. (2010), 'Multi-scale methods and complex processes: A survey and look ahead', *Computers & chemical engineering* **34**(9), 1467–1475. doi:10.1016/j.compchemeng.2009.10.004.

Luna-Ortiz, E. & Theodoropoulos, C. (2005), 'An input/output model reduction-based optimization scheme for large-scale systems', *Multiscale Modeling & Simulation* **4**(2), 691–708. doi:10.1137/040604716.

MacKenzie, T. & Roberts, A. J. (2006), 'Accurately model the kuramoto–sivashinsky dynamics with holistic discretization', *SIAM Journal on Applied Dynamical Systems* **5**(3), 365–402. doi:10.1137/050627733.

Maslov, V. P. & Fedoriuk, M. V. (2001), *Semi-classical approximation in quantum mechanics*, Vol. 7, Springer Science & Business Media. doi:10.1007/978-94-009-8410-3.

Mercer, G. N. & Roberts, A. J. (1994), 'A complete model of shear dispersion in pipes', *Japan journal of industrial and applied mathematics* **11**(3), 499–521. doi:10.1007/BF03167234.

Meron, E. & Procaccia, I. (1986), 'Theory of chaos in surface waves: The reduction from hydrodynamics to few-dimensional dynamics', *Physical review letters* **56**(13), 1323. doi:10.1103/PhysRevLett.56.1323.

Miyoshi, T., Kondo, K. & Imamura, T. (2014), ‘The 10,240-member ensemble kalman filtering with an intermediate agcm’, *Geophysical Research Letters* **41**(14), 5264–5271. doi:10.1002/2014GL060863.

Möller, J., Runborg, O., Kevrekidis, P. G., Lust, K. & Kevrekidis, I. G. (2005), ‘Equation-free, effective computation for discrete systems: A time stepper based approach’, *International Journal of Bifurcation and Chaos* **15**(03), 975–996. doi:10.1142/S0218127405012399.

Morari, M. & Zafiriou, E. (1989), *Robust process control*, Vol. 488, Prentice hall Englewood Cliffs, NJ.

Murashima, T., Yasuda, S., Taniguchi, T. & Yamamoto, R. (2012), ‘Multiscale modeling for polymeric flow: particle-fluid bridging scale methods’, *Journal of the Physical Society of Japan* **82**(1), 012001. doi:10.7566/JPSJ.82.012001.

Namachchivaya, N. S. & Lin, Y. (1991), ‘Method of stochastic normal forms’, *International journal of non-linear mechanics* **26**(6), 931–943. doi:10.1016/0020-7462(91)90042-R.

Nguyen, T. D., Carrillo, J.-M. Y., Matheson, M. A. & Brown, W. M. (2014), ‘Rupture mechanism of liquid crystal thin films realized by large-scale molecular simulations’, *Nanoscale* **6**(6), 3083–3096. doi:10.1039/C3NR05413F.

Nielsen, M., Johansen, P., Olsen, O. F. & Weickert, J. (2003), *Scale-Space Theories in Computer Vision: Second International Conference, Scale-Space’99, Corfu, Greece, September 26-27, 1999, Proceedings*, Springer. doi:10.1007/3-540-48236-9.

Ortega, D. R., Yang, C., Ames, P., Baudry, J., Parkinson, J. S. & Zhulin, I. B. (2013), ‘A phenylalanine rotameric switch for signal-state control in bacterial chemoreceptors’, *Nature communications* **4**. doi:10.1038/ncomms3881.

OConnell, S. T. & Thompson, P. A. (1995), ‘Molecular dynamics–continuum hybrid computations: a tool for studying complex fluid flows’, *Physical Review E* **52**(6), R5792. doi:10.1103/PhysRevE.52.R5792.

Parlange, J. (1980), ‘Water transport in soils’, *Annual Review of Fluid Mechanics* **12**(1), 77–102. doi:10.1146/annurev.fl.12.010180.000453.

Pavliotis, G. A. & Stuart, A. (2008), *Multiscale methods: averaging and homogenization*, Springer Science & Business Media. `http://www.springer.com/mathematics/analysis/book/978-0-387-73828-4`.

Plimpton, S., Thompson, A., Shan, R., Moore, S., Kohlmeyer, A., Crozier, P. & Stevens, M. (2016), 'Large-scale atomic/molecular massively parallel simulator'. `http://lammps.sandia.gov`.

Pötzsche, C. & Rasmussen, M. (2006), 'Taylor approximation of integral manifolds', *Journal of Dynamics and Differential Equations* **18**(2), 427–460. doi:10.1007/s10884-006-9011-8.

Presmeg, N. C. (2006), 'Research on visualization in learning and teaching mathematics', *Handbook of research on the psychology of mathematics education* pp. 205–235.

Procaccia, I. (1988), 'Universal properties of dynamically complex systems-the organization of chaos', *Nature* **333**, 618–623. doi:10.1038/333618a0.

Rahman, A. (1964), 'Correlations in the motion of atoms in liquid argon', *Physical Review* **136**(2A), A405. doi:10.1103/PhysRev.136.A405.

Ren, W. et al. (2005), 'Heterogeneous multiscale method for the modeling of complex fluids and micro-fluidics', *Journal of Computational Physics* **204**(1), 1–26. doi:10.1007/978-94-007-0412-1_18.

Roberts, A. J. (1988), 'The application of centre-manifold theory to the evolution of system which vary slowly in space', *The Journal of the Australian Mathematical Society. Series B. Applied Mathematics* **29**(04), 480–500. doi:10.1017/S0334270000005968.

Roberts, A. J. (1996), 'Low-dimensional models of thin film fluid dynamics', *Physics Letters A* **212**(1), 63–71. doi:10.1016/0375-9601(96)00040-0.

Roberts, A. J. (1997), 'Low-dimensional modelling of dynamics via computer algebra', *Computer physics communications* **100**(3), 215–230. doi:10.1016/S0010-4655(96)00162-2.

Roberts, A. J. (2001), 'Holistic discretization ensures fidelity to burgers' equation', *Applied numerical mathematics* **37**(3), 371–396. doi:10.1016/S0168-9274(00)00053-2.

Roberts, A. J. (2003*a*), 'Derive boundary conditions for holistic discretisations of burgers' equation', *ANZIAM Journal* **44**, 664–686.

Roberts, A. J. (2003*b*), 'A holistic finite difference approach models linear dynamics consistently', *Mathematics of Computation* **72**(241), 247–262. `http://www.jstor.org/stable/4099990`.

Roberts, A. J. (2014), *Model emergent dynamics in complex systems*, SIAM.

Roberts, A. J. & Kevrekidis, I. G. (2005), 'Higher order accuracy in the gap-tooth scheme for large-scale dynamics using microscopic simulators', *ANZIAM Journal* **46**, 637–657. doi:10.21914/anziamj.v46i0.981.

Roberts, A. J. & Kevrekidis, I. G. (2007), 'General tooth boundary conditions for equation free modeling', *SIAM Journal on Scientific Computing* **29**(4), 1495–1510. doi:10.1137/060654554.

Roberts, A. J., MacKenzie, T. & Bunder, J. E. (2011), 'Accurate macroscale modelling of spatial dynamics in multiple dimensions', *Journal of Engineering Mathematics* **86**(1), 175–207. doi:10.1007/s10665-013-9653-6.

Roberts, A. J., MacKenzie, T. & Bunder, J. E. (2014), 'A dynamical systems approach to simulating macroscale spatial dynamics in multiple dimensions', *Journal of Engineering Mathematics* **86**(1), 175–207. doi:10.1007/s10665-013-9653-6.

Roberts, A. J., Mei, Z. & Li, Z. (2003), 'Modelling the dynamics of turbulent floods', *SIAM Journal on Applied Mathematics* **63**(2), 423–458. doi:10.1137/S0036139999358866.

Roose, D., Nies, E., Li, T., Vandekerckhove, C., Samaey, G. & Frederix, Y. (2009), 'Lifting in equation-free methods for molecular dynamics simulations of dense fluids', *Discrete and Continuous Dynamical Systems—Series B* **11**(4), 855–874. doi:10.3934/dcdsb.2009.11.855.

Rosencrans, S. (1997), 'Taylor dispersion in curved channels', *SIAM Journal on Applied Mathematics* **57**(5), 1216–1241. doi:10.1137/S003613999426990X.

Roy, R. V., Roberts, A. J. & Simpson, M. (2002), 'A lubrication model of coating flows over a curved substrate in space', *Journal of Fluid Mechanics* **454**(10), 235–261. doi:10.1017/S0022112001007133.

Runborg, O., Theodoropoulos, C. & Kevrekidis, I. G. (2002), 'Effective bifurcation analysis: a time-stepper-based approach', *Nonlinearity* **15**(2), 491. `http://stacks.iop.org/0951-7715/15/i=2/a=314`.

Sadiku, M. & Obiozor, C. (2000), 'A simple introduction to the method of lines', *International Journal of Electrical Engineering Education* **37**(3), 282–296. doi:10.7227/IJEEE.37.3.8.

Samaey, G., Kevrekidis, I. G. & Roose, D. (2005), 'The gap-tooth scheme for homogenization problems', *Multiscale Modeling and Simulation* **4**, 278–306. doi:10.1137/030602046.

Samaey, G., Kevrekidis, I. G. & Roose, D. (2006), 'Patch dynamics with buffers for homogenization problems', *Journal of Computational Physics* **213**(1), 264–287. doi:0.1016/j.jcp.2005.08.010.

Samaey, G., Roberts, A. J. & Kevrekidis, I. G. (2010), 'Equation-free computation: an overview of patch dynamics.', *Multiscale methods: bridging the scales in science and engineering* **8**, 216–246. doi:10.1093/acprof:oso/9780199233854.003.0008.

Samaey, G., Roose, D. & Kevrekidis, I. (2004), Combining the gap-tooth scheme with projective integration: patch dynamics, *in* 'Multiscale Methods in Science and Engineering', Vol. 44, pp. 227–242. doi:10.1007/3-540-26444-2_12.

Satoh, A. (2010), *Introduction to practice of molecular simulation: molecular dynamics, Monte Carlo, Brownian dynamics, Lattice Boltzmann and dissipative particle dynamics*, Elsevier.

Schlick, T. (2010), *Molecular modeling and simulation: an interdisciplinary guide: an interdisciplinary guide*, Vol. 21, Springer Science & Business Media. doi:10.1007/978-1-4419-6351-2.

Schöner, G. & Haken, H. (1986), 'The slaving principle for Stratonovich stochastic differential equations', *Zeitschrift für Physik B Condensed Matter* **63**(4), 493–504. doi:10.1007/BF01726198.

Shilkrot, L., Miller, R. & Curtin, W. (2002), 'Coupled atomistic and discrete dislocation plasticity', *Physical review letters* **89**(2), 025501. doi:10.1103/PhysRevLett.89.025501.

Showalter, R. E. (1997), 'Microstructure models of porous media', *Homogenization and porous media* **6**. doi:10.1007/978-1-4612-1920-0_9.

Smith, J. A. & Todd, P. E. (2001), 'Reconciling conflicting evidence on the performance of propensity-score matching methods', *The American Economic Review* **91**(2), 112–118. doi:10.1257/aer.91.2.112.

Solhjoo, S. & Vakis, A. I. (2015), 'Definition and detection of contact in atomistic simulations', *Computational Materials Science* **109**, 172–182. doi:10.1016/j.commatsci.2015.07.026.

Sotomayor, M. M. (2007), *Life under tension: Computational studies of proteins involved in mechanotransduction*, ProQuest. `http://hdl.handle.net/2142/80566`.

Stein, E. M. & Murphy, T. S. (1993), *Harmonic analysis: real-variable methods, orthogonality, and oscillatory integrals*, Vol. 3, Princeton University Press.

Succi, S. (2001), *The lattice Boltzmann equation: for fluid dynamics and beyond*, Oxford university press. doi:10.1016/S0997-7546(02)00005-5 .

Szymkiewicz, A. & Lewandowska, J. (2008), 'Micromechanical approach to unsaturated water flow in structured geomaterials by two-scale computations', *Acta Geotechnica* **3**(1), 37–47. doi:10.1007/s11440-007-0049-5.

Tamarkin, J. (1928), 'Some general problems of the theory of ordinary linear differential equations and expansion of an arbitrary function in series of fundamental functions', *Mathematische Zeitschrift* **27**(1), 1–54. doi:10.1007/BF01171084.

Vanderbauwhede, A. (1989), Centre manifolds, normal forms and elementary bifurcations, *in* 'Dynamics reported', Springer, pp. 89–169. doi:10.1007/978-3-322-96657-5_4.

Weinberger, H. F. (2012), *A first course in partial differential equations: with complex variables and transform methods*, Courier Corporation.

Wright, E. M. (1946), 'The non-linear difference-differential equation', *The Quarterly Journal of Mathematics* (1), 245–252. doi:10.1093/qmath/os-17.1.245.

Xu, K. & Prendergast, K. H. (1994), 'Numerical Navier-Stokes solutions from gas kinetic theory', *Journal of Computational Physics* **114**(1), 9–17. doi:10.1006/jcph.1994.1145.

Yoshida, H. (1993), 'Recent progress in the theory and application of symplectic integrators', *Celest Mech & Dyn Astron* **56**, 27–43. doi:10.1007/BF00699717.

Zill, D. & Wright, W. (2012), *Differential equations with boundary-value problems*, Cengage Learning.